COMPACT BIHARMONIC COMPUTATION OF THE NAVIER-STOKES EQUATIONS: EXTENSION TO COMPLEX FLOWS

A Thesis Submitted

in Partial Fulfillment of the Requirements

for the Degree of

DOCTOR OF PHILOSOPHY

by

Shuvam Sen

(Roll Number: 07612306)

to the

DEPARTMENT OF MATHEMATICS

INDIAN INSTITUTE OF TECHNOLOGY GUWAHATI

July, 2012

DECLARATION

It is certified that the work contained in the thesis titled **"Compact Biharmonic Computation of the Navier-Stokes Equations: Extension to Complex Flows"** has been done by me, a student in the Department of Mathematics, Indian Institute of Technology Guwahati under the guidance of Dr. Jiten C Kalita for the award of Doctor of Philosophy and that this work has not been submitted elsewhere for a degree.

July, 2012

Shuvam Sen
Department of Mathematics
Indian Institute of Technology Guwahati

CERTIFICATE

It is certified that the work contained in the thesis titled **"Compact Biharmonic Computation of the Navier-Stokes Equations: Extension to Complex Flows"** by **Shuvam Sen**, a student in the Department of Mathematics, Indian Institute of Technology Guwahati for the award of the degree of Doctor of Philosophy has been carried out under my supervision and this work has not been submitted elsewhere for a degree.

July, 2012

Dr. Jiten C Kalita
Associate Professor
Department of Mathematics
Indian Institute of Technology Guwahati

Dedicated to

all those who have

Wished, Prayed and Endured for this work

Acknowledgement

I would like to thank my thesis supervisor Dr. Jiten C Kalita and my past and present doctoral committee members Prof. Durga C Dalal, Dr. Siddhartha P Chakrabarty and Dr. Swaroop N Bora of the Department of Mathematics and Prof. Anoop K Dass of the Department of Mechanical Engineering for reviewing my research work regularly and for all their valuable suggestions.

I owe a huge debt of gratitude to my thesis supervisor Dr. Jiten C Kalita for his intensity and inspiration. Thank you for all the knowledge and experience that you have shared with me so freely. I am extremely grateful to you for the opportunities that you have given when there were actually very few and the trouble that you have taken for me. I owe a huge debt of gratitude to Mrs. Deepshikha Choudhury who has truly been a *gurumata* to me. I would like to thank Dr. Jiten C Kalita and Mrs. Deepshikha Choudhury for opening up their home to me. I imposed on them frequently, often with little notice and I will certainly never be able to repay their hospitality.

I also thank sincerely my course instructors Prof. Rajen K Sinha from the Department of Mathematics and Prof. Uday S Dixit, Prof. Anupam Dewan and Prof. Anoop K Dass from the Department of Mechanical Engineering. The courses taught by them have helped me immensely in my research work. I take this opportunity to thank all the faculty members of the Department of Mathematics especially the heads of the department Prof. Rafikul Alam and Prof. Rajen K Sinha for their kind assistance and discussions.

I express my deep sense of appreciation for Prof. Mihir K Chaudhuri, Vice-Chancellor, Tezpur University. Without his constant encouragement, concern, help and affection this journey may not have been possible.

In the same vein I will like to acknowledge the contribution of all the heads of the Department of Mathematical Sciences, Tezpur University, Prof. Munindra Borah, Prof. Nayandeep D Baruah and Prof. Debajit Hazarika under whose leadership I have served for their flexibility and warmth. They have always gone out of their way to help me. Thanks are also due to other faculty members of the

Department of Mathematical Sciences, Tezpur University.

I express my sincere thanks to Mr. Santanu Majumdar, Jr. Technical Superintendent, IIT Guwahati for technical support and Mr. Sridhar Samal, Jr. Assistant, IIT Guwahati for his help in official matters.

I am thankful to all the research scholars of the Department of Mathematics, IIT Guwahati with whom I have shared the research scholars room for all these years.

On the personal level, I am fortunate to have great friends and surely no word is enough to express their encouragement and involvement. I thank them from the core of my heart.

My revered regard goes to my parents. I am deeply indebted to them for their blessing, love, patience, inspiration and special care during my studies. They have an immense influence on my life and work. I owe a huge debt of gratitude to my wife and son. Indeed they have endured the most. I would like to thank my wife for her support, love, encouragement and patience through out the period of my Ph. D. work.

Last but not least, though it is beyond the scope of any acknowledgement for all of my family members especially my brothers whose hearty wishes and affectionate love enable me accomplish this journey. Here my elder brother deserve special mention with whom I have had always enjoyed discussions.

I am thankful to the University Grants Commission (UGC), Government of India for supporting a part of the work by providing financial support in the form of a minor project (Project No. F. No. 37-537/2009(SR)).

July, 2012

(Shuvam Sen)

Abstract

The work is mainly concerned with the development of compact finite difference formulations for the biharmonic equation in irregular geometries. We specifically focus our attention towards the computation of solutions of complex flow problems by using biharmonic form of the Navier-Stokes (N-S) equations. When irregular physical domains are transformed onto computational domains that are expressible in terms of conformal mappings, the system of incompressible two dimensional N-S equations reduces to a single biharmonic semi-linear equation. The formulation has the advantage that the entire flow field can be described in terms of only one equation with stream function as the dependent variable. Other flow field variables can easily be post processed from stream function.

The work has been divided into two parts. In the first part we develop a new fourth order accurate essentially compact finite difference scheme for the steady N-S equations. The efficiency of the scheme is highlighted by performing numerical experiments on (i) a known constructed solution and is followed by its application on three different problems with varied complexities, *viz.* (ii) fluid flow in a constricted channel, (iii) driven polar cavity, and (iv) flow past an impulsively started circular cylinder. The computed solutions are then compared with the existing experimental and standard numerical results, and excellent agreement is found in all the cases.

In the second part we propose a new compact implicit scheme for transient biharmonic form of the N-S equations. This scheme is second order accurate both temporally and spatially. Our main objective here is not only to document the versatility of biharmonic pure stream function formulation, but also the efficiency of the newly proposed scheme in simulating the dynamics of flow inside curved regions as well as fluid-embedded body interaction. We have carried out a von Neumann stability analysis of this scheme and have also provided an algorithm for

the flow computation. In addition to the advantage that the entire flow field can be described in terms of only one equation, the formulation has the advantage that the stream function and velocity boundary conditions are sufficient to carry out flow simulation, thus avoiding difficulties associated with pressure field and nonphysical vorticity boundary conditions. Being compact, the scheme circumvents the need for special treatment at the boundaries. The scheme has been used to replicate the time development of two dimensional viscous flows in different geometrical settings and has been tested on as many as seven different setups. At first we establish the accuracy of the scheme by considering the problems of (i) Taylor-Green decaying vortices and (ii) constricted channel. We then extensively study the flow past stationary circular cylinders for the Reynolds numbers (Re) ranging from 5 to 9500 with extensive streakline analysis for the cases where vortex shedding characterized by the von Kármán vortex street is a regular feature. We further use the scheme to explore the effects of perturbation induced through three different techniques on the eventual behavior of the flow past circular cylinder and delve into the flow features in a narrow subrange of the threshold region leading to the determination of the critical Reynolds number. Next we consider flows past (i) rotating cylinder and (ii) in-line oscillating cylinder in a fluid at rest. This is followed by flows past (i) elliptic cylinders with angle of attack and (ii) symmetric aerofoils with angle of attack. The results obtained have been compared qualitatively and quantitatively with experimental and numerical results available in literature. As in the steady formulation, excellent comparison is seen in all cases, validating the accuracy and effectiveness of the proposed scheme. In this process, we also report some new flow features connected with the problems considered.

Contents

List of Figures

List of Tables

Chapter 1

Introduction

1.1 Background

The system of Navier-Stokes (N-S) equations, which describe the flow of viscous fluids through momentum balance, has its origin in Newton's second law of motion [2, 6, 11]. It is the most familiar model for fluid flow predictions and is a good tool for interpreting some interesting phenomena in science and engineering. The N-S equations are seen to describe the flow of Newtonian fluid quite accurately. These equations are nonlinear coupled partial differential equations (PDEs) and are difficult to solve analytically except for a few cases where analytic solutions can be found in the most simplified settings [11]. Therefore, one has to resort to numerical methods in order to solve the N-S equations in majority of the physical situations. This approach of using numerical methods and algorithms to solve and analyze problems that involve fluid flows is often known as Computational Fluid Dynamics (CFD) [1, 3, 13]. With the remarkable advancement in computer architecture, it has now become possible to venture into fluid flow situations which were beyound the reach of the CFD community a few decades earlier. The most popular one amongst the approaches that has been historically used in CFD is the finite difference method (FDM). Here, the basic methodology involves discretizing the problem domain by setting up a structured grid and then approximating the derivatives appearing in the governing N-S equations by difference quotients at each grid point. Such approximation yields a system of algebraic equations which can then be solved by some matrix solution algorithm.

The emergence and growing popularity of compact schemes [17, 22, 25, 55, 56, 58, 59, 73, 74, 75, 77, 79, 81, 137, 138, 139, 140, 155] have brought about a renewed interest towards the finite difference (FD) approach. A compact finite difference scheme is one which utilizes grid points located only directly adjacent to the node

about which the differences are taken. These schemes offer higher accuracy even when the grid is coarse. In contrast to the wide-molecule methods [31, 61, 62, 141] the compact schemes are able to determine the flow with information solely from the nearest neighbours. The major advantage of compact discretization is that it leads to a system of equations resulting in a coefficient matrix with smaller bandwidth as compared to non-compact schemes.

Traditionally, the primitive variable and stream function-vorticity (ψ-ω) formulations of the N-S equations have been the most popular approaches for computing viscous incompressible fluid flows. A review of fundamental formulations of incompressible N-S equations can be found in [54]. For flows in two dimensions (2D), ψ-ω formulation is more popular for its computational economy; it requires handling of only two unknowns as opposed to three in the case of primitive variables. Furthermore, it ensures exact satisfaction of the mass conservation equation. However, in the case of flows in three dimensions, the primitive variable formulation is the preferred one. The three dimensional counterpart of the stream function-vorticity formulation also exists in the literature [3], but there, one needs to deal with six unknowns in six equations. Over the years, the CFD community has seen the extensive use of both the primitive variable and ψ-ω formulations to compute incompressible viscous flows governed by the N-S equations. Both these formulations have their relative advantages and disadvantages over each other. While the primitive variable formulation has been traditionally difficult because of the presence of pressure term in the governing equations, a typical difficulty with the ψ-ω formulation is that the vorticity ω is not prescribed on the boundaries. Considering these facts, the stream function-velocity (ψ-v) [56, 75] and pure stream function formulations [23, 24, 25, 87] that use the biharmonic form of the N-S equations have emerged as attractive alternative approaches of solving the N-S equations. This approach eliminates the need to compute pressure and vorticity as a part of the computational process and therefore computationally much efficient than the primitive variable and ψ-ω formulations. The main advantages of the biharmonic pure stream function formulation are:

1. Avoids difficulties associated with primitive variables mainly pressure.

2. Avoids use of artificial vorticity boundary conditions.

3. Iterations involve only a single variable.

The biharmonic pure stream function formulation for the time dependent N-S system in rectangular planar domains has been used [53] almost two decades ago.

But the application of compact schemes to the biharmonic form of N-S equations is fairly recent [23, 24, 25, 56, 75, 87]. The pioneering work on the development of compact schemes for pure stream function formulation of the incompressible viscous N-S equations was carried out by Kupferman [87] in 2001. He used a central difference scheme and demonstrated the accuracy and robustness of the method by computing high Reynolds number (Re) flows in a lid-driven cavity. This biharmonic pure stream function formulation was later used by Ben-Artzi *et al.* [25] in 2005 to revisit the problems of driven cavity and double driven cavity. They used a second order compact formulation to compute solution for various Re values. In their work they have also shown uniqueness and decaying character of solution of pure stream function formulation derived in rectangular Cartesian coordinate system. Later in the year 2006, Ben-Artzi *et al.* [23] proved the convergence and consistency of the scheme for the full nonlinear system. The authors continued with their study of biharmonic formulation of N-S equations in Cartesian coordinates and were able to enhance the accuracy of their schemes in 2010 [24]. They again proved the efficiency of the scheme developed by recovering analytical solutions and solving the problem of lid-driven cavity. In the year 2005, Gupta and Kalita [56] proposed stream function-velocity formulation that uses the biharmonic form of the N-S equations. They used this formulation to compute steady flows for different Re values in lid-driven cavity. In addition they have also successfully tackled rectangular cavity flow with aspect ratio 2. The extension of the same approach to transient flows was done by the same authors in 2010 [75]. Here, in addition to the lid-driven cavity problem they used the formulation to simulate flows for the problem of backward facing step and the problem of flow past a square prism. Thus we see that the schemes developed so far for the biharmonic form of the N-S equations were limited to Cartesian coordinates only, and hence lacked the mechanism to handle CFD problems where there is a contact between fluid and non rectangular solid surface. Moreover, the extension of stream function-velocity formulation to non-rectangular domain is not immediate. Note that, many challenging and interesting physical problems involve viscous, incompressible fluid flow in geometrically complex regions. Curvilinear coordinate systems provide the key to the development of finite difference solutions of PDEs on regions with arbitrarily shaped boundaries. With coordinate systems generated to maintain coordinate lines coincident with the boundaries, FD codes can be written which are applicable to general configurations without the need of special procedures at the boundaries. Even when the boundaries are in motion, the use of

such coordinate systems allows all computation to be done on a fixed grid with a uniform square mesh in the transformed plane. This greatly simplifies the coding, particularly with regard to boundary conditions, which can now be represented without the need of interpolation or approximation. The major advantages of body fitted curvilinear coordinate system are:

1. Dirichlet boundary conditions are exactly satisfied.

2. No approximations are needed at the boundaries.

3. Avoids addition of any ghost point to the computational domain.

The curvilinear coordinate system covers the flow field with coordinate lines coincident with all boundaries. It is also possible to distribute the curvilinear grid lines in the physical plane with concentration of lines in regions of high gradients while maintaining the square grid in the transformed computational plane. Although different types of coordinate system may better serve different situations, the conformal mapping has the advantage that the partial differential equations acquire a minimal number of extra terms in the transformed system compared to other transformations. Moreover, the use of conformal transformation guarantees the smoothness and orthogonality of the generated system of coordinates. Conformal mappings satisfy Laplace equations with boundary conditions from the Cauchy-Riemann conditions. Such mappings can be built up from complex transformations, from superposition of harmonic functions, and from several different numerical approaches [147]. Note that conformal mapping has benefitted from the decreasing cost and increasing speed of digital computers. Developed algorithms have been updated and are being used to rapidly evaluate many hitherto intractable mappings. New numerical approaches are also being developed [7, 10]. It is well known that the inherent speed of conformal mapping makes it a valuable ally in raising the efficiency of other numerical techniques. Conformal mappings can transform difficult boundaries and then generate approximate grids to make subsequent FD calculations more efficient. It should be noted here that although the stream function-vorticity formulation is invariant under conformal mapping up to a scaling factor, which enables the use of schemes developed for Cartesian grid, the biharmonic form of the N-S equation is not invariant and hence some of the efficient solvers derived for rectangular Cartesian coordinate system can not be implemented straightway. Conformably transformed form of the biharmonic N-S equation has many more terms but still retains its basic nature.

1.2 Motivation

A careful study of the works discussed so far reveals that there are certain issues concerning compact schemes and their applicability to the fourth order pure stream function form of the N-S equations which are yet to be addressed. The compact schemes developed for the biharmonic differential equation so far do not cover problems on irregular geometries described in curvilinear coordinate system. In particular, no compact scheme has been developed for solving the complex flow problems such as the flow past circular cylinders thereby failing to exploit the full potential of pure stream function formulation. To resolve such complex flow phenomena accurately, we need to develop compact schemes for body fitted coordinate system. It must be mentioned here that the works on fourth order pure stream function form of the N-S equation discussed in the previous section have been typically used to examine the flow fields in Cartesian coordinate systems in simple rectangular domains. This is where the motivation to develop HOC schemes on nonuniform grids comes from. The idea of constructing a rectangular grid on irregular domains has its inherent limitations. If we embed the irregular region in a uniform Cartesian grid, the geometry of irregular domain does not generally align with the underlying grid and special treatment is required at the boundaries. Moreover accurate imposition of boundary condition is another issue; to circumvent this problem, instead of placing a computational grid on the physical domain, we have adopted a more flexible approach by means of coordinate transformation which can convert a complex flow region containing non-uniform grid into a rectangular computational domain with uniform orthogonal grid. We restrict ourselves to conformal transformation because of their obvious advantages [147] as pointed earlier. Therefore we focus our attention to fluid flow problems on irregular physical domains which are conformably mappable to rectangular computational domains. The strategy can also be used in cases where the conformal mapping is generated numerically. Note that there exists a large class of domains for which one can numerically generate a conformable mapping [7, 10].

1.3 Objectives

We enumerate the objectives of the work in the following sentences:

1. To develop efficient compact finite difference algorithms for fourth order biharmonic pure stream function form of the N-S equation in domains beyond Cartesian coordinates, more specifically for conformably mappable domains.

2. We are interested in exploring both steady and transient forms of N-S equations.

3. Schemes thus developed will be tested for their stability and convergence both analytically and computationally.

4. We aim to validate these algorithms by applying them to problems like symmetric constricted channel flow and polar cavity flow where flow evolves inside a closed region, as also open flow problems like flow past an impulsively started circular cylinder *etc.*, where there is an interaction between fluid and solid surface.

5. We give emphasis to the flow past circular cylinder and attempt to gain new physical understanding related to this flow field.

6. We also explore the effectiveness of the schemes in tackling problems with moving boundaries by considering the flow past rotating cylinder and in-line oscillating cylinder.

7. The study also validates the scheme developed by carrying out simulation of unsteady incompressible flow around geometrically complex and interesting bluff bodies such as elliptic cylinders and aerofoils.

Our aim here is not only to document the versatility of the fourth order stream function formulation, but also the efficiency of the compact approach in general and of the schemes developed here in particular in simulating the dynamics of flow inside curved regions as well as fluid-embedded body interactions.

1.4 Overview of the work

The FD schemes developed in this thesis work essentially combines all the advantages of compact schemes and biharmonic formulation listed above. The associated methodology is that the space derivatives of the governing equations are approximated compactly. The compact finite difference approximation which is presented here is based on only the eight nodal points in 2D surrounding each nodal point. The approach involves discretizing the equation using not only the nodal values of the unknown but also the values of its gradients at some selected nodal points. Introduction of derivatives may seem to increase the computational cost but as will be seen later it has the advantage that the gradients need not be approximated

from the computed values of the solution as they are already available at all grid points.

In the first part, we develop a fourth order accurate semi compact scheme for the steady N-S equations. This formulation is capable of numerically solving the 2D steady N-S on non-rectangular physical geometries that are expressible in terms of conformal mappings. The formulation is then tested on a known constructed solution and is followed by its application on three different problems with varied complexities, *viz.* fluid flow in a constricted channel, driven polar cavity flow, and flow past an impulsively started circular cylinder.

In the second part we develop second order space and time accurate implicit compact scheme for the transient N-S equation. The scheme is specifically designed for flows in fluid-embedded body interaction as well as curved regions. We use this scheme to simulate the time development of 2D viscous flows of varied physical complexities in different geometrical settings. The numerical rate of convergence of the scheme is established by applying it to a problem having known analytical solution and to the problem of flow through constricted channel, an internal flow problem which serves as a suitable test case for convergence analysis of problems having no analytical solution.

Next the above scheme is applied to the flow past impulsively started circular cylinder. We make a comprehensive study of this problem by capturing the time evolution of flow for Reynolds number (Re) ranging from 5 to 9500. Excellent match with experimental and numerical works can be seen.

Apart from this we also discuss three different pertubation techniques, including an untested one in order to trigger asymmetry into the flow past circular cylinder in the intriguing threshold range around the critical Reynolds number (Re_c). Here we are able to establish that Re_c resides in the regime 46.5 to 47. In the process, all the stages of a laboratory experiment for $Re = 44$ starting from an initial perturbed stage till the flow finally settling to a steady state is numerically replicated by streakline simulation

Finally we deal with two different sets of physically interesting and complex flows. In the first set we take up the case of moving boundaries. We consider the problems of flow past rotating and in-line oscillating circular cylinders. In the second set the flow past an elliptic cylinder and symmetric aerofoils with various angles of attack are studied. The robustness of the scheme is exemplified by the closeness of our computed solutions with the ones obtained through experimental visualizations and other numerical works.

The coefficient matrix resulting from the algebraic systems associated with the newly proposed FD approximations is not usually diagonally dominant and the conventional iterative methods such as Gauss-Seidel are of little help in solving the resulting system. In our work, we have used the biconjugate gradient stabilized method (BiCGStab) [4] without any preconditioning. This mechanism has been adopted throughout the present work.

1.5 Organization of the work

This thesis work is organized in eight chapters. Chapter 2 describes the development of a fourth order accurate essentially compact finite difference scheme for the steady N-S equations in biharmonic pure stream function form in non-rectangular geometries. In Chapter 3, we develop a compact, implicit second order temporally and spatially accurate FD scheme for unsteady N-S equations for incompressible viscous flows. Chapter 4 discusses the application of the scheme developed in Chapter 3 to the flow past an impulsively started circular cylinder problem for Re ranging from 5 to 9500. Chapter 5 deals with the mechanisms of triggering asymmetry into the flow past a circular cylinder in the vicinity of Re_c and Chapter 6 with some flow problems with moving boundaries. In Chapter 7 we consider flow around bluff bodies with high curvatures. Finally Chapter 8 summarizes and comments on the whole work and discusses the scope for future work.

Chapter 2

Essentially Compact High Order Scheme for the Fourth Order Navier-Stokes Equation in Non-rectangular Domain

2.1 Introduction

In the previous chapter we have discussed about the biharmonic form of the N-S equations emerging as an attractive alternative approach of solving the N-S equation. Some of the recent works on linear biharmonic equation that deserve special mention are by Altas *et al.* [17], Lai and Liu [88], Chen *et al.* [33], Ben-Artzi *et al.* [22] and Mai-Duy *et al.* [96]. Note that all these works deal with inhomogeneous pure biharmonic equation and are not related to the biharmonic form of the N-S equations with which we are concerned with. In their work Altas *et al.* [17] use a symbolic algebra package to derive a family of compact finite difference approximations for the biharmonic equation. On the other hand, in the work of Lai and Liu [88], biharmonic equation is not discretized directly; instead the equation is split into a coupled system of harmonic equations. In their work, Chen *et al.* [33] use a wider stencil and propose a second order accurate scheme; while Ben-Artzi *et al.* [22] use an interpolating polynomial based approach while Mai-Duy *et al.* [96] use an approach based on Chebyshev polynomial. While the work of Altas *et al.* [17] is on rectangular Cartesian coordinates, in [22, 33, 96], an irregular domain is embedded in Cartesian grid and as such the treatment of the boundaries require specific adjustment. Further more the extension of all the above mentioned schemes except that of Lai and Liu [88] to the fourth order nonlinear N-S equations is not immediate. In [88] biharmonic equation gets decoupled and

hence when extended to the biharmonic form of the N-S equations it reduces the problem to the ψ-ω formulation and as such all the difficulties associated with vorticity boundary conditions remain intact.

In the present study, we extend the use of finite difference approximation in [17] which was obtained using a mathematical package. We propose a fourth order accurate essentially compact scheme for the biharmonic steady N-S equations on non-uniform grids, which is capable of tackling geometries other than rectangular as well[1]. In contrast to the use of mathematical package by Altas *et al.* [17] we present the detailed derivation of the compact approximation and also present possibilities of alternative compatible approximations for the derivatives. The grid is constructed using conformal mappings, yielding a general orthogonal grid, where the degree and nature of the non-uniformity can be specified so as to meet the needs of the problem under consideration. The scheme being essentially compact there is absolutely no need for special treatment at the boundaries. Further, the transformation being conformal, the system of N-S equations reduces to a single fourth order semi-linear partial differential equation which governs stream function (ψ) values; the compact approach involves discretizing this biharmonic equation using unknown solution ψ and its gradients ψ_x and ψ_y at the interior grid points.

To validate the proposed scheme, we apply it on four problems of varied complexities and physical domains of different geometric shapes. They are (i) problem with a known constructed solution, (ii) fluid flow in a constricted symmetric channel, (iii) driven polar cavity flow, and (iv) flow past an impulsively started circular cylinder. We also carry out an error analysis to establish the theoretical order of convergence of the scheme. As no analytical solution exists for the last three numerical test cases, an implicit formula which requires the solution to be computed on three different grid sizes is used. The robustness of the scheme can be gauged by the fact that in all these three problems, our solutions agree very well, both qualitatively and quantitatively with established numerical and experimental results. Moreover, the scheme is also seen to handle both Dirichlet and Neumann boundary conditions with ease in all the four test cases.

This chapter is organized in five sections. Section 2.2 deals with the mathematical formulation, section 2.3 with discretization, section 2.4 with the solution of the algebraic system of equations and accuracy, section 2.5 with the numerical test cases and finally, section 2.6 summarizes the entire work of the chapter.

[1]Part of this work is under review in *Appl. Num. Math.*

2.2 Mathematical formulations

The steady incompressible viscous flows are governed by the N-S equations along with the equation of continuity. The non-dimensional forms of the equation of continuity and the N-S equations are

$$\boldsymbol{\nabla}.\boldsymbol{V} = 0, \tag{2.1}$$

$$(\boldsymbol{V}.\boldsymbol{\nabla})\boldsymbol{V} - \frac{1}{Re}\nabla^2\boldsymbol{V} = -\boldsymbol{\nabla}p \tag{2.2}$$

where $\boldsymbol{V}$ is the velocity vector, p is the pressure, and Re is the Reynolds number. Here all lengths and velocity components are non-dimensionalised with respect to the characteristic length L and characteristic velocity U respectively so that $Re = UL/\nu$, ν being the kinematic viscosity. In two dimensions, introducing stream function ψ and vorticity ω, the above formulation can be written as

$$\nabla^2\psi = -\omega, \tag{2.3}$$

$$(\boldsymbol{V}.\boldsymbol{\nabla})\omega = \frac{1}{Re}\nabla^2\omega. \tag{2.4}$$

Here $\omega = \boldsymbol{\omega}.\widehat{k}$, the out-of-plane component of vorticity vector $\boldsymbol{\omega}$ and the velocity is related to the stream function by $\boldsymbol{V} = (u, v, 0) = \boldsymbol{\nabla} \times \boldsymbol{\psi}$ where $\boldsymbol{\psi} = (0, 0, \psi)$. Eliminating ω from equations (2.3) and (2.4) and using the notation $\boldsymbol{\nabla}^{\perp}\psi = (\psi_y, -\psi_x) = (u, v)$ we obtain the biharmonic pure stream function form of the steady N-S equations

$$\nabla^4\psi = Re[(\boldsymbol{\nabla}^{\perp}\psi).\boldsymbol{\nabla}]\nabla^2\psi. \tag{2.5}$$

If the physical (x, y) plane is transformed onto a computational (ξ, η) plane using a conformal transformation

$$z = z(\zeta), \tag{2.6}$$

$z = x + Iy$ and $\zeta = \xi + I\eta$ ($I = \sqrt{-1}$), then in the transformed plane the steady biharmonic pure stream function form of the N-S equations is

$$\begin{aligned} \nabla^4\psi \;\; = \;\; & \big(2C + Re\psi_\eta\big)\nabla^2\psi_\xi + \big(2D - Re\psi_\xi\big)\nabla^2\psi_\eta \\ & -\big(E + CRe\psi_\eta - DRe\psi_\xi\big)\nabla^2\psi \end{aligned} \tag{2.7}$$

where

$$C = \frac{J_\xi}{J}, \quad D = \frac{J_\eta}{J}, \text{ and } E = 2C^2 + 2D^2 - \frac{J_{\eta\eta}}{J} - \frac{J_{\xi\xi}}{J},$$

J being the jacobian of the transformation (2.6). The details of this derivation can be found in Appendix A. In Appendix A we have pointed out that the stream

function - vorticity (ψ-ω) formulation represented by the equations (2.3)-(2.4) is invariant under conformal mapping upto a scaling factor, which enables equivalently solving the equations on the Cartesian grid, but as seen from equation (2.7) the biharmonic form of the N-S equation in Cartesian coordinate system (2.5) is not invariant. The equation (2.7) is a fourth order nonlinear partial differential equation having the form

$$\Delta^2\psi = f(\xi, \eta, \psi_\xi, \psi_\eta, \psi_{\xi\xi}, \psi_{\xi\eta}, \psi_{\eta\eta}, \psi_{\xi\xi\xi}, \psi_{\xi\xi\eta}, \psi_{\xi\eta\eta}, \psi_{\eta\eta\eta}) \tag{2.8}$$

where we use $\Delta \equiv \nabla^2$. Equation (2.8) can be considered as the semi-linear version of the classical biharmonic equation. The presence of derivatives of the dependent variable ψ in the forcing function f renders nonlinearity into the equation. As will be seen later, approximations of these higher order derivatives despite being approximated compactly, introduce non compactness to the overall nature of the finite difference scheme.

Note that equation (2.7) contains ψ as the only dependent variable from which other flow variables can be post processed in contrast to the three dependent variables u, v, and p associated with the two dimensional version of the primitive variable formulation (2.1)-(2.2) and two dependent variables ψ and ω in the ψ-ω formulation in (2.3)-(2.4). Hence it is computationally more efficient in numerically simulating incompressible viscous flows governed by the 2D N-S equations than primitive variable or ψ-ω formulations.

2.3 Discretization procedures

We consider the inhomogeneous biharmonic equation

$$\Delta^2\psi = f. \tag{2.9}$$

for specified forcing function f on a domain Ω in the computational (ξ-η) plane with appropriate boundary conditions on $\partial\Omega$. We assume $\Omega = [a, b] \times [c, d]$ to be comprised of a union of small squares. We wish to approximate the solution of (2.9) to high order by finite differences on a structured grid of uniform mesh $a = \xi_0 < \xi_1 < ... < \xi_m = b$, $c = \eta_0 < \eta_1 < ... < \eta_n = d$ having size h. We assume that the solution and the forcing function carry sufficient smoothness. In two dimensions, (2.9) can be written as

$$\frac{\partial^4\psi}{\partial\xi^4} + 2\frac{\partial^4\psi}{\partial\xi^2\partial\eta^2} + \frac{\partial^4\psi}{\partial\eta^4} = f. \tag{2.10}$$

Let $\psi_{i,j}$, $\psi_{\xi_{i,j}}$ and $\psi_{\eta_{i,j}}$ refer to the approximate values of $\psi(\xi_i, \eta_j)$, $\psi_\xi(\xi_i, \eta_j)$ and $\psi_\eta(\xi_i, \eta_j)$ respectively where (ξ_i, η_j) is a typical node. For our convenience we write the standard central difference approximations to the first and second order derivatives with respect to ξ and η $\forall$ $1 \le i \le m-1$, $1 \le j \le n-1$ below

$$\begin{aligned}
\delta_\xi \psi_{i,j} &\equiv \frac{1}{2h}(\psi_{i+1,j} - \psi_{i-1,j}), \\
\delta_\xi^2 \psi_{i,j} &\equiv \frac{1}{h^2}(\psi_{i+1,j} - 2\psi_{i,j} + \psi_{i-1,j}), \\
\delta_\eta \psi_{i,j} &\equiv \frac{1}{2h}(\psi_{i,j+1} - \psi_{i,j-1}), \\
\delta_\eta^2 \psi_{i,j} &\equiv \frac{1}{h^2}(\psi_{i,j+1} - 2\psi_{i,j} + \psi_{i,j-1}).
\end{aligned} \tag{2.11}$$

Using the above central differences we can define the Stephenson finite difference operators [140] at each internal grid point (ξ_i, η_j) as

$$\begin{aligned}
\delta_\xi^4 \psi_{i,j} &\equiv \frac{12}{h^2}(\delta_\xi \psi_{\xi_{i,j}} - \delta_\xi^2 \psi_{i,j}), \\
\delta_\eta^4 \psi_{i,j} &\equiv \frac{12}{h^2}(\delta_\eta \psi_{\eta_{i,j}} - \delta_\eta^2 \psi_{i,j}).
\end{aligned} \tag{2.12}$$

It is easy to see that

$$\begin{aligned}
(\partial_\xi^4 \psi)_{i,j} &= \delta_\xi^4 \psi_{i,j} - \frac{h^2}{15}(\partial_\xi^6 \psi)_{i,j} + O(h^4), \\
(\partial_\eta^4 \psi)_{i,j} &= \delta_\eta^4 \psi_{i,j} - \frac{h^2}{15}(\partial_\eta^6 \psi)_{i,j} + O(h^4)
\end{aligned} \tag{2.13}$$

where we use the notations

$$\frac{\partial^i}{\partial \xi^i} \equiv \partial_\xi^i \quad \text{and} \quad \frac{\partial^{i+j}}{\partial \xi^i \partial \eta^j} \equiv \partial_\xi^i \partial_\eta^j.$$

Also note that

$$(\partial_\xi^2 \partial_\eta^2 \psi)_{i,j} = \delta_\xi^2 \delta_\eta^2 \psi_{i,j} - \frac{h^2}{12}(\partial_\xi^4 \partial_\eta^2 \psi + \partial_\xi^2 \partial_\eta^4 \psi)_{i,j} + O(h^4). \tag{2.14}$$

Using (2.13) and (2.14) in (2.10) we get

$$(\partial_\xi^4 \psi + 2\partial_\xi^2 \partial_\eta^2 \psi + \partial_\eta^4 \psi)_{i,j} = \delta_\xi^4 \psi_{i,j} + 2\delta_\xi^2 \delta_\eta^2 \psi_{i,j} + \delta_\eta^4 \psi_{i,j} + T_{i,j} \tag{2.15}$$

where

$$T_{i,j} = -\frac{h^2}{15}[(\partial_\xi^6 \psi)_{i,j} + \frac{5}{2}(\partial_\xi^4 \partial_\eta^2 \psi + \partial_\xi^2 \partial_\eta^4 \psi)_{i,j} + (\partial_\eta^6 \psi)_{i,j}] + O(h^4). \tag{2.16}$$

The approximation (2.15) is obviously $O(h^2)$ but if the leading term of $T_{i,j}$ can be approximated compactly to order h^2 then we will have an $O(h^4)$ approximation

of (2.10). In order to achieve this, we take appropriate derivative of (2.10) with respect to ξ and η so that

$$\partial_\xi^6\psi + \partial_\eta^6\psi = f_{\xi\xi} + f_{\eta\eta} - 3\,(\partial_\xi^4\partial_\eta^2\psi + \partial_\xi^2\partial_\eta^4\psi). \tag{2.17}$$

Therefore,

$$T_{i,j} = -\frac{h^2}{15}(\delta_\xi^2 f + \delta_\eta^2 f)_{i,j} + \frac{h^2}{30}(\partial_\xi^4\partial_\eta^2\psi + \partial_\xi^2\partial_\eta^4\psi)_{i,j} + O(h^4). \tag{2.18}$$

Again,

$$(\partial_\xi^2\partial_\eta^2\psi)_{i,j} = \delta_\xi\delta_\eta^2\psi_{\xi_{i,j}} - \frac{h^2}{12}(\partial_\xi^2\partial_\eta^4\psi)_{i,j} - \frac{h^2}{6}(\partial_\xi^4\partial_\eta^2\psi)_{i,j} + O(h^4), \tag{2.19}$$

$$(\partial_\xi^2\partial_\eta^2\psi)_{i,j} = \delta_\xi^2\delta_\eta\psi_{\eta_{i,j}} - \frac{h^2}{12}(\partial_\xi^4\partial_\eta^2\psi)_{i,j} - \frac{h^2}{6}(\partial_\xi^2\partial_\eta^4\psi)_{i,j} + O(h^4). \tag{2.20}$$

Adding (2.19) and (2.20), and using (2.14) we get

$$\frac{h^2}{12}(\partial_\xi^4\partial_\eta^2\psi + \partial_\xi^2\partial_\eta^4\psi)_{i,j} = \delta_\xi\delta_\eta^2\psi_{\xi_{i,j}} + \delta_\xi^2\delta_\eta\psi_{\eta_{i,j}} - 2\,\delta_\xi^2\delta_\eta^2\psi_{i,j} + O(h^4). \tag{2.21}$$

Thus (2.18) reduces to

$$T_{i,j} = \frac{2}{5}(\delta_\xi\delta_\eta^2\psi_{\xi_{i,j}} + \delta_\xi^2\delta_\eta\psi_{\eta_{i,j}} - 2\,\delta_\xi^2\delta_\eta^2\psi_{i,j}) - \frac{h^2}{15}(\delta_\xi^2 f + \delta_\eta^2 f)_{i,j} + O(h^4). \tag{2.22}$$

The fourth order approximation of (2.10) can now be written

$$\begin{aligned}\delta_\xi^4\psi_{i,j} + 2\,\delta_\xi^2\delta_\eta^2\psi_{i,j} + \delta_\eta^4\psi_{i,j} \;+\; & \frac{2}{5}(\delta_\xi\delta_\eta^2\psi_{\xi_{i,j}} + \delta_\xi^2\delta_\eta\psi_{\eta_{i,j}} - 2\,\delta_\xi^2\delta_\eta^2\psi_{i,j}) \\ = \; & \frac{h^2}{15}(\delta_\xi^2 f + \delta_\eta^2 f)_{i,j} + f_{i,j}.\end{aligned} \tag{2.23}$$

Multiplying both sides by h^4 and expanding all the terms, (2.23) leads to

$$\begin{aligned}&6\psi_{i-1,j-1} - h\psi_{\xi_{i-1,j-1}} - h\psi_{\eta_{i-1,j-1}} - 72\psi_{i,j-1} - 28h\psi_{\eta_{i,j-1}} + 6\psi_{i+1,j-1} + h\psi_{\xi_{i+1,j-1}} \\ &-h\psi_{\eta_{i+1,j-1}} - 72\psi_{i-1,j} - 28h\psi_{\xi_{i-1,j}} + 264\psi_{i,j} - 72\psi_{i+1,j} + 28h\psi_{\xi_{i+1,j}} \\ &+6\psi_{i-1,j+1} - h\psi_{\xi_{i-1,j+1}} + h\psi_{\eta_{i-1,j+1}} - 72\psi_{i,j+1} + 28h\psi_{\eta_{i,j+1}} + 6\psi_{i+1,j+1} + h\psi_{\xi_{i+1,j+1}} \\ &+h\psi_{\eta_{i+1,j+1}} = \frac{h^4}{3}(11f_{i,j} + f_{i+1,j} + f_{i,j+1} + f_{i-1,j} + f_{i,j-1}).\end{aligned} \tag{2.24}$$

Since in the above discretization of biharmonic equation (2.10) the gradients of ψ have also been used at selected nodal points apart from the unknown solution ψ, it is necessary to determine finite difference approximations for ψ_ξ and ψ_η. Note that approximation (2.23) or its expanded from (2.24) being fourth order accurate stencils, the compatible approximations for the gradients should be of order six. We write down the step for approximating ψ_ξ; ψ_η can be identically approximated.

We begin by observing that

$$\psi_{\xi_{i,j}} = (\delta_\xi \psi_{i,j} - \frac{h^2}{6}\delta_\xi^2 \psi_{\xi_{i,j}}) + \frac{h^4}{180}(\partial_\xi^5 \psi)_{i,j} + O(h^6). \tag{2.25}$$

Thus to obtain a sixth order approximation of ψ_ξ we need second order compact approximation of $(\partial_\xi^5 \psi)_{i,j}$.

We find,

$$(\frac{9}{60}\partial_\xi^5 \psi + \frac{1}{60}\partial_\xi^3 \partial_\eta^2 \psi)_{i,j} = \frac{1}{h^2}(\delta_\xi \delta_\eta^2 \psi_{i,j} - \delta_\eta^2 \psi_{\xi_{i,j}}) + O(h^2), \tag{2.26}$$

$$(\partial_\xi^3 \partial_\eta^2 \psi)_{i,j} = \delta_\xi^2 \delta_\eta^2 \psi_{\xi_{i,j}} + O(h^2), \tag{2.27}$$

$$(\frac{1}{12}\partial_\xi \partial_\eta^4 \psi + \frac{1}{6}\partial_\xi^3 \partial_\eta^2 \psi)_{i,j} = \frac{1}{h^2}(\delta_\xi \delta_\eta \psi_{\eta_{i,j}} - \delta_\eta^2 \psi_{\xi_{i,j}}) + O(h^2). \tag{2.28}$$

Also by differentiating (2.10) with respect to x, we get

$$\partial_\xi^5 \psi + 2\,\partial_\xi^3 \partial_\eta^2 \psi + \partial_\xi \partial_\eta^4 \psi = f_\xi. \tag{2.29}$$

Using (2.25) - (2.29), various sixth order approximations for ψ_ξ can be found. One such approximation is

$$\begin{aligned} \frac{93}{8}\psi_{\xi_{i,j}} &- \frac{93}{8}(\delta_\xi \psi_{i,j} - \frac{h^2}{6}\delta_\xi^2 \psi_{\xi_{i,j}}) + \frac{h^2}{8}(\delta_\xi \delta_\eta^2 \psi_{i,j} - \delta_\eta^2 \psi_{\xi_{i,j}}) \\ &- \frac{h^4}{480}\delta_\xi^2 \delta_\eta^2 \psi_{\xi_{i,j}} + h^2(\delta_\xi \delta_\eta \psi_{\eta_{i,j}} - \delta_\eta^2 \psi_{\xi_{i,j}}) = \frac{h^4}{12}\delta_\xi f_{i,j}. \end{aligned} \tag{2.30}$$

Another sixth order approximation that can be found using equations (2.25) to (2.27) is

$$27\psi_{\xi_{i,j}} + \frac{9}{2}h^2 \delta_\xi^2 \psi_{\xi_{i,j}} + \frac{h^4}{60}\delta_\xi^2 \delta_\eta^2 \psi_{\xi_{i,j}} + h^2 \delta_\eta^2 \psi_{\xi_{i,j}} = 27\delta_\xi \psi_{i,j} + h^2 \delta_\xi \delta_\eta^2 \psi_{i,j}. \tag{2.31}$$

Note that the above approximation uses only ψ and ψ_ξ values at different nodal points of the compact computational stencil as compared to ψ, ψ_ξ, ψ_η and f used

in (2.30). But the approximation (2.30) being a tested one [17], we will use it for our present numerical computation.

Similar to (2.30) a sixth order approximation for ψ_η is,

$$\begin{aligned}\frac{93}{8}\psi_{\eta_{i,j}} &- \frac{93}{8}(\delta_\eta\psi_{i,j} - \frac{h^2}{6}\delta_\eta^2\psi_{\eta_{i,j}}) + \frac{h^2}{8}(\delta_\eta\delta_\xi^2\psi_{i,j} - \delta_\xi^2\psi_{\eta_{i,j}}) \\ &- \frac{h^4}{480}\delta_\xi^2\delta_\eta^2\psi_{\eta_{i,j}} + h^2(\delta_\xi\delta_\eta\psi_{\xi_{i,j}} - \delta_\xi^2\psi_{\eta_{i,j}}) = \frac{h^4}{12}\delta_\eta f_{i,j}. \qquad (2.32)\end{aligned}$$

In expanded form the approximations (2.30) and (2.32) are

$$\begin{aligned}&3\psi_{i-1,j-1} + h\psi_{\xi_{i-1,j-1}} + h\psi_{\eta_{i-1,j-1}} - 3\psi_{i+1,j-1} + h\psi_{\xi_{i+1,j-1}} - h\psi_{\eta_{i+1,j-1}} \\ &+24\psi_{i-1,j} + 8h\psi_{\xi_{i-1,j}} + 40h\psi_{\xi_{i,j}} - 24\psi_{i+1,j} + 8h\psi_{\xi_{i+1,j}} \\ &+3\psi_{i-1,j+1} + h\psi_{\xi_{i-1,j+1}} - h\psi_{\eta_{i-1,j+1}} - 3\psi_{i+1,j+1} + h\psi_{\xi_{i+1,j+1}} + h\psi_{\eta_{i+1,j+1}} \\ &= \frac{h^4}{6}(f_{i+1,j} - f_{i-1,j}) \qquad (2.33)\end{aligned}$$

and

$$\begin{aligned}&3\psi_{i-1,j-1} + h\psi_{\xi_{i-1,j-1}} + h\psi_{\eta_{i-1,j-1}} + 24\psi_{i,j-1} + 8h\psi_{\eta_{i,j-1}} + 3\psi_{i+1,j-1} \\ &-h\psi_{\xi_{i+1,j-1}} + h\psi_{\eta_{i+1,j-1}} + 40h\psi_{\eta_{i,j}} - 3\psi_{i-1,j+1} - h\psi_{\xi_{i-1,j+1}} \\ &+h\psi_{\eta_{i-1,j+1}} - 24\psi_{i,j+1} + 8h\psi_{\eta_{i,j+1}} - 3\psi_{i+1,j+1} + h\psi_{\xi_{i+1,j+1}} + h\psi_{\eta_{i+1,j+1}} \\ &= \frac{h^4}{6}(f_{i,j+1} - f_{i,j-1}), \qquad (2.34)\end{aligned}$$

respectively.

In all the above approximations we restrict ourselves to the compact square cell only. The presence of f in (2.30) and (2.32) is attributed to the use of differential equation (2.9) in the discretizing process. The compact approach involves discretizing the biharmonic equation using not just the grid values of the unknown solution ψ but also the values of the gradients ψ_ξ and ψ_η at selected grid points as well. As evident from (2.23), the finite difference approximation uses eight neighboring values of ψ; six values of ψ_ξ at $(i+1,j)$, $(i-1,j)$, $(i\pm1,j\pm1)$; and six values of ψ_η at $(i,j+1)$, $(i,j-1)$, $(i\pm1,j\pm1)$. Note that the introduction of ψ_ξ

and ψ_η as unknowns does not involve additional computation. This is because of the fact that the scheme has the advantage of the gradients being already available at all grid points and need not be approximated from the computed values of the solution ψ.

The relation (2.23) in conjunction with (2.30) and (2.32) have truncation errors of order four. But in order to make the scheme truly fourth order accurate we need to approximate the forcing function given in equation (2.8) *viz.* f consistently so that, the proposed approach retains its overall fourth order accuracy. This can be accomplished by approximating the derivatives $\psi_{\xi\xi_{i,j}}$, $\psi_{\eta\eta_{i,j}}$, $\psi_{\xi\xi\xi_{i,j}}$, $\psi_{\xi\xi\eta_{i,j}}$, $\psi_{\xi\eta\eta_{i,j}}$, $\psi_{\eta\eta\eta_{i,j}}$ upto fourth order accuracy by using ψ, ψ_ξ and ψ_η only. We achieve this by using the following approximations:

$$\psi_{\xi\xi_{i,j}} = -\delta_\xi\psi_{\xi_{i,j}} + 2\delta_\xi^2\psi_{i,j} + O(h^4), \tag{2.35}$$

$$\psi_{\eta\eta_{i,j}} = -\delta_\eta\psi_{\eta_{i,j}} + 2\delta_\eta^2\psi_{i,j} + O(h^4), \tag{2.36}$$

$$\psi_{\xi\xi\xi_{i,j}} = 3\left[\frac{5}{h^2}\delta_\xi\psi_{i,j} - \frac{1}{2}\delta_\xi^2\psi_{\xi_{i,j}} - \frac{5}{h^2}\psi_{\xi_{i,j}}\right] + O(h^4), \tag{2.37}$$

$$\psi_{\xi\xi\eta_{i,j}} = \left[\frac{\delta_\xi\psi_{\eta_{i,j+1}} + \delta_\xi\psi_{\eta_{i,j-1}} + 10\delta_\xi\psi_{\eta_{i,j}}}{6} - \frac{\delta_\xi\psi_{\xi_{i,j+1}} - \delta_\xi\psi_{\xi_{i,j-1}}}{2h}\right] + O(h^4), \tag{2.38}$$

$$\psi_{\xi\eta\eta_{i,j}} = \left[\frac{\delta_\eta\psi_{\xi i,j+1} + \delta_\eta\psi_{\xi_{i,j-1}} + 10\delta_\eta\psi_{\xi_{i,j}}}{6} - \frac{\delta_\eta\psi_{\eta_{i,j+1}} - \delta_\eta\psi_{\eta_{i,j-1}}}{2h}\right] + O(h^4), \tag{2.39}$$

$$\psi_{\eta\eta\eta_{i,j}} = 3\left[\frac{5}{h^2}\delta_\eta\psi_{i,j} - \frac{1}{2}\delta_\eta^2\psi_{\eta_{i,j}} - \frac{5}{h^2}\psi_{\eta_{i,j}}\right] + O(h^4). \tag{2.40}$$

Using (2.35)-(2.40) we discretize f as follows

$$\begin{aligned}
f_{i,j} &= (2C + Re\psi_{\eta_{i,j}})(\psi_{\xi\xi\xi_{i,j}} + \psi_{\xi\eta\eta_{i,j}}) + (2D - Re\psi_{\xi_{i,j}})(\psi_{\xi\xi\eta_{i,j}} + \psi_{\eta\eta\eta_{i,j}}) \\
&- (E + CRe\psi_{\eta_{i,j}} - DRe\psi_{\xi_{i,j}})(\psi_{\xi\xi_{i,j}} + \psi_{\eta\eta_{i,j}}) \\
\Rightarrow f_{i,j} &= \frac{1}{6}(2C + Re\psi_{\eta_{i,j}})\left[18\left(\frac{5}{h^2}\delta_\xi\psi_{i,j} - \frac{1}{2}\delta_\xi^2\psi_{\xi_{i,j}} - \frac{5}{h^2}\psi_{\xi_{i,j}}\right)\right. \\
&+ \left.\delta_\eta\psi_{\xi i,j+1} + \delta_\eta\psi_{\xi_{i,j-1}} + 10\delta_\eta\psi_{\xi_{i,j}} - \frac{3}{h}(\delta_\eta\psi_{\eta_{i,j+1}} - \delta_\eta\psi_{\eta_{i,j-1}})\right] \\
&+ \frac{1}{6}(2D - Re\psi_{\xi_{i,j}})\left[18\left(\frac{5}{h^2}\delta_\eta\psi_{i,j} - \frac{1}{2}\delta_\eta^2\psi_{\eta_{i,j}} - \frac{5}{h^2}\psi_{\eta_{i,j}}\right)\right. \\
&+ \left.\delta_\xi\psi_{\eta_{i,j+1}} + \delta_\xi\psi_{\eta_{i,j-1}} + 10\delta_\xi\psi_{\eta_{i,j}} - \frac{3}{h}(\delta_\xi\psi_{\xi_{i,j+1}} - \delta_\xi\psi_{\xi_{i,j-1}})\right] \\
&- 3(E + CRe\psi_{\eta_{i,j}} - DRe\psi_{\xi_{i,j}})\left[-\delta_\eta\psi_{\eta_{i,j}} + 2\delta_\eta^2\psi_{i,j} - \delta_\xi\psi_{\xi_{i,j}} + 2\delta_\xi^2\psi_{i,j}\right] \\
&+ O(h^4).
\end{aligned} \tag{2.41}$$

In (2.41), a fourth order approximation of f is obtained using ψ, ψ_ξ and ψ_η. This approximation when used in (2.23) results in a fourth order approximation of the semi-linear biharmonic pure stream function formulation of the N-S equation (2.8); note that this formulation uses not only the grid values of the unknown solution ψ but also the values of the gradients ψ_ξ and ψ_η at selected grid points as well. Approximation (2.41) is also used in (2.30) and (2.32) for obtaining compatible approximations for ψ_ξ and ψ_η. It is the use of (2.41) in (2.23), (2.30), and (2.32) which renders non-compactness into the overall nature of the scheme, although we are still in a position to exploit the compact nature of (2.23). This is the reason we call our scheme essentially compact.

Having obtained an accuracy of order four throughout our calculation, the challenge now is to approximate boundary conditions for all the derivatives present in equation (2.7) up to the fourth order of accuracy. As we will see later, for different problems and different boundaries, the boundary conditions vary in their form. We will estimate the boundary values by using one sided finite difference approximations in conjunction with the physical condition of the flow. Only at few places we will deviate from our compact approach and will use a wider stencil. The derivation of such higher order approximation of the boundary conditions, which are problem dependent, would be discussed at appropriate places.

It may be mentioned that even when conformal mappings described by equation (2.6) are not available explicitly, one can generate the conformal mapping numerically [32, 92] and the proposed scheme can be easily implemented in those cases as well. However, the overall accuracy of the scheme may get affected as one may require a succession of transformations to transform the physical domain onto a rectangular computational domain.

2.4 Solution of algebraic system and order of convergence

We now discuss the solution of algebraic systems associated with the newly proposed finite difference approximations. By writing equations (2.24), (2.33), and (2.34) at every interior grid point (i, j) for a grid of size $m \times n$, one obtains a system of three algebraic equations for the equation (2.8). Defining $\phi_{i,j} = (\psi_{i,j}, \psi_{\xi_{i,j}}, \psi_{\eta_{i,j}})^T$ as the unknown vector at each grid point, we can assort equations (2.24), (2.33),

and (2.34) as

$$S_1\phi_{i-1,j-1} + S_2\phi_{i,j-1} + S_3\phi_{i+1,j-1} + S_4\phi_{i-1,j} + S_5\phi_{i,j}$$
$$+S_6\phi_{i+1,j} + S_7\phi_{i-1,j+1} + S_8\phi_{i,j+1} + S_9\phi_{i+1,j+1} = F_{i,j}.$$

where,

$$S_1 = \begin{pmatrix} 6 & -1 & -1 \\ 3 & 1 & 1 \\ 3 & 1 & 1 \end{pmatrix}, \quad S_2 = \begin{pmatrix} -72 & 0 & -28 \\ 0 & 0 & 0 \\ 24 & 0 & 8 \end{pmatrix}, S_3 = \begin{pmatrix} 6 & 1 & -1 \\ -3 & 1 & -1 \\ 3 & -1 & 1 \end{pmatrix},$$
$$S_4 = \begin{pmatrix} -72 & -28 & 0 \\ 24 & 8 & 0 \\ 0 & 0 & 0 \end{pmatrix}, S_5 = \begin{pmatrix} 264 & 0 & 0 \\ 0 & 40 & 0 \\ 0 & 0 & 40 \end{pmatrix}, \quad S_6 = \begin{pmatrix} -72 & 28 & 0 \\ -24 & 8 & 0 \\ 0 & 0 & 0 \end{pmatrix},$$
$$S_7 = \begin{pmatrix} 6 & -1 & 1 \\ 3 & 1 & -1 \\ -3 & -1 & 1 \end{pmatrix}, \quad S_8 = \begin{pmatrix} -72 & 0 & 28 \\ 0 & 0 & 0 \\ -24 & 0 & 8 \end{pmatrix}, \quad S_9 = \begin{pmatrix} 6 & 1 & 1 \\ -3 & 1 & 1 \\ -3 & 1 & 1 \end{pmatrix},$$

and

$$F_{i,j} = \frac{h^4}{6}\left(2(11f_{i,j} + f_{i+1,j} + f_{i,j+1} + f_{i-1,j} + f_{i,j-1}), f_{i+1,j} - f_{i-1,j}, f_{i,j+1} - f_{i,j-1}\right)^T.$$

The above equation when written at each grid point yields the system of equations

$$S\Phi = F \tag{2.42}$$

where the coefficient matrix S is an asymmetric block nona-diagonal sparse matrix having 3×3 matrices as entries, *i.e.*, blocks. For a grid of size $m \times n$, S is of size $3mn \times 3mn$, and Φ and F are $3mn$-component vectors. The main objective now is to solve the equation (2.42), thereby evaluating the unknown vector

$$\Phi = (\psi_{1,1}, \psi_{\xi_{1,1}}, \psi_{\eta_{1,1}}, \psi_{1,2}, \psi_{\xi_{1,2}}, \psi_{\eta_{1,2}}, ..., \psi_{m,n}, \psi_{\xi_{m,n}}, \psi_{\eta_{m,n}})^T.$$

The differential equation (2.7) presented symbolically via equation (2.8) being nonlinear, the system of difference equations represented by the single matrix equation (2.42) is also nonlinear. A quick look at equation (2.8) and its finite difference approximation (2.24) reveals that all the nonlinear terms of equation (2.8) are contained on the right hand side of (2.42). Note that the coefficient matrix S of (2.42) is a constant matrix. We tackle the nonlinearity by a linearization strategy which is a slight modification of Newton's method. As is well known, Newton's method for nonlinear difference equations leads to a sequence of linear problems. The detailed discussion and subsequent analysis of this linearization strategy for biharmonic N-S equations can be found in works of Schreiber and Keller [125]. For the sake of self containment of our work, we recall below a few steps from [125].

The application of the Newton's method to the continuous problem (2.8) starts with some sufficiently smooth initial guess say ψ^0 that satisfies the boundary conditions. Then the sequence $\{\psi^\mu\}$ is defined by

$$\psi^{\mu+1} = \psi^\mu + \delta^\mu,$$

where the correction term δ^μ is the solution of the linearized problem about ψ^μ satisfying zero Dirichlet and/or Neumann boundary conditions. Hence δ^μ satisfy the differential equation

$$L[\psi^\mu]\delta^\mu = -H[\psi^\mu]. \tag{2.43}$$

Here $L[\psi]\delta \equiv \Delta^2\delta - \bar{f}'[\psi]\delta$, $H[\psi] \equiv \Delta^2\psi - \bar{f}[\psi]$ where $\bar{f}[\psi]$ is the right hand side of (2.8), *viz.*, $\bar{f}[\psi] = (2C + Re\partial_\eta\psi)(\Delta\partial_\xi\psi) + (2D - Re\partial_\xi\psi)(\Delta\partial_\eta\psi) - (E + CRe\partial_\eta\psi - DRe\partial_\xi\psi)(\Delta\psi)$. Thus one can obtain

$$\begin{aligned}\bar{f}'[\psi]\delta \;=\; & (2C + Re\partial_\eta\psi)(\Delta\partial_\xi\delta) + (2D - Re\partial_\xi\psi)(\Delta\partial_\eta\delta) \\ & -(E + CRe\partial_\eta\psi - DRe\partial_\xi\psi)(\Delta\delta) + (Re\partial_\eta\delta)(\Delta\partial_\xi\psi) \\ & +(-Re\partial_\xi\delta)(\Delta\partial_\eta\psi) - (CRe\partial_\eta\delta - DRe\partial_\xi\delta)(\Delta\psi).\end{aligned}$$

The linearized problem (2.43) can now be written as

$$\begin{aligned}\Delta^2\delta^\mu - \bar{f}'[\psi^\mu]\delta^\mu &= -\Delta^2\psi^\mu + \bar{f}[\psi^\mu] \\ \Rightarrow \Delta^2[\psi^\mu + \delta^\mu] &= \bar{f}[\psi^\mu] + \bar{f}'[\psi^\mu]\delta^\mu \\ \Rightarrow \Delta^2\psi^{\mu+1} &= \bar{f}[\psi^\mu] + \bar{f}'[\psi^\mu]\delta^\mu.\end{aligned}$$

Neglecting $\delta^\mu = \psi^{\mu+1} - \psi^\mu$ term on right which is of infinitesimal magnitude, we have,

$$\Delta^2\psi^{\mu+1} = \bar{f}[\psi^\mu]. \tag{2.44}$$

Eventually equation (2.44) is the linearized equation which we solve iteratively. The resulting system of equations (2.42) can now be solved as a linear system. In the traditional stream function-vorticity and the primitive variable formulation of the steady N-S equations, discretization of the governing equations results in a variable coefficient matrix irrespective of whether one retains δ^μ in the linearized equation (2.44) or not. As such the coefficient matrix needs to be updated after every outer iteration till convergence is obtained. However, in the current approach, a constant coefficient matrix is obtained by neglecting the δ^μ term. Contrary to the traditional approaches, we update only the right hand side of (2.42) containing the nonlinear terms after every outer iteration. This approach has been adopted

elsewhere [56, 57] also. As one is dealing with a constant coefficient matrix, computational workload is drastically reduced as opposed to the traditional approaches. Introducing the notations

$$\Psi = (\psi_{1,1}, \psi_{1,2}, ..., \psi_{m,n})^T,\ \Psi_\xi = (\psi_{\xi_{1,1}}, \psi_{\xi_{1,2}}, ..., \psi_{\xi_{m,n}})^T,\ \Psi_\eta = (\psi_{\eta_{1,1}}, \psi_{\eta_{1,2}}, ..., \psi_{\eta_{m,n}})^T$$

the entire strategy here can be summarized as an algorithm:

1. At the initial step $\mu = 0$ start with a smooth Ψ^μ.
2. Estimate derivatives of Ψ^μ *viz.* Ψ^μ_ξ, Ψ^μ_η and hence F^μ.
3. Obtain $\Phi^{\mu+1}$ using (2.42) yielding $\Psi^{\mu+1}$, $\Psi^{\mu+1}_\xi$ and $\Psi^{\mu+1}_\eta$.
4. If $\|\Phi^{\mu+1} - \Phi^\mu\| < \epsilon$, $\Phi^{\mu+1} = \Phi$, stop else $\Phi^\mu = \Phi^{\mu+1}$.
5. Estimate other derivatives by using equation (2.35)-(2.40) and hence F^μ.
6. Upgrade the boundary conditions wherever necessary.
7. Goto step 3.

Direct solution of the linear system (2.42), in each inner iteration, is impractical because of the huge size of the coefficient matrix and enormous storage requirements even for moderate values of step length h. On the other hand condition number of the coefficient matrix increases rapidly with reduced grid spacing h and one must be very cautious while attempting to solve such linear systems using iterative solvers. As the coefficient matrix S is not diagonally dominant, conventional solvers such as Gauss-Seidel also cannot be used. Note that when these iterative solvers are used they invariably leads to slow convergence or divergence for high Re flows [55, 56]. Therefore all the computations were performed using the biconjugate gradient stabilized (BiCGStab)[4, 135] method without preconditioning, where, thanks to the compact grid, it is easy to implement matrix vector multiplication $S\Phi$ without the need of storing all the entries of the matrix S.

It is worth mentioning here that an alternative to solving (2.42) also exists as pointed out by Altas *et al.* [17]. In this approach equation (2.24) is solved for ψ at all grid points and then subsequently equations (2.33) and (2.34) are used to obtain upgraded values of ψ_ξ and ψ_η on the entire domain. Thus instead of solving a system of equations of the type (2.42), where the coefficient matrix is of size $3mn \times 3mn$, one is required to solve three such systems where the coefficient matrix is of size $mn \times mn$. Since we use iterative method to solve system of

equations, the efficiency of an approach will depend mostly on how the matrix vector multiplication is carried out for the inner BiCGStab iterations in conjunction with the outer iterations to reach steady state. In our previous approach a single matrix vector multiplication requires $(21 + 17 + 17)mn = 55mn$ multiplication operations and $(20+16+16)mn = 52mn$ addition operations, making a grand total of $107mn$ operation count. This is due to the fact that the coefficient matrix S in equation (2.42) resulting from (2.24) is a 21-diagonal matrix with at most 21 non-zero entries in a particular row. On the other hand, in the alternative approach, the matrix equations for ψ, ψ_ξ and ψ_η have at most 9, 7 and 7 non-zero entries in a particular row of their respective coefficient matrices. As such, this approach requires $(9+7+7)mn = 23mn$ multiplication operations and $(8+6+6)mn = 20mn$ addition operations, *i.e.* a total of $46mn$ operation count. Hence it seems that the second approach will be faster as compared to the first approach at least for steady state problems. For unsteady problems, an inner-outer loop strategy needs to be implemented and hence such comparison requires further analysis. But for the steady state problems considered here, it is observed that although the inner BiCGStab iterations in the second approach are faster, yet steady state is achieved in higher number of outer steps. Hence overall CPU time may even be more. Moreover, one of the advantages of using BiCGStab iterative solvers is that despite the coefficient matrix being nine times larger than the three matrices arising out of (2.24), (2.33), and (2.34), the CPU time is still competitive for the first approach vis a vis the alternatives as pointed out by Altas *et al.* [17]. Our computation also confirms this fact.

All the computations were carried out on a Intel Core 2 Duo based PC with 2 GB RAM using double precision floating point arithmetic. For the inner BiCGStab iterations, the computations were stopped when the norm of the residual vector $\boldsymbol{r} = F - S\Phi$ arising out of equation (2.42) fell below 10^{-7}. Steady-state solution is assumed to reach when the maximum ψ-error between two successive outer iteration steps is smaller than 10^{-8}.

Except the first problem, the other numerical test cases considered here do not posses any analytical solutions. Therefore, for problems 2, 3, and 4, we estimate the perceived order of convergence, denoted as σ, by calculating results for three different grid sizes following the approach adopted in [9]. If $\psi^{(P)}$ is the exact solution at any point P in the solution domain, h_1, h_2, h_3 are mesh sizes in three different uniform grids used to compute solutions $\psi_1^{(P)}$, $\psi_2^{(P)}$, $\psi_3^{(P)}$ respectively at

the point P then

$$\psi^{(P)} - \psi_1^{(P)} \doteq C^{(P)} h_1^\sigma \tag{2.45}$$

$$\psi^{(P)} - \psi_2^{(P)} \doteq C^{(P)} h_2^\sigma \tag{2.46}$$

$$\psi^{(P)} - \psi_3^{(P)} \doteq C^{(P)} h_3^\sigma \tag{2.47}$$

where $C^{(P)}$ is some constant.
Eliminating $\psi^{(P)}$ and $C^{(P)}$ from the equation (2.45) - (2.47),

$$\frac{\psi_2^{(P)} - \psi_1^{(P)}}{\psi_3^{(P)} - \psi_2^{(P)}} \doteq \frac{h_1^\sigma - h_2^\sigma}{h_2^\sigma - h_3^\sigma}.$$

Converting the locally defined relation $\psi_2^{(P)} - \psi_1^{(P)}$ to a global one through the use of the root mean square (RMS) value, one gets

$$\|\Psi_2 - \Psi_1\| = \sqrt{\frac{1}{N} \sum_P \left(\psi_2^{(P)} - \psi_1^{(P)} \right)^2}.$$

The summation being take over all the N grid points common to the three grids. Thus

$$\|\Psi_2 - \Psi_1\| \doteq \sqrt{\frac{1}{N} \sum_P C^{(P)^2}} \left(h_1^\sigma - h_2^\sigma \right),$$

$$\|\Psi_3 - \Psi_2\| \doteq \sqrt{\frac{1}{N} \sum_P C^{(P)^2}} \left(h_2^\sigma - h_3^\sigma \right),$$

finally yielding

$$\frac{\|\Psi_2 - \Psi_1\|}{\|\Psi_3 - \Psi_2\|} \doteq \frac{h_1^\sigma - h_2^\sigma}{h_2^\sigma - h_3^\sigma} \tag{2.48}$$

from which σ can be approximated. Also if h_3 is our finest grid and we have $h_1 = \lambda_1 h_3$ and $h_2 = \lambda_2 h_3$ then (2.48) can be rewritten as

$$\frac{\|\Psi_2 - \Psi_1\|}{\|\Psi_3 - \Psi_2\|} \doteq \frac{\lambda_1^\sigma - \lambda_2^\sigma}{\lambda_2^\sigma - 1}. \tag{2.49}$$

This is the formula that will be used to compute the perceived order of discretization convergence throughout this thesis work.

2.5 Numerical experiments

In order to study the validity and effectiveness of the proposed scheme, it is applied to four problems. These are (i) problem with a known constructed solution, (ii)

fluid flow in a constricted symmetric channel, (iii) driven polar cavity, and (iv) flow past an impulsively started circular cylinder.

Note that all the problems considered here have domains that can be mapped through known conformal mappings and therefore values of C, D, E, and J following equation (2.7) are known exactly. However, in order to examine the effect of these metrics on the numerical solutions, these terms were computed using the exact mappings as well as numerical approximations. The difference between these computations were found to be insignificant and as such, for all the results presented in this work, we have used the exact expressions for the metrics.

2.5.1 Problem 1: Test for accuracy

Here we take a problem defined in the domain

$$\mathcal{D} = \{(x, y) : x + Iy = \sqrt{\xi + I\eta},\ \ -1 \leq \xi \leq 1,\ \ 1.25 \leq \eta \leq 0.25\}$$

governed by the stream function-vorticity formulation of the N-S equations containing a source function

$$\gamma = 4e^{(x+y)}.$$

The equations (2.3)-(2.4) can thus be written as

$$\nabla^2\psi = -\omega,$$

$$\nabla^2\omega = Re\big(u\omega_x + v\omega_y\big) + \gamma.$$

Consequently the pure stream function biharmonic formulation of the N-S equation in the transformed plane is

$$\begin{aligned}\nabla^4\psi \ \ = \ \ & \big(2C + Re\psi_\eta\big)\nabla^2\psi_\xi + \big(2D - Re\psi_\xi\big)\nabla^2\psi_\eta \\ & -\big(E + CRe\psi_\eta - DRe\psi_\xi\big)\nabla^2\psi + J^2\gamma.\end{aligned}$$

The exact solution of this problem is

$$\psi = e^{(x+y)}.$$

In order to solve the problem we transform the physical domain into a rectangular computational domain and use the analytical solution to obtain the boundary conditions. At interior grid points we set zero values as initial approximation. Figure 2.1 shows a typical 21×11 grid. We have computed solution using three different grids 6×11, 11×21, 21×41 with $Re = 1$. In figure 2.2, we present the

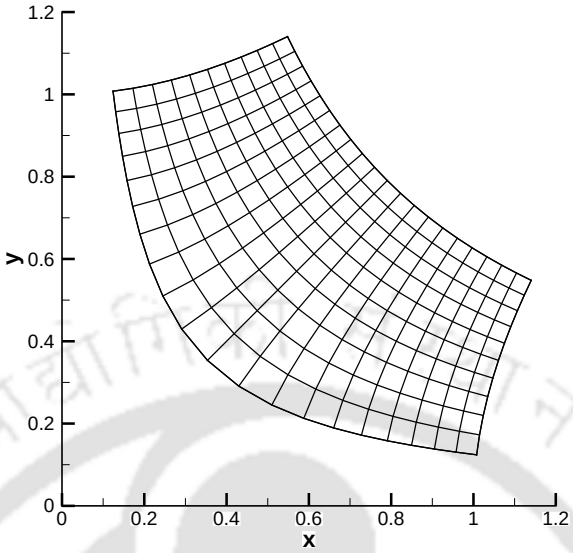

Figure 2.1: *Problem 1: A typical* 21×11 *grid.*

Table 2.1: *Problem 1:* L_1*-error,* L_2*-error,* L_∞*-error and order of convergence*

Grid Size	L_1 Error	Order	L_2 Error	Order	L_∞ Error	Order
$[6 \times 11]$	2.233×10^{-5}		3.813×10^{-5}		1.390×10^{-4}	
		3.62		3.41		3.42
$[11 \times 21]$	1.820×10^{-6}		3.597×10^{-6}		1.300×10^{-5}	
		3.19		3.37		3.70
$[21 \times 41]$	2.000×10^{-7}		3.472×10^{-7}		1.000×10^{-6}	

surface and contours plots of the analytical and the numerical solutions computed on this grid; it is heartening to note that in a grid of size as coarse as 21×11, the numerical solution is almost indistinguishable from the analytical one. In table 2.1 we present the order of discretization convergence based on L_1, L_2 and L_∞ errors. A convergence order of around four could be seen in the table. The L_1, L_2 and L_∞ errors are given by the formulae

$$||\Psi^{num} - \Psi^{ana}||_{L_1} = \frac{1}{i_{\max} j_{\max}} \sum_{i=1}^{i_{\max}} \sum_{j=1}^{j_{\max}} |\psi_{i,j}^{num} - \psi_{i,j}^{ana}|,$$

$$||\Psi^{num} - \Psi^{ana}||_{L_2} = \sqrt{\frac{1}{i_{\max} j_{\max}} \sum_{i=1}^{i_{\max}} \sum_{j=1}^{j_{\max}} \left(\psi_{i,j}^{num} - \psi_{i,j}^{ana}\right)^2}$$

and

$$||\Psi^{num} - \Psi^{ana}||_{L_\infty} = \max_{i,j} |\psi_{i,j}^{num} - \psi_{i,j}^{ana}|$$

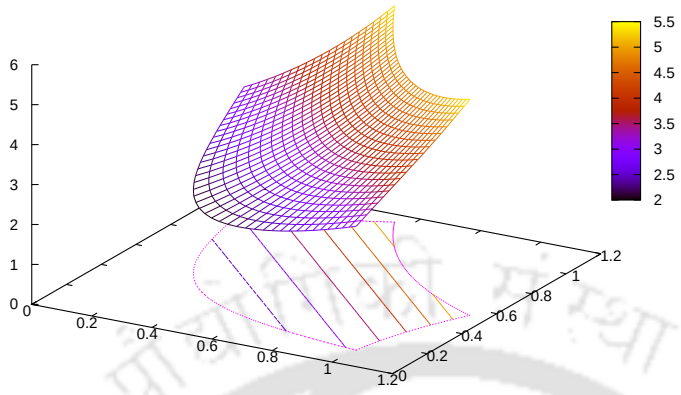

(a)

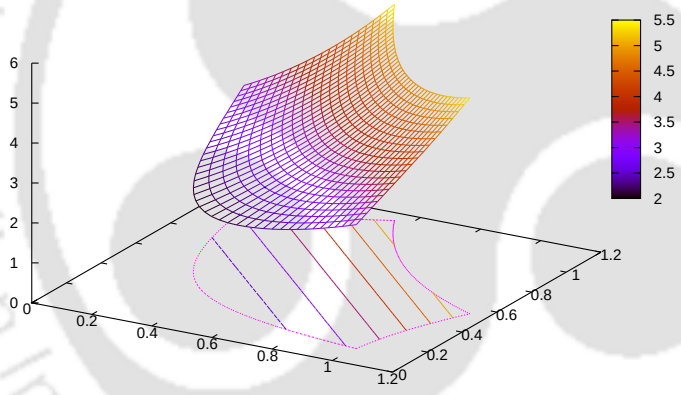

(b)

Figure 2.2: *Problem 1: Surface and contour plots of the (a) Numerical and (b) Analytical solution.*

respectively. The surface plots of the absolute errors in the numerical solution corresponding to three different grids have been plotted in figure 2.3; these figures clearly depict the decaying nature of the error with decreasing grid size.

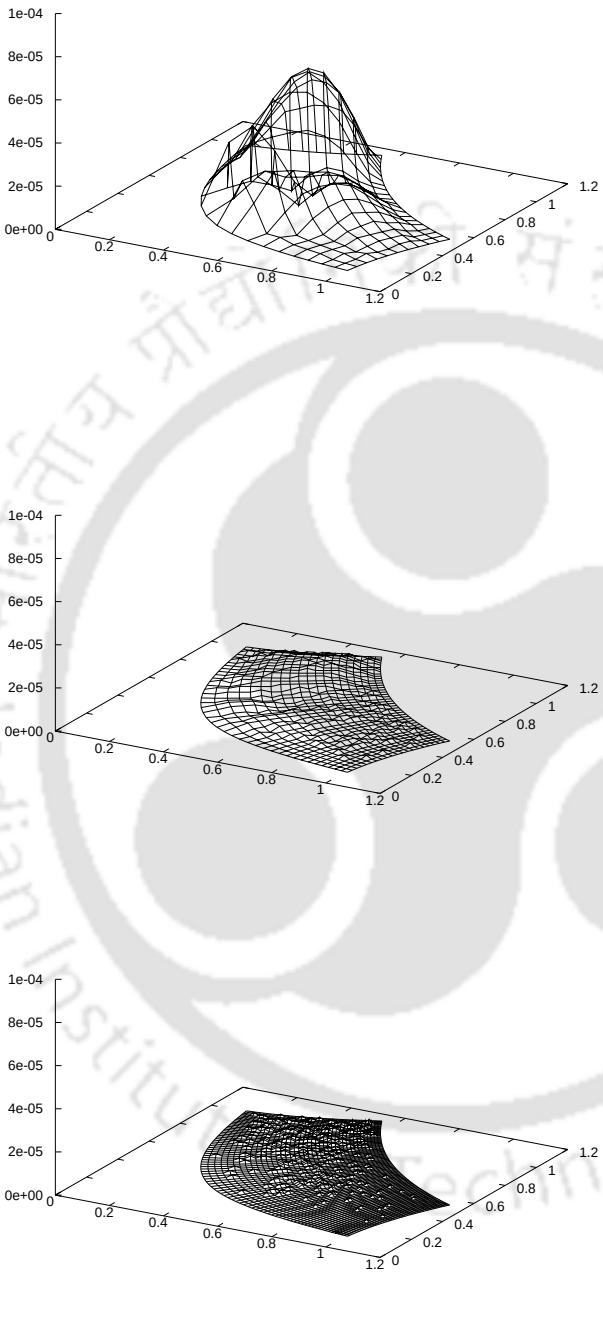

Figure 2.3: *Problem 1: Surface plot of absolute error on three different grids (a)* 21×11, *(b)* 41×21, *(c)* 81×41.

2.5.2 Problem 2: Fluid flow in a constricted symmetric channel

In this section, we consider numerical solution of the N-S equations for steady flow in a rigid step down constricted channel. This is an idealization of flows in geometries that contains a reentrant corner. At such a corner the flow becomes singular and to obtain accurate results near such a corner, it is necessary to have a highly refined non-uniform grid there. In order to transform the physical channel into a rectangular computational plane, we use an algebraic conformal mapping. One such possible mapping is

$$x = A\xi + \frac{B}{H}[\xi\ \sinh(2\xi) - \eta\ \sin(2\eta)]$$

$$y = A\eta + \frac{B}{H}[\eta\ \sinh(2\xi) + \xi\ \sin(2\eta)]$$

where $H = \cosh(2\xi) + \cos(2\eta)$, $A = \dfrac{b+a}{2\tau}$, and $B = \dfrac{b-a}{2\tau}$.

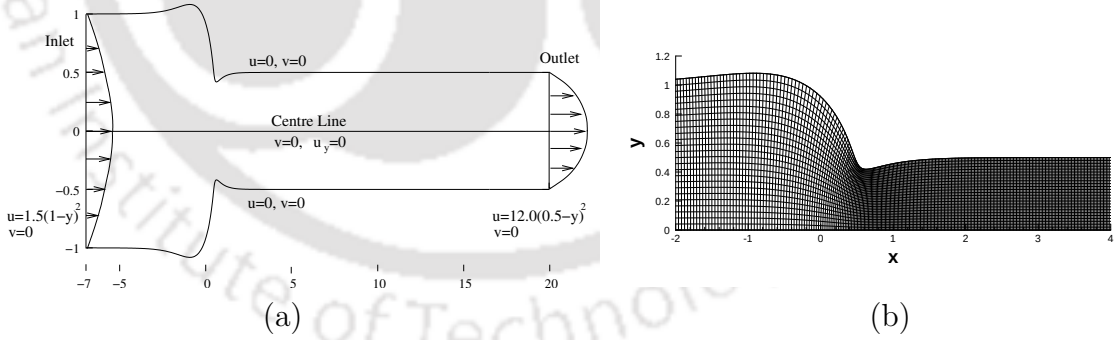

(a) (b)

Figure 2.4: *Problem 2: (a) Schematic diagram with* $\tau = 0.8$*, (b) Close up view of a typical* 1176×26 *grid.*

The constants a and b being the radii of the channel far upstream and far downstream respectively. In our computation, we take $a = 1.0$ and $b = 0.5$. In addition, $0 < \tau \leq 1$ controls the sharpness of the constriction, with a higher

value of τ indicating a sharper corner in the domain of the flow. We study two cases here, namely, $\tau = 0.8$ representing a reasonably smooth corner and $\tau = 1.0$ representing a channel with a sharp corner. The Re for this problem is defined as $Re = \dfrac{au_0}{\nu}$, where u_o is the average velocity at the entrance and ν is the kinematic viscosity. A Poiseuille parabolic velocity profile is introduced at the inlet and outlet [98]. A schematic diagram of the problem showing the boundary conditions is presented in figure 2.4(a). These boundary conditions are designed to satisfy conservation of mass in the computational domain. At the walls, a no slip condition is assumed while at the centreline, $\dfrac{\partial u}{\partial y} = 0$, $v = 0$. The boundary conditions can be summarized as:

$$\psi = 1 \quad \text{and} \quad \frac{\partial \psi}{\partial \eta} = 0 \qquad \text{on the wall} \quad \eta = \tau$$

$$\psi = \frac{\eta}{2\tau}\left(3 - \frac{\eta^2}{\tau^2}\right) \quad \text{and} \quad \frac{\partial \psi}{\partial \xi} = 0 = \frac{\partial^2 \psi}{\partial \xi^2} = \frac{\partial^3 \psi}{\partial \xi^3} \quad \text{as} \quad \xi \to \pm\infty$$

$$\psi = 0 \quad \text{and} \quad \frac{\partial^2 \psi}{\partial \eta^2} = 0 = \frac{\partial^3 \psi}{\partial \eta^3} \quad \text{on the line of symmetry} \quad \eta = 0$$

Note that we have considered $\psi_{\xi\xi} = 0 = \psi_{\xi\xi\xi}$ as $\xi \to \pm\infty$ and $\psi_{\eta\eta\eta} = 0$ on $\eta = 0$ since the derivatives are defined on free surfaces on which there is a respective zero lower order derivative. We estimate the value for $\psi_{\eta\eta}$ on $\eta = \tau$ by the second order approximate finite difference formula

$$\psi_{\eta\eta_{i,j}} \doteq \frac{1}{2h^2}\Big[-7\psi_{ij} + 8\psi_{i,j\pm1} - \psi_{i,j\pm2} \mp 6h\psi_{\eta_{i,j}}\Big] \tag{2.50}$$

The other higher order derivatives left to be estimated on the boundaries are $\psi_{\eta\eta\eta}$, $\psi_{\xi\eta\eta}$ on $\eta = \tau$ and $\psi_{\xi\xi\eta}$ on $\eta = 0$. This is done by using second order extrapolation formula

$$F_I \doteq 2F_{I\pm1} - F_{I\pm2}, \tag{2.51}$$

with F representing a third order mixed derivative of ψ as mentioned above. Higher order approximation of the derivatives are known to produce some oscillations in the solutions at the boundaries [73, 137] and were also seen in our computations; hence some of the derivatives have been approximated only up to second order of accuracy instead of desired fourth. As pointed out by Spotz and Carey [137], this oscillation occurs probably due to the convective component of the fourth order boundary condition. As would be seen from our numerical results, the reduction in the order of approximation of the derivatives however does not pollute the accuracy of the solution at the interior.

As pointed out by Pandit *et al.* [116], the positioning of the inlet and outlet boundaries has a direct bearing on the computed flow. Therefore, the minimum distances of the inlet and outlet boundaries were fixed at $x \approx -7$ and $x \approx 20$ respectively. The ratio between the length and the breadth of the channel needs to be kept larger so as to allow the flow to be fully developed at the outlet and as such there are many more grid points along ordinate axis than abscissa. Since the flow pattern in the constricted channel is axisymmetric, we consider only the upper half of the channel for numerical computation. A typical grid of size 1176×26 is shown in figure 2.4(b).

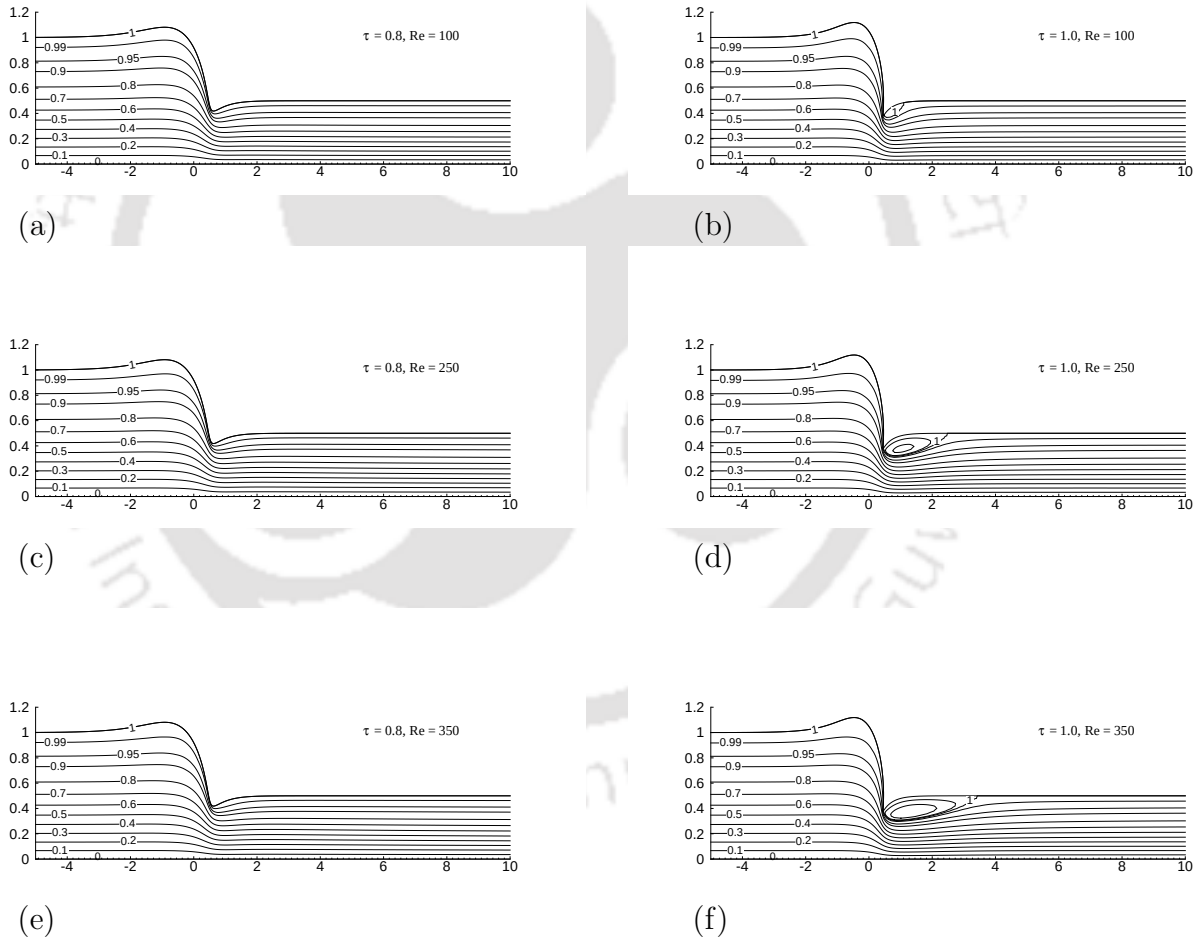

Figure 2.5: *Problem 2: Steady state stream function contours.*

In figure 2.5, we present the streamline contours for $Re = 100$, 250, and 350. Here, the first column represents streamlines for $\tau = 0.8$ and the second one for

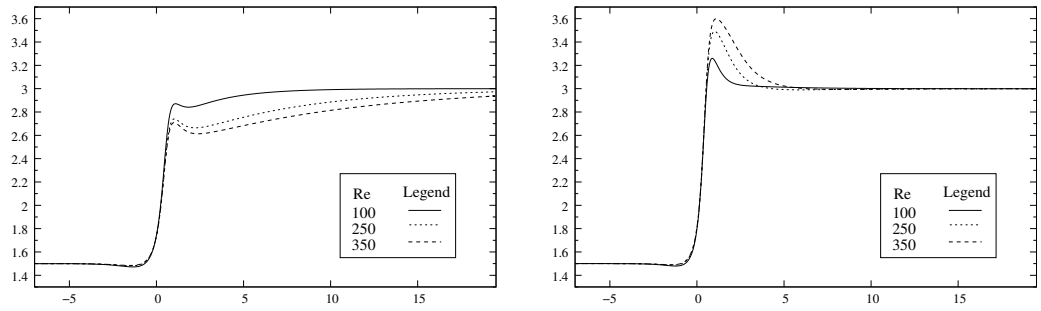

(a) (b)

Figure 2.6: *Problem 2: Centreline velocity profile for different Re with (a)* $\tau = 0.8$*, (b)* $\tau = 1.0$.

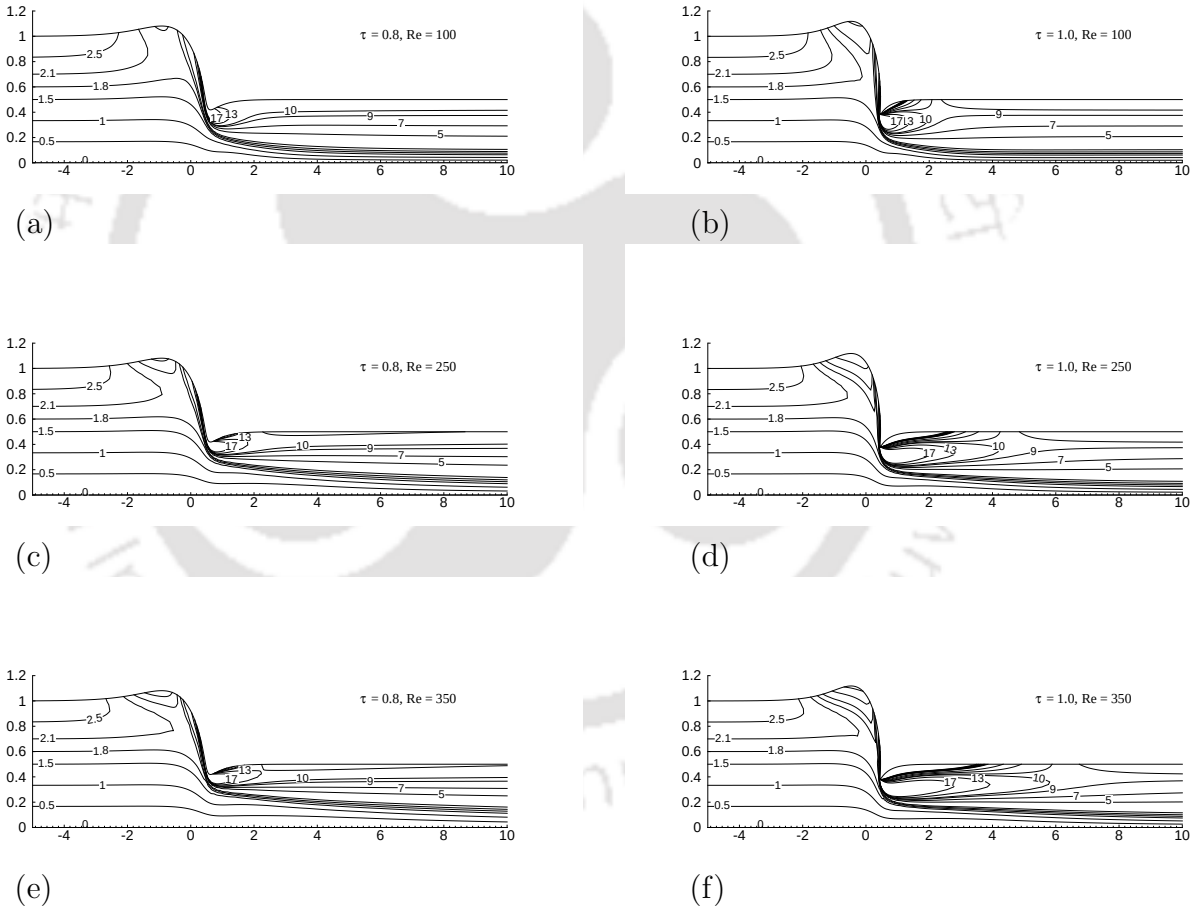

(a) (b) (c) (d) (e) (f)

Figure 2.7: *Problem 2: Steady state vorticity contours.*

$\tau = 1.0$. Figure 2.6 represents the centreline velocity profile for different *Re*. It is noticed that upstream of the throat velocity profile is almost same for different *Re* but in the vicinity of the throat, where the flow encounters the constriction, there

is a significant jump in velocity, the quantum of which varies with the difference in Re. As expected, the phenomenon is more pronounced for $\tau = 1.0$ as compared to $\tau = 0.8$. For lower value of τ there is no vortex formation at the throat. The size of this vortex for $\tau = 1.0$ is seen to increase with increasing Re. These facts are also reflected by the post processed wall vorticity contours for different Re and τ in figure 2.7. Downstream of the throat, the velocity profile for different Re and τ approach the outlet velocity field asymptotically. As was noticed in earlier studies [116], we observe that for $\tau = 0.8$, higher the Re, longer the distance to approach the conserved outlet velocity. All our stream function and vorticity results are in conformity with those of [98, 116].

Table 2.2: *Problem 2: CPU time and relaxation parameter associated with convergence history*

τ	Re	Grid size	CPU time (in seconds)	Relaxation parameter (Inner, Outer)
0.8	25	$[376 \times 9]$	3.025	(0.3, 0.6)
		$[565 \times 13]$	15.717	(0.3, 0.6)
		$[753 \times 17]$	76.214	(0.3, 0.6)
	100	$[376 \times 9]$	9.480	(0.1, 0.5)
		$[565 \times 13]$	38.196	(0.18, 0.5)
		$[753 \times 17]$	242.420	(0.1, 0.5)
1.0	25	$[376 \times 9]$	2.897	(0.3, 0.6)
		$[565 \times 13]$	14.209	(0.3, 0.6)
		$[753 \times 17]$	69.752	(0.3, 0.6)
	100	$[376 \times 9]$	5.806	(0.1, 0.5)
		$[565 \times 13]$	23.942	(0.18, 0.5)
		$[753 \times 17]$	251.386	(0.1, 0.5)

We will like to make it clear that all vorticity plots that are shown in this thesis are post processed from stream function field using the discretized version of equation (A.14). Most often we discretize equation (A.14) using central differences. Since vorticity does not appear in our formulation we make no effort to increase accuracy or efficiency of computation of vorticity field. The purpose of calculating vorticity field is threefold: (i) To give the readers an idea of vorticity field associated with the flow under consideration. (ii) To help describe the physics of the flow. (iii) To compare with other available results thereby indirectly establishing the accuracy of the underlying stream function field.

In figure 2.8, we show the convergence history; here the horizontal axis represents the number of outer iterations and the vertical axis, the maximum ψ-error between two successive outer iteration steps. In all the cases, good convergence

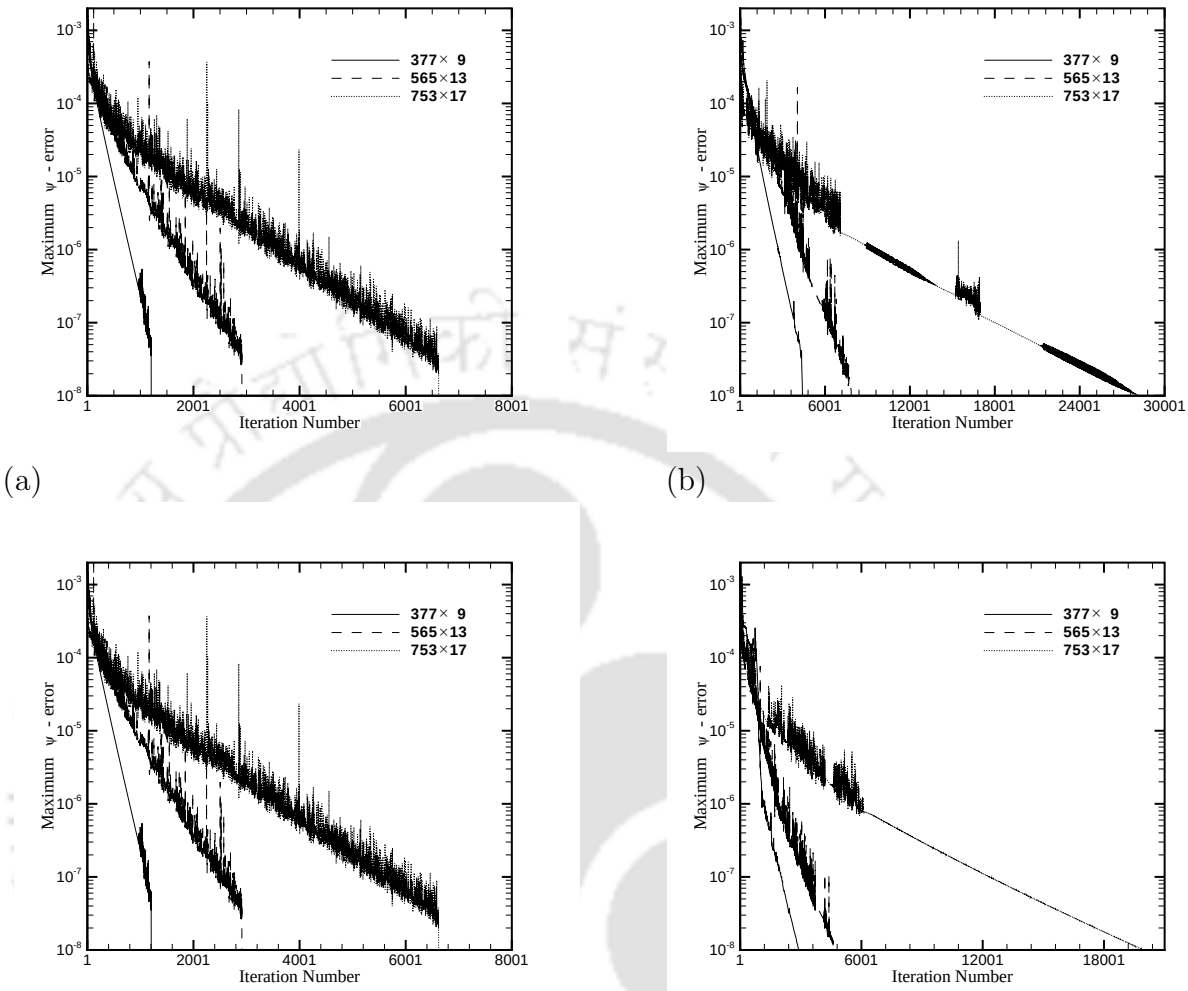

Figure 2.8: *Problem 2: Convergence history showing maximum ψ-error versus iteration number for (a) $\tau = 0.8$, $Re = 25$; (b) $\tau = 0.8$, $Re = 100$; (c) $\tau = 1.0$, $Re = 25$; (d) $\tau = 1.0$, $Re = 100$.*

patterns were observed. In table 2.2 we present CPU time and convergence parameters associated with figure 2.8.

2.5.3 Problem 3: Driven polar cavity flow

This problem was first studied both experimentally as well as numerically by Fuchs and Tillmark [50] and is now being frequently used to validate numerical algorithms, particularly for physical domains having circular arcs as boundaries. Due

to its special geometry, this problem is more challenging for the present numerical scheme than the square cavity flow [25, 55, 56, 57, 73, 75, 116]. Figure 2.9 represents a schematic diagram of the problem along with a typical non-uniform 55×79 mesh as well as a diagram for nomenclature used in this study. In their work,

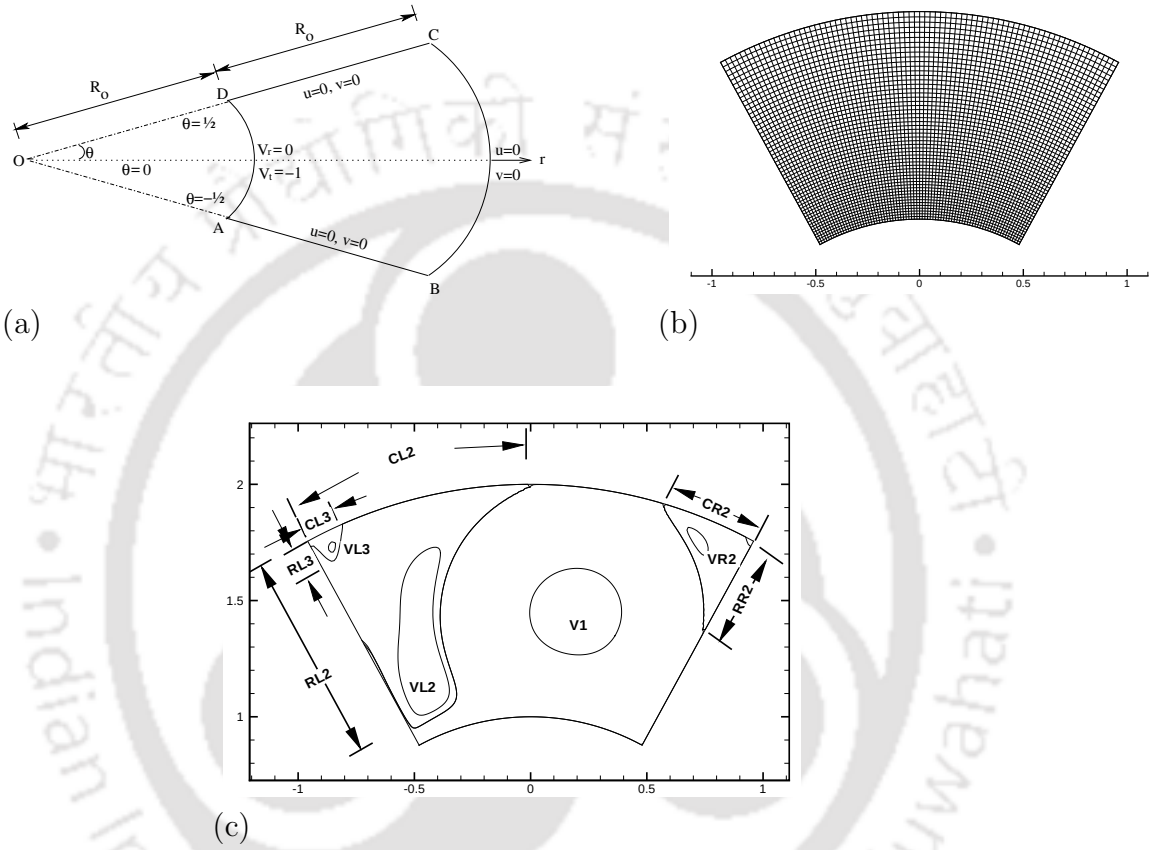

Figure 2.9: *Problem 3: (a) Schematic diagram, (b) A typical* 55×79 *grid, (c) Nomenclature.*

Lee and Tsuei [90] observed that large solution errors propagate near the rotating boundary. Therefore we cluster grids in the vicinity of the rotating boundary.

The region $ABCD$ is the domain of the problem; the height AB of the cavity is equal to the radius R_0, of the boundary $\widehat{DA}$. The inner circular arc DA is moving with an angular clock-wise velocity $V_t = -1$ which is the driving mechanism behind the flow. All the other boundary walls are fixed. For this problem, the Re is defined as $Re = \dfrac{v_0 R_0}{\nu}$, where v_0 is the magnitude of surface velocity of the rotating cylinder and ν is the kinematic viscosity of the fluid.

Grid points are clustered near the lower wall by using the transformation

$$x = e^{(\pi\xi)}\cos(\pi\eta), y = e^{(\pi\xi)}\sin(\pi\eta).$$

Zero velocity is specified on all the boundaries, except on the boundary AD, where a unit tangential velocity in clock-wise direction is specified. The steady flow is calculated for $Re = 55$, 350, 500, 1000, 3000, and 5000 which is based on the height of the wall AB and the tangential velocity of the lid AD. Here radial velocity $V_r = u\cos\phi + v\sin\phi = \dfrac{1}{\pi e^{\pi\xi}}\dfrac{\partial\psi}{\partial\eta}$ and tangential velocity $V_t = -u\sin\phi + v\cos\phi = -\dfrac{1}{\pi e^{\pi\xi}}\dfrac{\partial\psi}{\partial\xi}$. Since there is no slip on the solid walls, we have the following boundary conditions:

On AD, $\psi_\xi = \pi$, $\psi_\eta = 0$, and on all other boundaries, $\psi_\xi = 0$, $\psi_\eta = 0$.

Using normal velocity boundary conditions, we set $\psi = 0$ on all the boundary walls. The next task is to obtain boundary conditions for higher order derivatives used in the computation. From the above boundary conditions we immediately see that:

On AD and BC, $\psi_{\eta\eta} = \psi_{\eta\eta\eta} = \psi_{\xi\eta\eta} = 0$, and on AB and CD, $\psi_{\xi\xi} = \psi_{\xi\xi\xi} = \psi_{\xi\xi\eta} = 0$.

Next, $\psi_{\xi\xi}$ are estimated on AD and BC by using the second order approximation described by equation (2.50). The same approach is used for estimating $\psi_{\eta\eta}$ on AB and CD as well. The other higher order derivatives, namely $\psi_{\xi\xi\xi}, \psi_{\xi\xi\eta}$ on AD and BC, and $\psi_{\eta\eta\eta}, \psi_{\xi\eta\eta}$ on AB and CD are calculated by using second order extrapolation formula (2.51).

We present our computed solutions in figures 2.10-2.16 and tables 2.3-2.6 . In Figure 2.10, we present streamlines obtained from our numerical computation on a 55×79 grid side by side with the one obtained from the experimental results of [50] for $Re = 55$ and $Re = 350$. It is clear from the figures that our simulations are extremely close to the experimental results. Streamlines for $Re = 500$, $Re = 1000$, $Re = 3000$ and $Re = 5000$ are being presented in figure 2.11. As in the case of the square cavity flow, with increasing Re, the secondary vortices at the corners opposite to the moving wall grow in size and the strength of the primary vortex almost become invariant. But contrary to the phenomena of two distinct secondary vortices in square cavities, one on the top right (top left in [56, 57, 116]) and another at the bottom right corner for $Re \geq 1500$, only one secondary vortex on the top right corner is observed here for Re as high as 5000. Also, for higher Re, the secondary vortex on the left begins occupying the entire left side of the cavity as can be seen in figure 2.11(c) and (d). For $Re = 5000$, this secondary vortex

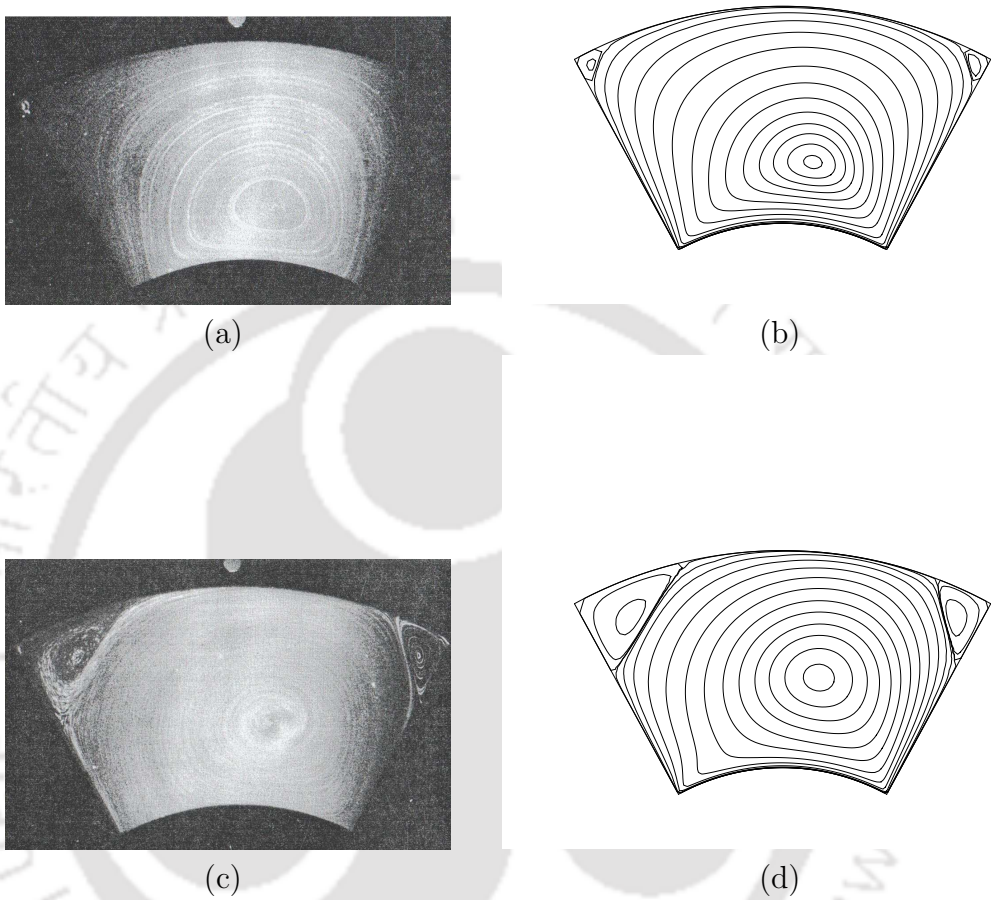

Figure 2.10: *Problem 3: Comparison of steady state stream function contours (a) $Re = 55$ Experimental, (b) $Re = 55$ Numerical, (c) $Re = 350$ Experimental, (d) $Re = 350$ Numerical.*

breaks into two (figure 2.11(d)). To the best of our knowledge, this phenomenon has not been reported elsewhere. The post processed vorticity contours for all the values of Re considered here are presented in figure 2.12. In figure 2.13, we present the u and v-velocities along the radial line $\theta = 0$ obtained through our computation on a 82×118 grid for $Re = 55$ and $Re = 350$ side by side, along with the experimental results of [50]. For $Re = 55$, our numerical results are very

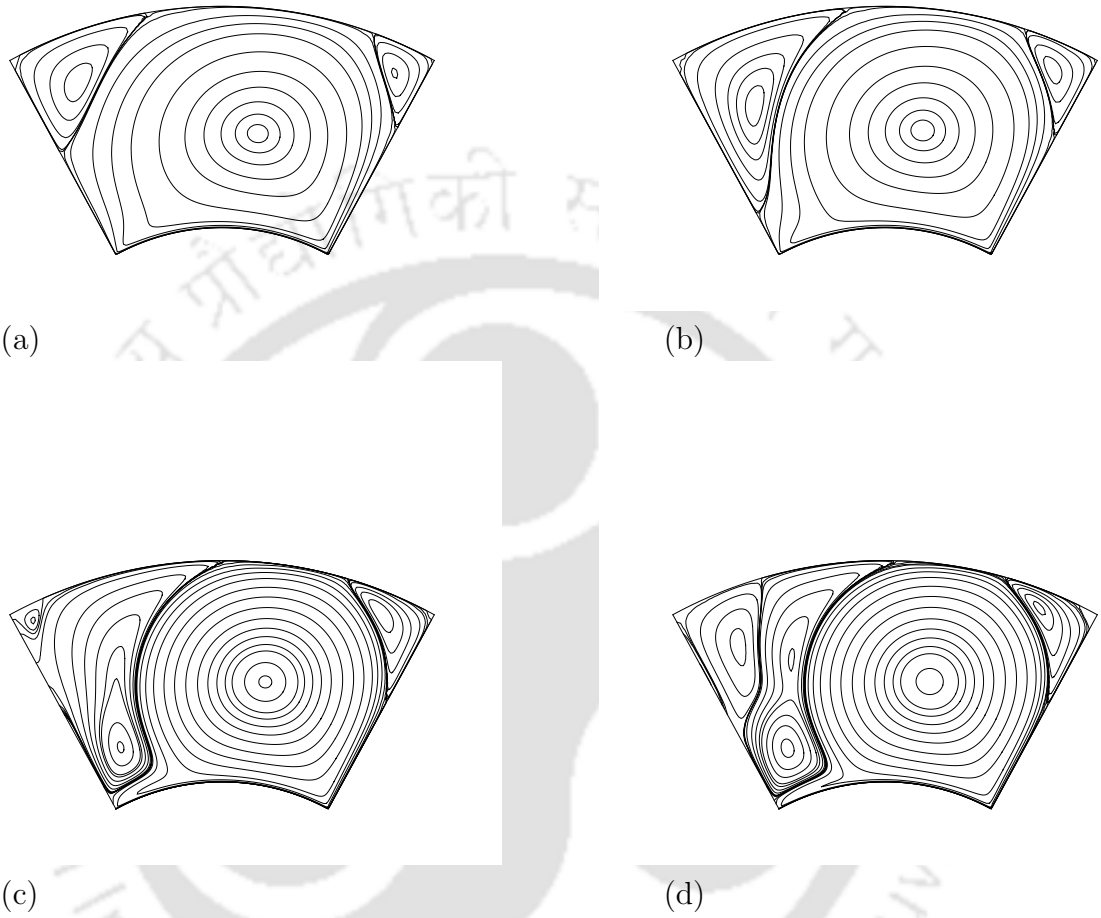

Figure 2.11: *Problem 3: Steady state stream function contours (a)* $Re = 500$*, (b)* $Re = 1000$*, (c)* $Re = 3000$*, (d)* $Re = 5000$.

close to the experimental ones while for $Re = 350$, a slight discrepancy is seen between the numerical and the experimental results which had been observed by Fuchs and Tillmark [50] as well and may be attributed to slower convergence rate at higher Re. In Figures 2.14(a) and 2.14(b), we present the u and v velocity profiles along $\theta = 0$ on three different grid sizes 28×40, 55×79, and 82×118 for two different Re values, 55 and 350 respectively. From these figures, it is clear that a 55×79 grid is enough to achieve grid-independence for these Re's. The velocity profile for $v-$ and $u-$ velocities along $\theta = 0$ line for $Re = 500$, 1000, 3000

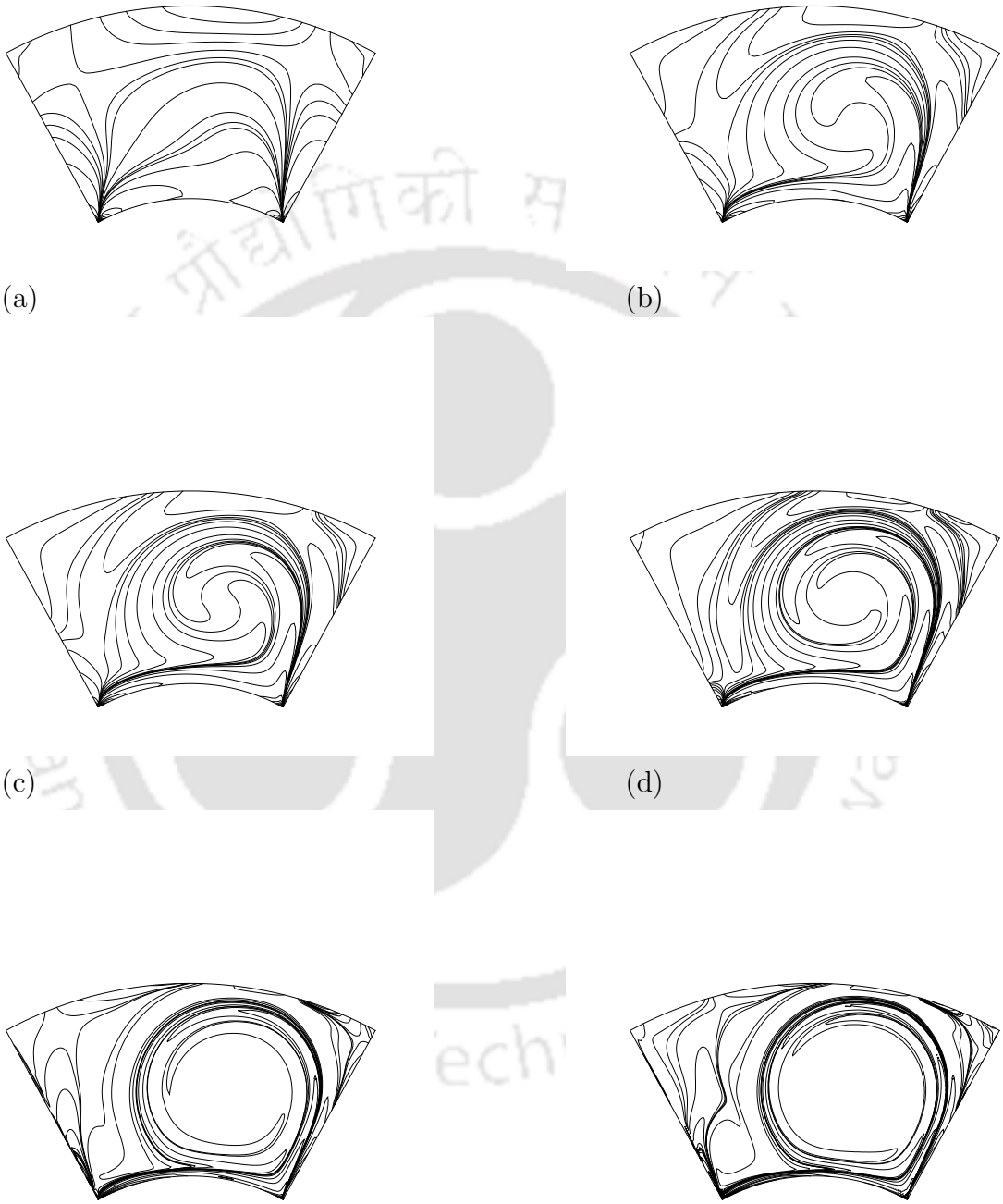

(a) (b)

(c) (d)

(e) (f)

Figure 2.12: *Problem 3: Steady state vorticity contours (a) $Re = 55$, (b) $Re = 350$, (c) $Re = 500$, (d) $Re = 1000$, (e) $Re = 3000$, (f) $Re = 5000$.*

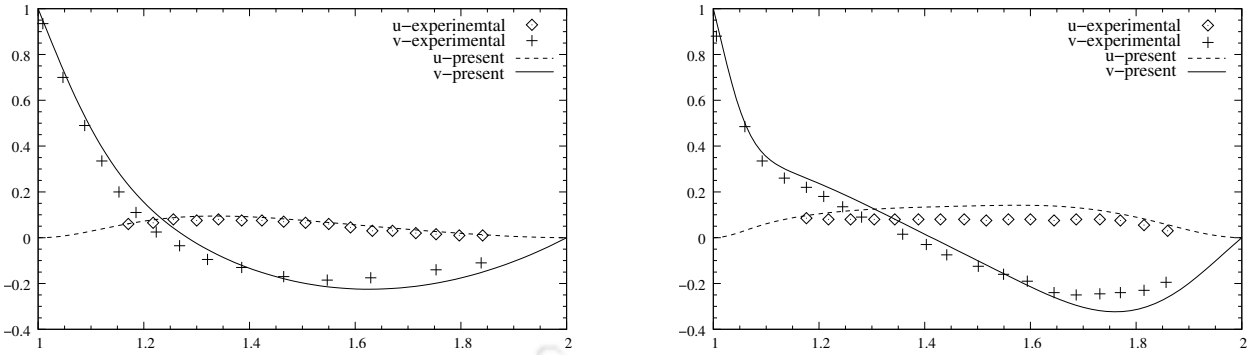

(a) (b)

Figure 2.13: *Problem 3: Comparison between experimental and numerical u- and v- velocities along $\theta = 0$ for (a) $Re = 55$, (b) $Re = 350$.*

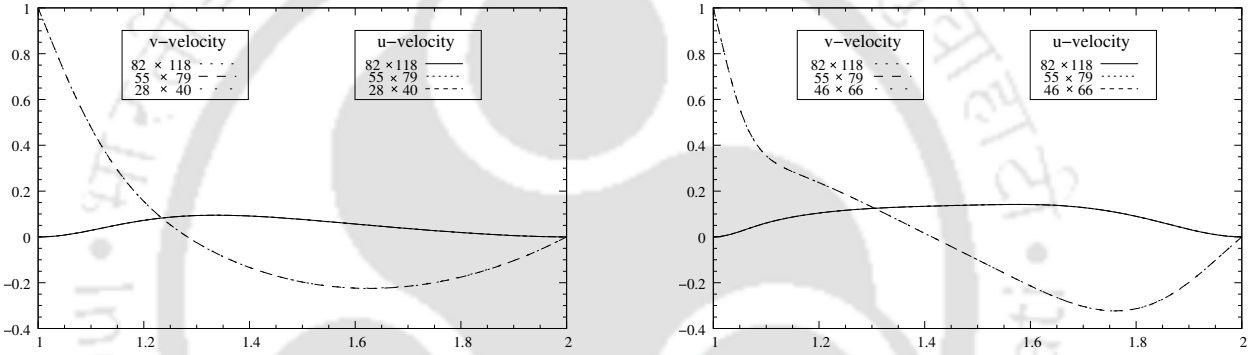

(a) (b)

Figure 2.14: *Problem 3: u- and v- velocity profiles on different grid sizes along $\theta = 0$ for (a) $Re = 55$, (b) $Re = 350$.*

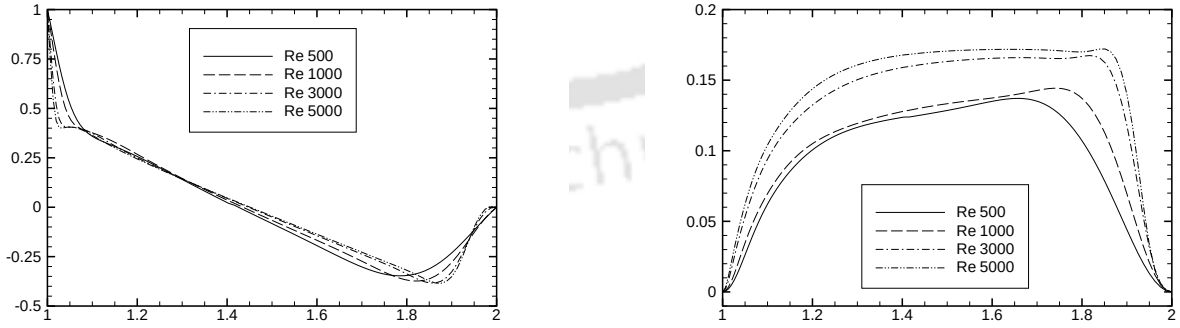

(a) (b)

Figure 2.15: *Problem 3: Velocity profiles along $\theta = 0$ (a) v- velocity, (b) u- velocity.*

and 5000 has been plotted in figure 2.15. We also calculate the perceived order of convergence for $Re = 55$ and $Re = 350$ by the formula described in section 2.4. As is evident from the tables 2.3 and 2.4, the order of convergence is close to four. The order of convergence drops a bit with increase in Re which may be attributed to the increase in flow complexity and slower convergence. Figure

Table 2.3: *Problem 3: Perceived order of convergence for* $Re = 55$

Grid Size	λ	Error	Order of Convergence
$[28 \times 40]$			
	$\lambda_1 = 3.0$	$\|\psi_2 - \psi_1\|_{L_2} = 1.332 \times 10^{-4}$	
$[55 \times 79]$			σ =3.936
	$\lambda_2 = 1.5$	$\|\psi_3 - \psi_2\|_{L_2} = 7.423 \times 10^{-6}$	
$[82 \times 118]$			

Table 2.4: *Problem 3: Perceived order of convergence for* $Re = 350$

Grid Size	λ	Error	Order of Convergence
$[46 \times 66]$			
	$\lambda_1 = 1.8$	$\|\psi_2 - \psi_1\|_{L_2} = 2.599 \times 10^{-5}$	
$[55 \times 79]$			σ =3.506
	$\lambda_2 = 1.5$	$\|\psi_3 - \psi_2\|_{L_2} = 2.203 \times 10^{-5}$	
$[82 \times 118]$			

Table 2.5: *Problem 3: CPU time and relaxation parameter associated with convergence history*

Re	Grid size	CPU time (in seconds)	relaxation parameter (Inner, Outer)
	$[28 \times 40]$	26.037	(0.15, 0.8)
55	$[46 \times 66]$	99.848	(0.3, 0.8)
	$[55 \times 79]$	273.538	(0.3, 0.8)
	$[28 \times 40]$	24.203	(0.15, 0.8)
100	$[46 \times 66]$	84.858	(0.2, 0.8)
	$[55 \times 79]$	243.316	(0.2, 0.8)

2.16 shows the convergence history for two Re values 55 and 100. Note that, the higher Reynolds number $Re = 100$ shows slightly less number outer iterations than for $Re = 55$; this is because of the fact that the converged solution of $Re = 55$ had been used as the initial guess for the computation of flow for $Re = 100$. In table 2.5 we present CPU time and convergence parameters associated with figure 2.16.

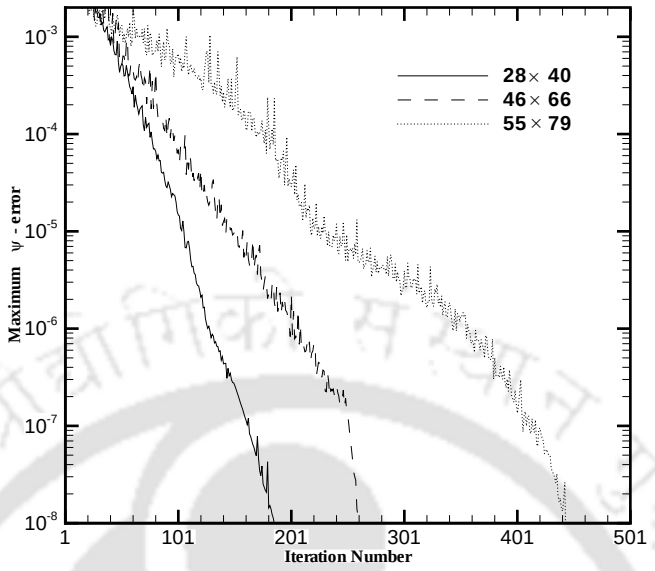

(a)

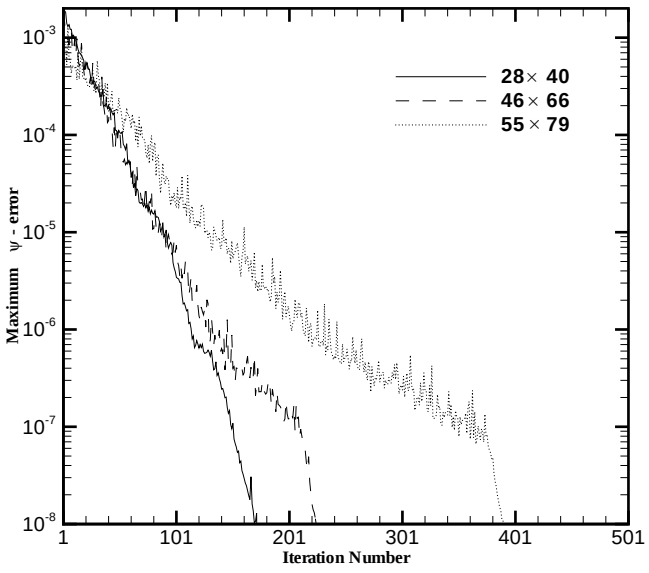

(b)

Figure 2.16: *Problem 3: Convergence history showing maximum ψ-error versus iteration number for (a) $Re = 55$, (b) $Re = 100$.*

Finally in table 2.6 we present all our quantitative data pertaining to the primary, secondary and tertiary vortices for $55 \leq Re \leq 5000$. These include the strength and location of the vortices as well as sizes (lenghts) of the secondary and tertiary vortices in conjunction with the nomenclature depicted in figure 2.9(c).

Table 2.6: *Problem 3: Properties of primary, secondary and tertiary vortices for Re ranging from 55 to 5000.*

		Re					
Vortex	Property	55	350	500	1000	3000	5000
Primary	ψ_{max}	0.1155	0.1263	0.1273	0.1275	0.1240	0.1220
	Location x, y	0.138, 1.285	0.163, 1.411	0.165, 1.423	0.166, 1.436	0.196, 1.447	0.206, 1.455
Secondary							
VL2	ψ_{min}	-4.994e-6	-4.009e-4	-1.190e-3	-3.480e-3	-7.089e-3	(a) -8.850e-3
							(b) -3.501e-3
	Location x, y	-0.876, 1.742	-0.696, 1.699	-0.650, 1.655	-0.589, 1.549	-0.459, 1.156	(a) -0.441, 1.154
							(b) -0.423, 1.555
	$RL2$	0.132	0.357	0.474	0.790	0.927	0.943
	$CL2$	0.137	0.539	0.658	0.821	0.994	1.038
VR2	ψ_{min}	-7.964e-6	-5.469e-4	-1.008e-3	-2.099e-3	-3.325e-3	-3.635e-3
	Location x, y	0.883, 1.731	0.796, 1.690	0.781, 1.696	0.755, 1.717	0.724, 1.757	0.695, 1.782
	$RR2$	0.132	0.315	0.341	0.385	0.439	0.458
	$CR2$	0.128	0.265	0.291	0.342	0.417	0.442
Tertiary							
VL3	ψ_{max}	—	—	—	—	3.637e-6	6.398e-4
	Location x, y	—	—	—	—	-0.853, 1.730	-0.666, 1.616
	$RL3$	—	—	—	—	0.127	0.708
	$CL3$	—	—	—	—	0.167	0.436
VR3	ψ_{max}	—	—	—	—	—	3.980e-6
	Location x, y	—	—	—	—	—	0.913, 1.751
	$RR3$	—	—	—	—	—	0.750e-1
	$CR3$	—	—	—	—	—	0.897e-1
Grid Size		82×118	82×118	82×118	82×118	109×157	109×157

2.5.4 Problem 4: Flow past an impulsively started circular cylinder

The problem of viscous incompressible flow past a circular cylinder has for a long time continued to generate tremendous interest amongst researchers [2, 42, 47, 76, 84, 93, 107, 123, 142] over the last century in all the three forms: theoretical, experimental and numerical. This is due to the fact that it is a good model problem for flows past bluff bodies of practical importance and it displays almost all the fluid mechanical phenomena for incompressible viscous flows in the simplest of geometric settings. However, the flow structure is very complex, especially for large Re, thus making the computation of the flow even more challenging and intriguing.

We assume the cylinder to be of unit radius placed in an infinite domain. The schematic diagram is presented in figure 2.17(a). At the upstream far-field, a potential flow is assumed with uniform free-stream velocity $U_\infty = D/2 = 1$ where $D = 2a$ is the diameter of the cylinder. The flow variables are non-dimensionalized by using $x = x^*/a$, $y = y^*/a$, $u = u^*/U_\infty$, $v = v^*/U_\infty$ and the Reynolds number Re is defined as $Re = DU_\infty/\nu$ following Fornberg [47]; here the asterisk sign * denotes the dimensional quantities. A typical computational grid of size 61×101 are shown in figure 2.17(b). The stream-wise length l and separation angle θ_s are defined in figure 2.17(c). We employ a uniform grid spacing along the cross radial direction and nonuniform grid spacing in the radial direction with clustering around the surface of the cylinder using the same transformation as that of polar cavity flow in section 2.5.3. Following [48], we assume the far field to be at a distance $R_\infty \approx 43a$.

We now derive the boundary conditions for stream function and its higher derivatives. On the surface of the cylinder $\xi = 0$, $u = v = 0 \Rightarrow \psi = 0$. In the far stream $\xi = \xi_\infty$, velocity becomes uniform, $u = U_\infty$, $v = 0$. Using these conditions, we obtain $\psi_\xi = \pi e^{(\pi\xi)} \sin(\pi\eta)$ and $\psi_\eta = \pi e^{(\pi\xi)} \cos(\pi\eta)$. In terms of stream function, this condition is expressed as $\psi = e^{(\pi\xi)} \sin(\pi\eta)$. In accordance with Franke *et al.* [48], the values for ψ_ξ and ψ_η obtained here are also used as boundary conditions for the upstream far flow while for the downstream far flow we use the condition that $\dfrac{\partial V_r}{\partial \xi} = 0$, $\dfrac{\partial V_t}{\partial \xi} = 0$. Use of one-sided second order accurate scheme translates these conditions to $\psi_{\eta_{imax,j}} \doteq \frac{1}{3}(4e^{\pi h}\psi_{\eta_{imax-1,j}} - e^{2\pi h}\psi_{\eta_{imax-2,j}})$, $\psi_{\xi_{imax,j}} \doteq \frac{1}{3}(4e^{\pi h}\psi_{\xi_{imax-1,j}} - e^{2\pi h}\psi_{\xi_{imax-2,j}})$ respectively. On the other hand, on the surface of the cylinder $u = 0$, $v = 0$ implying $\psi_\xi = 0$, $\psi_\eta = 0$.

Having obtained closed form expressions for ψ_ξ and ψ_η in the upstream far field

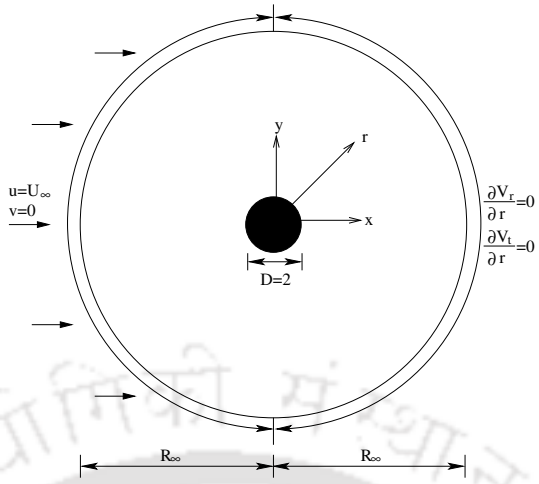

(a)

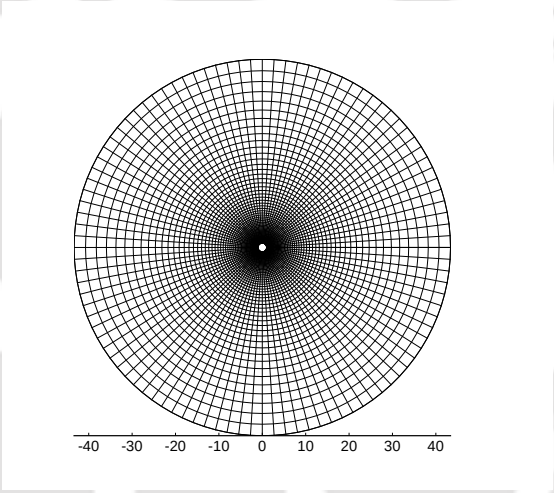

(b)

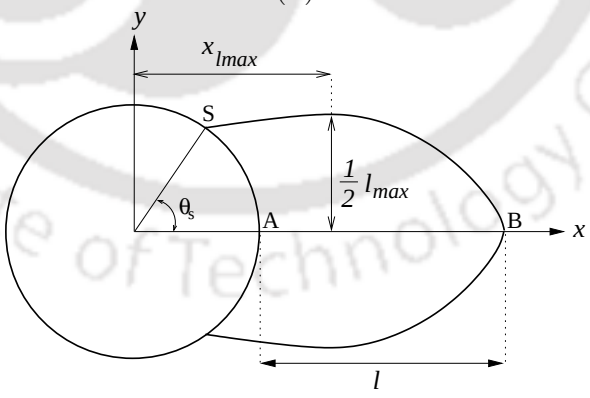

(c)

Figure 2.17: *Problem 4: (a) Flow configuration, (b) A typical* 61×101 *grid, (c) Geometrical parameters of the closed wake.*

we differentiate these expressions to obtain $\psi_{\xi\xi}$, $\psi_{\eta\eta}$, $\psi_{\xi\xi\eta}$, $\psi_{\xi\eta\eta}$, $\psi_{\eta\eta\eta}$. Next, using the relations $\frac{\partial V_r}{\partial \xi} = 0 \Rightarrow \psi_{\xi\eta} = \pi\psi_\eta$, $\frac{\partial V_t}{\partial \xi} = 0 \Rightarrow \psi_{\xi\xi} = \pi\psi_\xi$ and considering the fact that vorticity as given by equation (A.14) is zero at the far field we infer that for the downstream at far flow, $\psi_{\xi\xi} = \pi\psi_\xi$, $\psi_{\eta\eta} = -\pi\psi_\xi$, $\psi_{\xi\xi\xi} = \pi^2\psi_\xi$, $\psi_{\xi\xi\eta} = \pi^2\psi_\eta$, $\psi_{\xi\eta\eta} = -\pi^2\psi_\xi$, $\psi_{\eta\eta\eta} = -\pi^2\psi_\eta$. At $\xi = 0$ $\psi_{\xi\xi}$ can be calculated using (2.50). Finally, we estimate remaining boundary conditions namely $\psi_{\xi\xi\xi}$, $\psi_{\xi\xi\eta}$ at $\xi = 0$ by using (2.51).

Earlier studies [2, 42, 47, 76, 142] have shown that at a value of Re around 40, the steady flow appears to become unstable to small disturbances as the dissipative action of viscosity becomes relatively weak. The instability first affects the wake, at some distance downstream from the cylinder, and gives rise to slow oscillation of the wake with an amplitude which increases with distance downstream. As Re increases further the oscillation of the wake moves closer to the cylinder and, when Re is in the vicinity of 45, oscillations start affecting the two standing eddies immediately behind the cylinder. we shall discuss on the topic in more details in chapter 5.

We present steady state results for this flow for Re =10, 20, 40 and 60 in figures 2.18 and 2.19 and tables 2.7 and 2.8. Simulation for higher Re was not considered because earlier experimental and numerical studies [2, 42, 47, 76, 142] indicated that the flow no longer remains steady for Re beyond 50. Therefore, we present flow profiles for Re up to 60 only, more so for $Re = 20$ and $Re = 40$, for which experimental and numerical results [42, 47, 60, 84, 93, 107, 123, 142] exist in plenty; note that the results presented here for $Re = 60$ may be termed as the converged solution of the N-S equations governing the flow.

In Figure 2.18, we exhibit the streamlines from $Re = 10$ to 60. In all the cases, two symmetrical, stationary circulating eddy develops behind the cylinder. With increase in Re values, one can see the increase in the sizes of the vortices. The corresponding post processed vorticity contours for the same range of Re are shown in figure 2.19.

We also compute the wake length l, the distance between the rear most point of the cylinder to the end of the wake, and the angle of separation θ_s. These parameters are then compared to verify the grid-independence of the numerical results. In table 2.7, we present these parameters on grid sizes ranging from 61×101 to 121×201. Hence we can conclude that a grid of size 121×201 is enough for accurate resolution of the flow. In table 2.8, we present our computed l, θ_s and the drag coefficient C_D with those obtained by [42, 47, 60, 93, 107, 123, 142].

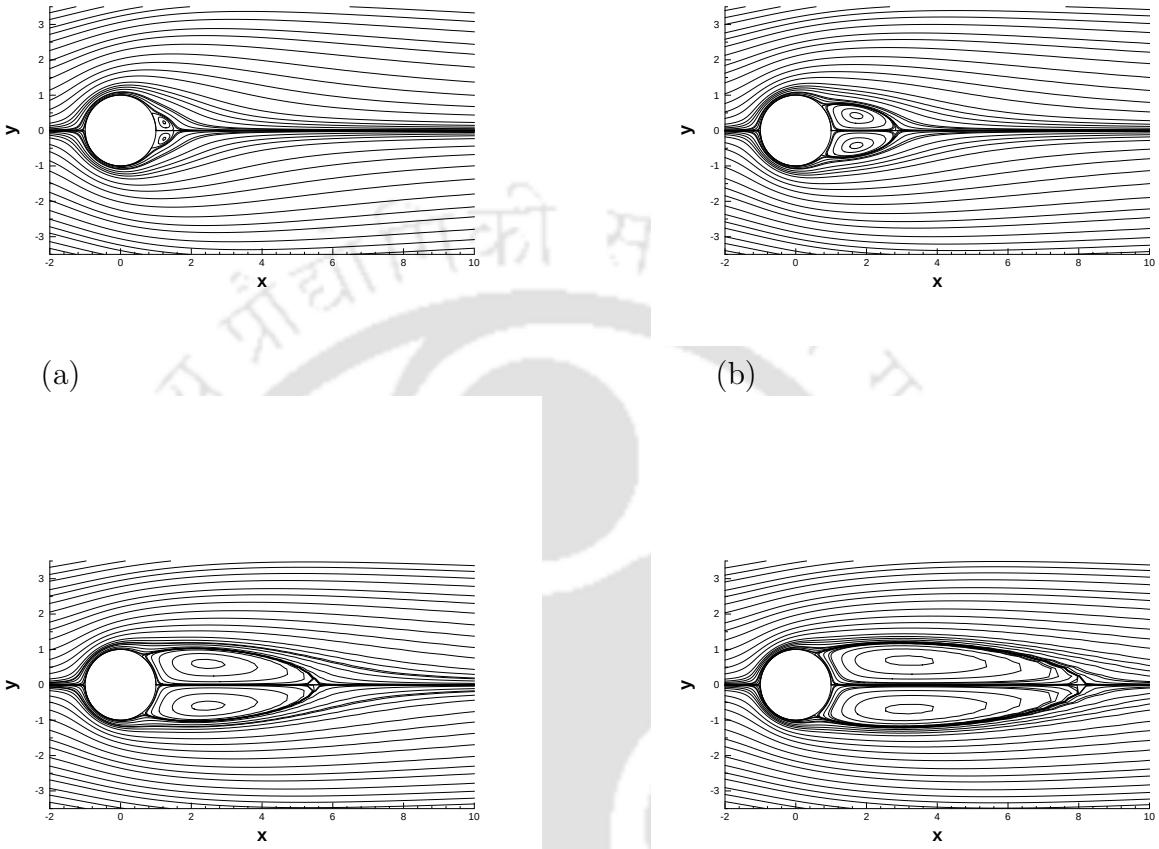

Figure 2.18: *Problem 4: Steady state stream lines (a) $Re = 10$, (b) $Re = 20$, (c) $Re = 40$, (d) $Re = 60$.*

Table 2.7: *Problem 4: Effect of grid size on wake length and separation angle.*

	$Re = 10$			$Re = 20$			$Re = 30$		
Grid	61×101	91×151	121×201	61×101	91×151	121×201	61×101	91×151	121×201
l	0.505	0.505	0.504	1.841	1.849	1.851	3.211	3.263	3.316
θ_s	29.321	29.078	29.732	43.517	43.196	43.141	50.085	49.640	49.579

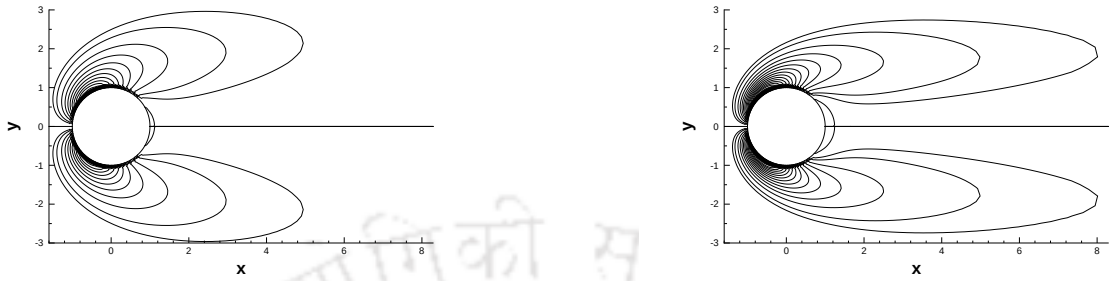

(a) (b)

(c) (d)

Figure 2.19: *Problem 4: Steady state vorticity contours (a)* $Re = 10$*, (b)* $Re = 20$*, (c)* $Re = 40$*, (d)* $Re = 60$*.*

The drag $\mathfrak{D}$ on the surface of a cylinder of radius r in a fluid of density ρ is $\mathfrak{D} = \rho r U_\infty^2 C_D$, where C_D is a non-dimensional coefficient. Following [47], the formula for evaluating the drag co-efficient on the surface of the cylinder may be written as:

$$C_D = \frac{1}{2\pi r}\int_0^2 \{(\psi_\xi^2 - \psi_\eta^2)\cos(\pi\eta) - \psi_\xi\psi_\eta \sin(\pi\eta)\}d\eta$$
$$-r\int_0^2 \psi_\eta \omega \sin(\pi\eta)d\eta + \frac{2r}{Re}\int_0^2 (\omega_\xi - \pi\omega)\sin(\pi\eta)d\eta. \qquad (2.52)$$

Using the expression for ω given by (A.14) and the boundary conditions on the

surface of the cylinder with radius $r = 1$ the above formula can be simplified as:

$$C_D = \frac{2}{Re\pi^2} \int_0^2 (3\pi\psi_{\xi\xi} - \psi_{\xi\xi\xi}) \sin(\pi\eta) d\eta,$$

which enables us to describe the entire problem purely in terms of stream function. The above integral has been evaluated by using Simpson's one-third formula. The vorticity and its derivative has been post processed from ψ, ψ_ξ, ψ_η by using fourth order accurate schemes. As can be seen from the figures and tables presented here, in all the cases, excellent comparison with the established numerical results are obtained, both qualitatively and quantitatively.

Table 2.8: *Problem 4: Comparison of wake length and separation angle for different Re.*

	Re	[142]	[42]	[47]	[93]	[60]	[107]	[123]	*present*
l	10	0.500	0.53	-	-	0.474	-	-	0.504
	20	1.870	1.88	1.82	1.87	1.842	1.92	1.77	1.851
	30	3.223	-	-	-	-	-	-	3.316
	40	4.650	4.69	4.48	4.27	4.49	4.51	4.21	4.625
	50	6.10	-	-	-	-	-	-	5.861
	60	7.53	-	-	-	-	-	-	7.206
θ_s	10	29.3	29.6	-	-	26.89	-	-	29.732
	20	43.65	43.7	42.9	-	42.96	42.79	41.3277	43.141
	30	49.6	-	-	-	-	-	-	49.579
	40	53.55	53.8	51.5	-	52.84	52.84	51.0249	53.226
	50	56.6	-	-	-	-	-	-	56.668
	60	59.0	-	-	-	-	-	-	59.565
C_D	10	2.7541	2.846	-	-	3.170	-	-	2.699
	20	2.0027	2.045	2.000	-	2.152	2.111	2.0597	1.949
	30	1.7167	-	-	-	-	-	-	1.640
	40	1.5359	1.522	1.498	-	1.499	1.574	1.5308	1.439
	50	1.4182	-	-	-	-	-	-	1.349
	60	1.3246	-	-	-	-	-	-	1.238

2.6 Conclusion

In this chapter, we extend a fourth order compact finite difference scheme for the classical biharmonic equation of the form $\Delta^2\psi = f(x, y)$ in rectangular Cartesian coordinates to its semi-linear form where the forcing function f contains higher order derivative of the dependent variable as well. This approach enables us to solve numerically the two dimensional steady N-S on nonuniform grids in non-rectangular physical geometries that are expressible in terms of conformal mappings. The use of conformal mapping makes possible the 2D physical domain to

be transformed onto a rectangular one where computations are performed for the transformed equations on uniform grids. The conformal nature of the mapping reduces the N-S equations into a quasi linear biharmonic equation in the transformed plane. In a departure from the rigidity of the earlier compact schemes for the biharmonic equations on irregular domains that could be applied only to Cartesian coordinates, the present formulation easily computes the flows governed by the N-S equations in situations where there is contact between solid and fluid requiring the use of a body-fitted coordinate system. To bring out different aspects of the scheme, we apply this new approach to four problems not only of varied physical complexities, but also on physical domains of different geometric settings: a problem with a known analytical solution, the flow past a constricted channel, the driven polar cavity and finally the motion past an impulsively started circular cylinder problem. In the first problem, Dirichlet boundary conditions are used and for the other two, compact higher order approximations have been developed and successfully implemented for the Neumann boundary conditions. The robustness of the scheme is illustrated by its successful implementation and, accurate and efficient computation of the flow for these three problems. The accuracy of the computed solutions can be judged by the results obtained in all the test cases on relatively coarser grids, which are in excellent agreement with analytical, experimental and established numerical results. As the proposed essentially compact scheme has the added advantage of low demand in CPU time, it has potential for efficient computation of more complex problems of incompressible viscous flows.

Chapter 3

A Robust Implicit Compact Scheme for Two Dimensional Unsteady Flows in Fluid-Embedded Body Interaction

3.1 Introduction

The N-S equations governing the flow of fluids have applications in a wide range of physics and engineering problems. In recent years, several important numerical techniques have been developed for solving N-S equations [31, 65, 101, 150] where simulations have been carried out for flows as diverse as the flow inside a complex biological region to the interaction between fluid and different types of embedded bodies.

Many problems of interest involve dynamics of coupled fluid-embedded body interaction. The most common occurrences are associated with fluid flowing over a bluff body or with the movement of a natural or artificial body. Bluff bodies exist in different shapes and sizes and include the flows past an airplane, automobile, submarine and wind blowing past a bridge, a high-rise building *etc.* At low Reynolds number the flow over a bluff body is highly viscous; as the Reynolds number increases beyond a critical value, vortex shedding occurs, resulting in a significant pressure drop on the rear surface of the body.

In this chapter, we propose a new compact finite difference scheme for the transient counterpart of the biharmonic form of the steady N-S equation which is second order accurate both temporally and spatially[1]. Here we use the new finite difference scheme to simulate the time development of 2D viscous flows for:

[1]Part of this work is under review in *Comp. Fluids.*

(i) Taylor-Green decaying vortices and (ii) Constricted channel. In the remaining chapters we will not only document the versatility of the fourth order stream function formulation, but also the efficiency of this scheme in simulating the dynamics of fluid-embedded body flow by using it for problems consisting of a variety of geometrical settings.

The first problem of Taylor-Green decaying vortices has a known closed form solution, which allows us to compare our numerical solutions with the exact ones and establish the order of convergence of our method. The second problem of flow through constricted channel is an internal flow problem, where we time march to steady state and serves as a test case for convergence analysis of fluid flow problems without known analytical solutions. For both the cases, our results are validated through comparisons with existing qualitative and quantitative results; excellent agreement is obtained in all cases.

The outline of the chapter is as follows. Section 3.2 deals with mathematical formulations, section 3.3 with discretization procedure, section 3.4 with stability analysis, section 3.5 with the solution of the algebraic system of equations and the related algorithm, section 3.6 with the numerical results and finally in section 3.7, we offer a few conclusions.

3.2 Mathematical formulations

As pointed out in Chapter 1, the primitive variable and stream function-vorticity formulations of the N-S equations are the most sought after approaches for computing viscous incompressible fluid flows. For flows in two dimensions, stream function-vorticity formulation is more popular for its computational economy. It also ensures exact satisfaction of mass conservation equation. However, in the case of flows in three dimensions, the primitive variable formulation is the preferred one. The three dimensional counterpart of the stream function-vorticity formulation deals with six unknowns in six equations. Another approach is to use the fourth order stream function vector equation, where each component results in a biharmonic equation and overall, there are only three variables to deal with. Following Chung [3] we write down the three dimensional pure stream function formulation

$$\frac{\partial}{\partial t}(\nabla^2\boldsymbol{\psi}) + [(\boldsymbol{\nabla}\times\boldsymbol{\psi}).\boldsymbol{\nabla}]\nabla^2\boldsymbol{\psi} - (\nabla^2\boldsymbol{\psi}.\boldsymbol{\nabla})(\boldsymbol{\nabla}\times\boldsymbol{\psi}) = \frac{1}{Re}\nabla^4\boldsymbol{\psi}. \qquad (3.1)$$

Here $\boldsymbol{\psi} = (\psi_1, \psi_2, \psi_3)$ is known as the three dimensional stream function vector. The vorticity $\boldsymbol{\omega} = (\omega_1, \omega_2, \omega_3)$ and the velocity $\boldsymbol{V} = (u, v, w)$ are respectively

expressed as

$$\boldsymbol{\omega} = -\nabla^2 \boldsymbol{\psi} \quad \text{and} \quad \boldsymbol{V} = \boldsymbol{\nabla} \times \boldsymbol{\psi},$$

the details of which may be found in [3]. This approach has been used quite successfully in solving the three dimensional cubic cavity problem [3]. In two dimensions $\boldsymbol{\psi} = (0, 0, \psi)$, and this system of three biharmonic equations reduces to one biharmonic evolution equation

$$\frac{\partial}{\partial t}(\nabla^2 \psi) + [(\nabla^{\perp}\psi).\nabla]\nabla^2\psi = \frac{1}{Re}\nabla^4\psi. \tag{3.2}$$

having the scaler stream function (ψ) as the only dependent variable. The out of plane component of vorticity is $\omega = \boldsymbol{\omega}.\widehat{k} = -\nabla^2\psi$ and the velocity field is $(u, v) = \nabla^{\perp}\psi = \left(\frac{\partial \psi}{\partial y}, -\frac{\partial \psi}{\partial x}\right)$. This biharmonic pure stream function form of the N-S equations eliminates the need to compute both pressure and vorticity, and has emerged as an attractive alternative [23, 24, 25, 56, 75, 87] to the classical formulations. This approach has the advantage of requiring the solution of a single fourth order partial differential equation (PDE) instead of a system of second order PDEs. The computation of flows using equation (3.2) has so far been restricted to only rectangular domains [23, 24, 25, 56, 75, 87], and the objective of the present study is to widen the scope of this formulation to non-rectangular physical domains.

Similar to our observations in Chapter 2, here also we note that the biharmonic equation (3.2) is not invariant under conformal mapping and hence solvers derived for rectangular Cartesian coordinate system can not be implemented. However, biharmonic character of (3.2) is retained under such transformations; therefore we focus our attention to fluid flow problems on irregular physical domains that are conformably mappable to rectangular computational domains.

We assume that the physical (x, y) plane can be transformed into a computational (ξ, η) plane by a conformal transformation of the form

$$z = z(\zeta), \tag{3.3}$$

where $z = x + Iy$ and $\zeta = \xi + I\eta$. The equations (3.2) in the computational plane takes the form

$$\begin{aligned} \frac{\partial}{\partial t}\nabla^2\psi &= a(\xi,\eta)\nabla^4\psi + b(\xi,\eta,\psi_\xi,\psi_\eta)\nabla^2\psi_\xi + c(\xi,\eta,\psi_\xi,\psi_\eta)\nabla^2\psi_\eta \\ &\quad + d(\xi,\eta,\psi_\xi,\psi_\eta)\nabla^2\psi \end{aligned} \tag{3.4}$$

with the velocities u and v given by

$$u = \frac{1}{J}\big(\psi_\eta x_\xi - \psi_\xi x_\eta\big), \tag{3.5}$$

$$v = \frac{1}{J}\big(- \psi_\xi y_\eta + \psi_\eta y_\xi \big). \tag{3.6}$$

where

$$a(\xi,\eta) = \frac{1}{ReJ}, \quad b(\xi,\eta,\psi_\xi,\psi_\eta) = \frac{1}{J}\left(-\frac{2C}{Re} - \psi_\eta\right),$$

$$c(\xi,\eta,\psi_\xi,\psi_\eta) = \frac{1}{J}\left(-\frac{2D}{Re} + \psi_\xi\right), \quad d(\xi,\eta,\psi_\xi,\psi_\eta) = \frac{1}{J}\left(\frac{E}{Re} + C\psi_\eta - D\psi_\xi\right),$$

$$C = \frac{J_\xi}{J}, \quad D = \frac{J_\eta}{J}, \quad E = 2C^2 + 2D^2 - \frac{J_{\eta\eta}}{J} - \frac{J_{\xi\xi}}{J},$$

J being the Jacobian of the transformation (3.3). The complete derivation of equation (3.4) is shown in Appendix A (equation (A.17)).

Equation (3.4) is the fourth order semi-linear pure stream function form of the N-S equation in the transformed plane. This PDE can be used to simulate fluid flow in any region which is conformably mappable to a rectangular domain and hence has much broader applicability. Note that our comments made in Chapter 2 on numerically generated conformal mappings, post processing of other flow variables and avoidance of difficulties related to primitive variable and ψ-ω formulations also apply in the transient case as well.

3.3 Discretization procedures

Amongst the several approaches of discretizing and numerically solving the N-S equations, we are interested in compact finite difference approximation because of its relative ease in implementation. Note that equation (3.4) can be written in terms of the harmonic operator $\Delta \equiv \nabla^2$ as

$$\begin{aligned}\frac{\partial}{\partial t}\Delta\psi &= a(\xi,\eta)\Delta^2\psi + b(\xi,\eta,\psi_\xi,\psi_\eta)\Delta\psi_\xi + c(\xi,\eta,\psi_\xi,\psi_\eta)\Delta\psi_\eta \\ &\quad + d(\xi,\eta,\psi_\xi,\psi_\eta)\Delta\psi.\end{aligned}$$

Our aim now is to discretize equation (3.4) compactly using only the eight neighbouring grid points surrounding each node. The main advantages of such an approach will be twofold: (i) the coefficient matrix resulting from the system of linear equations after discretization will have a smaller bandwidth and (ii) no modification will be needed at grid points near the boundaries, thus facilitating easier and at times exact implementation and satisfaction of the boundary conditions. The approach here involves discretizing the biharmonic equation (3.4) using not just the grid values of the unknown solution ψ but also the values of the gradients ψ_ξ and ψ_η at some grid points inside the computational stencil as shown in figure

3.1. This approach has its roots in the works of Gupta and Manohar [58] and was formulated by Stephenson [140]; later on, significant contributions in this direction were made by Altas *et al.* [17].

We use the following second order discretizations for space derivatives $\Delta^2\psi$ and $\Delta\psi$ appearing in (3.4)

$$\begin{aligned}\Delta_h^2\psi_{i,j} &= \delta_\xi^4\psi_{i,j} + 2\,\delta_\xi^2\delta_\eta^2\psi_{i,j} + \delta_\eta^4\psi_{i,j} \\ &= \frac{2}{h^4}\Big(28\psi_{i,j} - 8(\psi_{i+1,j} + \psi_{i,j+1} + \psi_{i-1,j} + \psi_{i,j-1}) \\ &\quad +(\psi_{i+1,j+1} + \psi_{i-1,j+1} + \psi_{i+1,j-1} + \psi_{i-1,j-1}) \\ &\quad +3h(\psi_{\xi_{i+1,j}} - \psi_{\xi i-1,j} + \psi_{\eta_{i,j+1}} - \psi_{\eta_{i,j-1}})\Big) \end{aligned} \tag{3.7}$$

$$\begin{aligned}\Delta_h\psi_{i,j} &= \delta_\xi^2\psi_{i,j} + \delta_\eta^2\psi_{i,j} \\ &= \frac{1}{h^2}\Big(\psi_{i+1,j} + \psi_{i,j+1} - 4\psi_{i,j} + \psi_{i-1,j} + \psi_{i,j-1}\Big). \end{aligned} \tag{3.8}$$

The details of the symbols used in equations (3.7) and (3.8) have already been given in section 2.3 of Chapter 2. Note that the presence of ψ_ξ and ψ_η in (3.7) may give the impression of complicating the associated linear system, instead, in the present case, it is an added advantage as these gradients, which are explicitly present in equation (3.4), being already available at all grid points, need not be approximated from the computed values of the solution ψ. Compatible fourth order approximations for ψ_ξ and ψ_η may be chosen as

$$\psi_{\xi_{i,j}} = (\delta_\xi\psi_{i,j} - \frac{h^2}{6}\delta_\xi^2\psi_{\xi_{i,j}}),$$
$$\psi_{\eta_{i,j}} = (\delta_\eta\psi_{i,j} - \frac{h^2}{6}\delta_\eta^2\psi_{\eta_{i,j}}).$$

By expanding the above equations one gets

$$\psi_{\xi_{i+1,j}} + 4\psi_{\xi_{i,j}} + \psi_{\xi_{i-1,j}} = \frac{3}{h}\big(\psi_{i+1,j} - \psi_{i-1,j}\big) \tag{3.9}$$

$$\psi_{\eta_{i,j+1}} + 4\psi_{\eta_{i,j}} + \psi_{\eta_{i,j-1}} = \frac{3}{h}\big(\psi_{i,j+1} - \psi_{i,j-1}\big). \tag{3.10}$$

Having obtained a second order approximations for space derivatives of equation (3.4), our next step is to discretize time derivative and obtain a stable numerical scheme. We introduce weighted time average parameter κ such that the evaluation time $t_\kappa = (1-\kappa)t_\kappa^{(n)} + \kappa t_\kappa^{(n+1)}$ is the weighted average of $t^{(n)}$, the time

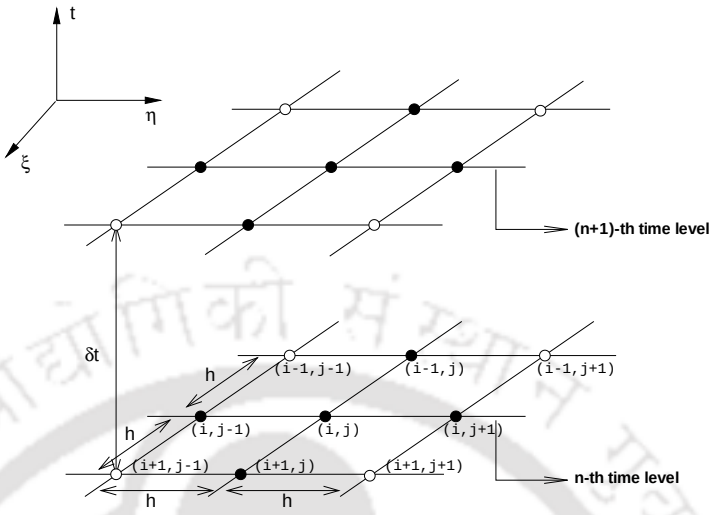

Figure 3.1: *Computational stencil for the transient scheme: all the nodes are used for ψ, the nodes denoted by "•" are used for ψ_ξ and ψ_η.*

at nth, and $t^{(n+1)}$, the time at $n+1$ step, for $0 \leq \kappa \leq 1$, and approximate equation (3.4) to

$$\begin{aligned}\Delta_h\psi_{i,j}^{(n+1)} &= \Delta_h\psi_{i,j}^{(n)} + \delta t(1-\kappa)\big[a_{i,j}\Delta_h^2\psi_{i,j}^{(n)} + b_{i,j}\Delta_h\psi_{\xi_{i,j}}^{(n)} + c_{i,j}\Delta_h\psi_{\eta_{i,j}}^{(n)} \\ &\quad + d_{i,j}\Delta_h\psi_{i,j}^{(n)}\big] + \delta t\kappa\big[a_{i,j}\Delta_h^2\psi_{i,j}^{(n+1)} \\ &\quad + b_{i,j}\Delta_h\psi_{\xi_{i,j}}^{(n+1)} + c_{i,j}\Delta_h\psi_{\eta_{i,j}}^{(n+1)} + d_{i,j}\Delta_h\psi_{i,j}^{(n+1)}\big]. \qquad (3.11)\end{aligned}$$

Varying κ provides a class of integrators, for example forward Euler for $\kappa = 0$, backward Euler for $\kappa = 1$ and Crank-Nicolson for $\kappa = \frac{1}{2}$. Using the last option, we obtain an $O(h^2; \delta t^2)$ accurate scheme for (3.4).

The finite difference approximation (3.11) along with (3.9) and (3.10) of the N-S equations, although only second order accurate in space and time, has three major advantages listed below:

1. Apart from initial condition, stream function and velocity boundary conditions are sufficient to carry out numerical computation.

2. It is applicable in any domain which can be conformably mapped to a rectangular domain.

3. The scheme being compact, it avoids use of ghost points at any stage of approximation.

Note that whenever the need for computing the velocities arises, equations (3.5) and (3.6) in conjunction with equations (3.9) and (3.10) can be used. To the best of our knowledge this is probably the only of its kind scheme for numerical solution of N-S equation in non-rectangular domains which avoids difficulties associated with pressure field and nonphysical vorticity boundary conditions and uses only stream function and velocity conditions at boundaries. In contrast to the fourth order accurate scheme developed in Chapter 2 this second order accurate scheme does not require approximation of any higher order derivative.

3.4 Stability analysis

We perform a von Neumann stability analysis to the linearized version of equation (3.4)

$$\frac{\partial}{\partial t}\Delta\psi = a\Delta^2\psi + b\Delta\psi_\xi + c\Delta\psi_\eta + d\Delta\psi, \tag{3.12}$$

where $a > 0$, b, c, d are considered to be independent of ψ and its derivatives. Note that $a(\xi, \eta) > 0$ in equation (3.4). The scheme (3.11) with $\kappa = \frac{1}{2}$ when applied to equation (3.12) gives

$$\begin{aligned}&(1-\kappa_1)\Delta_h\psi_{i,j}^{(n+1)} - \kappa_2 h^2\Delta_h^2\psi_{i,j}^{(n+1)} - \kappa_3\Delta_h\psi_{\xi_{i,j}}^{(n+1)} - \kappa_4\Delta_h\psi_{\eta_{i,j}}^{(n+1)}\\ &= (1+\kappa_1)\Delta_h\psi_{i,j}^{(n)} + \kappa_2 h^2\Delta_h^2\psi_{i,j}^{(n)} + \kappa_3\Delta_h\psi_{\xi_{i,j}}^{(n)} + \kappa_4\Delta_h\psi_{\eta_{i,j}}^{(n)}\end{aligned} \tag{3.13}$$

with $\kappa_1 = \dfrac{d\delta t}{2}$, $\kappa_2 = \dfrac{a\delta t}{2h^2}$, $\kappa_3 = \dfrac{b\delta t}{2}$, $\kappa_4 = \dfrac{c\delta t}{2}$.

Theorem 1 (Stability)**.** *The finite difference scheme (3.13) is unconditionally stable, in the von Neumann sense, if $d \leq 0$ and for $d > 0$ the scheme is stable under sufficient condition $\delta t < \dfrac{2}{d}$.*

Proof. Let $\psi_{i,j}^{(n)} = b^{(n)} e^{I\theta_\xi i} e^{I\theta_\eta j}$ where $b^{(n)}$ is the amplitude at time level n and $\theta_\xi = 2\pi h/\Lambda_1$, $\theta_\eta = 2\pi h/\Lambda_2$ are the phase angles with wavelengths Λ_1 and Λ_2 respectively, then from relations (3.9) and (3.10) we get

$$\psi_{\xi_{i,j}}^{(n)} = I\frac{3\sin\theta_\xi}{h(2+\cos\theta_\xi)}\psi_{i,j}^{(n)} \tag{3.14}$$

and

$$\psi_{\eta_{i,j}}^{(n)} = I\frac{3\sin\theta_\eta}{h(2+\cos\theta_\eta)}\psi_{i,j}^{(n)}. \tag{3.15}$$

Hence we can write

$$\Delta_h \psi_{i,j}^{(n)} = \frac{2}{h^2}(\cos\theta_\xi + \cos\theta_\eta - 2)\psi_{i,j}^{(n)}, \tag{3.16}$$

$$\Delta_h \psi_{\xi_{i,j}}^{(n)} = I\frac{6\sin\theta_\xi}{h^3(2+\cos\theta_\xi)}(\cos\theta_\xi + \cos\theta_\eta - 2)\psi_{i,j}^{(n)}, \tag{3.17}$$

$$\Delta_h \psi_{\eta_{i,j}}^{(n)} = I\frac{6\sin\theta_\eta}{h^3(2+\cos\theta_\eta)}(\cos\theta_\xi + \cos\theta_\eta - 2)\psi_{i,j}^{(n)}, \tag{3.18}$$

$$\begin{aligned}\Delta_h^2 \psi_{i,j}^{(n)} &= \frac{4}{h^4}\Bigg(14 - 8(\cos\theta_\xi + \cos\theta_\eta) + 2\cos\theta_\xi\cos\theta_\eta \\ &\quad -9(\frac{\sin^2\theta_\xi}{2+\cos\theta_\xi} + \frac{\sin^2\theta_\eta}{2+\cos\theta_\eta})\Bigg)\psi_{i,j}^{(n)}.\end{aligned} \tag{3.19}$$

If G is the amplification factor associated with the finite difference equation (3.13) then

$$G = \frac{(1+\kappa_1)A - 2\kappa_2 B + IC}{(1-\kappa_1)A + 2\kappa_2 B - IC}$$

where now

$$A = (2 - \cos\theta_\xi - \cos\theta_\eta),$$

$$B = 14 - 8(\cos\theta_\xi + \cos\theta_\eta) + 2\cos\theta_\xi\cos\theta_\eta - 9(\frac{\sin^2\theta_\xi}{2+\cos\theta_\xi} + \frac{\sin^2\theta_\eta}{2+\cos\theta_\eta}),$$

$$C = \frac{3}{h}\left(\frac{\sin\theta_\xi}{2+\cos\theta_\xi}\kappa_3 + \frac{\sin\theta_\eta}{2+\cos\theta_\eta}\kappa_4\right)A.$$

Clearly $0 \le A \le 4$ and $0 \le B \le 32$ and

$$|G|^2 = \frac{((1+\kappa_1)A - 2\kappa_2 B)^2 + C^2}{((1-\kappa_1)A + 2\kappa_2 B)^2 + C^2}.$$

Thus for $\kappa_1 \le 0 \Rightarrow d \le 0$, $|G| \le 1$ and the scheme is stable.

For $\kappa_1 > 0 \Rightarrow d > 0$ so the fourth term on right hand side of (3.12) is a growth term and the stability condition requires $|G| < 1 + K\delta t$ with K independent of δt [12]. This is obviously true for $\kappa_1 < 1 \Rightarrow \delta t < \frac{2}{d}$.

This completes the proof. □

3.5 Solution of algebraic systems of equations

Let us now discuss the solution of algebraic systems associated with the finite difference approximation (3.11). As we are interested in second order accuracy in time we chose $\kappa = \frac{1}{2}$. Using the notations introduced in section 2.4 of Chapter 2 the resulting system of equation in matrix form is

$$M_1 \Psi^{(n+1)} = F_1\big(\Psi^{(n)}, \Psi_\xi^{(n)}, \Psi_\eta^{(n)}, \Psi_\xi^{(n+1)}, \Psi_\eta^{(n+1)}\big) \tag{3.20}$$

For a grid of size $m \times n$, the matrix M_1 has the dimension mn. Due to the compact nature of our scheme M_1 is a banded matrix with nine non zero diagonals. Also $\Psi^{(n)}$, $\Psi_\xi^{(n)}$, $\Psi_\eta^{(n)}$, $\Psi^{(n+1)}$, $\Psi_\xi^{(n+1)}$, $\Psi_\eta^{(n+1)}$ are all mn component vectors. At any time step, once $\Psi^{(n)}$ has been approximated $\Psi_\xi^{(n)}$, $\Psi_\eta^{(n)}$ can be obtained by solving tridiagonal systems

$$M_2 \Psi_\xi^{(n)} = F_2\big(\Psi^{(n)}\big) \tag{3.21}$$

$$M_3 \Psi_\eta^{(n)} = F_3\big(\Psi^{(n)}\big) \tag{3.22}$$

respectively. The equations (3.21) and (3.22) are the corresponding matrix forms of the relations (3.9) and (3.10). Thus the main objective now is to solve the equation (3.20), thereby evaluating unknown vector $\Psi^{(n+1)}$. But a difficulty arises due to the presence of $(n+1)$th time level gradients of Ψ on the right hand side of equation (3.20) as those quantities will be available only after solving for stream function at the $(n+1)$th time level. To overcome this difficulty we adopt a predictor-corrector approach. By setting $\kappa = 0$ in equation (3.11) we get a first order time accurate formula which has the matrix representation

$$M_4 \Psi_{old}^{(n+1)} = F_4\big(\Psi^{(n)}, \Psi_\xi^{(n)}, \Psi_\eta^{(n)}\big) \tag{3.23}$$

Here M_4 is a matrix with only five non zero diagonals and we have the advantage that $\Psi^{(n+1)}$ can be estimated directly. Thus we have the following algorithm:

1. Predict $\Psi_{old}^{(n+1)}$ using (3.23).
2. Predict $\Psi_{\xi_{old}}^{(n+1)}$, $\Psi_{\eta_{old}}^{(n+1)}$ using (3.21) and (3.22) respectively.
3. Correct to $\Psi_{new}^{(n+1)}$ using (3.20).
4. Correct to $\Psi_{\xi_{new}}^{(n+1)}$, $\Psi_{\eta_{new}}^{(n+1)}$ using (3.21) and (3.22) respectively.
5. If $\|\Psi_{new}^{(n+1)} - \Psi_{old}^{(n+1)}\| < \epsilon$ then $\Psi^{(n+1)} = \Psi_{new}^{(n+1)}$.

6. $\Psi_{old}^{(n+1)} = \Psi_{new}^{(n+1)}$, goto step 3.

Direct solution of any of the above linear system is impractical because of huge size of the coefficient matrix and enormous storage requirements even for moderate values of step length h. On the other hand condition number of the coefficient matrix increases rapidly with reduced step length h and one must be very cautious while using iterative solvers. As the coefficient matrix M_1 is not diagonally dominant, conventional solvers such as Gauss-Seidel also cannot be used. Therefore all the computations were performed using the biconjugate gradient stabilized (BiCGStab) [4] method without preconditioning, where, thanks to the compact grid, it is easy to implement matrix vector multiplication $M_1\Psi$ without the need of storing all the entries of the matrix M_1. It is worth mentioning here that in solving all the linear systems mentioned above we found that there was no need to under-relax or over-relax any of the parameters. This is indeed a refreshing experience as compared to solving formulations based of vorticity-stream function or primitive variable where there is a severe need to under relax quite a few parameters.

The convergence criterion for BiCGStab iteration based on norm of residual was set at 10^{-8} and the stopping criterion for the corrector was set at 10^{-12}. All our computations were carried out on a Pentium Dual-Core processor based PC with 2 GB RAM using double precision floating point arithmetic.

3.6 Numerical experiments

3.6.1 Problem 1: Taylor-Green decaying vortices

At first we consider the Taylor-Green problem of flow decayed by viscosity. This problem is often used as a model problem for analyzing the spatial accuracy of schemes [25, 75, 119, 152]. The analytical solution of this problem expressed in terms of stream function is

$$\psi = -\cos(x)\cos(y)e^{-\frac{2t}{Re}}.$$

We solve this problem inside the domain $\mathbb{D} = \{(x, y) : x + Iy = (1 + I)(\xi + I\eta),\ \ -\pi/2 \leq \xi \leq \pi/2,\ \ -\pi/2 \leq \eta \leq \pi/2\}$, with $Re = 1$ and $\delta t = 0.01$. The initial and boundary conditions have been derived from the analytical solution. We carry out computation with four different grids having sizes 9×9, 17×17, 33×33 and 65×65. Results obtained for $t = 1.0$ $t = 2.0$ and $t = 5.0$ have been tabulated in table 3.1. In figures 3.2(a) and (b) respectively, we plot the

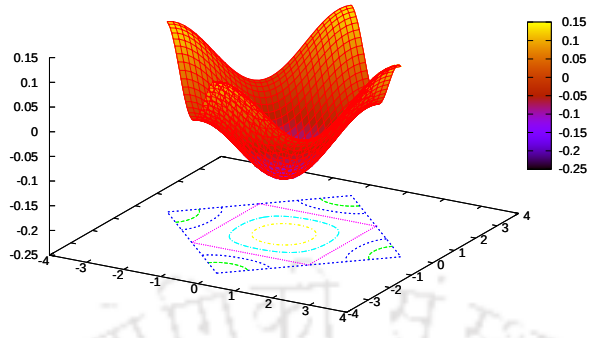

(a)

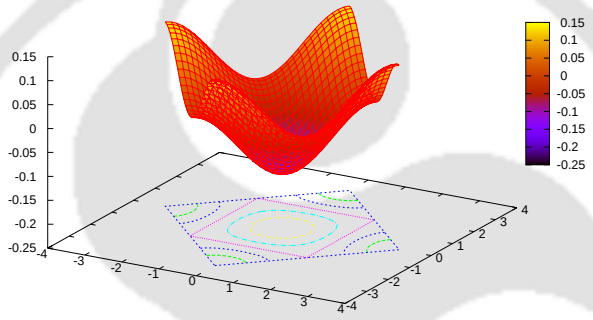

(b)

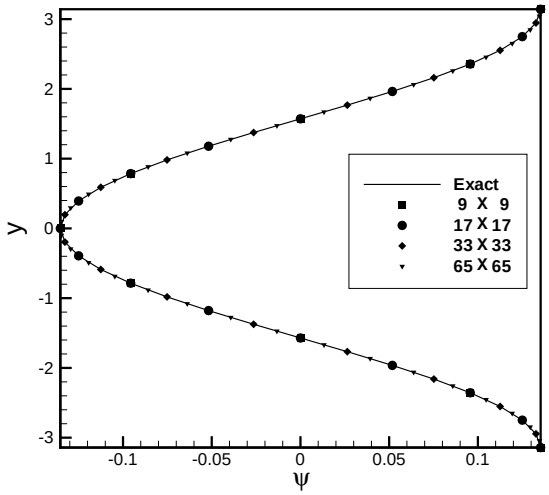

(c)

Figure 3.2: *Problem 1: Scheme validation (a) Numerical, (b) Exact surface with the contours; and (c) Grid convergence along the line* $x = 0$.

numerical and exact surfaces along with the stream function contours at time $t = 1.0$. It is heartening to see that on a grid as coarse as 33×33, the numerical solution is almost indistinguishable from the exact one. In figure 3.2(c) we present a comparison between our numerical solution and the exact solution along the $x = 0$ line on four grids of increasing sizes. As can be seen from the figure, grid-independence is obtained on a grid as coarse as 17×17 onwards. The L_1, L_2 and L_∞ errors presented in table 3.1 are as defined in section 2.5.1 of Chapter 2. This table shows that the present scheme achieves a better rate than the expected second order spatial accuracy. This may be due to the nature of the test problem being considered [25, 75].

Table 3.1: *Problem 1: L_1-error, L_2-error, L_∞-error and order of convergence*

Mesh		9×9	Order	17×17	Order	33×33	Order	65×65
$t = 1$	L_1	3.822×10^{-5}	4.21	2.063×10^{-6}	4.04	1.251×10^{-7}	3.85	8.687×10^{-9}
	L_2	4.722×10^{-5}	4.13	2.699×10^{-6}	4.00	1.683×10^{-7}	3.83	1.186×10^{-8}
	L_∞	9.861×10^{-5}	4.03	6.028×10^{-6}	3.96	3.881×10^{-7}	3.80	2.779×10^{-8}
$t = 2$	L_1	5.173×10^{-6}	4.21	2.792×10^{-7}	4.04	1.693×10^{-8}	3.85	1.176×10^{-9}
	L_2	6.390×10^{-6}	4.13	3.653×10^{-7}	4.00	2.278×10^{-8}	3.83	1.605×10^{-9}
	L_∞	1.335×10^{-5}	4.03	8.158×10^{-7}	3.96	5.253×10^{-8}	3.80	3.761×10^{-9}
$t = 5$	L_1	1.282×10^{-8}	4.21	6.919×10^{-10}	4.04	4.196×10^{-11}	3.85	2.914×10^{-12}
	L_2	1.584×10^{-8}	4.13	9.055×10^{-10}	4.00	5.646×10^{-11}	3.83	3.979×10^{-12}
	L_∞	3.308×10^{-8}	4.03	2.022×10^{-9}	3.96	1.302×10^{-10}	3.80	9.324×10^{-12}

3.6.2 Problem 2: Fluid flow in a constricted symmetric channel

We consider this problem because this is an idealization of flows in geometries that contains a re-entrant corner [31, 97, 115]. At such a corner the flow becomes singular as was pointed out in section 2.5.2 of Chapter 2. In order to obtain accurate results near such a corner, it is necessary to have a highly refined non-uniform grid there. In this problem the flow occurs in a non-uniform channel containing a step-down constriction. Another motive here is to establish order of convergence for problems having no analytical solution.

The algebraic transformation and other flow parameters are same as defined in previous chapter. But as our aim is to show the time development of the flow, we consider the entire channel as opposed to upper half of the channel considered in Chapter 2. The schematic diagram of the problem is presented in figure 2.4(a). A

close up view of the grid near the constriction for a typical grid of size 941×41 is shown below in figure 3.3. The boundary conditions are designed to satisfy

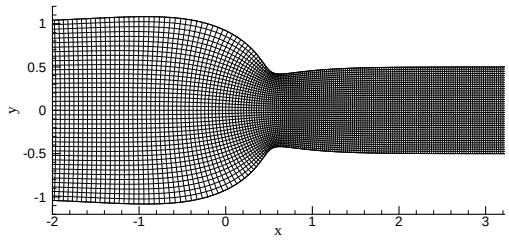

Figure 3.3: *Problem 2: Close up view of a typical* 941×41 *grid.*

conservation of mass in the computational domain. At the walls, a no slip condition is assumed. The boundary conditions can be summarized as:

$$\psi = 1 \quad \text{and} \quad \frac{\partial \psi}{\partial \eta} = 0 \qquad \text{on the wall} \quad \eta = \tau$$

$$\psi = -1 \quad \text{and} \quad \frac{\partial \psi}{\partial \eta} = 0 \qquad \text{on the wall} \quad \eta = -\tau$$

$$\psi = \frac{\eta}{2\tau}\left(3 - \frac{\eta^2}{\tau^2}\right) \quad \text{and} \quad \frac{\partial \psi}{\partial \xi} = 0 \quad \xi \to \pm\infty.$$

The two main controlling parameters for this flow are τ and Re, and several combinations of them have been tested in our computation. For all the computations we consider $\delta t = 0.001$. In table 3.2, we present the converged steady state error results for the cases $\tau = 0.6$, $Re = 100$ and $\tau = 0.8$, $Re = 10$ showing the spatial order of convergence σ.

Table 3.2: *Problem 2: Perceived order of convergence*

	Grid Size	Error in L_1	σ	Error in L_2	σ	Error in L_∞	σ
$\tau = 0.6$	$[471 \times 21]$	$\|\Psi_2 - \Psi_1\|_{L_1} = 8.388\times10^{-5}$		$\|\Psi_2 - \Psi_1\|_{L_2} = 2.060\times10^{-4}$		$\|\Psi_2 - \Psi_1\|_{L_\infty} = 1.603\times10^{-3}$	
	$[706 \times 31]$		2.131		2.178		2.252
$Re = 100$		$\|\Psi_3 - \Psi_2\|_{L_1} = 2.780\times10^{-5}$		$\|\Psi_3 - \Psi_2\|_{L_2} = 6.762\times10^{-5}$		$\|\Psi_3 - \Psi_2\|_{L_\infty} = 5.123\times10^{-4}$	
	$[941 \times 41]$						
$\tau = 0.8$	$[471 \times 21]$	$\|\Psi_2 - \Psi_1\|_{L_1} = 6.175\times10^{-6}$		$\|\Psi_2 - \Psi_1\|_{L_2} = 3.020\times10^{-5}$		$\|\Psi_2 - \Psi_1\|_{L_\infty} = 3.099\times10^{-4}$	
	$[706 \times 31]$		2.086		2.097		2.112
$Re = 10$		$\|\Psi_3 - \Psi_2\|_{L_1} = 2.095\times10^{-6}$		$\|\Psi_3 - \Psi_2\|_{L_2} = 1.020\times10^{-5}$		$\|\Psi_3 - \Psi_2\|_{L_\infty} = 1.042\times10^{-4}$	
	$[941 \times 41]$						

This table clearly reveals a convergence of order two for the method. Note that in the absence of an analytical solution, the order of convergence σ can be

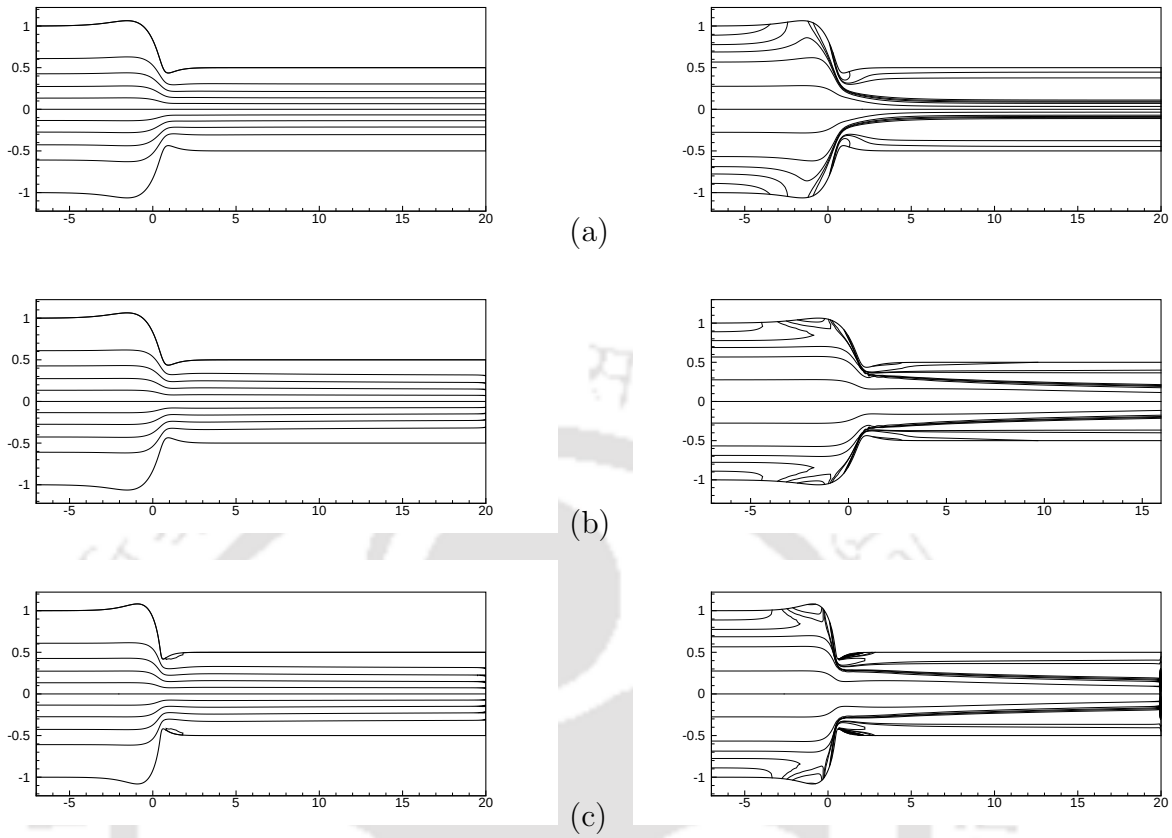

Figure 3.4: *Problem 2: Steady state stream lines (left) and vorticity contours (right) for (a)* $\tau = 0.6$, $Re = 100$; *(b)* $\tau = 0.6$, $Re = 1000$; *and (c)* $\tau = 0.8$, $Re = 1000$.

estimated using the relation

$$\frac{\|\Psi_2 - \Psi_1\|}{\|\Psi_3 - \Psi_2\|} \doteq \frac{h_1^\sigma - h_2^\sigma}{h_2^\sigma - h_3^\sigma}$$

obtained in Chapter 2. Here h_1, h_2, h_3 are mesh sizes in three different uniform grids used to compute solutions Ψ_1, Ψ_2, Ψ_3 respectively.

We show the streamline and post processed vorticity contours for $Re = 100$, $\tau = 0.6$ and for $Re = 1000$, $\tau = 0.6$ and 0.8 in figure 3.4. This figure (as well as figure 3.5) clearly indicates that vortices near the constriction are formed only for high values of τ . For the case $\tau = 1.0$, $Re = 500$ we present the evolution of streamlines in figure 3.5 where one can see the development of the main vortices at the top and bottom near constrictions. To begin with, there are two small vortices which grow in size as time elapses. As the main vortex acquires strength, smaller vortices are

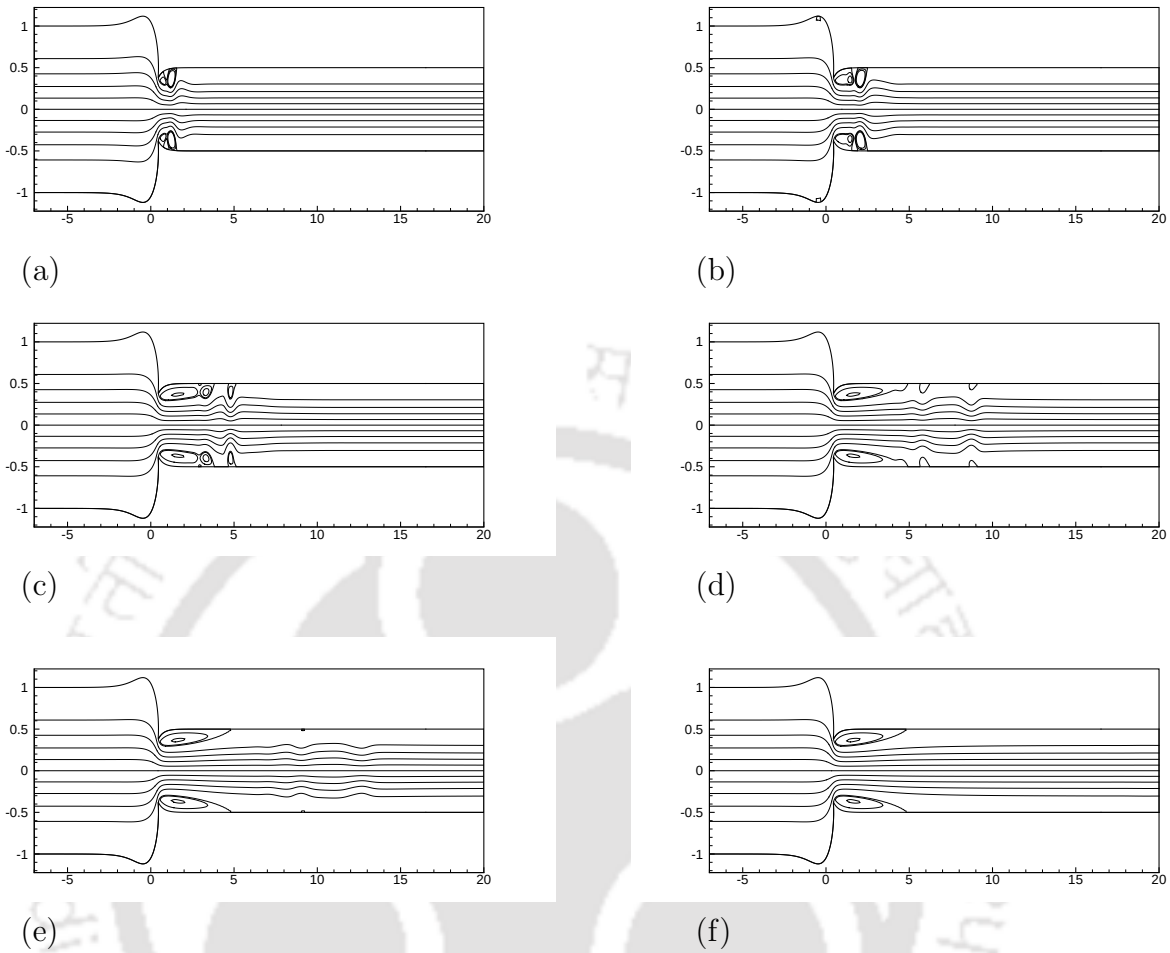

Figure 3.5: *Problem 2: Time evolution of stream line contours for* $Re = 500$, $\tau = 1.0$ *at (a)* $t = 1.0$, *(b)* $t = 2.0$, *(c)* $t = 4.0$, *(d)* $t = 6.0$, *(e)* $t = 8.0$, *(f)* $t = 15.0$.

shed. These vortices propagate towards the outlet and diffuse completely before the steady state is reached.

3.7 Conclusion

Numerical schemes based on pure stream function formulation of the transient N-S equations have so far been developed only on Cartesian coordinates for rectangular domains. Here we develop an implicit, temporally and spatially second order accurate compact finite difference scheme for such a formulation that allows us to effectively simulate unsteady viscous incompressible flows in irregular geometries that can be conformably mapped onto rectangular domains.

We perform numerical experiments on two different problems in order to investigate the efficiency of the scheme. In the process, we also carry out a stability and convergence analysis; the first problem considered is that of decaying vortices with known closed form solution, where the order of convergence of the present method is established. The problem of flow through constricted channel, where we time march to steady state, is an internal flow problem and serves as a suitable test case for convergence analysis of problems having no analytical solution. As mentioned in section 3.1 in the remaining chapters of this dissertation we consider the next series of numerical test cases.

Chapter 4

The Biharmonic Approach for Unsteady Flow Past an Impulsively Started Circular Cylinder

4.1 Introduction

Flow over a bluff body is a common phenomenon which occurs when fluid flows over an obstacle or along with the movement of a natural or artificial body. Common examples are the flows past an airplane, a submarine, an automobile, or wind blowing past a high-rise building. Although bluff bodies exist in many different shapes, the circular cylinder is considered to be the representative of a two dimensional bluff body. As such, the flow around a circular cylinder has been the subject of intense research in the last century and numerous theoretical, numerical and experimental investigations have been reported in the literature [2, 28, 39, 48, 52, 67, 72, 93, 94, 106, 117, 122, 126, 143, 149, 154, 158, 159]. A comprehensive study of the fundamentals of this flow is given by Zdravkovich [15]. The time development of an incompressible viscous flow induced by an impulsively started circular cylinder is now a classical problem in fluid mechanics. It displays almost all the fluid mechanical phenomena for incompressible viscous flows in the simplest of geometric settings.

In the context of numerical studies on this problem, with the advent of CFD, more and more computational methods for simulating fluid flows are coming into the fore [38, 39, 48, 60, 67, 72, 76, 93, 94, 107, 117, 123]; which has led to the better understanding of the characteristics of the flow. Numerical simulation could now invade areas hitherto unexplored by experimentalists where it is possible to analyze

all aspects of the flow at each stage of its development. A quick look at these works reveals that there exists only a few studies where a single numerical scheme has been employed to tackle the flow throughout the whole range of $10^0 \leq Re \leq 10^4$. The ranges of Reynolds numbers which came under the purview of these works, varied from one study to the other. Although investigations on vortex shedding has been quite popular with the experimentalists ever since Roshko [122] first measured the period of von Kármán vortex shedding behind a bluff body, the simulation and characteristic study of streak lines seem to have failed to attract the attention of numerical analysts. One of the objectives of the present study is also to address these two issues apart from capturing other flow characteristics for this problem.

Fluid flow problems governed by N-S equations can be solved by using a variety of numerical methods. As is well established, these methods can broadly be classified as finite difference, finite volume or finite element approach. Amongst these, FDM is the most popular approach that has been used quite frequently in CFD because of its easiness in implementation. In the FD set up, approximation of a higher order derivative generally requires more points and as such is associated with non-compact stencils. Such schemes, which are used for higher order differential equations on non-compact stencils, require additional conditions in order to tackle the difficulty of flow computation at the boundary. Contrary to these, compact finite difference schemes [55, 73, 138] such as the ones developed in our work, which utilize grid points located only directly adjacent to the node, computes the flow with information solely from the nearest neighbours and are gaining popularity via-a-vis wide-molecule schemes [31, 61, 62, 141].

We have already mentioned that the biharmonic pure stream function form of the N-S equations, is emerging as an attractive alternative to the ψ-ω and primitive variable formulations because of advantages associated with it. However, the schemes developed so far for the biharmonic pure stream function form of the N-S equations were capable of computing the flow only for simple rectangular geometries on uniform grids. Efficient implementation of the velocity stream function approach spearheaded by Gupta and Kalita [56, 75] in its original form is extremely difficult, if not impossible on nonrectangular physical domains. In the present study, we use the compact second order temporally and spatially accurate FD scheme for the biharmonic pure stream function form of transient N-S equations on non-uniform grids developed in Chapter 3. This scheme is capable of tackling geometries beyond rectangular and hence can be used to simulate the dynamics of fully coupled flow-body system. We chose the problem of impulsively

started circular cylinder because of the availability of benchmark experimental as well as numerical results and therefore serve very well as a suitable test case for accuracy and effectiveness of the newly proposed technique. The grid is constructed using a conformal mapping, which results in a general orthogonal grid, where the degree and nature of the non-uniformity can be specified to meet the needs of the problem being studied. The added advantage of our approach is that no other boundary condition is required except for stream function and velocity. To the best of our knowledge this is the first attempt to simulate flow around a bluff body by discretizing a single equation instead of a system of equations.

Our main focus in this chapter is to analyze the flow past an impulsively started circular cylinder in different laminar flow regimes using a single numerical scheme and compare our numerical results with established experimental and numerical ones[1]. Time evolution of flow structure is studied through numerical simulation for a wide range of Re ranging from 5 to 9500. This includes the visualization of the flow by numerically generating streak lines. The computations are performed by time marching, using the predictor-corrector approach discussed in section 3.5 of Chapter 3. Despite being spatially lower order accurate than traditional higher order compact schemes, the numerical solutions obtained through the proposed scheme are in excellent match with the available experimental and established numerical results as would be seen later. This is due to the fact that the scheme utilizes the advantage of grid clustering in the regions of small scales which invariably requires more grid points to resolve the scale irrespective of the spatial accuracy of the scheme.

The chapter has been arranged in five sections. Section 4.2 deals with the mathematical formulation and discretization procedures, section 4.3 with the problem and the numerical issues, section 4.4 with the numerical results and finally, section 4.5 summarizes the whole work.

4.2 Mathematical formulations and discretization procedures

The unsteady 2D incompressible viscous flows are governed by the N-S equations together with the equation of continuity. In Cartesian (x^*, y^*) coordinate system, these equations can be written as

$$u^*_{t^*} + u^* u^*_{x^*} + v^* u^*_{y^*} = -\frac{1}{\rho} p^*_{x^*} + \nu\left(u^*_{x^*x^*} + u^*_{y^*y^*}\right) \tag{4.1}$$

[1]Part of this work has been published in *Commun. Comput. Phys.*

$$v^*_{t^*} + u^* v^*_{x^*} + v^* v^*_{y^*} = -\frac{1}{\rho} p^*_{y^*} + \nu\big(v^*_{x^*x^*} + v^*_{y^*y^*}\big) \tag{4.2}$$

$$u^*_{x^*} + v^*_{y^*} = 0 \tag{4.3}$$

where u^*, v^* are dimensional velocities along x^*-, y^*- directions respectively, p^* is the dimensional pressure, ρ is the density and ν is the kinematic viscosity. We assume the cylinder to be of unit radius placed in an infinite domain. The flow variables are non-dimensionalized by writing $x = x^*/a$, $y = y^*/a$, $u = u^*/U_\infty$, $v = v^*/U_\infty$, $t = t^* U_\infty/D$, $p = p^*/(\rho U_\infty^2)$ and the Reynolds number Re is defined as $Re = DU_\infty/\nu$ where $D = 2a$ is the diameter of the cylinder, U_∞ being the free-stream velocity. The non-dimensionalization have been carried out following Bouard and Coutanceau [29] and is consistent with that of section 2.5.4. The above equations (4.1)-(4.3) now reduces to

$$\frac{1}{2}u_t + uu_x + vu_y = -p_x + \frac{2}{Re}\big(u_{xx} + u_{yy}\big) \tag{4.4}$$

$$\frac{1}{2}v_t + uv_x + vv_y = -p_y + \frac{2}{Re}\big(v_{xx} + v_{yy}\big) \tag{4.5}$$

$$u_x + v_y = 0. \tag{4.6}$$

We wish to employ a uniform grid spacing along the transient direction and nonuniform grid spacing in the radial direction with clustering around the surface of the cylinder so that propagation of large solution error can be avoided [90]. Keeping this in mind we consider the transformation

$$x = e^{(\pi\xi)} cos(\pi\eta), y = e^{(\pi\xi)} sin(\pi\eta)$$

introduced in Chapter 2. The resulting fourth order biharmonic pure stream function form of the N-S equation is

$$\begin{aligned} Re\frac{\pi^2 e^{2\pi\xi}}{4}\frac{\partial}{\partial t}\Delta\psi &= \Delta^2\psi - \big(4\pi + \frac{Re}{2}\psi_\eta\big)\Delta\psi_\xi + \frac{Re}{2}\psi_\xi\Delta\psi_\eta \\ &\quad +2\pi\big(2\pi + \frac{Re}{2}\psi_\eta\big)\Delta\psi \end{aligned} \tag{4.7}$$

It contains ψ as the only dependent variable from which other flow variables can be post processed in contrast to three dependent variables u, v, and p associated with the system of equations (4.4) to (4.6) and hence the equation (4.7) is much more handy for numerical simulation. The $O(h^2; \delta t^2)$ finite difference approximation

(3.11) for (4.7) is

$$
\begin{aligned}
Re\frac{\pi^2 e^{2\pi\xi_i}}{4}\Delta_h\psi_{i,j}^{(n+1)} &= Re\frac{\pi^2 e^{2\pi\xi_i}}{4}\Delta_h\psi_{i,j}^{(n)} \\
&+\frac{1}{2}\delta t\Big[\Delta_h^2\psi_{i,j}^{(n)} - \big(4\pi + \frac{Re}{2}\psi_{\eta_{i,j}}^{(n)}\big)\Delta_h\psi_{\xi_{i,j}}^{(n)} \\
&+\frac{Re}{2}\psi_{\xi_{i,j}}^{(n)}\Delta_h\psi_{\xi_{i,j}}^{(n)} + 2\pi\big(2\pi + \frac{Re}{2}\psi_{\eta_{i,j}}^{(n)}\big)\Delta_h\psi_{i,j}^{(n)}\Big] \\
&+\frac{1}{2}\delta t\Big[\Delta_h^2\psi_{i,j}^{(n+1)} - \big(4\pi + \frac{Re}{2}\psi_{\eta_{i,j}}^{(n+1)}\big)\Delta_h\psi_{\xi_{i,j}}^{(n+1)} \\
&+\frac{Re}{2}\psi_{\xi_{i,j}}^{(n+1)}\Delta_h\psi_{\xi_{i,j}}^{(n+1)} + 2\pi\big(2\pi + \frac{Re}{2}\psi_{\eta_{i,j}}^{(n+1)}\big)\Delta_h\psi_{i,j}^{(n+1)}\Big]
\end{aligned} \tag{4.8}
$$

with spatial operators $\Delta_h^2\psi_{i,j}$ and $\Delta_h\psi_{i,j}$ as defined in (3.7) and (3.8) respectively and $\psi_{\xi_{i,j}}$ and $\psi_{\eta_{i,j}}$ compactly approximated by (3.9) and (3.10) respectively.

4.3 The problem and the numerical issues

We stick to the same configuration, numerical grid and geometrical parameters presented in figure 2.17 in Chapter 2. The boundary conditions for stream function and its first order derivatives are obtained as:

1. On the surface of the cylinder $\xi = 0$, $u = v = 0 \Rightarrow \psi_\xi = 0$, $\psi_\eta = 0$, $\psi = 0$.
2. In the far upstream $u = U_\infty$, $v = 0 \Rightarrow \psi_\xi = \pi e^{(\pi\xi)} sin(\pi\eta)$, $\psi_\eta = \pi e^{(\pi\xi)} cos(\pi\eta)$ and $\psi = e^{(\pi\xi)} sin(\pi\eta)$ which corresponds to the potential flow.
3. In the far downstream we use the Neumann condition that $\frac{\partial V_r}{\partial \xi} = 0 = \frac{\partial V_t}{\partial \xi}$. One sided second order approximation translates these conditions to, $\psi_{\eta_{imax,j}} \doteq \frac{1}{3}(4e^{\pi h}\psi_{\eta_{imax-1,j}} - e^{2\pi h}\psi_{\eta_{imax-2,j}})$, $\psi_{\xi_{imax,j}} \doteq \frac{1}{3}(4e^{\pi h}\psi_{\xi_{imax-1,j}} - e^{2\pi h}\psi_{\xi_{imax-2,j}})$ respectively.
4. In the far downstream we use convective boundary condition for ψ given by $\frac{\partial \psi}{\partial t} + U_\infty\frac{\partial \psi}{\partial x} = 0$ appropriately translated onto the $\xi\eta$- plane.

For such flows, where there is a tendency to simulate vortex shedding, at the downstream of the flow, potential boundary condition for ψ has been replaced by convective boundary condition and was found to be quite efficient in correctly capturing the shedding process. It was seen in our computations that use of any other boundary condition at the downstream leads to severe oscillation as the shed

vortices are convected out of the computational domain. On the other hand, the continuous shedding of the vortices when they leave the computational domain in the direction of the flow can be best facilitated by the convective boundary condition. Again for flows with higher Re, the convective boundary condition at the very initial stage of flow does not work very well. Thus if one wishes to simulate a flow from very beginning until the final vortex shedding state is reached an ideal choice will be to march first few iterations till non-dimensional time 0.25 (say) with the potential boundary condition and then to proceed with the convective boundary condition. As far as the initial condition is concerned we have started with $\psi = 0$ every where except at the boundary as also $\psi_\xi = \psi_\eta = 0$ every where except at the upstream boundary. In order to accurately capture the time evolution of the flow, we use $\delta t = 0.001$ for all the simulations considered in this chapter. We use the formula obtained in Chapter 2 for evaluating C_D on the surface of the cylinder given by

$$C_D = \frac{2}{\pi^2 Re} \int_0^2 \left(3\pi\psi_{\xi\xi} - \psi_{\xi\xi\xi}\right) \sin(\pi\eta) d\eta.$$

Similarly the expression for lift coefficient becomes

$$C_L = \frac{2}{\pi^2 Re} \int_0^2 \left(3\pi\psi_{\xi\xi} - \psi_{\xi\xi\xi}\right) \cos(\pi\eta) d\eta.$$

This enables us to describe the entire problem purely in terms of stream function. The above integrals have been evaluated by using Simpson's one-third formula.

We also estimate the Strouhal number, defined as $St = \frac{fa}{U_\infty}$, where f is the dominant frequency of the lift variations, which characterizes the vortex shedding process.

We follow the strategy outlined in section 3.5 of Chapter 3 for solving the system of algebraic equation.

4.4 Numerical results

It is well established that immediately after the fluid motion starts, the flow is irrotational everywhere. But gradually, due to the fluid motion, vorticity is generated on the surface of the cylinder and slowly it is transported to the rear stagnation point and flow reversal takes place. After a short period of time for flows with $Re > 5$, a recirculating zone appears and it continues to grow eventually leading to flow separation. For $Re \leq 5$ no visible flow distortion takes place and it has also

been confirmed by this study. The time development of flow differs with Re increasing. At $Re \approx 6$, although the flow separates from the cylinder, is still steady and laminar. With the increase in Re, expectedly the flow becomes more complicated due to the appearance of secondary and tertiary vortices. A look at the literature suggests that there is some critical Reynolds number (Re_c), where $43 \leq Re_c \leq 50$, at which Hopf bifurcations takes place. For $Re > Re_c$ unsteady vortex shedding representing the so called von Kármán vortex street is known to occur. Keeping these points in mind and depending upon the characteristics observed within each range we have divided the flow regime into five parts of which four parts will be discussed in this chapter. Our focus is on the Re range 5 to 9500. In the first part we discuss about the flow structures for $5 \leq Re \leq 40$. Available experimental and the numerical results show that steady state is possible for this range. In the second part we discuss about the flow structures for $50 \leq Re \leq 300$, here the wake behind the cylinder becomes unstable. Oscillations in the wake grow in amplitude and finally forms a trail of vortices known as the von Kármán vortex street. For the next higher Re being discussed here, we consider only the early stage of the flow in the laminar regime. The first of these is the range $300 \leq Re \leq 1000$. Here the flow properties are unsteady; secondary vortices develop at the initial stages, but do not split up further. The flow is characterized by the secondary phenomena: (i) bulge phenomenon and (ii) isolated secondary eddy. In the last part, we discuss the range $3000 \leq Re \leq 9500$ which is characterized by the most complicated flow properties associated with the α- and β- phenomena. The remaining fifth part *viz.* $40 \leq Re \leq 50$ will be discussed in details in Chapter 5.

4.4.1 Flows for $5 \leq Re \leq 40$

It is well known that for $5 \leq Re < Re_c$, where $43 \leq Re_c \leq 50$, a recirculating zone appears behind the cylinder continuously growing in size with time that eventually leads to the steady state. This is probably the most well studied region for the problem of flow past a circular cylinder. In this region flow develops into what is known as steady state. Here the flow separates from the cylinder and two symmetric counter rotating eddies are formed just behind the cylinder. These eddies grow with time in wake length l, *i.e.* the distance between the rear most point A, stagnation point, of the cylinder to the end B of the wake and in angle of separation θ_s *i.e.* the angle between the x-axis and the line joining the center of the cylinder to the point of separation S on the cylinder as can be seen in figure 2.17(c). Finally these eddies settle down in the form of a wake. The characteristics of the

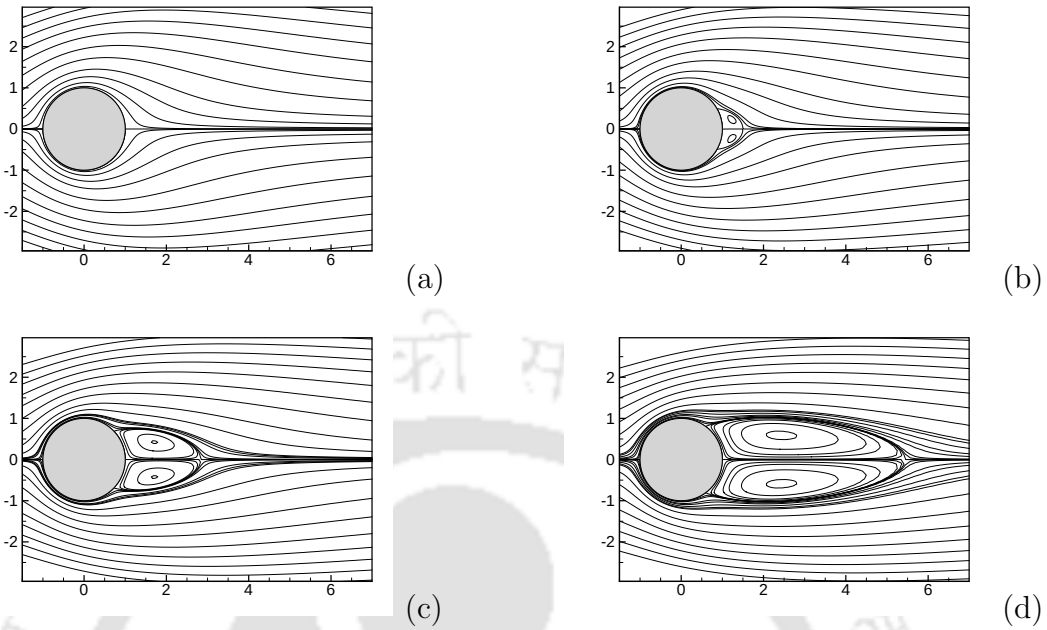

Figure 4.1: *Time marched to steady state stream lines (a) $Re = 5$, (b) $Re = 10$, (c) $Re = 20$, (d) $Re = 40$.*

final wake depend on the Re under consideration. Both steady as well as unsteady codes have been used previously to simulate final flow character in this region. But time marching procedure captures the flow development in a physically relevant manner. In this study we have simulated flow for $Re = 5$, 10, 20, and 40. The streamlines for different Re's as stated above have been shown in figure 4.1. This gives a clear idea of recirculation bubble formed behind the cylinder and its growth in size with increase in Re. The corresponding post processed vorticity contours are shown in figure 4.2. The drag coefficient as a function of the dimensionless time for different values of the Reynolds number is shown in figure 4.3. These graphs confirm the eventual steady nature of the flow for this range of Reynolds numbers.

We compare l, θ_s and C_D in table 4.1 in order to verify the grid-independence; the grid sizes range from 61×101 to 181×301 with $R_\infty \approx 43$. Table 4.2 shows the variation of the same parameters to check the dependence of the computed solution on the assumed far field $R_\infty \approx 23$, $R_\infty \approx 43$ and $R_\infty \approx 81$. Here the step length in either direction of the transformed plane has been fixed at $h = \frac{1}{75}$. These tables provide a good indication that a value of $R_\infty \approx 43$ on a grid of size 181×301

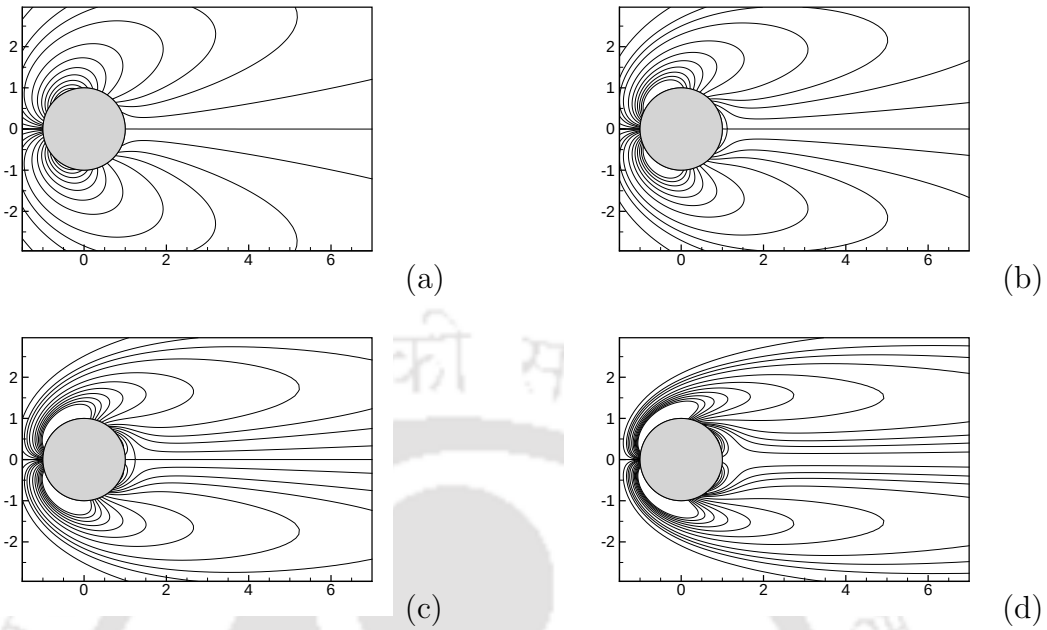

Figure 4.2: *Time marched to steady state vorticity contours (a) $Re = 5$, (b) $Re = 10$, (c) $Re = 20$, (d) $Re = 40$.*

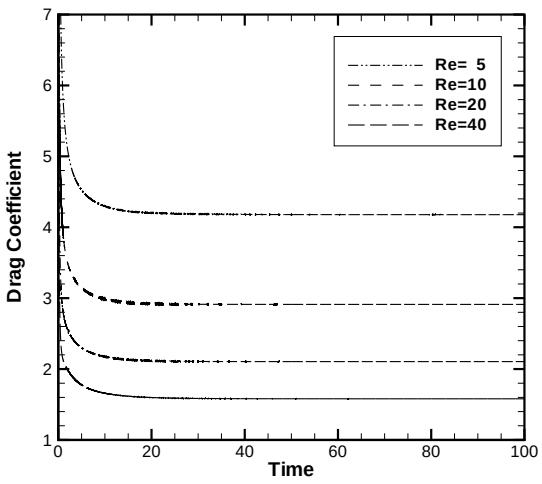

Figure 4.3: *Evolution of drag coefficient with time for $Re = 5$, 10, 20, 40.*

is enough for accurate resolution of the flow as would be seen in the following sections when we compare the numerical and experimental flow visualizations. In table 4.3, we present our computed l and θ_s and the drag coefficient C_D along with those obtained by [42, 47, 60, 93, 107, 123, 142]. In figure 4.4 we compare the

post processed vorticity values along the surface of the cylinder for the range of Re values considered here with those of references [42, 47]. In figures 4.5(a) and 4.5(b), we compare the evolution of the wake lengths and angles of separation at the early stages of the flow with the results of [40]. In all the cases, an excellent agreement has been obtained both qualitatively and quantitatively.

Table 4.1: *Effect of grid size on steady state properties.*

	Grid	61×101	91×151	181×301
$Re = 10$	l	0.549	0.518	0.504
	θ_s	27.591	28.946	29.558
	C_D	2.946	2.930	2.912
$Re = 20$	l	1.909	1.850	1.852
	θ_s	43.183	43.346	43.910
	C_D	2.168	2.138	2.148
$Re = 40$	l	4.491	4.412	4.433
	θ_s	53.567	53.130	53.270
	C_D	1.675	1.633	1.590

Table 4.2: *Effect of far field boundary on steady state properties.*

	$R_\infty \approx$	23	43	81
$Re = 10$	l	0.517	0.518	0.518
	θ_s	28.817	28.946	28.975
	C_D	3.101	2.930	2.877
$Re = 20$	l	1.850	1.850	1.852
	θ_s	44.053	43.346	43.446
	C_D	2.243	2.138	2.108
$Re = 40$	l	4.340	4.412	4.569
	θ_s	53.500	53.130	53.332
	C_D	1.702	1.633	1.614

Table 4.3: *Comparison of steady state wake length and separation angle for different Re.*

	Re	[142]	[42]	[47]	[93]	[60]	[107]	[123]	Present
l	10	0.500	0.53	-	-	0.474	-	-	0.504
	20	1.870	1.88	1.82	1.87	1.842	1.92	1.77	1.852
	40	4.650	4.69	4.48	4.27	4.49	4.51	4.21	4.433
θ_s	10	29.3	29.6	-	-	26.89	-	-	29.558
	20	43.65	43.7	42.9	-	42.96	42.79	41.3277	43.910
	40	53.55	53.8	51.5	-	52.84	52.84	51.0249	53.270
C_D	10	2.7541	2.846	-	-	3.170	-	-	2.912
	20	2.0027	2.045	2.000	-	2.152	2.111	2.0597	2.148
	40	1.5359	1.522	1.498	-	1.499	1.574	1.5308	1.590

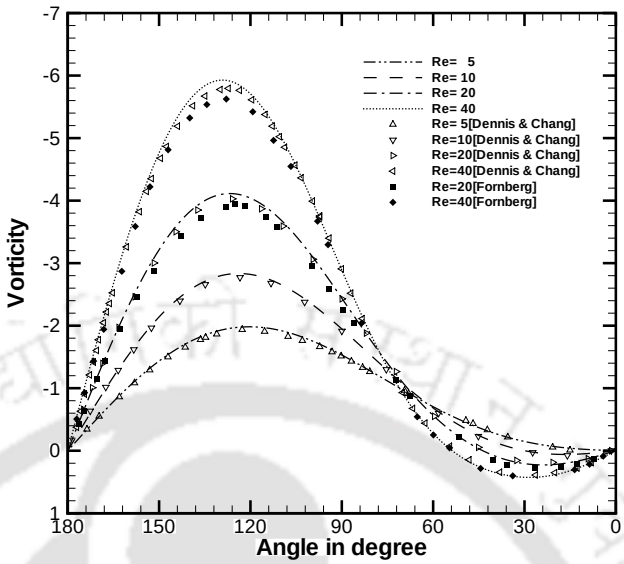

Figure 4.4: *Comparison of surface vorticity for low Res with other numerical results [42, 47].*

4.4.2 Flows for $50 \leq Re \leq 300$

The flow around an impulsively started circular cylinder for $50 \leq Re \leq 300$ eventually becomes periodic and is known to develop vortex shedding represented by the von Kármán vortex street. As the flow starts impulsively, a recirculating eddy quickly develops behind the cylinder. With time this recirculating zone evolves. For $Re = 200$ the evolution of the maximum width l_{max} and the abscissa of this maximum x_{lmax} of the recirculating zone (as seen in figure 2.17(c)) has been tabulated in table 4.4. In this table we also compare our numerical results with the experimental ones given by Bouard and Coutanceau [29].

During the development of the periodic vortex shedding, the flow goes through different phases. These phases are depicted in figures 4.6-4.10. Figure 4.6 shows the stream line contours corresponding to different stages of flow for $Re = 300$ as it develops. This may be considered as the representative of all the four Re presented in this section although the duration of the stages will vary for different Re. Figure 4.7 depicts the evolution of drag and lift coefficients for $Re = 200$ and 300. The streaklines for $Re = 50$, 100, 200, and 300 are presented in figure 4.8 while the streamlines and vorticity contours for the same Re corresponding to the peak value of the lift coefficient are presented in figures 4.9 and 4.10 respectively.

For the range of Re considered in this section, shortly after the flow has started,

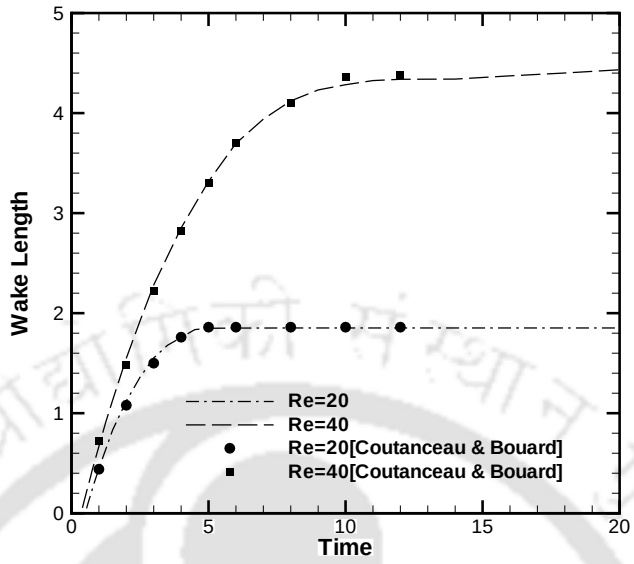

(a)

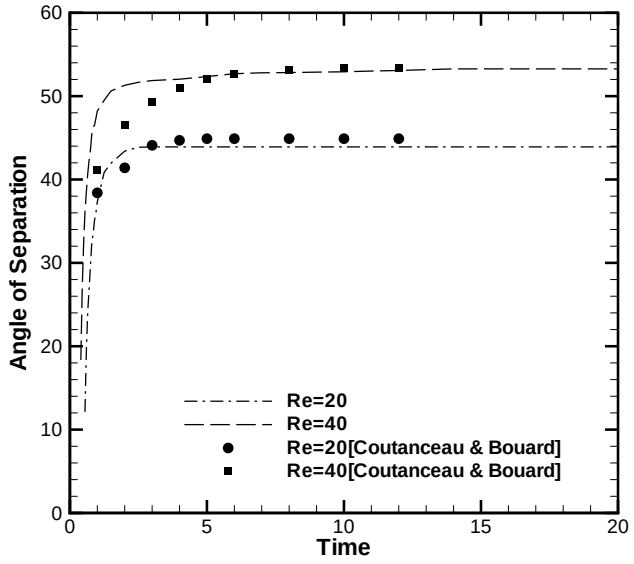

(b)

Figure 4.5: *Comparison of (a) Wake Length and (b) Angle of Separation for low Res with experimental results [40].*

a pair of symmetric eddies develop behind the cylinder (see figures 4.6(a)-(c)). As can be seen from figure 4.7(a), when the fluid flow starts, the drag coefficient attains a very high value. With time, the value of drag coefficient falls and the eddies grow in size (see figures 4.6(a)-(f)). As the flow settles down, a quasi-steady state develops with no lift force with the duration of this state decreasing

Table 4.4: *Comparison of numerical values of magnitude and abscissa of maximum width for various Re and t with experimental observations. (The values in parenthesis are from [29].)*

t		1.0	1.5	2.0	2.5	3.0
$Re = 200$	x_{lmax}/D	0.37	0.52	0.66	0.77	0.85
		(0.35)	(0.51)	(0.65)	(0.76)	(0.86)
	l_{max}/D	0.92	0.99	1.05	1.10	1.15
		(0.94)	(0.97)	(1.02)	(1.07)	(1.10)
$Re = 550$	x_{lmax}/D	0.26	0.43	0.65	0.73	0.80
		(0.30)	(0.50)	(0.66)	(0.76)	(0.85)
	l_{max}/D	0.95	1.00	1.05	1.12	1.18
		(0.94)	(0.98)	(1.03)	(1.10)	(1.16)
$Re = 3000$	x_{lmax}/D	0.16	0.27	0.36	0.67	0.80
		(0.19)	(0.26)	(0.40)	(0.73)	(0.84)
	l_{max}/D	0.98	1.02	1.08	1.14	1.20
		(0.93)	(0.98)	(1.04)	(1.11)	(1.20)

with increase in Re. From figure 4.6(d) onwards, it is clear that once some small fluctuation set in at the trail of the eddy, the flow symmetry is destroyed. With the loss of symmetry the lift force becomes nonzero. For $Re = 300$ the same can be seen at a time around $t = 40$ in figure 4.7(b) (also refer figure 4.6(d)). After some time, the vortices behind the cylinder start oscillating gradually (see figures 4.6(g)-(j)) and vortex shedding starts leading to the development of so called von Kármán vortex street. It may be mentioned that a small perturbation was artificially introduced to break the symmetry for $Re = 50$ while for the other Re considered here, asymmetry sets in automatically. The details of perturbation technique will be discussed in Chapter 5.

One of the objectives in this section of the present work is to examine the properties of the streamline and streakline patterns behind a circular cylinder during the process of vortex shedding. In incompressible flow, vorticity is generated only at solid boundaries, for this problem the surface of the cylinder, and this vorticity resides within the fluid. Thus the streaklines depicted in figure 4.8 provide an effective view of the spots in the flow field where the vorticity is inherent. Our computed streakline patterns for the range of Re in these figures are in conjunction with those depicted in [2, 14]. Note that the relationship between instantaneous streamlines and streaklines is extremely complex and visualization of both is necessary for proper understanding of flow field character. The streamline patterns show that in the initial stages the wake behind the cylinder is closed (see figures 4.6(a)-(c)). However, once the vortex-shedding process begins, this closed wake becomes open and fluid flows in from the surrounding. As is well known, our nu-

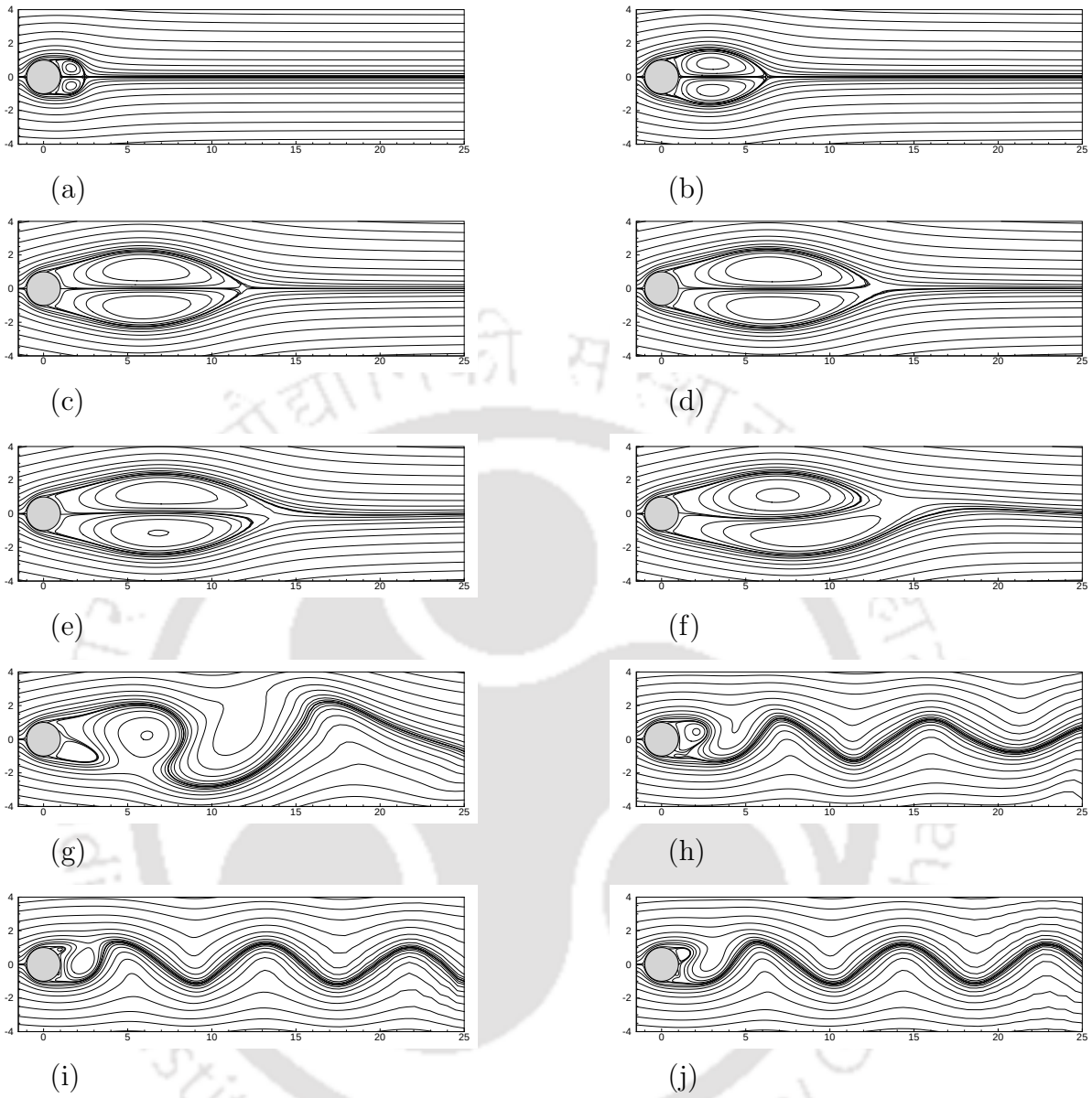

Figure 4.6: *Stream lines for* $Re = 300$ *at (a)* $t = 2.0$, *(b)* $t = 10$, *(c)* $t = 35$, *(d)* $t = 40$, *(e)* $t = 45$, *(f)* $t = 50$, *(g)* $t = 60$, *(h)* $t = 72.5$, *(i)* $t = 95$, *(j)* $t = 110$.

merical streaklines remain continuous without breakage although they get thinned up. Streaklines now represent a flexible barrier which a fluid can never cross, and is quite evident from the figures 4.8(a)-(d). The fluid entering the wake moves in and jumps towards the cylinder surface in turn from both sides and is eventually squeezed out of the wake and roll-up. The two sets of vortex sheets intertwine with each other in the far wake and this has been completely captured by our

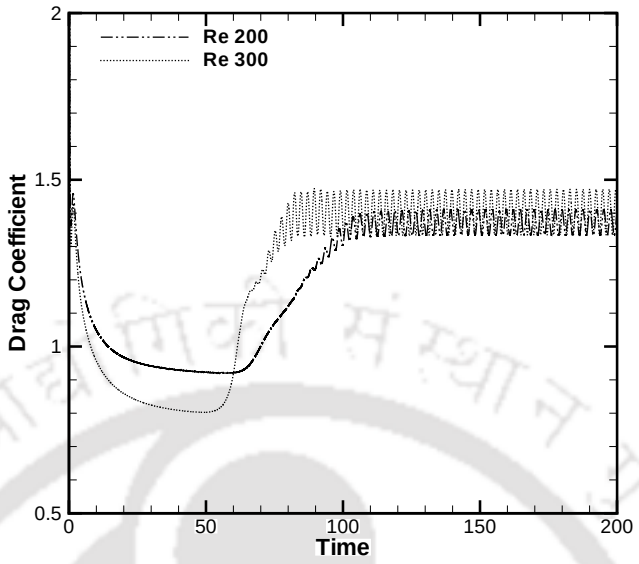

(a)

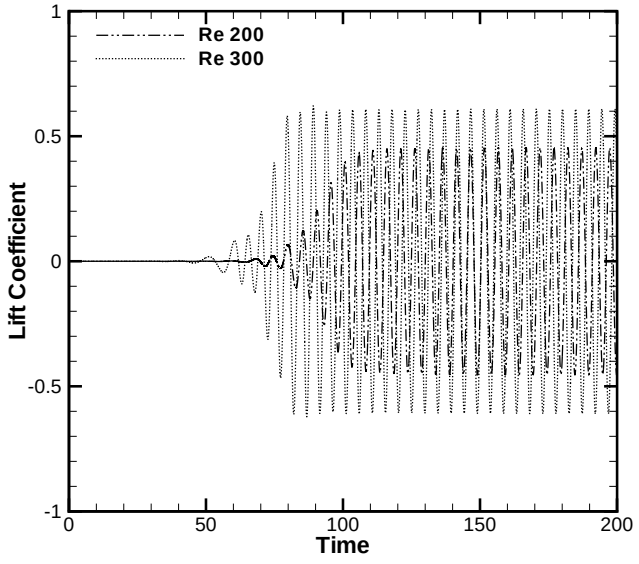

(b)

Figure 4.7: *Evolution of (a) Drag coefficient and (b) Lift coefficient for* $Re = 200$ *and* $Re = 300$.

simulation. Once shedding has been initiated, the vortices are shed in a routine manner alternatively from the two sides of the cylinder. This is also obvious from the crests and troughs of the sinuous waves in the streamlines shown in figure

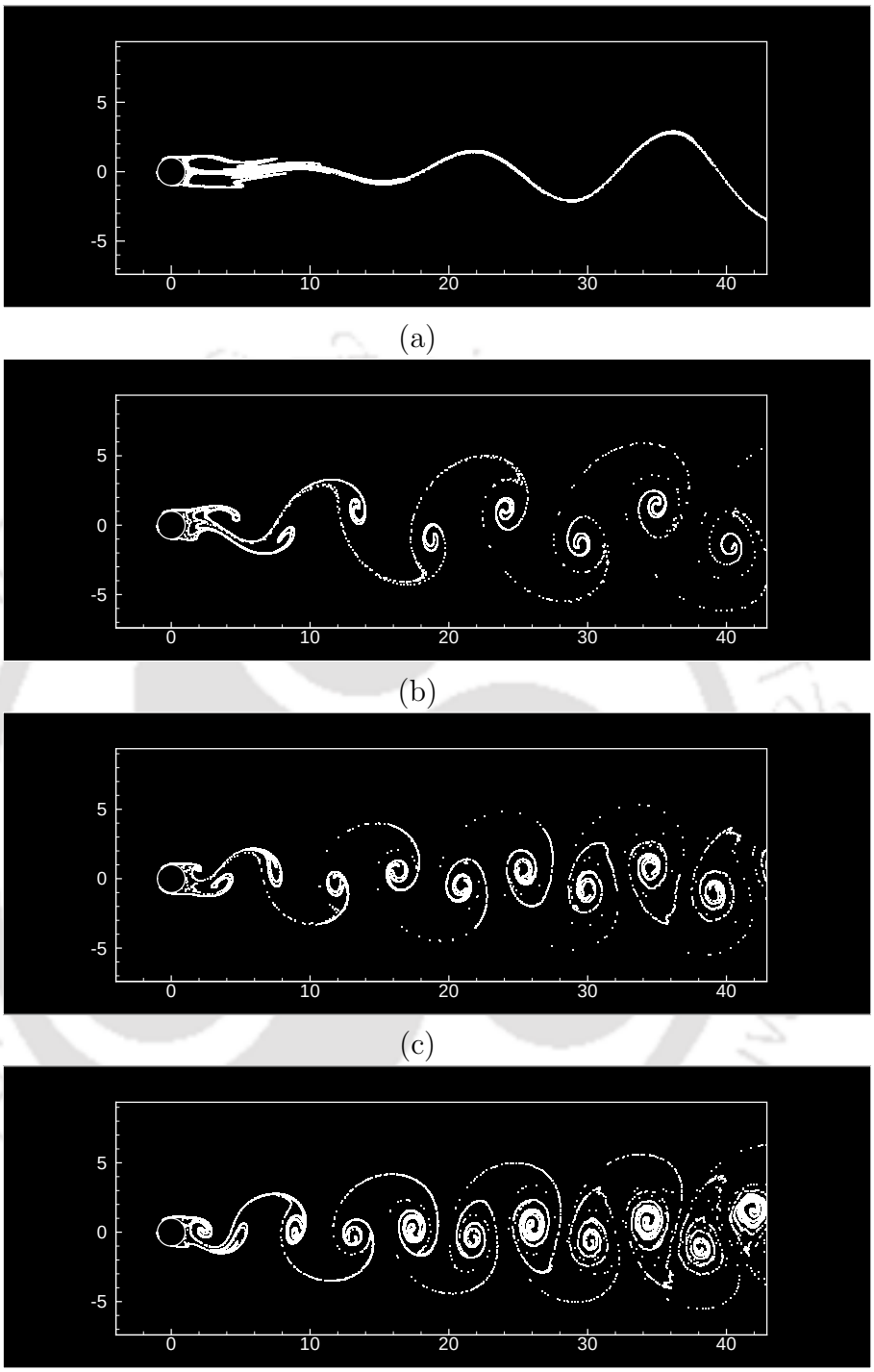

Figure 4.8: *Streak lines for (a) $Re = 50$, (b) $Re = 100$, (c) $Re = 200$, (d) $Re = 300$.*

4.9 which reflect the alternatively positive and negative vorticities of the eddies presented in figure 4.10. As time progresses, shedding frequency increases until

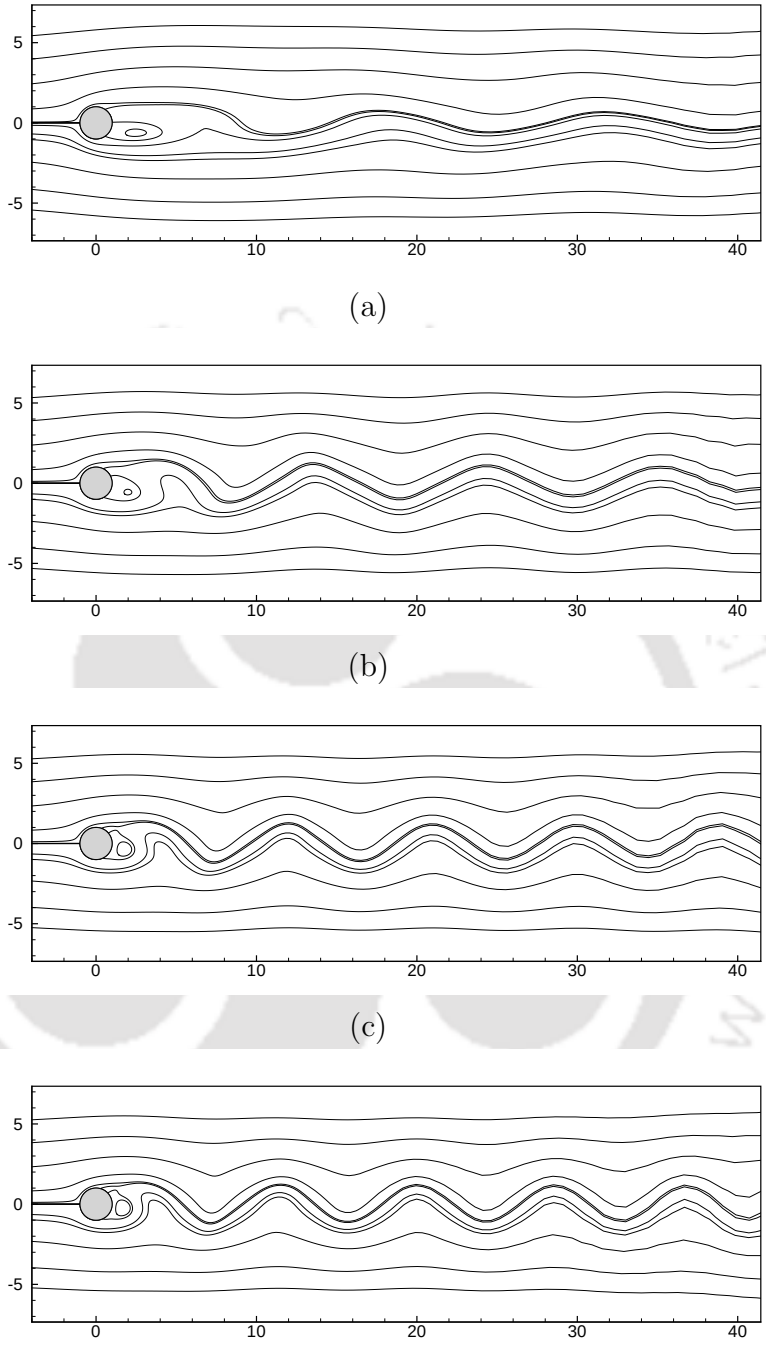

Figure 4.9: *Stream lines corresponding to the peak value of the lift coefficient for the temporally periodic solution (a) $Re = 50$, (b) $Re = 100$, (c) $Re = 200$, (d) $Re = 300$.*

a limiting condition is reached. With the onset of vortex shedding, the drag coefficient starts increasing again and eventually both the drag and lift coefficients

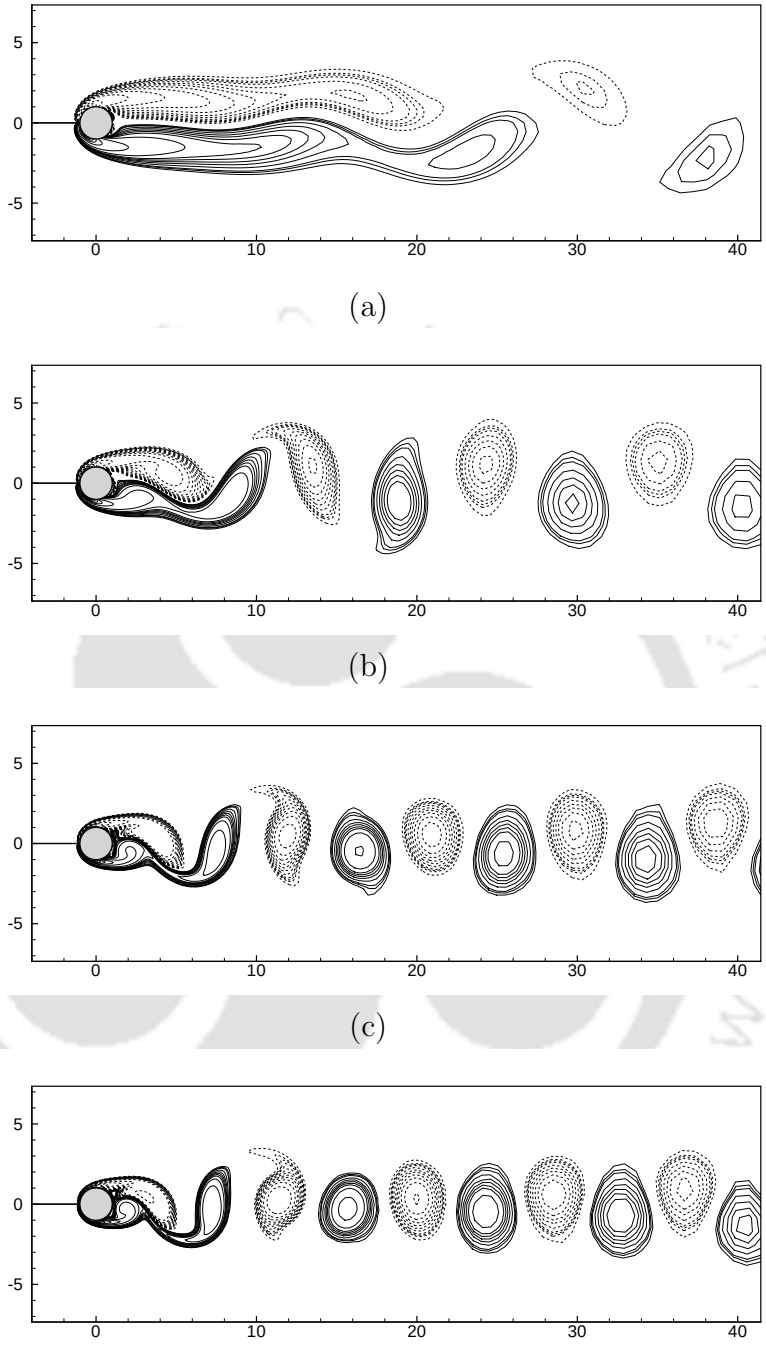

Figure 4.10: *Vorticity contours (the dotted lines representing to negative values) corresponding to the peak value of the lift coefficient for the temporally periodic solution (a)* $Re = 50$*, (b)* $Re = 100$*, (c)* $Re = 200$*, (d)* $Re = 300$*.*

ultimately reach periodic nature as the flow becomes fully develop (see figure 4.7).

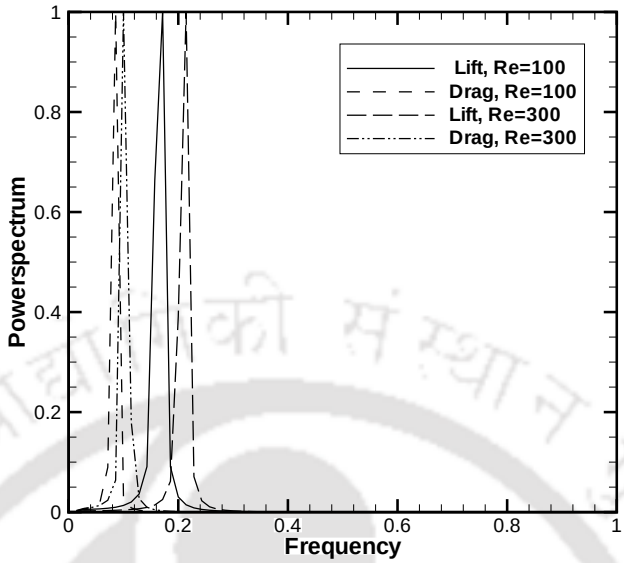

(a)

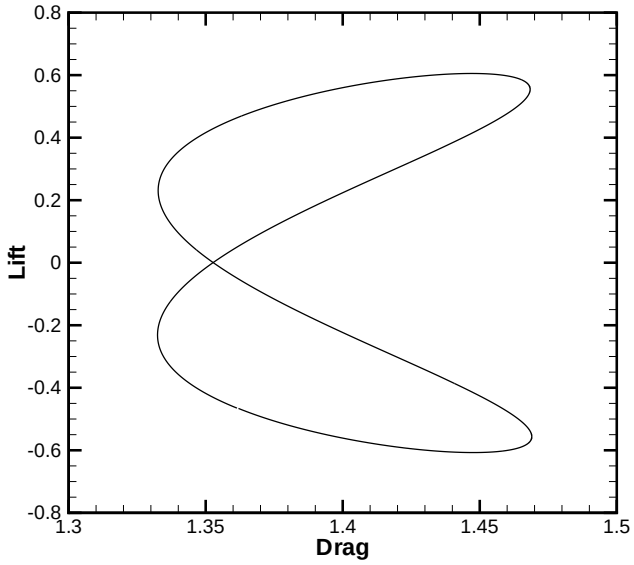

(b)

Figure 4.11: *(a) Power spectrum of drag and lift coefficients for* $Re = 100$*,* $Re = 300$ *and (b) Phase diagram of drag and lift coefficients for* $Re = 300$*.*

We also calculate Strouhal number which characterizes the vortex shedding process. The dominant frequency of the drag and lift variations, can be computed by a spectral analysis of time samples of these coefficients. The power density

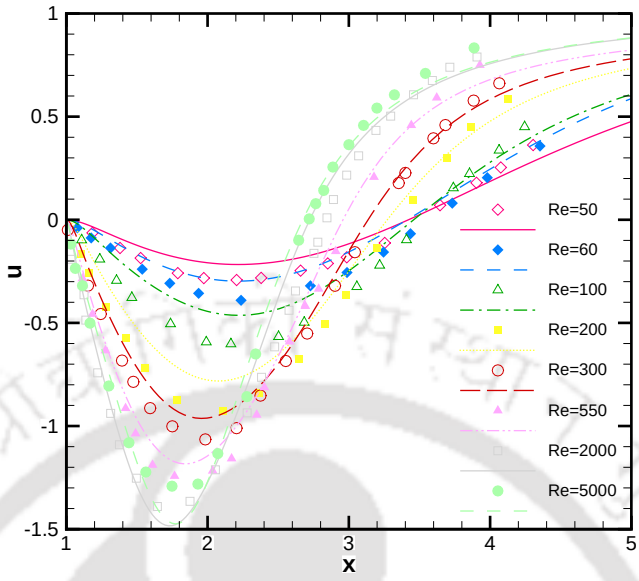

Figure 4.12: *Comparison with experimental [29] velocity distribution on flow axis at* $t = 3.0$.

spectra of this analysis normalized by the maximum value for $Re = 100$ and $Re = 300$ is shown in figure 4.11(a); figure 4.11(b) displays the phase plane of the drag and lift coefficients for the same time sample for $Re = 300$; it clearly establishes that the frequency of drag coefficients is twice that of the lift coefficients which is also exemplified by figure 4.7. In table 4.5, we compare our computed Strouhal numbers, drag and lift coefficients for these Re with established experimental and numerical results and observe very close agreements except for lift coefficient which compares well with the work of Le *et al.* [89] only. As can be seen from the table, the frequency of vortex shedding increases with the increase in Re which is also obvious from figures 4.8 and 4.10. In figure 4.12 we compare our computed flow field velocity along the flow axis at time $t = 3.0$ with the experimentally obtained results of [29].

4.4.3 Flows for $300 \leq Re \leq 1000$

The major point of analysis in this range is the numerical simulation of secondary phenomena *viz.* (i) the bulge phenomenon and (ii) secondary eddy phenomenon, for $Re = 300$, 550, and 1000. Experimental observations have shown that secondary phenomenon occurs during flow development for this Re range.

At first there is the distortion of streamlines somewhere midway between the

Table 4.5: *Comparison of Strouhal number, drag and lift coefficients of the periodic flow for* $Re = 50$, 100, 200, 300.

Re	50			100			200			300		
Reference	St	C_D	C_L	St	C_D	C_L	St	C_D	C_L	St	C_D	C_L
Frank *et al.* [48]	0.116	1.39	0.0	—	—	—	0.194	1.31	±0.65	0.205	1.32	±0.84
Williamson [158]	0.123	—	—	0.163	—	—	0.185	—	—	0.203	—	—
Silva [134]	0.120	1.46	—	0.160	1.39	—	0.180	—	—	0.200	1.27	—
Le *et al.* [89]	—	—	±0.07	0.160	1.37 ± 0.009	±0.323	0.187	1.34 ± 0.030	±0.430	0.200	—	—
Berthelsen and Faltinsen [26]	—	—	—	0.169	1.38 ± 0.010	±0.340	0.200	1.37 ± 0.046	±0.700	—	—	—
Wang *et al.* [153]	—	—	—	0.170	1.379	±0.357	0.195	1.262	±0.708	0.206	1.174	—
Present Study	0.120	1.461	±0.02	0.165	1.394 ± 0.007	±0.191	0.197	1.375 ± 0.038	±0.453	0.209	1.401 ± 0.068	±0.607

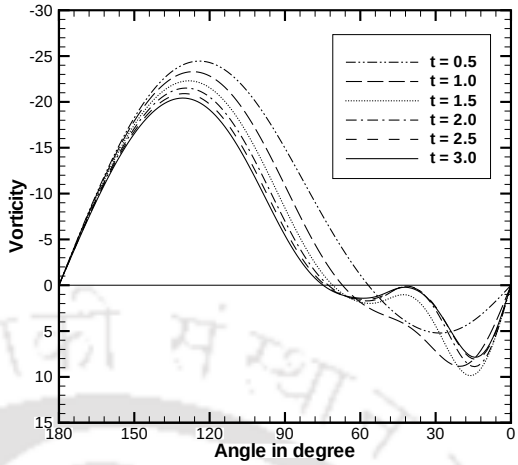

(a)

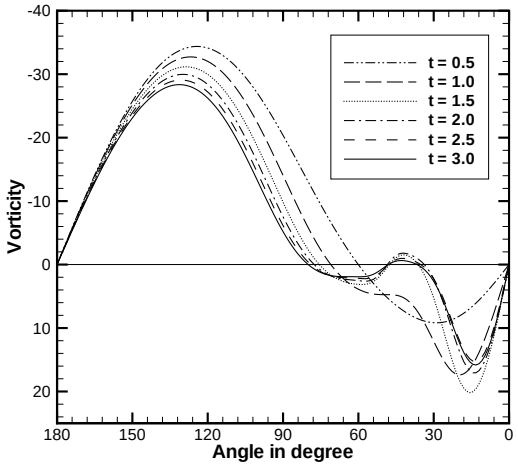

(b)

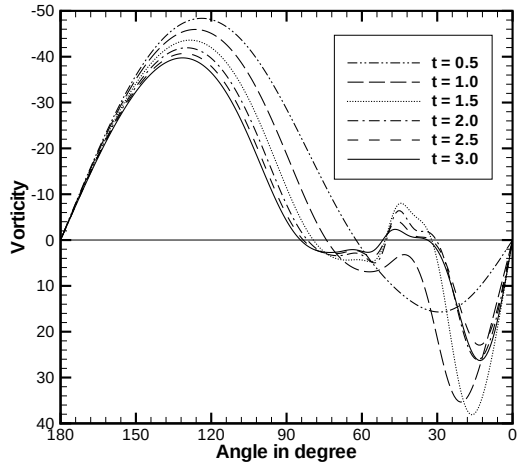

(c)

Figure 4.13: *Time evolution of surface vorticity (a)* $Re = 300$*, (b)* $Re = 550$*, (c)* $Re = 1000$.

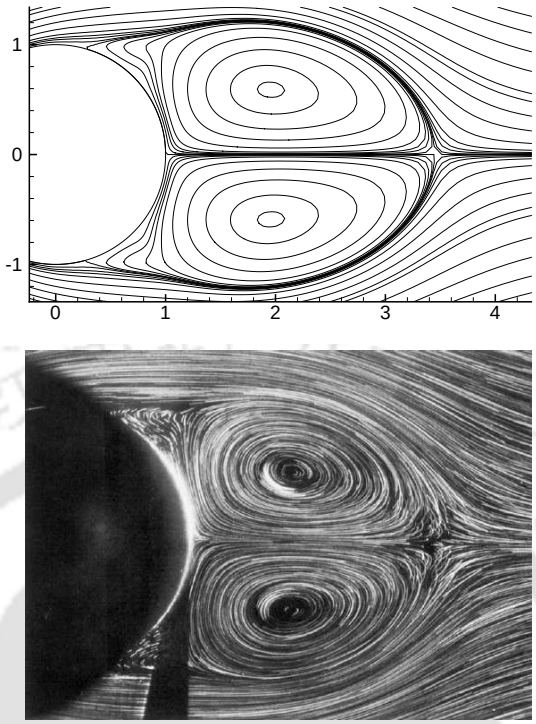

Figure 4.14: *The bulge phenomenon: Comparison of numerical and experimental [29] visualizations at time* $t = 2.5$ *for* $Re = 300$.

stagnation and separation points defined earlier and depicted in figure 2.17(c). Stream lines close to the cylinder deviate from the cylinder causing a bulge pattern, known as bulge phenomenon. The exact time of arrival of these phenomena can be found from the distribution of vorticity at the cylinder surface given in figure 4.13 where the graph touches the $\omega = 0$ line. The bulge phenomena for $Re = 300$ appears at dimensionless time $t = 2.5$ on the surface of the cylinder (see figure 4.14). For $Re = 550$, this phenomenon can be seen at time $t = 1.35$ approximately (see figure 4.15(a)).

For $Re > 300$, as time progresses, this bulge gives rise to a small secondary eddy known as secondary eddy phenomenon which can clearly be seen at $t = 2.5$ for $Re = 550$ (see figure 4.15(b)). With time the strength of this secondary eddy increases (see figure 4.15(c)). This secondary eddy which has a rotation opposite to the main eddy causes a second separation of flow.

A quantitative comparison of early flow evolution for $Re = 550$ with experimental results [29] can be found in table 4.4. In figures 4.14 and 4.15, we also compare the computed streamlines with the experimental results of [29] for $Re = 300$ and 550 respectively at time $t = 2.5$. These figures clearly depict the extreme close-

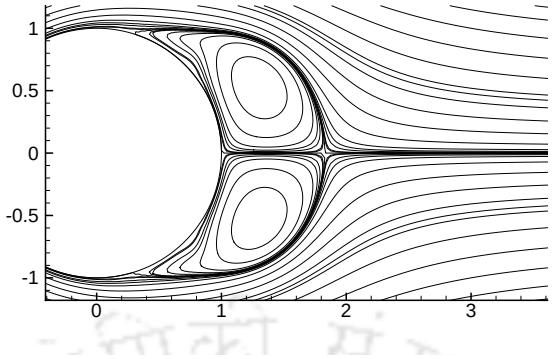

(a)

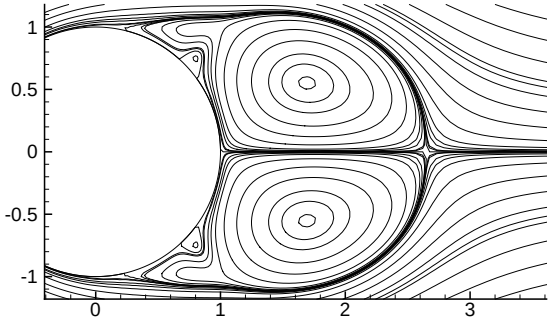

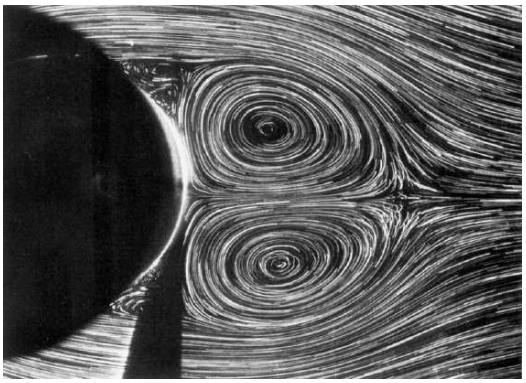

(b)

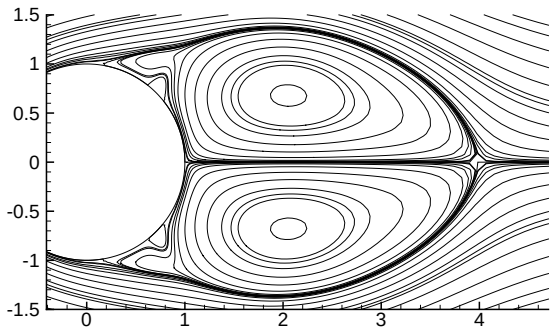

(c)

Figure 4.15: *For Re = 550 (a) Stream lines at t = 1.35, (b) Comparison of numerical and experimental [29] visualizations at t = 2.5, (c) Stream lines at t = 5.0*

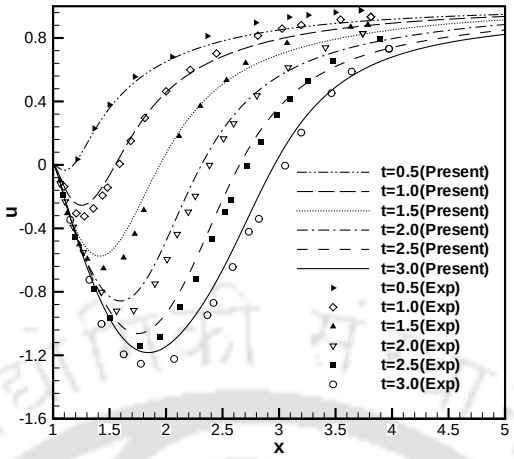

(a)

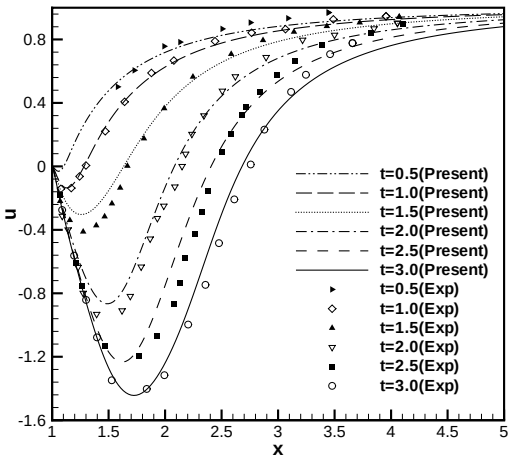

(b)

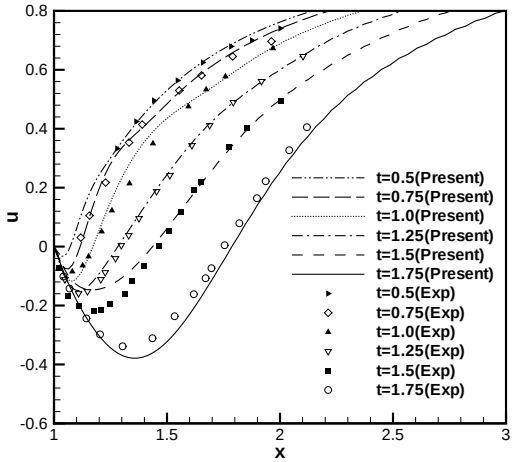

(c)

Figure 4.16: *Comparison between experimental [29] and numerical results for the velocity distribution on flow axis for (a) $Re = 550$, (b) $Re = 3000$, (c) $Re = 9500$.*

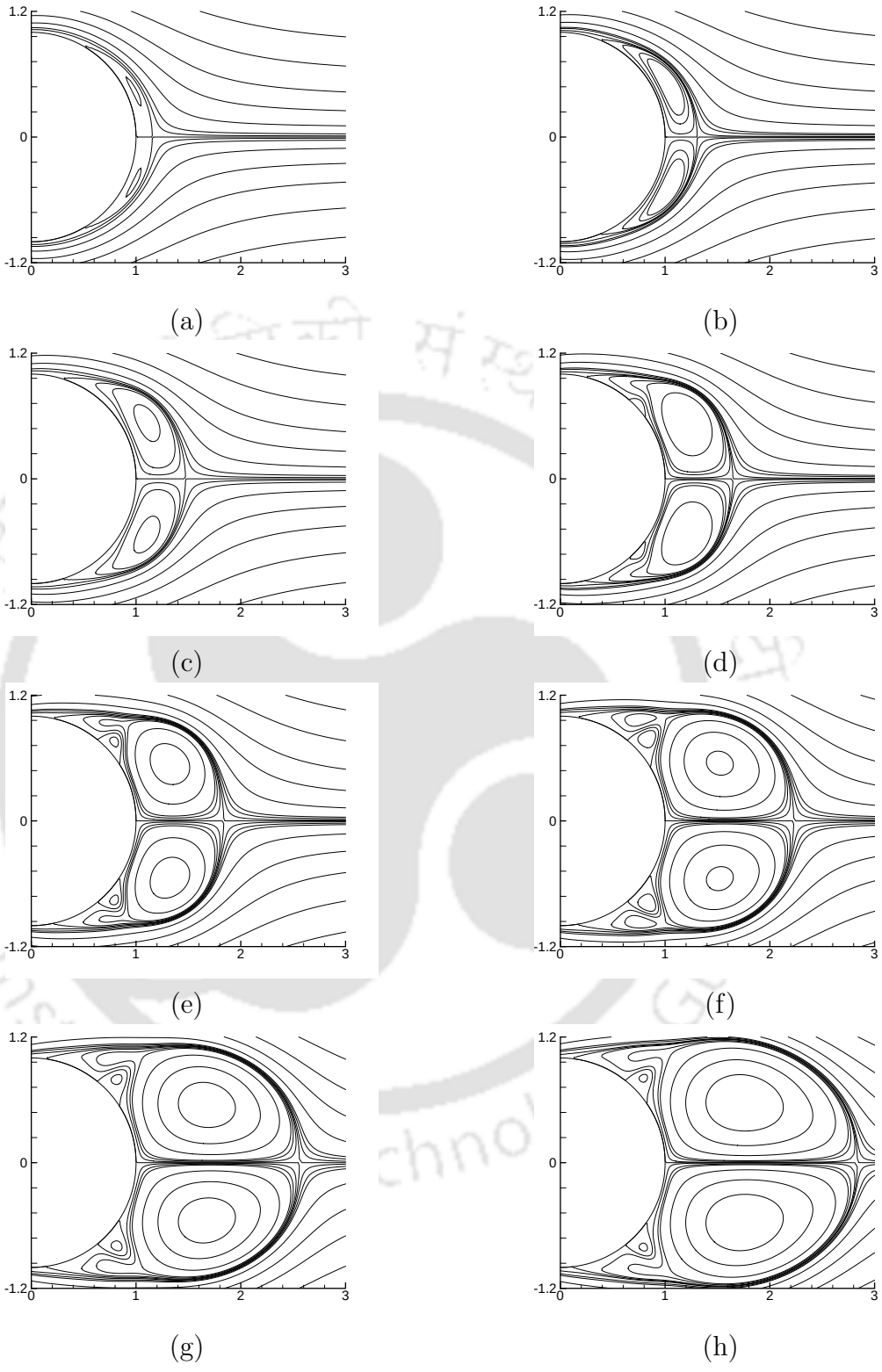

Figure 4.17: *Stream lines for* $Re = 1000$ *at time (a)* $t = 0.5$*, (b)* $t = 0.75$*, (c)* $t = 1.0$*, (d)* $t = 1.25$*, (e)* $t = 1.5$*, (f)* $t = 2.0$*, (g)* $t = 2.5$*, (h)* $t = 3.0$.

ness of our numerical results with the experimental ones thus demonstrating the efficiency of our scheme. Quantitative comparison of velocity along flow axis behind the cylinder with the same reference has been presented in figure 4.16(a) for $Re = 550$.

For $Re \geq 800$, the secondary eddy described above grows at an early stage to such an extent that it touches the boundary of the main eddy, thereby splitting the main one into two parts and isolating the region of the wake next to the separation point where another secondary eddy can now be seen. These two secondary eddies are equivalent in size and in strength and constitute a pair of secondary eddies. This phenomenon is called α-phenomenon. We show the evolution of stream lines for $Re = 1000$ at early stages in figure 4.17. Here, a single secondary vortex appears shortly after $t = 1.0$ (see figures 4.17(c), (d)), ultimately developing into a pair of secondary vortices at $t = 2.0$ (see figure 4.17(f)). This clearly depicts the α-phenomenon.

4.4.4 Flows for $3000 \leq Re \leq 9500$

Flow around a cylinder at these Re eventually becomes three dimensional and turbulence sets in. Therefore we simulate the flow only for the very early laminar stage and compare our results with those obtained from experiments. At first we compare our numerical results for $Re = 3000$ with the results of [29] in table 4.4. As observed in earlier subsections for $Re = 200$ and 550, a very good agreement of the values of l_{max} and x_{lmax} can be found for the early part of flow development. We also compare velocity distributions along the flow axis behind the cylinder for different times with the experimental results of [29] in figure 4.16(b). Next we compare our results with the works in [94] in figure 4.18. The α-phenomenon described in the previous section is distinctly visible here also; for this Re, the appearance of the secondary eddy and the constitution of the pair of secondary eddies occur at instants of time which is earlier than that of $Re = 1000$. This has been captured by our simulation in figures 4.18(b) and (c). As can be seen from figure 4.18, our computed solutions have excellent match with the experimental ones and closer to them than the numerical results presented by Loc and Bouard [94].

Next we consider the cases for $Re = 5000$ and 9500. The most important feature of this flow range is that the flow exhibits the so called β-phenomenon. In this range, at an early stage, as the back flow near the cylinder starts, a recirculating zone attached to the cylinder is created. As the flow of fluid develops in

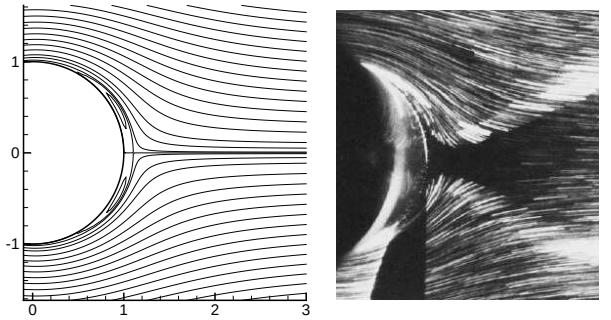

(a)

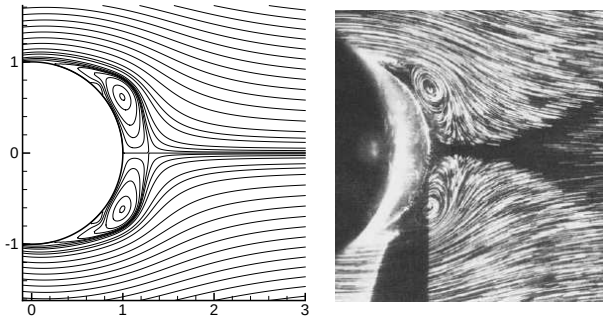

(b)

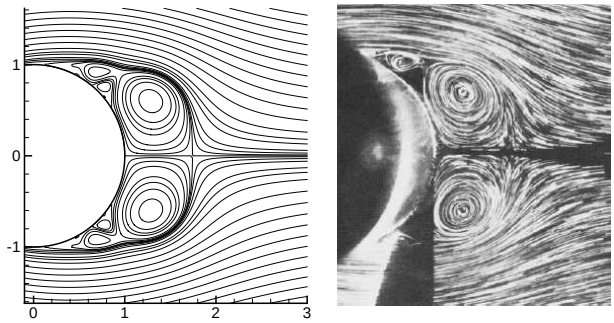

(c)

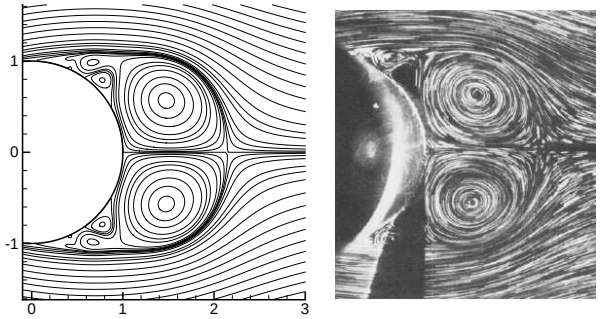

(d)

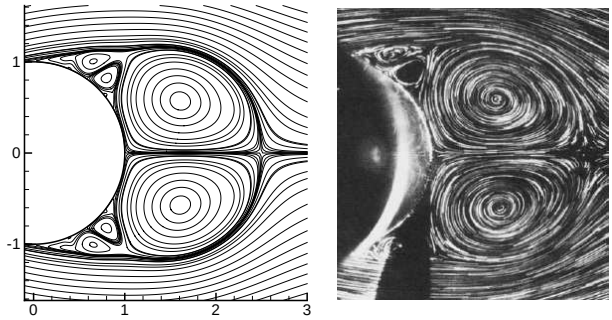

(e)

Figure 4.18: *For $Re = 3000$ comparison of numerical and experimental [94] visualizations at time (a) $t = 0.5$, (b) $t = 1.0$, (c) $t = 1.5$, (d) $t = 2.0$, (e) $t = 2.5$.*

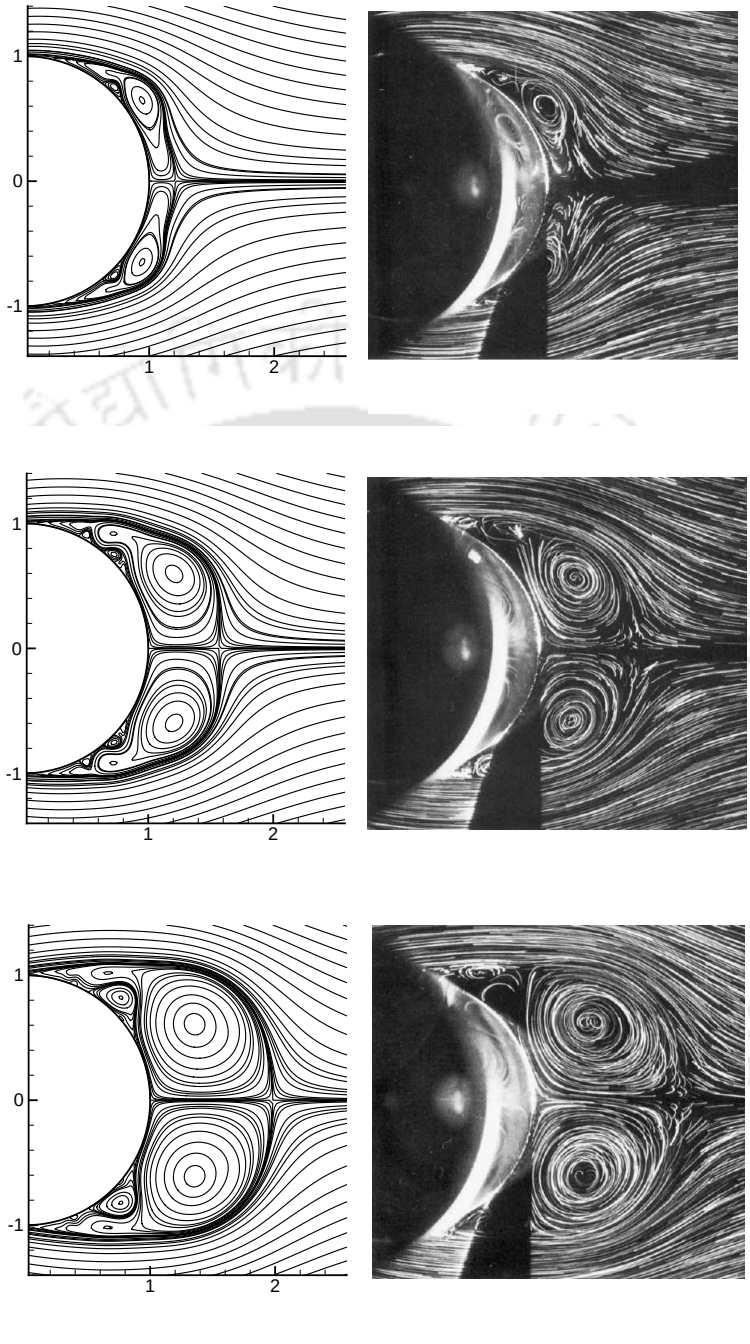

Figure 4.19: *For $Re = 5000$ comparison of numerical and experimental [29] visualizations at time (a) $t = 1.0$, (b) $t = 1.5$, (c) $t = 2.0$.*

downstream, due to the high Re of the flow, the core of this recirculating zone gets strengthened quickly. Though the rest of the recirculating zone gathers strength, it is slow compared to its core, thereby setting the stage for the development of secondary vortex. At around $t = 1.0$ this secondary vortex becomes prominent, di-

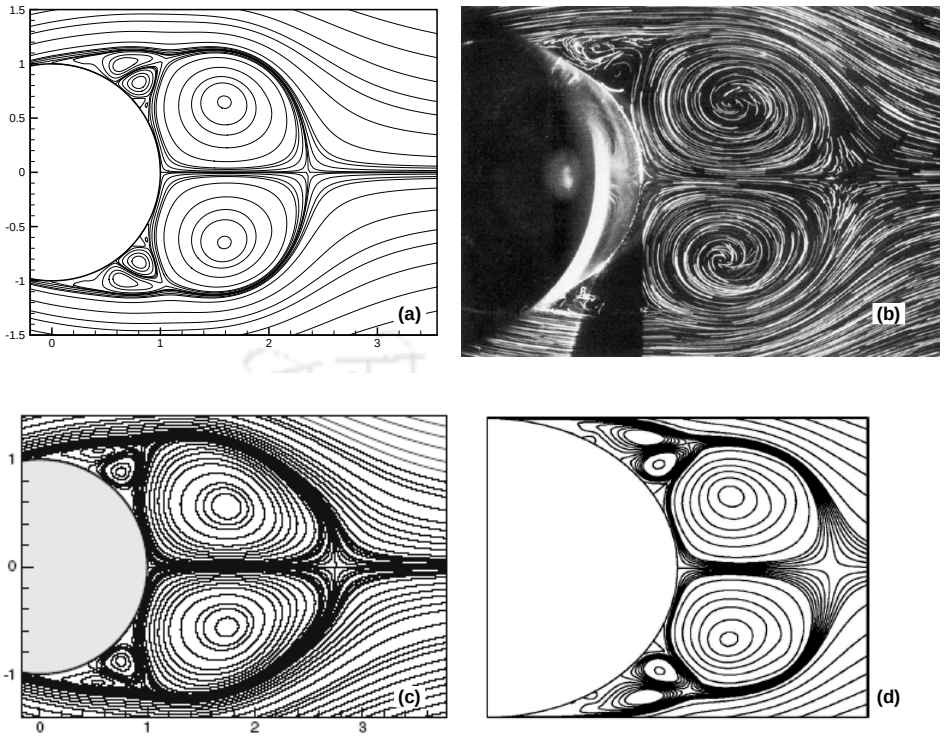

Figure 4.20: *For $Re = 5000$ comparison of (a) Our computation with (b) Experimental [29] visualization and other numerical solutions obtained using compact schemes by (c) Kalita and Ray [76], (d) Sanyasiraju and Manjula [123] at time $t = 2.5$*

viding the primary vortex into two chambers, one of which is the core. Nevertheless the second weaker part maintains some sort of communication with its core part. For some time both the core and the secondary vortex acquire strength and the channel of communication between the two parts of the primary vortex becomes narrow. But as the primary vortex becomes bigger in size again, both its parts starts getting stronger and devor the secondary vortex from left and right, reducing its strength and size. At time around $t = 1.5$ the secondary vortex becomes quite small. This is what is popularly known as β-phenomenon. The β-phenomena can be clearly seen for $Re = 5000$ and 9500 at times $t = 1.5$ and 1.0 in figures 4.19(b) and 4.21(d) respectively. For $Re = 5000$ this β-phenomenon quickly leads to the α-phenomenon described earlier which can be seen in figure 4.19(c) at time $t = 2.0$ and figure 4.20 at time 2.5. But for $Re = 9500$ the flow becomes unstable later on and α-phenomenon can not be observed (see figures 4.22(a) - 4.22(c)). Note that in the above mentioned figures we have presented our numerical results side by side with that of experimental results reported in [29, 94]. It is heartening to note

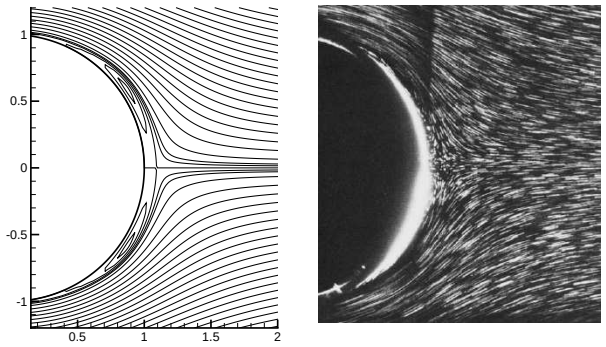

(a)

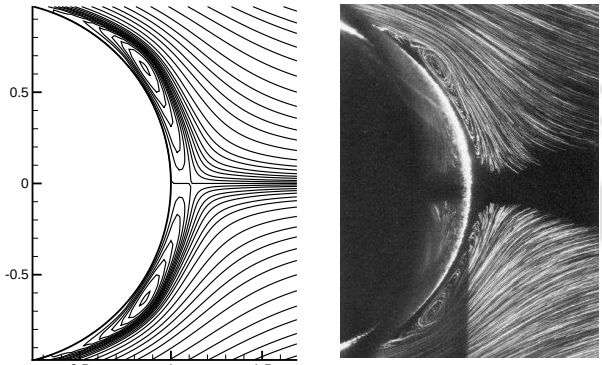

(b)

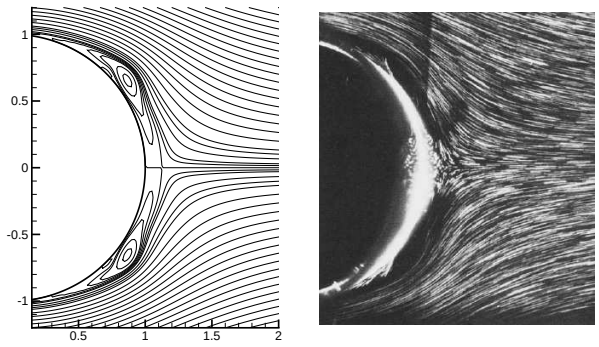

(c)

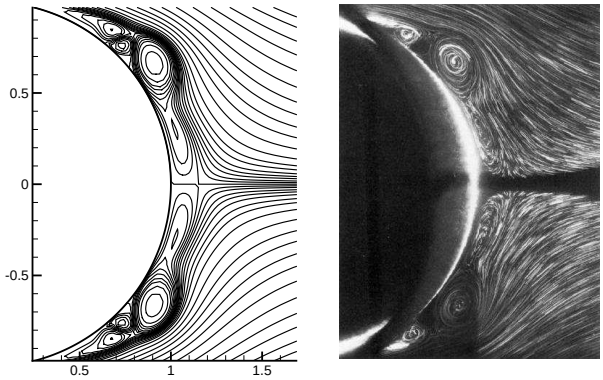

(d)

Figure 4.21: *For $Re = 9500$ comparison of numerical and experimental [29, 94] visualizations at times (a) $t = 0.6$, (b) $t = 0.75$, (c) $t = 0.8$, (d) $t = 1.0$.*

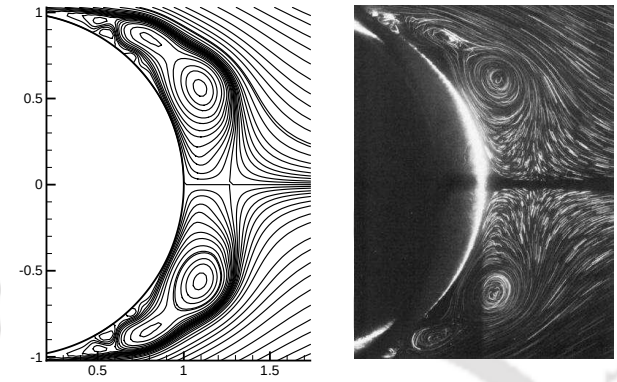

(a)

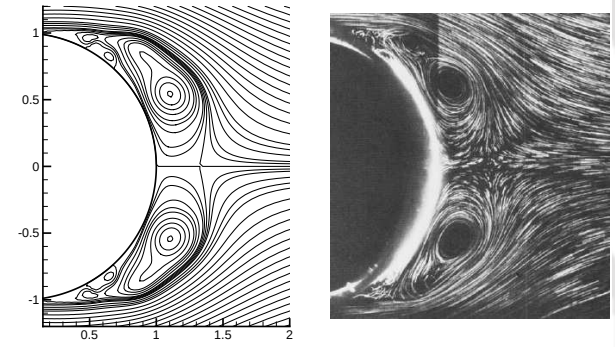

(b)

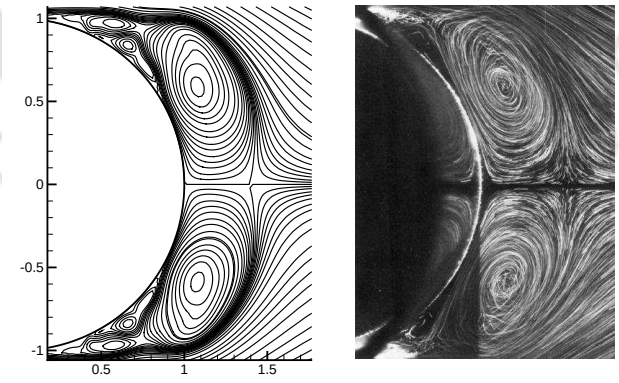

(c)

Figure 4.22: *For Re = 9500 comparison of numerical and experimental [29, 94] visualizations at times (a) t = 1.25, (b) t = 1.4, (c) t = 1.5.*

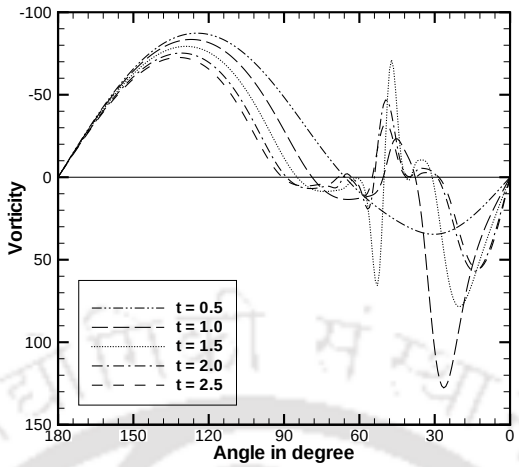

(a)

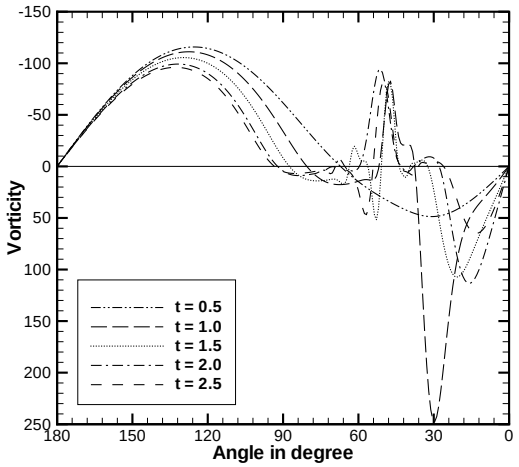

(b)

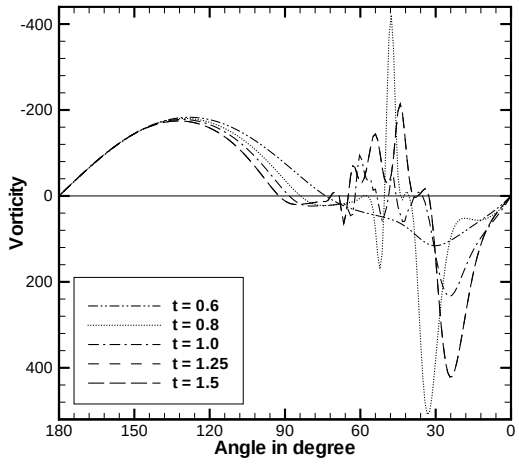

(c)

Figure 4.23: *Time evolution of surface vorticity for (a)* $Re = 3000$*, (b)* $Re = 5000$*, (c)* $Re = 9500$.

that our computed solutions almost exactly replicate the α- and β-phenomena of the experimental results of [29] as suggested by figures 4.19-4.22. In figure 4.20 we compare our computed results with two other numerical results obtained by Kalita and Ray [76] and Sanyasiraju and Manjula [123] at time $t = 2.5$ along side the experimental visualization of [29]. Our computation captures the shape of the primary vortex as also the small secondary vortices most accurately as compared to the other simulations. Figure 4.16(c) compares the velocity distribution on the flow axis with the experimental one for $Re = 9500$. As in the case of $Re = 550$ and 3000 a very close comparison is obtained in this case as well. The vorticity distributions on the surface of the cylinder at different times for the Re values considered in this subsection have been plotted in figure 4.23.

4.5 Conclusion

Compact schemes based on biharmonic pure stream function formulation of the transient N-S equations have so far been successfully used only on rectangular Cartesian coordinates. In this chapter, we carry out a comprehensive numerical validation of the classical problem of the transient flow past an impulsively started circular cylinder by specifically adopting the newly developed implicit scheme for biharmonic form of the N-S equation. At the downstream far field where we use one sided approximation, no adverse effect on flow computation due to the change of stencil was seen. We have computed the flow for a wide range of Re ranging from 5 to 9500 and have considered both long time as well as transient cases. The flow features which are typical of certain subranges of the Re are discussed in details. We compare our results with established experimental and numerical results, and obtain excellent comparison in all the cases, both qualitatively and quantitatively. The robustness of the scheme is highlighted not only when it captures the periodic nature of the flow for $50 \leq Re \leq 300$, which is characterized by vortex shedding represented by the von Kármán street for which a detailed streakline analysis is provided, but also by the fact that it very accurately captures the so called secondary phenomena for moderate Re and α- and β-phenomena for higher Re. The strength of the scheme is exemplified by the fact that flow simulations from our computations are much closer to the experimental visualization than other existing numerical simulations available in the literature, particularly for the higher Re. To the best of our knowledge, no pure stream function based scheme for the N-S equations has been employed to simulate the transient flow past a circular cylinder till date.

Chapter 5

Triggering Asymmetry for Flow Past Circular Cylinder at Low Reynolds Numbers

5.1 Introduction

In the last chapter we have documented dependence of flow features on Reynolds number for the problem of flow past an impulsively started circular cylinder. We have witnessed that with the increase in Re, the flow becomes more complicated due to the appearance of secondary and tertiary vortices. Flows above some critical Reynolds number eventually become periodic and ware shown to develop vortex shedding represented by the von Kármán vortex street. In the literature, both numerical and experimental studies have been made to pinpoint the critical Reynolds number and experimental efforts to locate Re_c is scattered over a wide interval (30, 65) [2, 5, 63, 83, 85]. Numerical simulation of flow past impulsively started circular cylinders in the region which is far beyond Re_c can be found in plenty of them [42, 47, 48, 60, 76, 107, 123, 153]. But simulation around Re_c is tricky as normal computational procedure may lead to the capture of some un-physical behavior of the flow. Also such computation puts a high demand in CPU time, the growth rate at the onset of instability being extremely slow. Most often, numerical analysts have studied the linear instability of this flow as a Hopf bifurcation problem. A look at the literature suggests that the data reported by various researchers about the threshold value of Re_c at which Hopf bifurcations takes place, are scattered in the range $43 \leq Re_c \leq 50$ [44, 71, 86, 104, 110, 111, 157]. However, recent studies indicate some agreement among the researchers over $Re_c \lesssim 47$ [30, 51, 99]. In this regard it is worth mentioning that in a very recent investigation, Sengupta *et al.* [129, 130] have concluded that the reporting of different Re_c by different experi-

mental and numerical facilities may be related to the receptivity of the flow field to background disturbances during the linear temporal growth of the disturbance field for post-critical Reynolds numbers. In their study they have made a detailed analysis of various results available in literature and have concluded that there may not be any fixed critical Reynolds number in the sense that such a value may be scheme and/or facility dependent. Nevertheless, numerical results [48, 89, 134] describing the flow properties accurately in the range of $45 \leq Re \leq 50$ are scanty.

A nominally two dimensional flow past a circular cylinder maintains its symmetry for a long time because of the absence of a preferred direction in the flow field. Note that a circular cylinder has perfect symmetry with identical body curvature everywhere and in this sense the circular cylinder is a special geometry. Further if the computational domain is also considered to be circular then the flow does not have a preferred direction. Thus it is necessary to introduce some artificial perturbation in order to trigger asymmetry into the flow behind the cylinder, especially for Re close to Re_c. Only some form of the immersed interface methods [89, 134] are seen to capture the asymmetry in the flow in the threshold regime without the introduction of this perturbation. In this study we report evolution and properties of flow field around the narrow threshold value of Re_c obtained by numerically solving the N-S equations[1]. The objective of the present study is threefold:

1. To apply the compact finite difference scheme developed in Chapter 3 to study the evolution of the flow in the threshold region. As mentioned above, simulation of the flow in the threshold region through FD is scanty; long time computation of the flow invariably results in high demand in CPU time. The approach used here eliminates the need to compute pressure and vorticity as a part of the computational process and therefore computationally much economical than the earlier computations that had been carried out through primitive variable and stream ψ-ω formulations.

2. To explore the effects of the perturbation induced through three different techniques on the eventual behavior of the flow; we are specifically interested in the perturbation effect on the flow induced through the transverse oscillation of the cylinder for which no other numerical results are seen in the literature.

3. To delve into the flow features in a narrow subrange of the threshold region leading to the determination of the Re_c.

[1]Part of this work has been published in *Comp. Fluids*

Initially we compute the flow for $Re = 80$ which is outside the threshold regime and the flow is known to be periodic. For such an Re, which is well beyond the threshold regime, there is no need to artificially trigger asymmetry and hence no perturbation is required. As we compare our results with the benchmark results available in the literature, this simulation again shows the efficiency of our scheme in capturing flow phenomena reported by experimentalists. Next, we turn our attention for flow for two Re in the threshold regime, namely, $Re = 44$ and $Re = 50$ where the three different perturbation techniques are employed to trigger asymmetry into the flow. We see that the flow for $Re = 44$ eventually retains its symmetry in all the cases while for $Re = 50$ the introduced perturbations leads to the periodic vortex shedding. Finally, we narrow down our study to the long time computation of the flow for $Re = 46.5$ and $Re = 47$ and ascertain that the critical $Re_c \in (46.5, 47]$. The different characteristics of the flow field are discussed in details for all the Reynolds numbers considered here. Towards the end we make a few observations on the effects of the three perturbation techniques that are being used to trigger asymmetry into the flow.

This chapter is divided into the five sections. In section 5.2, we talk about the perturbation technique, the numerical results have been presented in section 5.3, the effect of the perturbation techniques in section 5.4 and finally the work is summarized in section 5.5. Note that the governing equations, boundary conditions and discretization procedure followed here are same as those of Chapter 4.

5.2 Perturbation techniques

The regime $Re \leq 40$ is probably the most well studied region for the problem of flow past circular cylinder. Here the eddies grow with time and Re in wake length l and in angle of separation θ_s defined in figure 2.17 of Chapter 2. Finally these eddies settle down in the form of a wake. The characteristic of the final wake for different values of Re have been tabulated in Chapter 4. Nevertheless the flow remains steady. Several experimental and numerical results confirm that the flow losses its steady state character for some critical Reynolds number $Re = Re_c$ residing somewhere in the range of $43 \leq Re \leq 50$. For this Re_c this steady flow become unstable. As Re increases beyond Re_c, the instability keeps on increasing leading ultimately to the process of von Kármán vortex shedding. However in most of the cases long time transient numerical computation fails to capture this physics accurately and leads to converged state indicating steady state behavior [42, 47]. To circumvent this problem, some perturbation must be introduced in the

flow field or in the data being used for computation. This induced perturbation leads to the onset of asymmetry into the flow.

In our computation, we introduce the perturbation into the flow at a time when the flow corresponding to the particular Re has reached the converged steady state or is about to reach converged state while the two symmetric eddies behind the cylinder are still in place. The converged state is determined from the constancy of drag coefficients with respect to time. We have used three different types of perturbations. In the first case, we perturb the inlet boundary condition; here in either half of the flow, upper or lower, we double the velocity while at the same time, on the other, the velocity is reduced to zero (figure 5.1(a)). However, this perturbed state is maintained for only a unit interval of time δt which itself is enough to introduce asymmetry to the entire flow field. In the second type of perturbation a unit angular velocity is introduced on the cylinder surface (figure 5.1(b)). This angular velocity is also maintained for only one time step. The details of how the angular velocity is introduced onto the cylinder surface will be discussed in the next chapter. In the third type, a vertical sinusoidal oscillation is imposed on the cylinder for unit time period (figure 5.1(c)). This was inspired by the works of Camichel and Teissie-Solier [15] who conducted a similar physical experiment, probably first of its kind, in order to study the long term effect of the perturbation on the flow. Here again the exact mechanism by which the oscillation is imposed on the cylinder will be dealt with in the next chapter. In order to simulate this particular perturbation technique we actually shift to body fitted non-inertial frame of reference, the details of which will be discussed in Chapter 6. The net effect of the above perturbations is that the symmetry in flow field is instantly lost thereby introducing large lift force on the cylinder. It is observed that as the flow develops, this large lift force reduces rather quickly.

5.3 Numerical results

5.3.1 Flows for $Re = 80$

We begin our computation for $Re = 80$ where available experimental and the numerical results document convincingly the process of vortex shedding for this Re value represented by the von Kármán vortex street. The reason for starting with a Reynolds number other than a one in the threshold region $43 \leq Re \leq 50$ is that the confidence resulting from accurate validation of our numerical results with the established ones could be carried over to the threshold region where perturbation

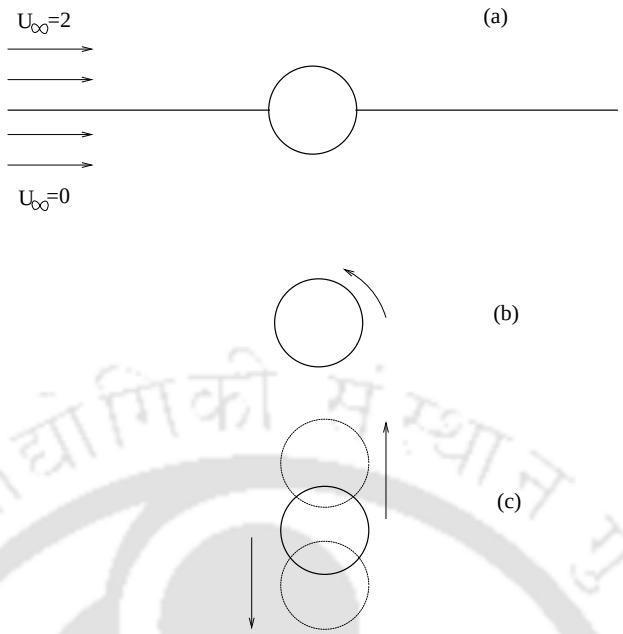

Figure 5.1: *Schematic diagram of different perturbation techniques: (a) Perturbation of the inlet boundary condition, (b) Perturbation by rotation, (c) Perturbation by oscillation.*

needs to be introduced to capture physically meaningful results. We carry out all our computations for this chapter with $\delta t = 0.005$ using a grid of size 181×301.

Flow development for $Re = 80$ follows the pattern described for $Re = 300$ in Chapter 4. Here also a pair of symmetric eddies develop behind the cylinder (see figures 5.2(a)). As the drag coefficient falls with time, the eddies grow in size (see figures 5.2(a)-(b)) finally settling down to a quasi-steady state with no lift force. Note that the duration of this quasi-steady state is much larger as compared to $Re = 300$ discussed in Chapter 4. From figure 5.2(d) onwards, it is clear that once some small fluctuation sets in at the trail of the eddy, the flow symmetry is destroyed. With the loss of symmetry the lift force becomes nonzero and gradually the vortices behind the cylinder start oscillating (see figures 5.2(d)-(f)) leading to the process of vortex shedding. It may be mentioned that no perturbation is required to break the symmetry and asymmetry sets in automatically. With the onset of vortex shedding, the drag coefficient starts increasing again and eventually both the drag and lift coefficients reach periodic nature as the flow fully develops (see figures 5.3). Note that figures 5.2(g) and (h) are half a vortex shedding cycle apart where one is the mirror image of the other with respect to the x-axis. The crests and troughs of the sinuous waves in the streamlines shown in figure 5.2(g)-

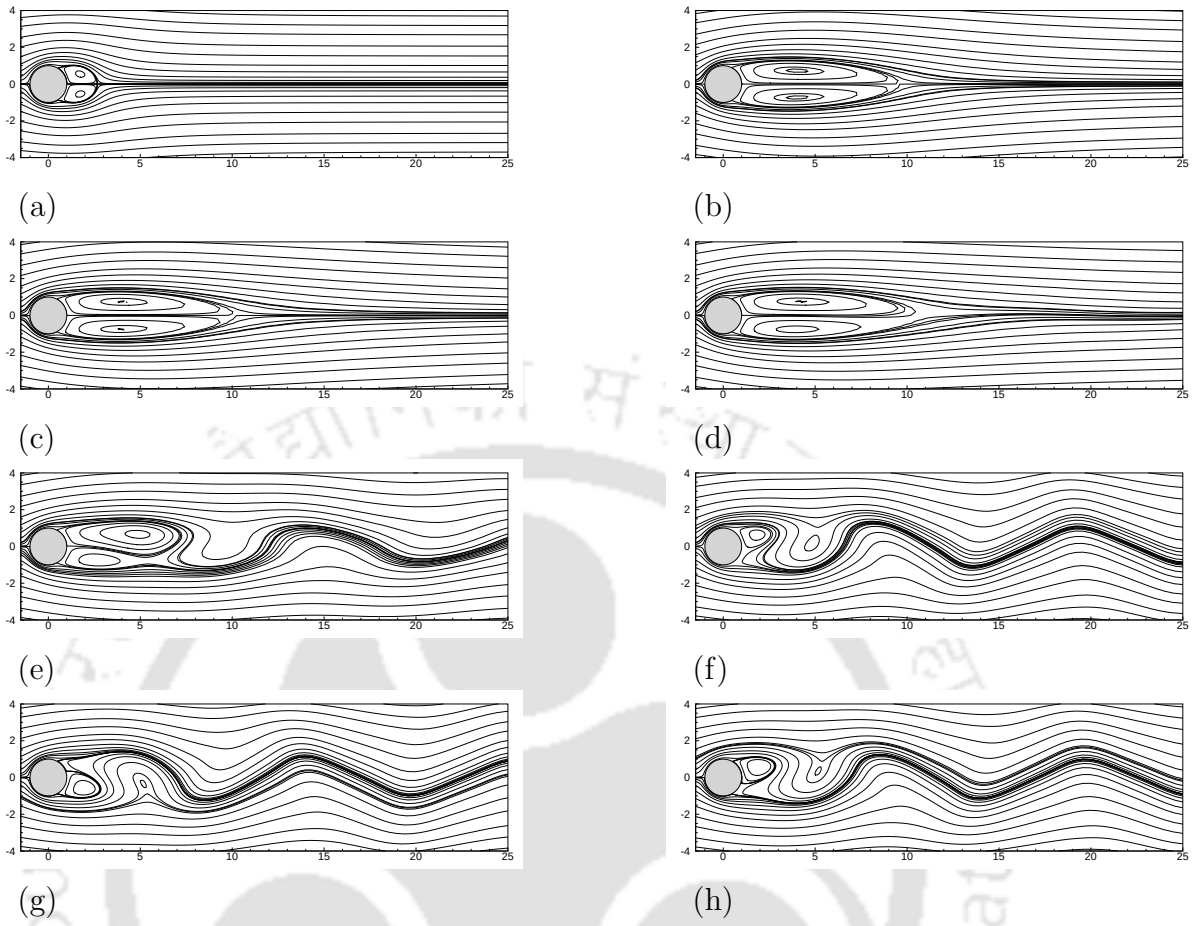

Figure 5.2: *Streamlines for* $Re = 80$ *at time (a)* $t = 2$, *(b)* $t = 20$, *(c)* $t = 30$, *(d)* $t = 80$, *(e)* $t = 120$, *(f)* $t = 180$, *(g)* $t = 244.9$, *(h)* $t = 248.1$.

(h) which reflect the alternatively positive and negative vorticities of the eddies presented in figure 5.4(d) and correspond respectively to the positive and negative peak values of the lift coefficient.

We also compute streaklines for this Reynolds number and depict them in figure 5.5(a). Our computed streakline patterns are very much in conjunction with the experimental streaklines reported by Perry *et al.* [120] (5.5(b)). The power density spectra of time sample normalized by the maximum value for $Re = 80$ is shown in figure 5.6. Based on this power spectrum we also calculate the Strouhal number which characterizes the vortex shedding process. In table 5.1, we compare our computed Strouhal numbers, drag and lift coefficients with established experimental and numerical results and obtain very close comparisons. Figure 5.7 displays the phase plane of the drag and lift coefficients for $Re = 80$.

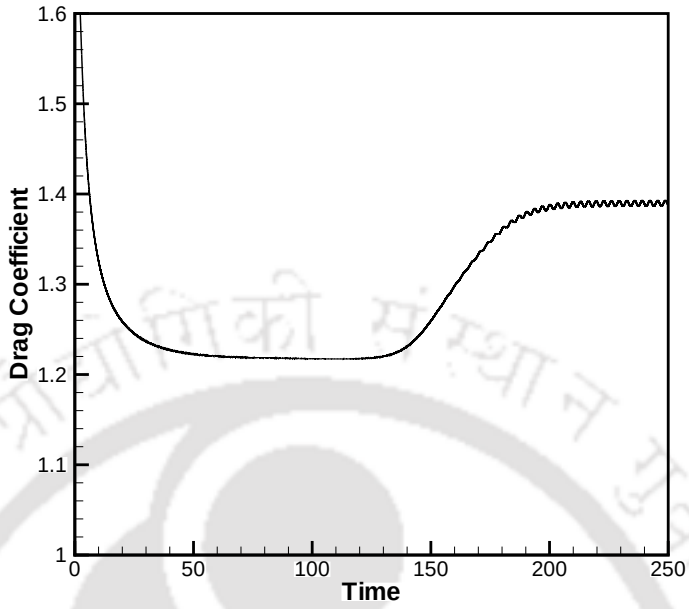

(a)

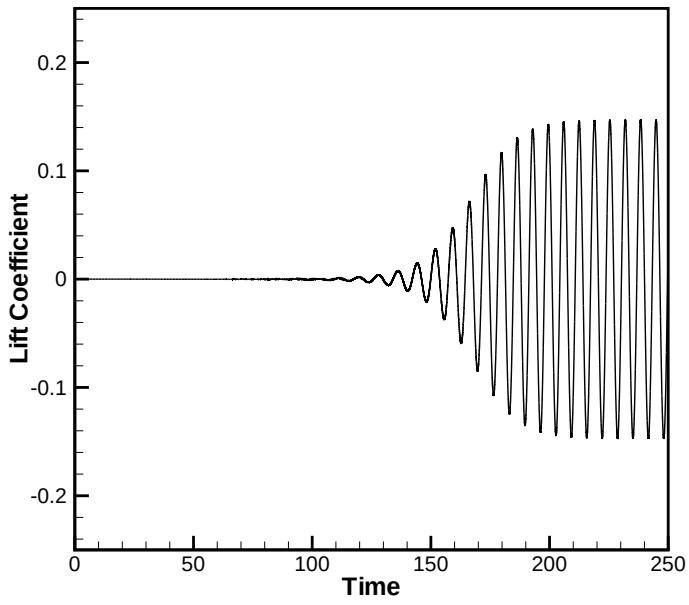

(b)

Figure 5.3: *Evolution of (a) Drag coefficient and (b) Lift coefficient for* $Re = 80$.

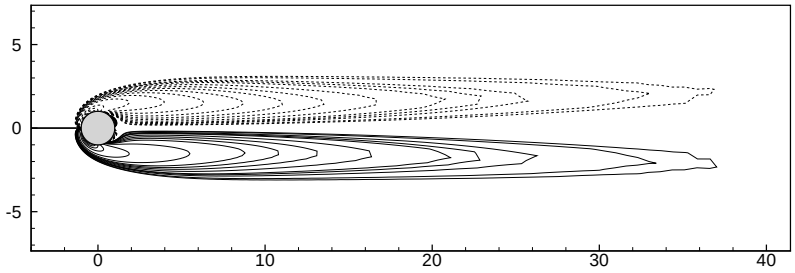

(a)

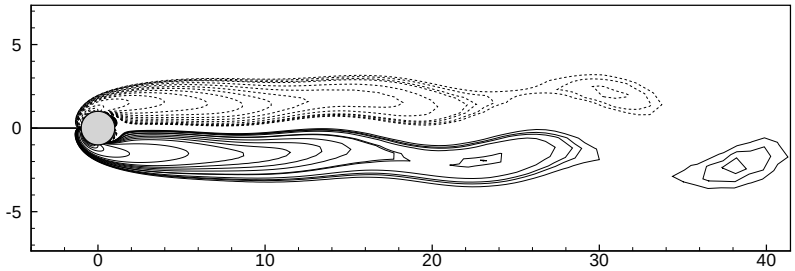

(b)

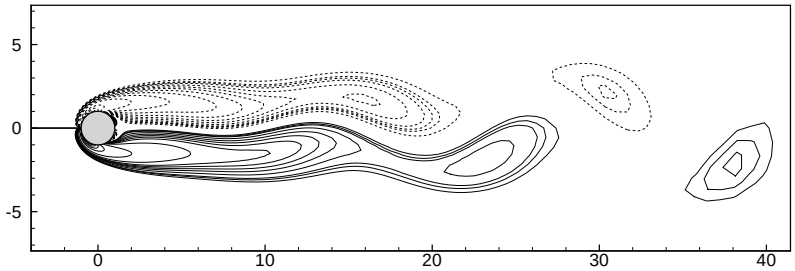

(c)

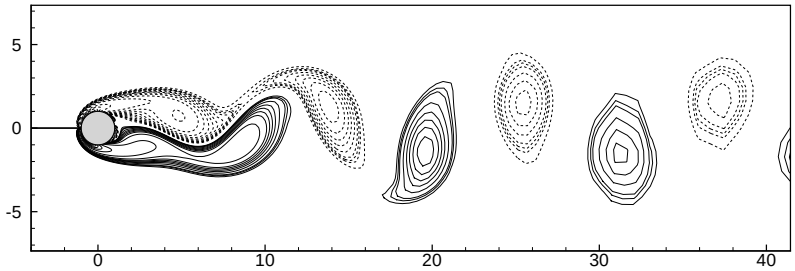

(d)

Figure 5.4: *Vorticity contours (the dotted lines representing to negative values) corresponding to the peak value of the lift coefficient for the temporally periodic solution (a)* $Re = 46.5$*, (b)* $Re = 47$*, (c)* $Re = 50$*, (d)* $Re = 80$*.*

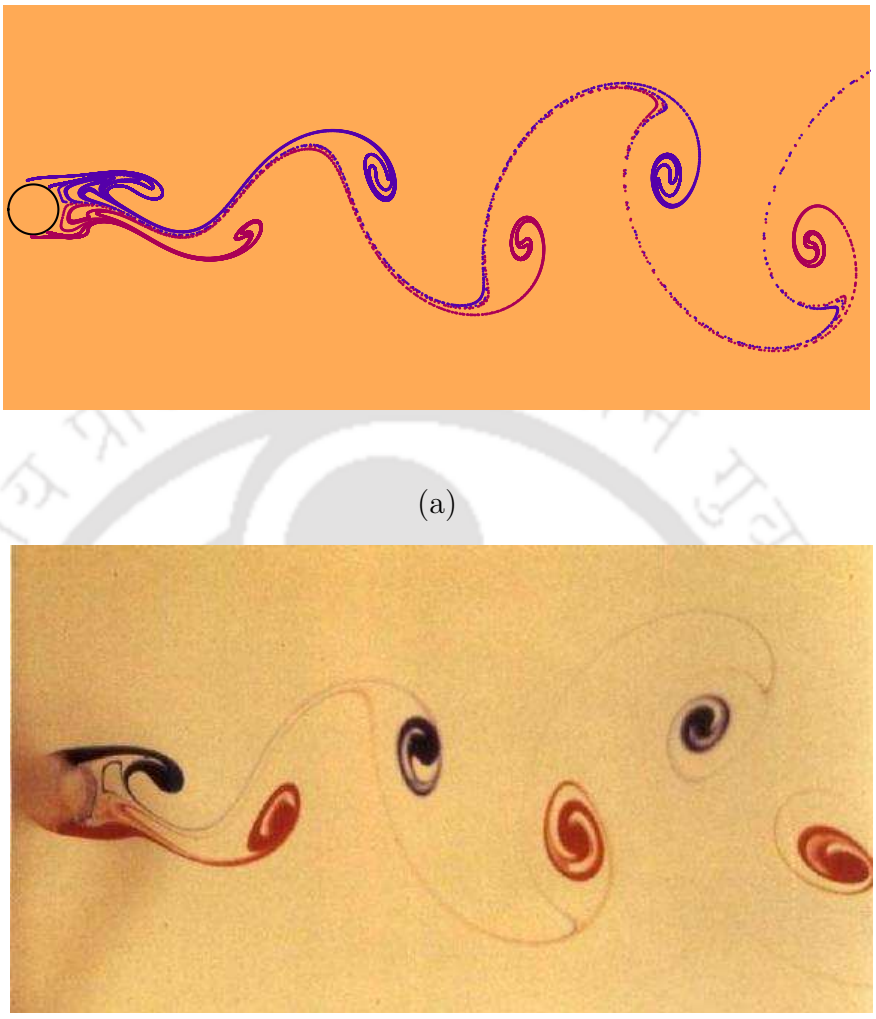

(a)

(b)

Figure 5.5: *Comparison of (a) Numerical and (b) Experimental [120] streaklines for* $Re = 80$.

5.3.2 Flows for $Re = 44$

Similar to the flow of $Re = 40$ which has been described in Chapter 4, in this case also the flow settles down to a steady state. Its importance lies in its closeness to the bifurcation point and hence will be ideal to test the behavior of perturbation techniques used in this work. The time evolution of this flow field and its response to the perturbations is the major point of study in this case. The evolution of drag coefficient has been shown in figure 5.8. A comparison with the evolution of drag coefficient for $Re = 40$ can also be seen in this figure. From the figure

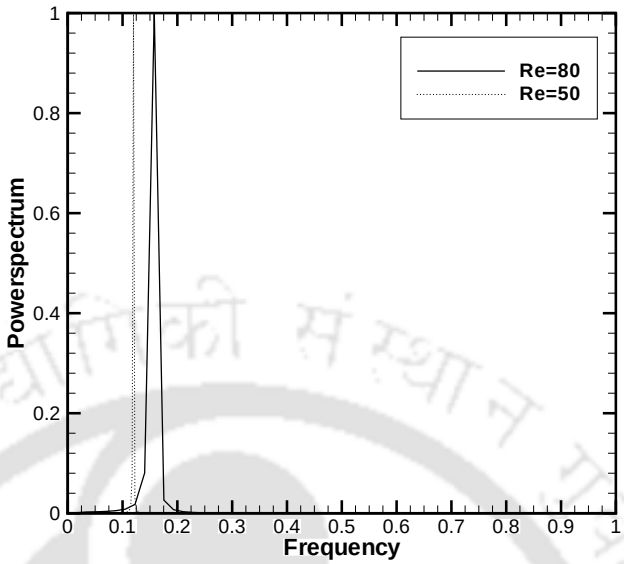

Figure 5.6: *Power spectrum of drag and lift coefficients for* $Re = 50$ *and* $Re = 80$.

Table 5.1: *Comparison of Strouhal number, drag and lift coefficients of the periodic flow for* $Re = 50$ *and* $Re = 80$.

Re	50			80		
Reference	St	C_D	C_L	St	C_D	C_L
Frank *et al.* [48]	0.116	1.39	0.0	0.152	1.35	$\pm$0.26
Williamson [158]	0.123	—	—	0.15	—	—
Silva *et al.* [134]	0.12	1.46	—	0.15	1.40	$\pm$0.23
Le *et al.* [89]	—	—	$\pm$0.07	0.15	—	—
Wang *et al.* [153]	—	—	—	0.158	1.428	$\pm$0.263
Present Study	0.120	1.461	$\pm$0.02	0.158	1.390 $\pm$0.003	$\pm$0.15

it is clear that a steady state has been reached with constancy of drag coefficient clearly established at time $t \approx 70$, although we continue to compute up to time $t = 100$. The steady state streamline contours and corresponding post-processed vorticity contours are shown in figure 5.9(a) and 5.9(b) respectively.

At the time $t \approx 30$ we introduce the three different types of perturbations described in section 5.2 separately and study their effect.

In the first method we perturb the inlet boundary condition where an inlet velocity $U_\infty = 2$ is introduced in the region above x-axis and $U_\infty = 0$ below it.

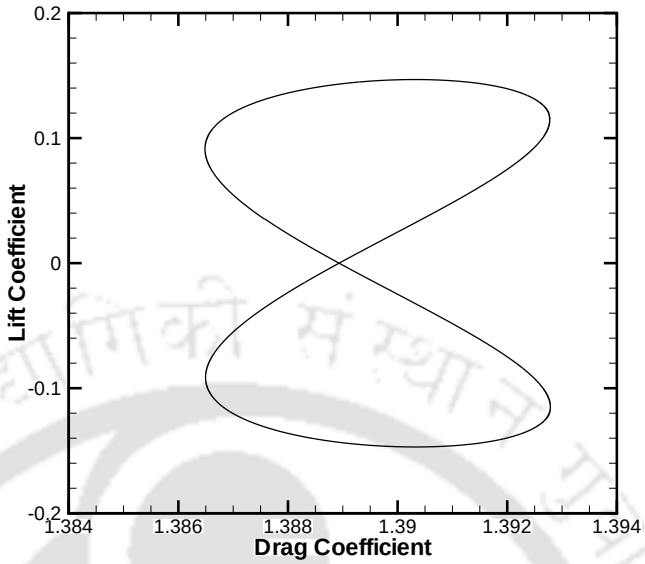

Figure 5.7: *Phase diagram of drag and lift coefficients for* $Re = 80$.

After a unit interval of time δt, the original velocity $U_\infty = 1$ is retained throughout the inlet. This introduces a huge fluctuation of the lift and drag coefficients as can be seen in figures 5.10(a) and 5.11(a) respectively. The drag coefficient quickly settles down but lift coefficient starts oscillating. With time these oscillations decays down due to viscous dissipation and at time around 100 becomes zero again, reestablishing the steady character of the flow.

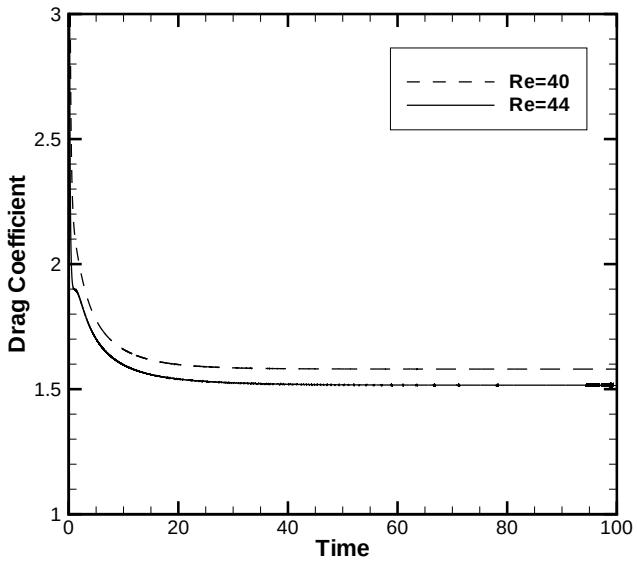

Figure 5.8: *Evolution of drag coefficient for* $Re = 40$ *and* $Re = 44$.

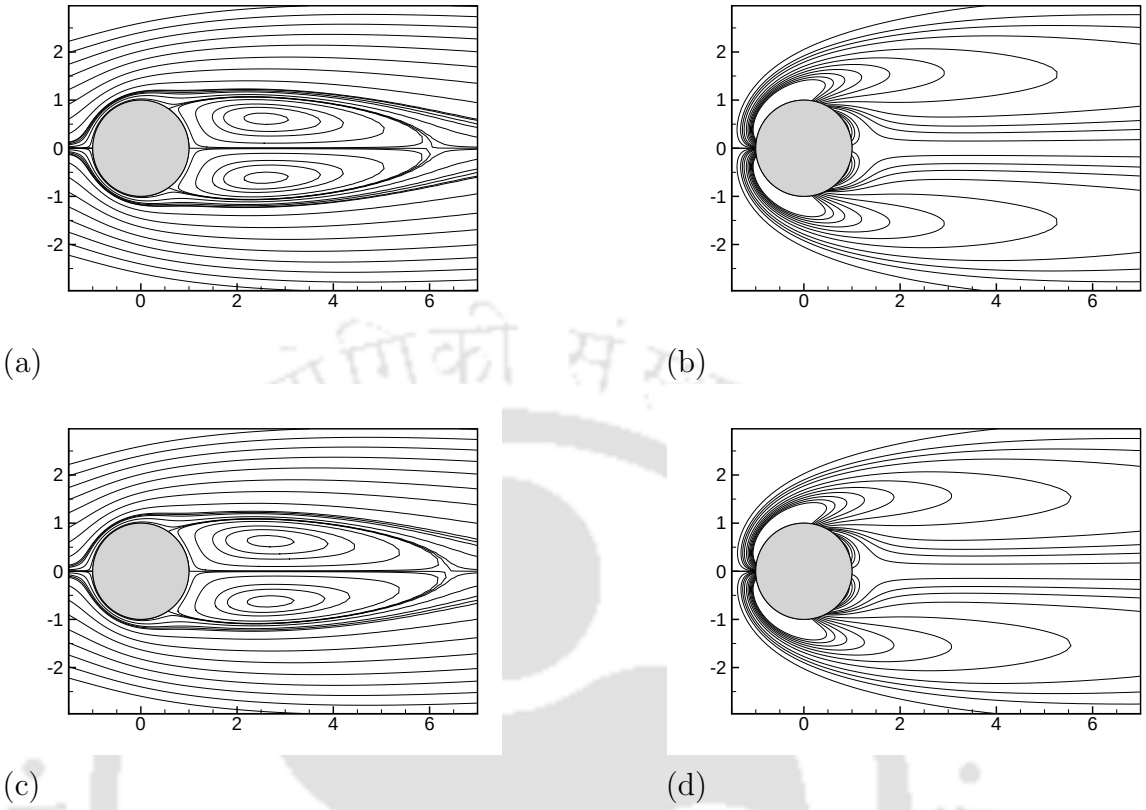

Figure 5.9: *Steady state (a) Stream lines for Re = 44, (b) Vorticity contours for Re = 44, (c) Stream lines for Re = 46.5, (d) Vorticity contours for Re = 46.5.*

The second perturbation technique corresponds to the cylinder being given a rotational velocity for only unit time interval. Within this small time δt the flow field loses its symmetry and a high lift is introduced into the flow field. As in the earlier case, the drag settles down quickly (figure 5.11(b)), but the lift oscillates (figure 5.10(b)) with higher amplitude compared to the previous case and takes more time to eventually become zero.

Lastly, we give the cylinder a vertical sinusoidal oscillation. A complete period up and down and back to its position takes unit time and the amplitude of the oscillation is same as that of the diameter of the cylinder. This oscillation severely destroys the symmetric nature of the steady state fluid flow field. This is associated with severe oscillation of the lift value which can be clearly seen in the figure 5.10(c). This artificial excitation triggers near wake instability. As this excitation stops and time progresses, vortices are shed due to the alternate formation of gathers at the end of the near wake. The near wake oscillations are suppressed by

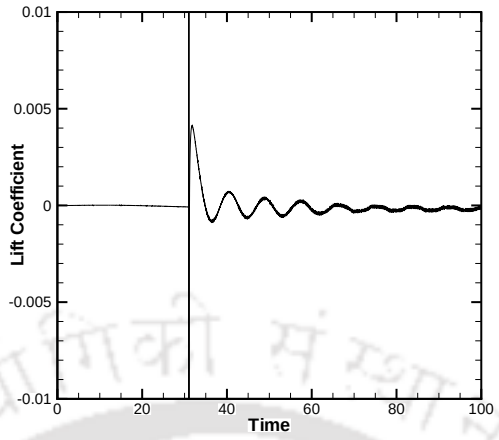

(a)

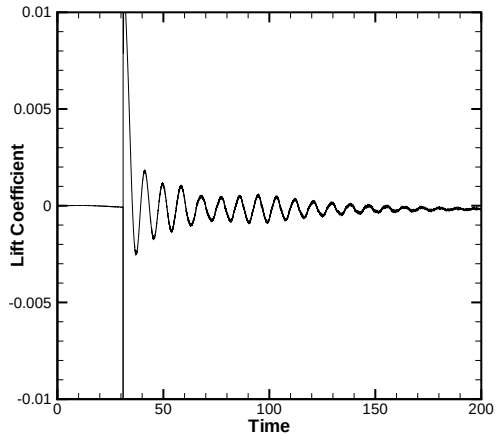

(b)

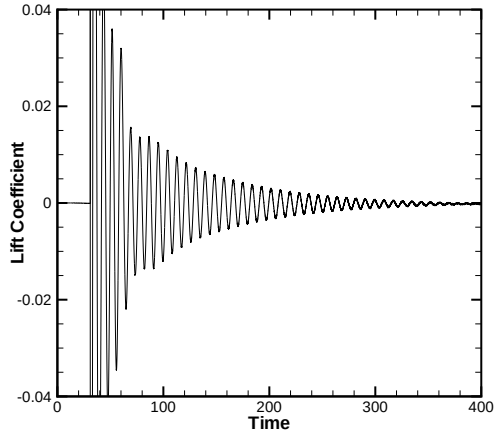

(c)

Figure 5.10: *Effect of different types of perturbations on lift coefficient for* $Re = 44$ *(a) Perturbation of the inlet boundary condition, (b) Perturbation by rotation, (c) Perturbation by oscillation.*

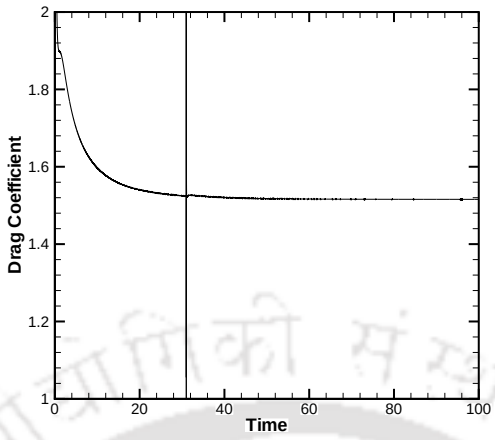

(a)

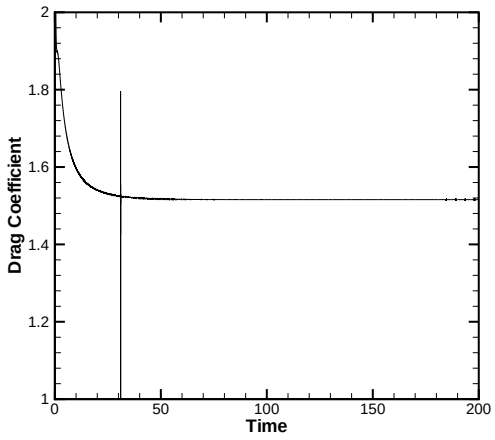

(b)

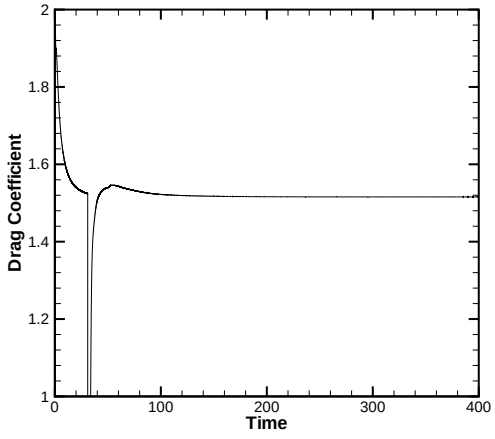

(c)

Figure 5.11: *Effect of different types of perturbations on drag coefficient for* $Re = 44$ *(a) Perturbation of the inlet boundary condition, (b) Perturbation by rotation, (c) Perturbation by oscillation.*

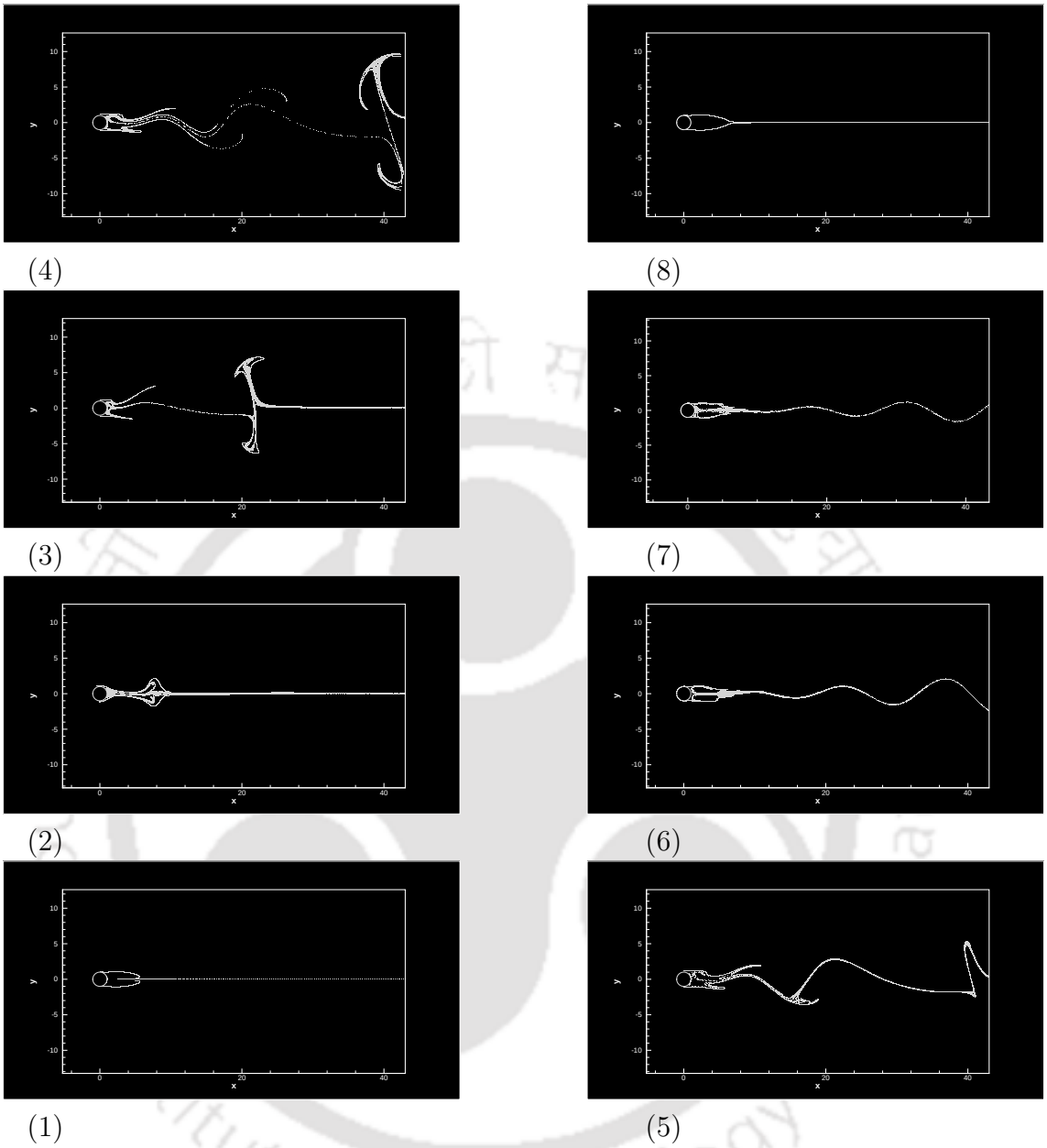

Figure 5.12: *Streaklines corresponding to oscillatory perturbation for* $Re = 44$.

the viscous damping with time and subsequent diminishing of waviness of the trail until a straight stable trail is reestablished. As can be seen from figure 5.11(c), in this case, drag coefficient takes much more time to reestablish. The reestablished value of drag and lift coefficients matches with the steady state value before the perturbation was introduced. The entire journey has been captured through streak lines in figure 5.12. As mentioned in section 5.2, this perturbation technique was

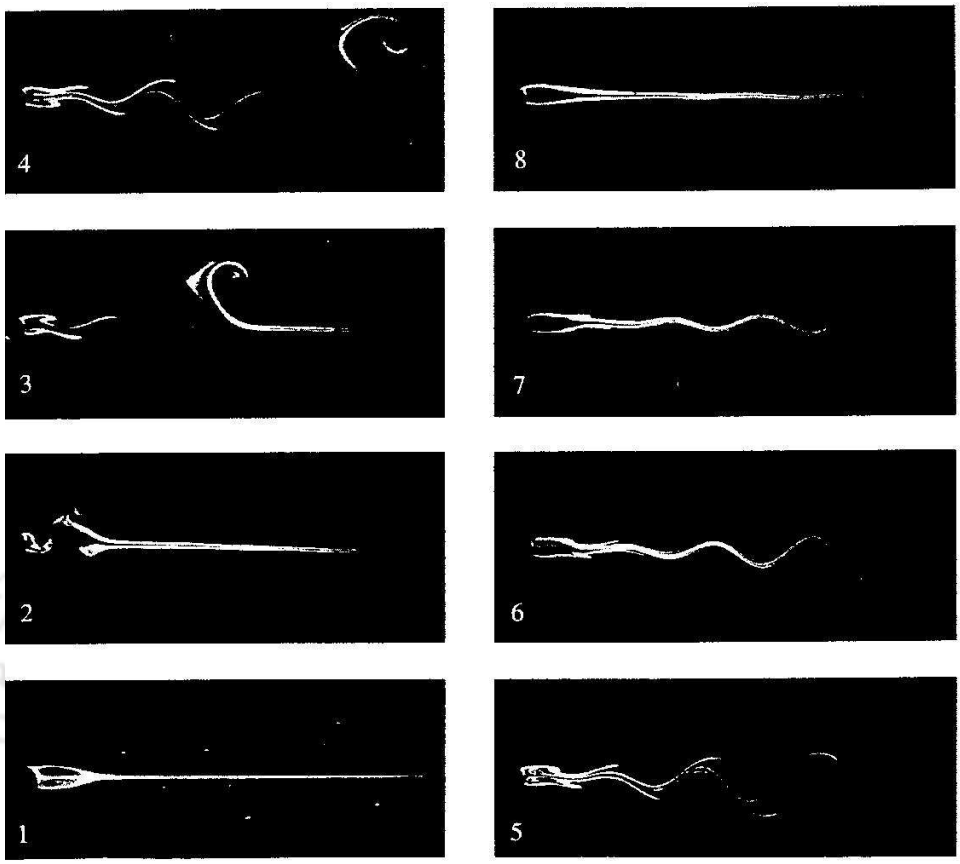

Figure 5.13: *Streaklines resulting from the experiment of Camichel and Teissie-Solier as reported in Zdravkovich [15] for* $Re = 44$.

inspired by the artificial excitation experiment carried out by Camichel and Teissie-Solier for $Re = 44$ as reported in Zdravkovich [15]. Experimental streak lines representing oscillation of disturbed near wake at $Re = 44$ as reported by Camichel and Teissie-Solier can be seen in figure 5.13. From these figures, it is clear that our computation has been able to replicate reasonably well all the stages of their experiment, starting from an initial perturbed stage till the flow finally settling to a steady state. The evolution of the streamlines in the pre and post perturbation (with the third technique) time regime is shown in figure 5.14. These figures are clearly in conformity with the discussion above; in particular, the onset of asymmetry is obvious just after the excitation of the cylinder at time $t = 33$ (5.14(c)). It is obvious from figures 5.14(b) and 5.14(h) that the flow eventually settles into a steady state as they are almost indistinguishable from each other.

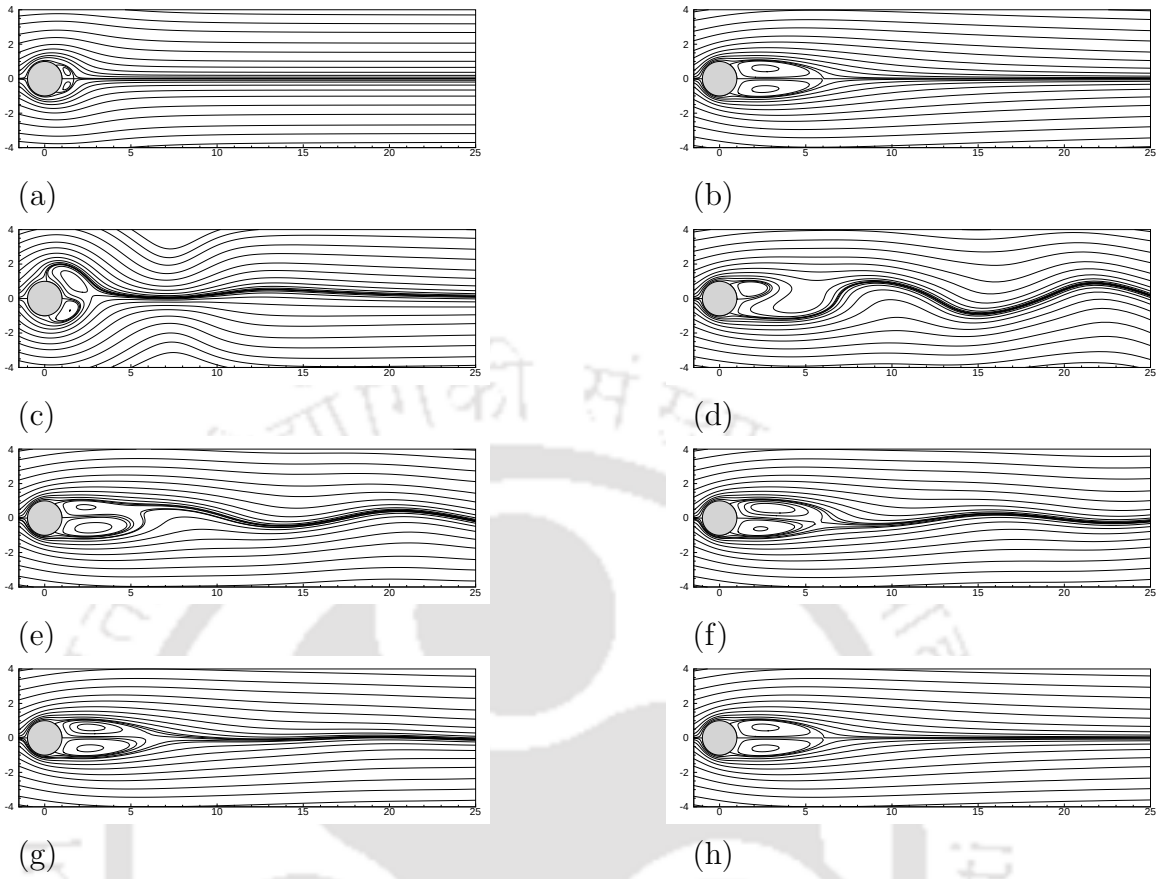

Figure 5.14: *Streamlines for $Re = 44$ corresponding to oscillatory perturbation at time (a) $t = 1$, (b) $t = 30$, (c) $t = 33$, (d) $t = 55$, (e) $t = 105$, (f) $t = 155$, (g) $t = 255$, (h) $t = 450$.*

5.3.3 Flows for $Re = 50$

We begin by simulating the flow without any perturbation. The evolution of drag and lift coefficients resulting from this computation can be seen in figure 5.15(a). This figure indicates an un-physical steady state for this Re with the drag coefficient attaining a constant value and lift coefficient remaining zero. Next, the three types of perturbation discussed in the above section are used to disturb the flow field symmetry. We introduce the perturbation at time $t = 80$. The evolution of the streamlines prior to the introduction of the perturbation and after are shown in figure 5.16. As in $Re = 44$, all the three methods instantly introduce asymmetry to the flow and is clearly visible from the evolution of drag and lift coefficients in figure 5.15(b)-(d) and 5.16(c). For this Reynolds number the perturbations to the flow are no longer damped out and hence affect the downstream wake. It is

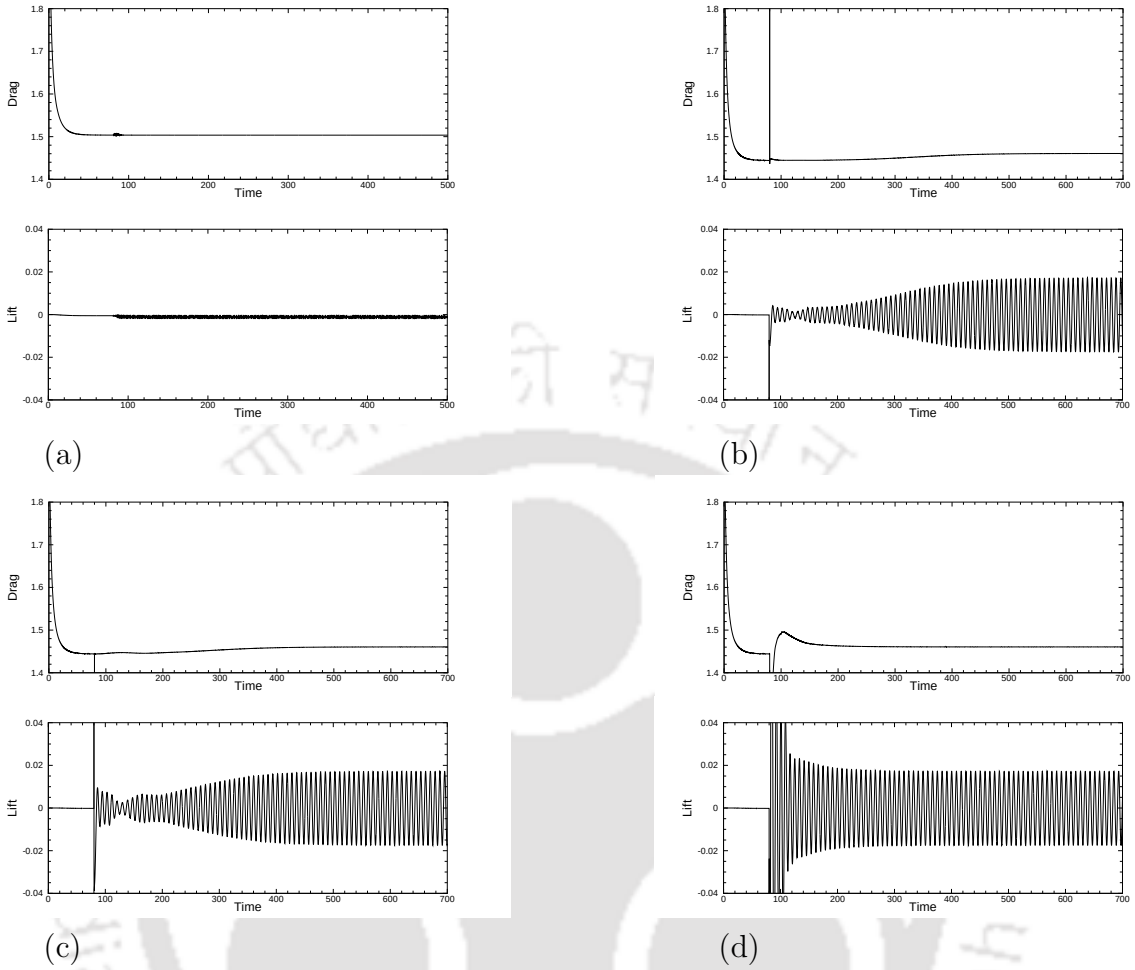

Figure 5.15: *Variation of drag and lift coefficients corresponding to different flow situations for* $Re = 50$*, (a) normal computation without any perturbation, (b) perturbation of the inlet boundary condition, (c) perturbation by rotation, (d) perturbation by oscillation.*

noticed that in all the cases the flow acquires the same eventual periodic state. As in the case of $Re = 80$, the mirror images depicted in figures 5.16(g) and (h) are half a vortex shedding cycle apart. Also noticed is that, greater the severity in perturbation, shorter is the time to reach the periodic state as evidenced by figure 5.15(d). The flow characteristics for this periodic state have been compared with the available experimental and numerical results in table 5.1. As mentioned earlier, compared to results reported for other range of Re, reports on the flow characteristics for $Re = 50$ are scanty. The power density spectrum for the lift coefficient normalized by its maximum value has been depicted in figure 5.6. Figure

5.17 displays the phase plane of the drag and lift coefficients for $Re = 50$. The vorticity contours corresponding to the peak value of lift coefficient can be found in figure 5.4(c). As in the case of $Re = 80$, the alternative positive and negative vorticities of the eddies clearly reconfirm the eventual periodic nature of the flow. One can clearly infer from figures 5.4 and 5.6 that the shedding frequency increases with increase in Reynolds number from 50 to 80; the St values presented in table 5.1 corroborate this fact.

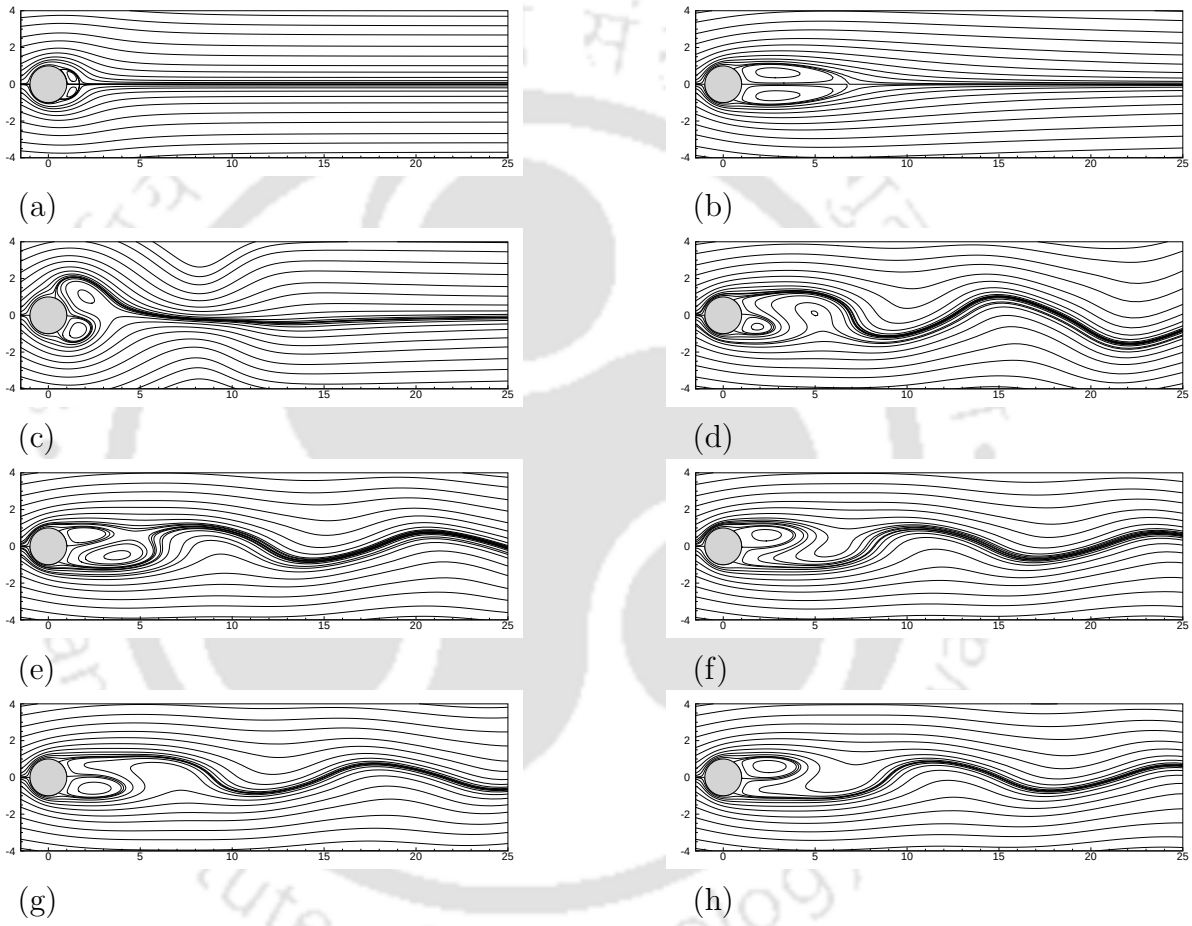

Figure 5.16: *Streamlines for* $Re = 50$ *corresponding to oscillatory perturbation at time (a)* $t = 1$, *(b)* $t = 35$, *(c)* $t = 82$, *(d)* $t = 100$, *(e)* $t = 160$, *(f)* $t = 220$, *(g)* $t = 693.3$, *(h)* $t = 697.5$.

5.3.4 Flows for $Re = 46.5$, 46.8 and 47

The long time computation of the flow for $Re = 44$ and 50 above indicates the residence of the critical Reynolds number Re_c in the range $44 < Re_c \leq 50$. We

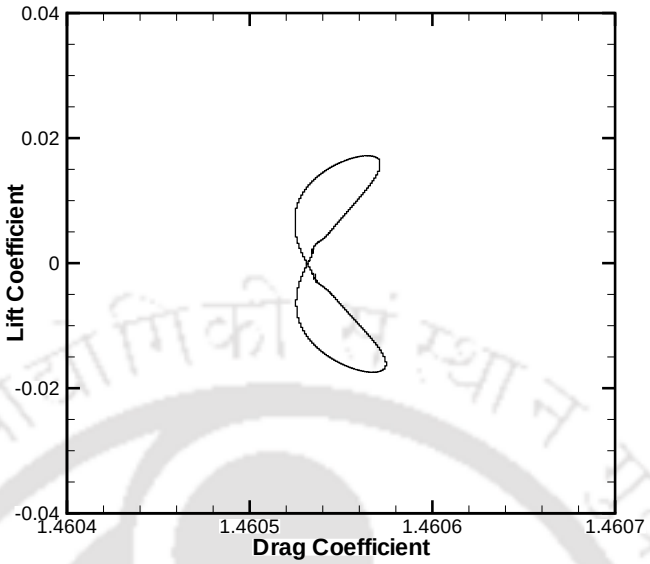

Figure 5.17: *Phase diagram of drag and lift coefficients for* $Re = 50$.

further narrow down this range to compute the flow for $Re = 46.5$ and $Re = 47$. The motivation for such computation comes from some recent studies [30, 51, 86, 99] that have shown the Re_c to be lying in the vicinity of 47 by using linear stability analysis. Moreover, very few studies highlighting the flow field at such a crucial value can be found in literature. Our effort here is dedicated to capturing the dynamics of the steady or periodic state at a Reynolds Number extremely close to the Re_c. We use the first and the third methods described in section 5.2, namely (a) the perturbation of the boundary condition and (c) perturbation by oscillation in order to trigger asymmetry into the flow at time $t = 36$. The evolution of drag and lift coefficients for $Re = 46.5$ and $Re = 47$ can be found in figures 5.18 and 5.19; from these figures is clear that for $Re = 46.5$ the flow settles into a steady state while the flow for $Re = 47$ eventually becomes periodic. The vorticity contours presented in figures 5.4(a) and 5.4(b) (corresponding to the peak value of lift coefficient) corroborate this fact as in case of the former, the contours are symmetric about $y = 0$ line while in case of the later, it is no longer so. From this, we conclude that the critical Reynolds number resides in the very close range $46.5 < Re_c \leq 47$, which in a way reconfirms the Re_c values found in [51, 86, 99]. Finally figure 5.4 serves as a comparison of vorticity contours for $Re < Re_c$, $Re \approx Re_c$, $Re > Re_c$, $Re \gg Re_c$. For $Re = 46.5$ an interesting phenomenon has been captured

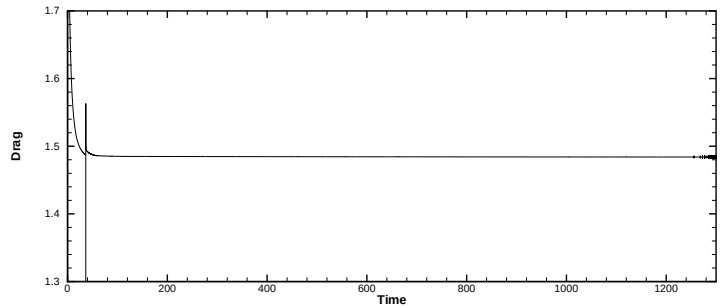

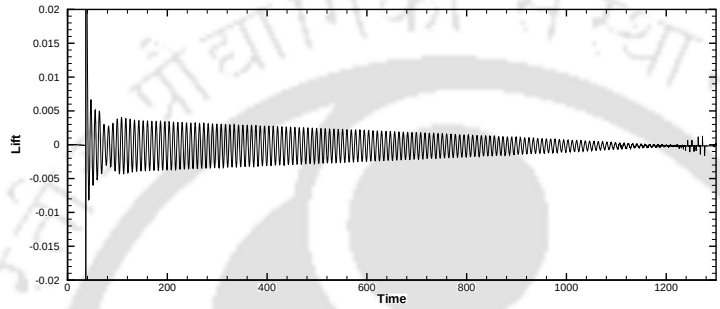

(a)

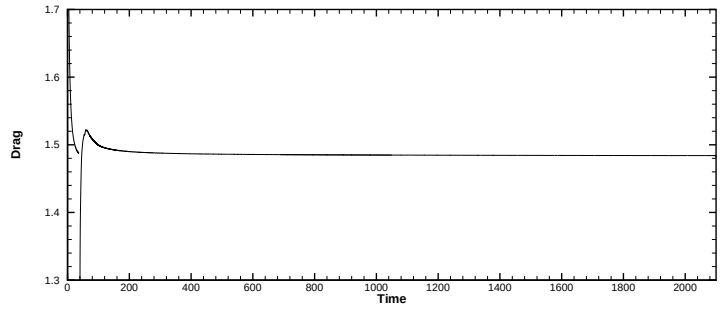

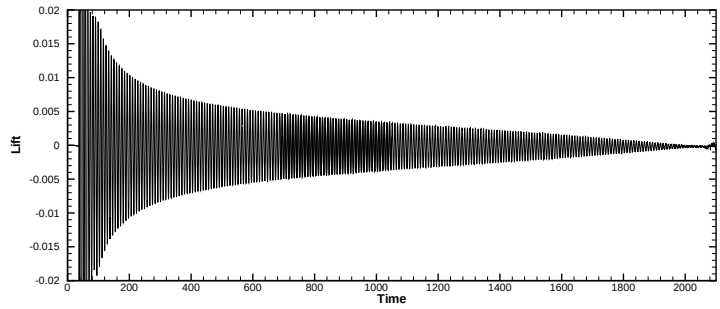

(b)

Figure 5.18: *Variation of drag and lift coefficients corresponding to two different flow situations for* $Re = 46.5$ *(a) Corresponds to perturbation of the inlet boundary condition, (b) Corresponds to perturbation by oscillation.*

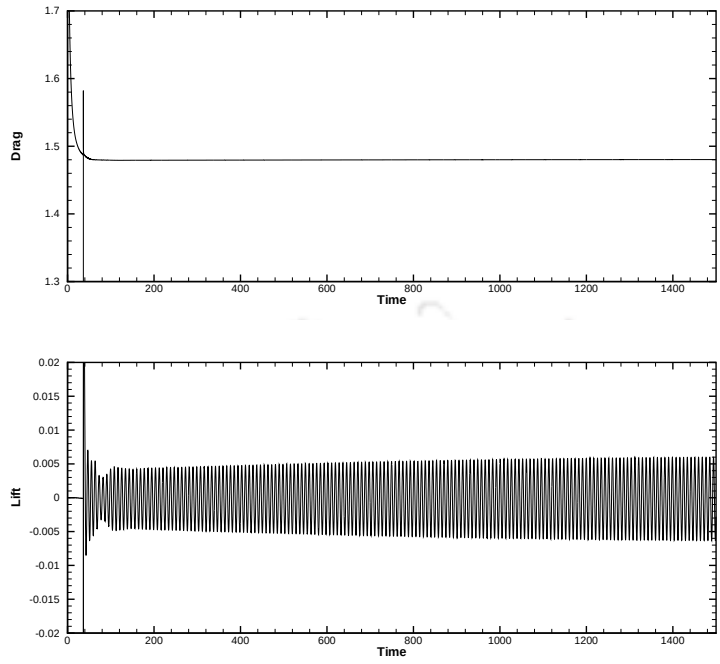

(a)

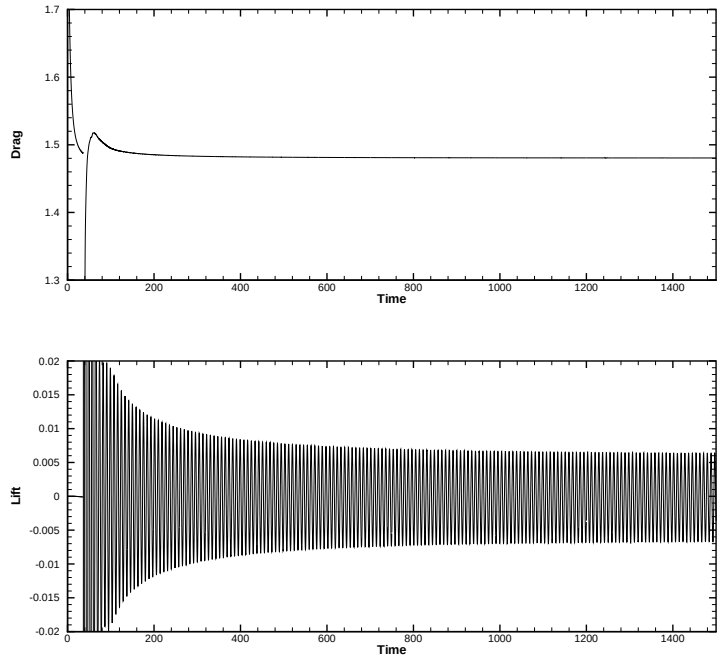

(b)

Figure 5.19: *Variation of drag and lift coefficients corresponding to two different flow situations for* $Re = 47$ *(a) Corresponds to perturbation of the inlet boundary condition, (b) Corresponds to perturbation by oscillation.*

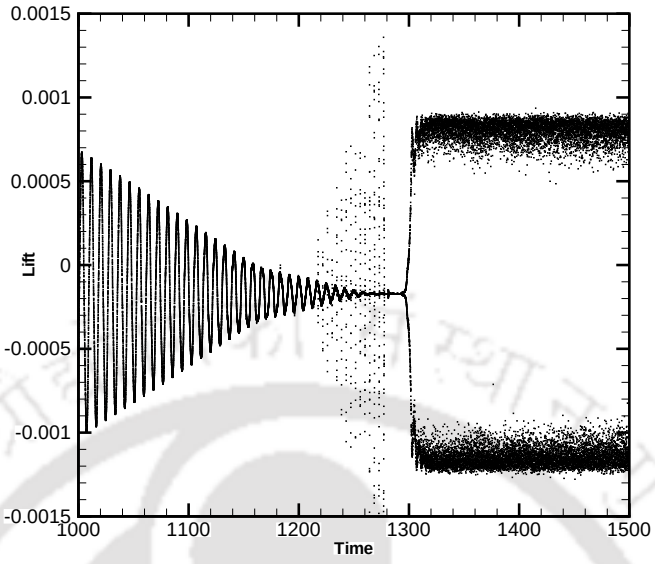

(a)

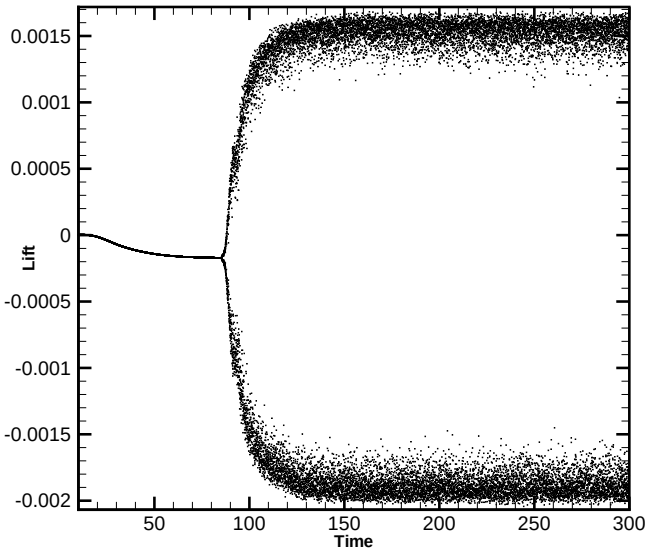

(b)

Figure 5.20: *Closeup view of the lift coefficients for (a) $Re = 46.5$ and (b) $Re = 40$ as they reach steady state.*

by our simulation. In figure 5.20(a) we present a closeup view of the lift coefficient as the flow approaches steady state. It is seen that at time around $t = 1220$, the lift coefficient despite maintaining its overall decaying nature starts fluctuating widely

for some isolated times. These fluctuations increase gradually and they suddenly vanish at time $t = 1280$. Thereafter upto time $t = 1300$, the lift coefficient maintains a steady value of 0.0001 revealing a peculiar pattern thereafter. Here the lift values fluctuate discontinuously at alternate time steps between 0.0008 and -0.0012 and is seen as two clusters (figure 5.20(a)). Note that in this figure, the points representing the lift coefficients are not joined by continuous lines unlike figure 5.18. This unphysical phenomena continues till $t = 1500$ when we stop computing. Notably this phenomenon was observed for $Re = 40$ (figure 5.20(b)) as well. In this case no perturbation was introduced and the flow becomes steady at time $t = 80$ but around the time $t = 90$ the lift coefficient suddenly starts fluctuating between 0.0015 and 0.0020.

Table 5.2: *Flow properties for Re values close to Re_c.*

Re	C_D	C_L $(Min., Max.)$	St
44.0	1.5157	-0.0001	-
46.5	1.4841	-0.0001	-
46.8	1.4816	$(-0.0046, +0.0043)$	0.117
47.0	1.4803	$(-0.0064, +0.0061)$	0.118
50.0	1.4605	$(-0.0175, +0.0172)$	0.120

Table 5.3: *Estimation of Re_c.*

	$Re \rightarrow$	50	47	46.8	Re_c
v_{2D}	$min.$	-0.0531	-0.0172	-0.0115	46.63
	$max.$	$+0.0531$	$+0.0172$	$+0.0115$	46.63
v_D	$min.$	-0.0214	-0.0069	-0.0045	46.65
	$max.$	$+0.0214$	$+0.0069$	$+0.0045$	46.65
C_L	$min.$	-0.0175	-0.0064	-0.0042	46.78
	$max.$	$+0.0172$	$+0.0061$	$+0.0040$	46.75

We continue with our effort to narrow down to the Re_c and compute the flow for $Re = 46.8$. Here we use the converged periodic state of $Re = 47$ as the initial data and compute upto non-dimensional time 3000 to reach a new periodic state with higher drag and lower lift values. The values of drag, lift and Strouhal numbers for different values of Re close to Re_c has been noted in table 5.2. In the table we report upto four decimal places of accuracy as the grid size and the accuracy of the scheme do not permit us to move beyond. Finally in table 5.3 we give a projection of Re_c by parabolic curve fitting using y- component of velocity at two different distances D and $2D$ denoted as v_D and v_{2D} respectively on the x- axis, and the lift coefficient. This table indicates that the bifurcation takes place around $Re = 46.7$.

5.4 Effect of the perturbation techniques

A close look at the evolution of the lift coefficients for $Re = 44$, 46.5, 47 and 50 (figures 5.10, 5.15, 5.18 and 5.19) reveals that in all the cases asymmetry sets in instantly after the perturbation is introduced. However, its intensity gradually increases as one moves from the first technique to the second one and then to the third as the magnitude of the lift coefficient suggests. Also the effect of the perturbation dies down slowest in case of the third method. Thus, whenever a steady state or a periodic state is reached eventually, the third method takes the largest amount of physical time. In case of the first two methods, steady or periodic state is attained relatively quickly and as such there is a possibility that when the Re considered is higher than Re_c and extremely close to it, the first two techniques may end up showing an un-physical steady state eventually. Therefore, the third technique is the most robust one and should be preferred over the other two. Also it is clear from these figures that closer the Re (sitting on the either side) to the Re_c, more the physical time required for the flow to settle into a periodic or steady state as the case may be. It is worth mentioning that all three perturbation techniques correspond to physical situations unlike some existing ones that stems out from purely numerical perspective.

5.5 Conclusion

For an impulsively started circular cylinder, above some critical Reynolds number, asymmetry sets in and as time progresses, vortex shedding occurs naturally in physical situations. However, in the range of $43 \leq Re \leq 50$ in the vicinity of Re_c, called by many as the threshold regime, only a few numerical simulations are

available that describe the physics of the flow accurately. Numerical computation is tricky in this range; normal computational procedure sometimes lead to the capture of some un-physical flow simulation. To initiate the shedding process, asymmetry needs to be triggered artificially. In this chapter, three different techniques, namely, (a) perturbation of the inlet boundary condition, (b) perturbation by rotation and (c) perturbation by oscillation, and their subsequent effect on the flow are discussed in details. Initially flow is computed without the artificial perturbation for $Re = 80$ which is beyond the range of the threshold regime and flow patterns are well established. Flow is then computed for two Re in the threshold regime, *viz.*, $Re = 44$ and $Re = 50$ where the above perturbation techniques are employed to trigger asymmetry into the flow. It is found that the flow for $Re = 44$ eventually retains its symmetry as well as steadiness while for $Re = 50$ the induced perturbations lead to periodic vortex shedding. The computation is finally narrowed down to $Re = 46.5$ and 47, the flow characteristics of which is similar to $Re = 44$ and 50 respectively. The different characteristics of the flow field are discussed in details for all the Re considered here. Note that for the range of Re considered here there is no three dimensional effect. Our numerical results are compared with experimental and numerical results whenever available and excellent comparison is obtained in all the cases.

In the following, we summarize the major accomplishments of this study: (i) For the first time, a pure stream function based finite difference scheme is used to compute the flow in the threshold regime for the flow past a circular cylinder problem. (ii) Perturbation induced through the transverse oscillation of the cylinder is introduced for which no numerical results are seen before. (iii) All the stages of a 1935 laboratory experiment by Camichel and Teissie-Solier as reported in Zdravkovich [15] for $Re = 44$ starting from an initial perturbed stage till the flow finally settling to a steady state is numerically replicated by streakline simulation. (iv) Our computed streakline patterns for $Re = 80$ are probably closest to the experimental results of Perry. (v) By direct numerical time integration, we have found a very narrow range for the Re_c, *viz.* $46.5 < Re_c \leq 47$ which is extremely close to the ones predicted by recent studies using linear stability analysis. Ultimately by parabolic curve fitting we conclude that $Re_c \approx 46.7$. (vi) The robustness of the newly introduced perturbation through transverse oscillation of the cylinder over other methods is established.

Chapter 6

Tackling Problems of Moving Boundaries Using the Biharmonic Approach

6.1 Introduction

In this chapter we consider the cases of rotating cylinder with constant and oscillatory rotations, and the case of in-line oscillatory cylinder[1]. It is worth mentioning that these rotatory and oscillatory cases symbolize moving boundaries.

Vortex shedding takes place in the near wake behind a bluff body due to flow instability and the control of this vortex shedding has been of great interest amongst the fluid dynamics community. As vortex shedding induces vibrations on the structure owing to the fluctuations of lift, modifying the strength of vortices shed is thus a way of modifying vibrations and drag as well. Although many different shapes of bluff bodies exist, the circular cylinder is considered to be the representative two dimensional bluff body. As we have seen in our previous chapters, in case of stationary cylinders, vortex shedding occurs for $Re \geq Re_c$, where $46.5 < Re_c \leq 47$. This shedding pattern gets more pronounced with increase in Reynolds number. Flow past a rotating cylinder is considered to be a prototypical problem in the study of unsteady flow separation. It is of practical importance in boundary layer control and lift enhancement schemes. Rotational effect plays an important role in the control of vortex shedding and has its consequences in wake modification and reductions of flow induced vibration. Unlike the flow past a translating circular cylinder where the flow becomes asymmetric only at higher Reynolds numbers and larger time, in the case of rotating cylinder the flow becomes asymmetric even for small Reynolds numbers as well as for times just after the start due to the impul-

[1]Part of this work is under review in *Int. J. Comput. Meth. Engrg. Sci. Mech.*

sive rotation of the body. This asymmetry introduces different complex behaviors in the fluid flow.

The problem of flow past a circular cylinder rotating with constant angular velocity, in an uniform flow dates back to the work of Prandtl and Tietjens [2] in the middle of the first half of the last century. Note that such flows are characterized by velocity ratio ($\alpha = \frac{aq}{U_\infty}$, where q is the angular velocity of the cylinder about its axis) and the Reynolds number (Re). In 1983 Ingham [68] studied this problem for $Re = 5$ and 20 with $0 \leq \alpha \leq 0.5$. In the year 1985 a detailed study corresponding to $Re = 200$ was carried out both experimentally [41] and numerically [19]: the experimental work was carried out by Coutanceau and Menard [41] for $0.5 \leq \alpha \leq 3.25$, and the numerical by Badr and Dennis [19] for $\alpha = 0.5$ and 1.0. They also carried out numerical simulation for $Re = 500$ with the same angular velocity. In 1989, Badr *et al.* [20] found that for low Reynolds numbers the flow approaches a steady state asymptotically. More studies in this direction were carried out by Ingham and Tang [69]. Badr *et al.* [20] also investigated the flow phenomena for the high Re range of $10^3 \leq Re \leq 10^4$ with $0.5 \leq \alpha \leq 3.0$ in 1990. In 1994 Norberg [110] made significant experimental investigation of the flow around a rotating circular cylinder and the influence of the aspect ratio; a fairly comprehensive summary can also be found in [34]. The problem continues to hold interest amongst researchers which is evidenced by some of the most recent experimental and numerical works [36, 78, 102, 109, 114, 124].

As most of the studies were done in order to understand the effect of rotation, a parallel effort can be seen in the literature on mechanisms to control of vortex shedding and subsequent drag reduction. From the implementation perspective, rotary control of the cylinder wake is considered to be the simplest one. In the experiments of Tokumaru and Dimotakis [148], this mechanism was observed to yield up to 80% drag reduction at $Re = 15000$ for certain ranges of frequency and amplitude of sinusoidal rotary oscillation. Following this pioneering experimental work, numerous systematic numerical and experimental studies have been reported in the literature and several explanations of the physical mechanisms responsible for drag reduction have been proposed. Shiels and Leonard [133], who carried out numerical simulations using a two dimensional high-resolution viscous vortex method over a range of $Re = 150$-15000 in order to verify the experimental observation of drag reduction by Tokumaru and Dimotakis [148], suggested that the decrease in drag comes from a time averaged separation delay induced by an appropriate rotational oscillation. In their numerical investigation for $Re = 150$,

Protas and Wesfreid [121] proposed that the modification of the drag was directly related to the mean flow correction caused by the forcing through the action of the divergence of the Reynolds stress tensor of the fluctuating forced flow. The recent trend amongst researchers in this direction is to understand the phenomena of drag reduction; the first direct drag measurements and visualizations of the vortex shedding for a rotating oscillating cylinder at $Re = 150$ was carried out by Thiria *et al.* [146]. In this study the authors have shown that the value of drag starts to increase with forcing frequency until its maximum value close to the resonant case is reached and only afterwards it starts decreasing.

Flows due to bodies oscillating in a stationary or unsteady fluid and stationary bodies in an oscillating unsteady flow are considered to be fluid-structure interaction problem and is of immense importance in many fields of science and engineering. It has been proved to be a challenging area for research, since it provides a simplified tool for the investigation of flow around a cylinder immersed in a wave environment. Being a fluid structure interaction problem it has attracted the attention of the fluid mechanics community as well as structural engineers.

The vortex dynamics behind a bluff body causes fluctuating forces that act on the body. As the induced vibration of a structure forms an important issue for its stability, much of the literature deals with the cause, nature and the consequences of what is known as 'flow-induced vibration'. A common approach to study fluid-structure interactions is to force the body to oscillate with a predefined motion that approximates the flow. In this type of study flow features are examined by subjecting the body subjected to forced oscillation. Such a study was initiated by Keulegan and Carpenter [82]. Pioneering contribution in understanding the character of flow around an oscillating circular cylinder were made by Williamson [156], Bearman *et al.* [21], Tatsuno and Bearman [145]. Later on significant works were carried out by Iliadis and Anagnostopoulos [66], Dutsch *et al.* [45], Uzunoğlu *et al.* [151], Nobari and Naderan [108]. Of late this problem has been used extensively to validate newly developed numerical schemes [35, 152, 153]. In the same vein, we consider the case of an in-line oscillating cylinder in a fluid at rest to validate the scheme developed in Chapter 3 and to test its ability in handling moving boundaries.

The N-S equations used in the previous chapter represent the flow of incompressible viscous fluid in an inertial or space fixed frame of reference and are appropriate to the analysis of the fluid-structure interaction between a fixed body and moving flow. For a body moving in an incompressible fluid it is desirable to simu-

late the flow in a non-inertial frame attached to the body facilitating computational convenience by avoiding the re-meshing of the whole domain which is required if a fixed inertial frame were instead used. In case of a cylinder performing rotatory motion, due to the rotational symmetry of the cylinder structure, no re-meshing is required even in inertial frame of reference and as such we will stick to inertial frame of reference. For in-line oscillating cylinder we shift to non-inertial frame of reference. For a body accelerating in a fluid the unsteady force components such as Basset's history force, added mass effect *etc.* will also be present. These forces in addition to the steady forces *viz.* pressure force and shear stress force need to be taken into account while calculating drag and lift coefficients. But here in our calculations we have only considered the steady forces. The main goal of the study done here is to test the robustness of the proposed scheme rather than to study the individual flow physics of different configurations being considered.

6.2 Flow past a rotating cylinder

In this section, we investigate the flow past a circular cylinder which starts translating and rotating impulsively from rest in a viscous fluid. Two different types of oscillations are considered. In the first case the cylinder is considered to be rotating with constant angular velocity while in the second case we consider rotatory oscillation of the cylinder. Both these cases have importance of their own. The first one exhibits the suppression of the separated vortex where studies have shown that for high enough velocity ratios, steady flows with no vortex shedding is possible even for high Re values [18]. The second case has the richness of the vortex structure associated with such flows. Here the rotary oscillation of the cylinder causes separation of the flow from the cylinder surface, interrupting the formation of regular von Kármán vortices in the wake, leading to the creation of small scale vortices at the cylinder surface [127, 146]. It is a true test of efficiency for any numerical scheme to be able to capture these small physical vortices and record how strongly the vorticity distribution is affected in the near wake by the forcing frequency.

For this problem the initial and far stream boundary conditions are same as in section 4.3 of Chapter 4. On the surface of the cylinder we impose rotational velocity. If we consider Ω to be the non-dimensional velocity at a point on the surface of the cylinder of radius $r = a$ having polar angle θ then $u = -\Omega \sin\theta$ and $v = \Omega \cos\theta$. With respect to the transformation considered in Chapter 4 section 4.2 this reduces to $\psi_\xi = -\pi\Omega$, $\psi_\eta = 0$. On the surface of the cylinder $\psi = 0$ is

prescribed. For all the simulations carried out in this section we take $\delta t = 0.001$ and use the grid 181×301.

6.2.1 Case 1: Constant rotation

As pointed out by Badr *et al.* [18] the flow field in this case depends on three main parameters *viz.* Re, velocity ratio and time. We define Re and non-dimensional time as in section 4.2 of Chapter 4. The velocity ratio is defined as $\alpha = \frac{aq}{U_\infty}$, where q is the angular velocity of the cylinder about its axis. We consider four different flow fields for $Re = 1000$ with $\alpha = 0.5,\ 1.0,\ 2.0,$ and 3.0. As mentioned in [18], the flow fields corresponding to higher velocity ratios have distinctly different characters compared to the lower ones. The evolution of drag and lift coefficients for all the cases are shown in figure 6.1(a) and 6.1(b) respectively. From the

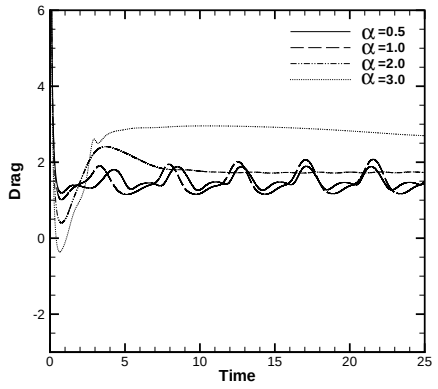

(a)

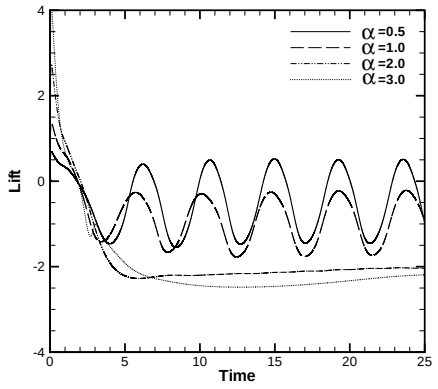

(b)

Figure 6.1: *Evolution of (a) Drag coefficient, (b) Lift coefficient for* $Re = 1000$ *with* $\alpha = 0.5,\ 1.0,\ 2.0,\ 3.0$.

figure it is clear that for $\alpha = 1.0$ and 2.0, both drag and lift assume a periodic

nature implying periodic state of flow. This is inconformity with the earlier studies reported in literature [18, 34, 102, 114]. This is also amply demonstrated in the phase portrait of drag and lift coefficients as shown in figure 6.2. For $\alpha = 2.0$ and 3.0, the coefficients seems to march towards a steady state. Since our main intention is to demonstrate the capability of the scheme we leave the study of long time behavior of these flow fields as a future endeavor.

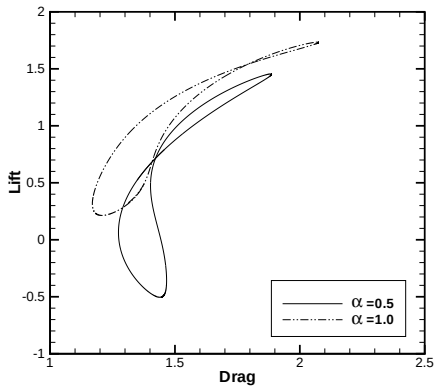

Figure 6.2: *Phase portrait for* $Re = 1000$, $\alpha = 0.5$ *and* 1.0.

To provide a qualitative comparison between our computed and the experimental results of [18], as the development of vortices take place we plot the path of the first vortex centre for $Re = 1000$ with $\alpha = 0.5, 1.0, 2.0$ in figure 6.3. A very good comparison can be seen.

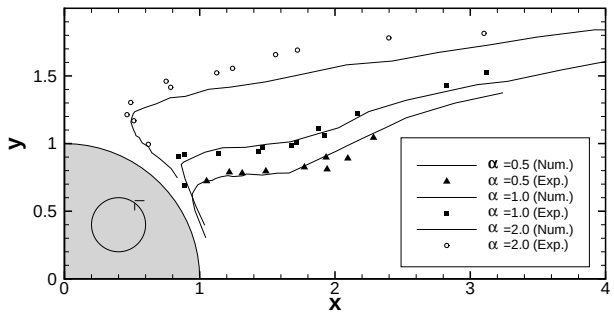

Figure 6.3: *Comparison between the paths of the first vortex obtained numerically by our computation and experimentally [18].*

We continue to validate the present numerical results and compare the present results on initial velocity profiles for $\alpha = 0.5$ with the experimental results [18] in

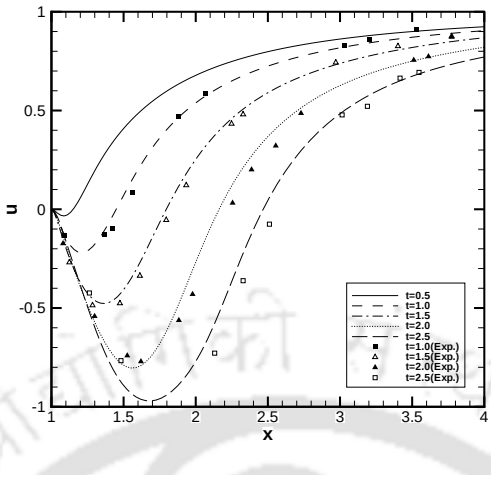

(a)

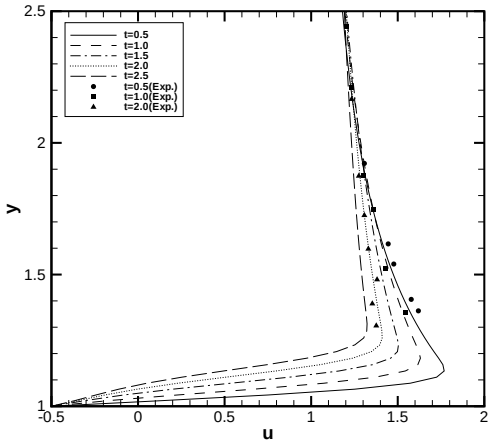

(b)

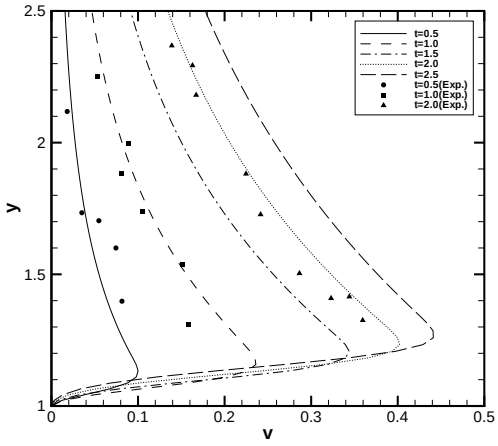

(c)

Figure 6.4: *Comparison of velocity profiles for* $Re = 1000$, $\alpha = 0.5$ *(a)* u *versus* x *along horizontal axis, (b)* u *versus* y *along vertical axis, (c)* v *versus* y *along vertical axis.*

figure 6.4. The comparison has been done after converting the time to the present definition. Note that in reference [18] the authors non-dimensionalise the time variable by using radius a of the cylinder but in our computation we use $D = 2a$ for the same. The streamline profiles at different instants of times along with one experimental visualizations of [18] have been shown in figure 6.5(i). Here soon after the impulsive start, the first vortex starts to form above the x-axis, growing in size. Shortly a secondary vortex also develops just below the x-axis as can be seen. It is also seen that with time these vortices acquire strength and reach a maximum size. During this process one can also observe development of tertiary vortices adjacent to the cylinder surface. Our computed solution exactly captures all these developments as evident from 6.5(i). For $\alpha = 1.0$ vortex development is almost similar but at time around $t = 2.0$ vortices start to open up and move upwards the downstream seen in figure 6.5(ii). Here again, one finds an excellent match between the computed and experimental streamlines.

The time development of vortices for $\alpha = 0.5$ as it lead to periodic state can be seen in figure 6.6. In this figure we present the stream lines side by side the vorticity contours. Regular vortex shedding have been captured with the development growth and subsequent detachment of vortices on the cylinder surface. The vorices thus shed have the tendency to move upwards due to the anticlockwise motion of the cylinder surface.

For $\alpha = 2.0$, in figure 6.7 we compare our computed solutions with the flow visualization reported in Badr *et al.* [18]. Good comparison can be seen between the computational results. However at higher times ($t = 6.5$) some disagreement between the two computational works can be noticed in the vicinity of the cylinder. Our numerical simulation captures two counter rotating vortices on the cylinder surface as seen in the experimental visualization. The same can not be said about the computational work of Badr *et al.* [18]. Our simulation also captures the down stream movement of the vortex far from the cylinder.

In figure 6.8 we compare our results with the numerical results obtained by Mittal and Kumar [102] who used stabilized finite element method and with the experimental results of Badr *et al.* [18]. Again close comparison with both the results can be found. As can be seen from the figures, our scheme has exactly captured the appearance and subsequent development of two vortices on the surface of the cylinder at time $t = 1.5$ and $t = 2.0$. Note that in the computational result of Mittal and Kumar [102] the vortex on the windward side of the cylinder appears to be located at a higher angle to the free-stream direction as compared

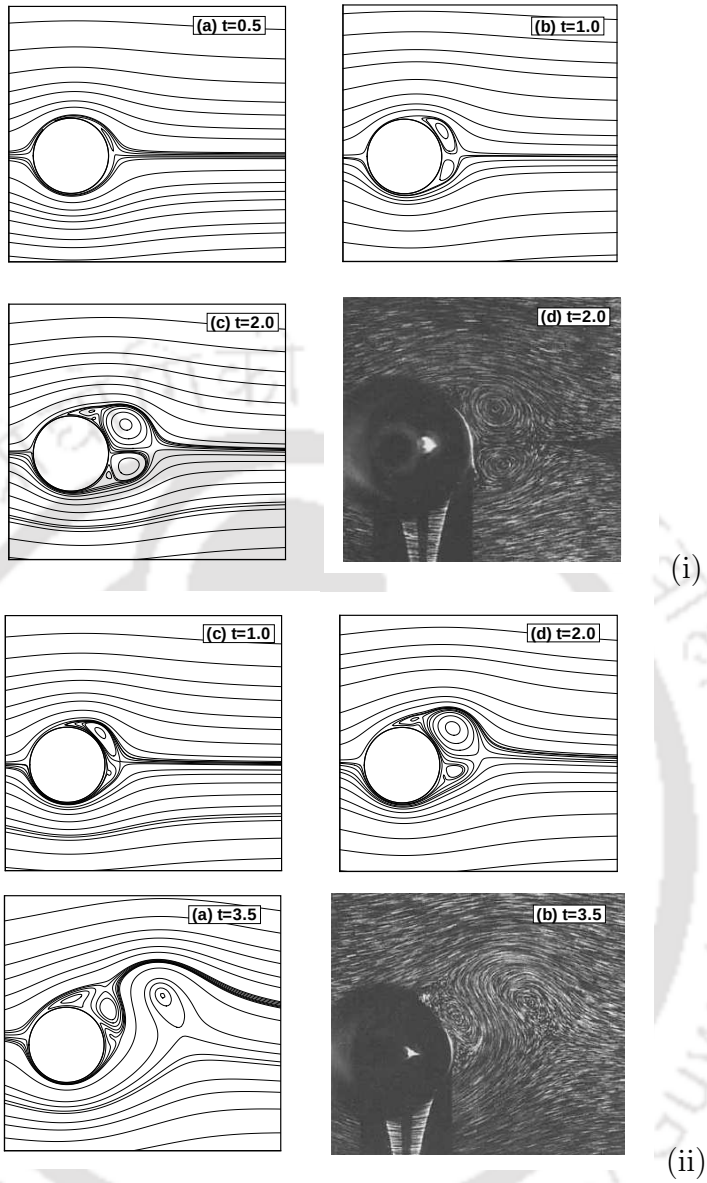

Figure 6.5: *Computed and experimental [18] stream lines at different times for* $Re = 1000$ *(i)* $\alpha = 0.5$, *(ii)* $\alpha = 1.0$.

to the flow visualization. Mittal and Kumer [102] have attributed this to the three dimensionality of flow. But when compared to our numerical result one can see a better resemblance. The subsequent downstream motion of the vortex generated have also been captured quite accurately by our computation.

The time development of the flow field for $\alpha = 3.0$ is presented in figure 6.9. In contrast to the flow for $\alpha = 0.5$ presented in figure 6.6 no generation of vortices subsequent to the first vortex as captured in figure 6.8 can be seen here. The

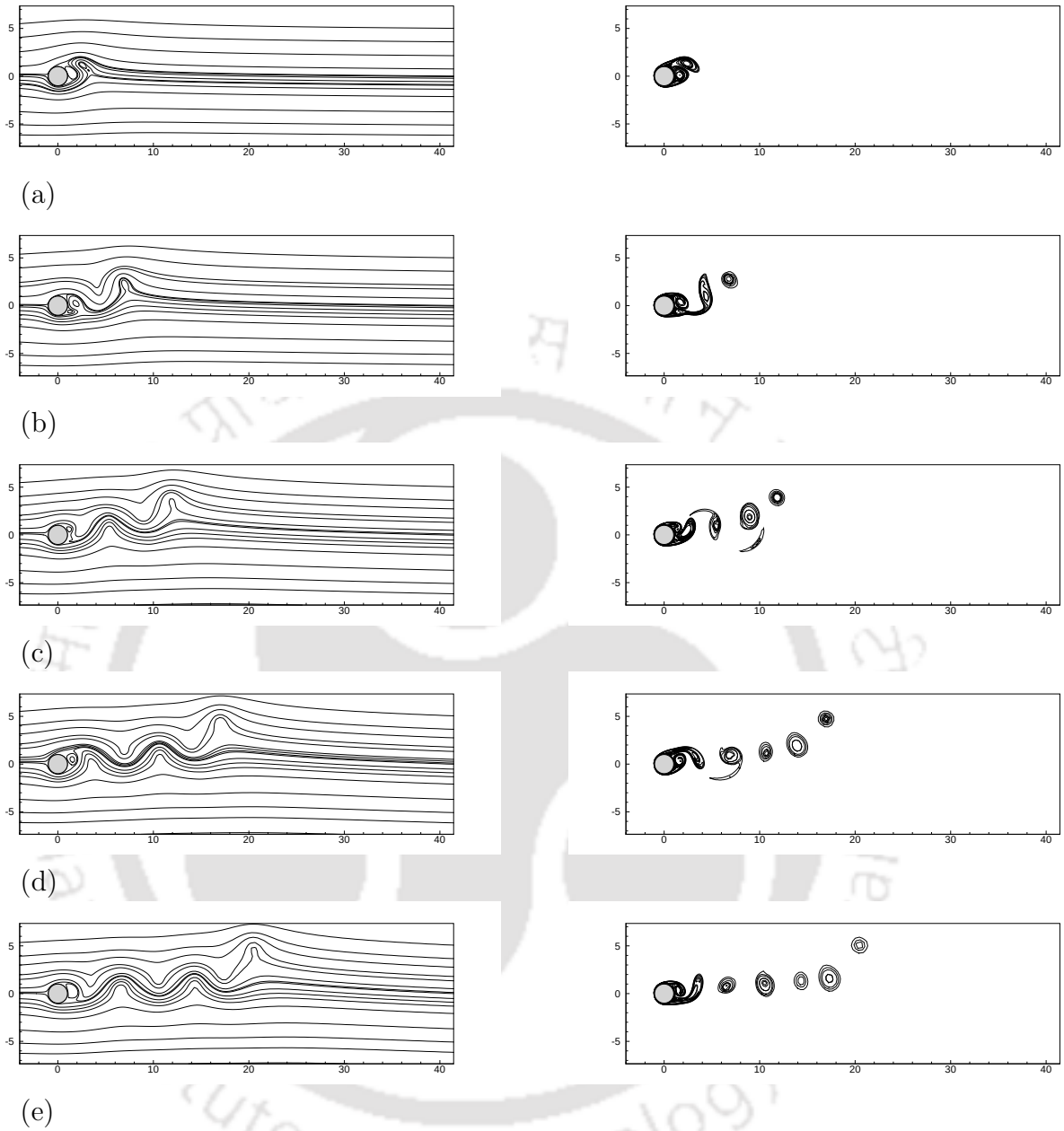

Figure 6.6: *Time evolution of stream lines (left) and vorticity contours (right) for* $Re = 1000$, $\alpha = 0.5$ *at time (a)* $t = 4.0$, *(b)* $t = 7.0$, *(c)* $t = 10.0$, *(d)* $t = 13.0$, *(e)* $t = 15.0$.

vortex is convected downstream of the flow. This explains the near constancy of drag and lift coefficients as reported earlier (figure 6.1).

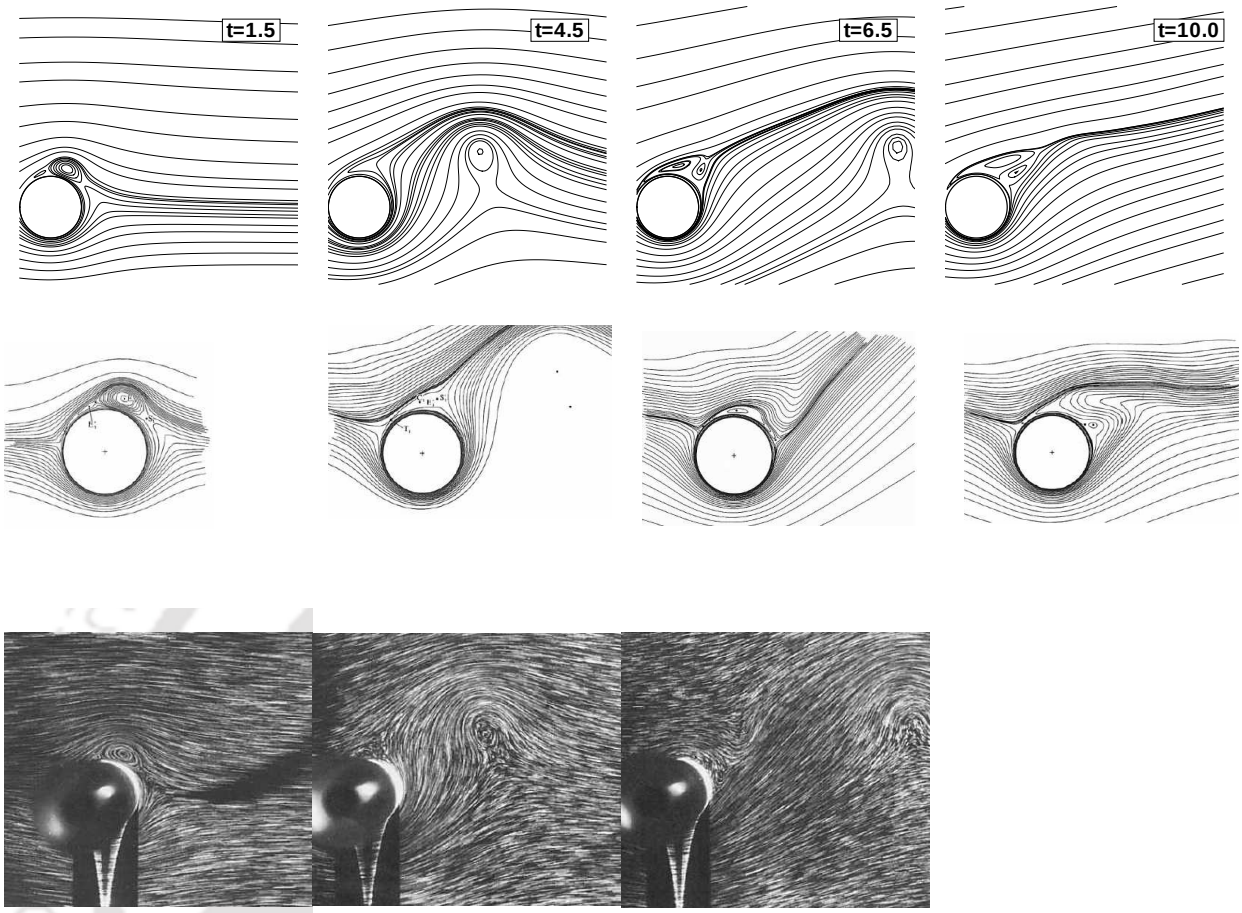

Figure 6.7: *Comparison of the instantaneous streamline patterns at various time instants from the present computations (top), computation of Badr* et al. *[18] (middle) and experimental result of Badr* et al. *[18] (bottom) for* $Re = 1000$, $\alpha = 2$.

6.2.2 Case 2: Oscillatory rotation

The angular velocity $q = \dot{\theta}$ of the cylinder about its axis in this case is characterized by two non-dimensional parameters: (i) forcing amplitude (A) and (ii) frequency ratio (f_f/f_0) [146] where $\theta(t) = \theta_0 \cos(2\pi f_f t)$. Here f_f is called the forcing frequency, f_0 is the shedding frequency of the stationary cylinder corresponding to the same value of Re and $A = \dfrac{a(2\pi f_f \theta_0)}{U_\infty}$. Note that some authors prefer to use Strouhal ratio (St_f/St_0) as the control parameter [121] instead of the forcing ratio (f_f/f_0). For oscillatory rotation we consider four different cases of frequency ratio $f_f/f_0 = 0.8,\ 1.0,\ 1.5,\ 3.0$ while keeping the values of Re and A fixed at 150 and 2 respectively. The time variation of drag coefficients for all the four cases leading

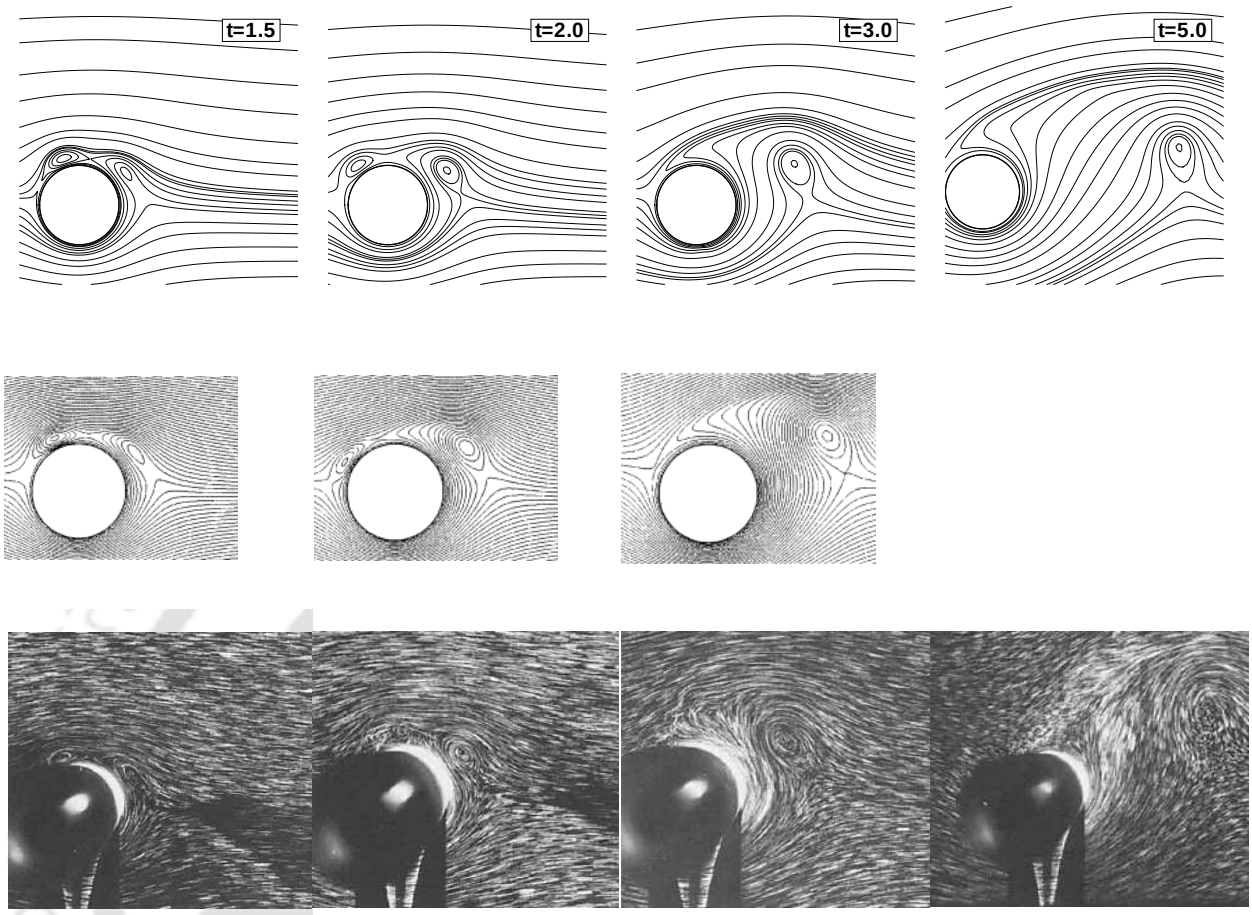

Figure 6.8: *Comparison of the instantaneous streamline patterns at various time instants from the present computations (top), computation of Mittal and Kumar [102] (middle) and experimental result of Badr* et al. *[18] (bottom) for* $Re = 1000$, $\alpha = 3$.

Table 6.1: *Quantitative comparison of the normalized drag coefficient.*

Cases	Experimental C_D/C_{D_0}, [146]	Numerical C_D/C_{D_0}, [127]	Numerical C_D/C_{D_0}, Present
$A = 2,\ f_f/f_0 = 0.8$	2.408	–	2.338
$A = 2,\ f_f/f_0 = 1.0$	1.735	–	1.601
$A = 2,\ f_f/f_0 = 1.5$	1.155	1.245	1.077
$A = 2,\ f_f/f_0 = 3.0$	0.869	0.855	0.846

to the periodic state is presented in figure 6.10. As expected a higher forcing ratio leads to a higher frequency of shedding as can be seen from the figure. We carry out a quantitative comparison of the drag coefficients for the cases considered here

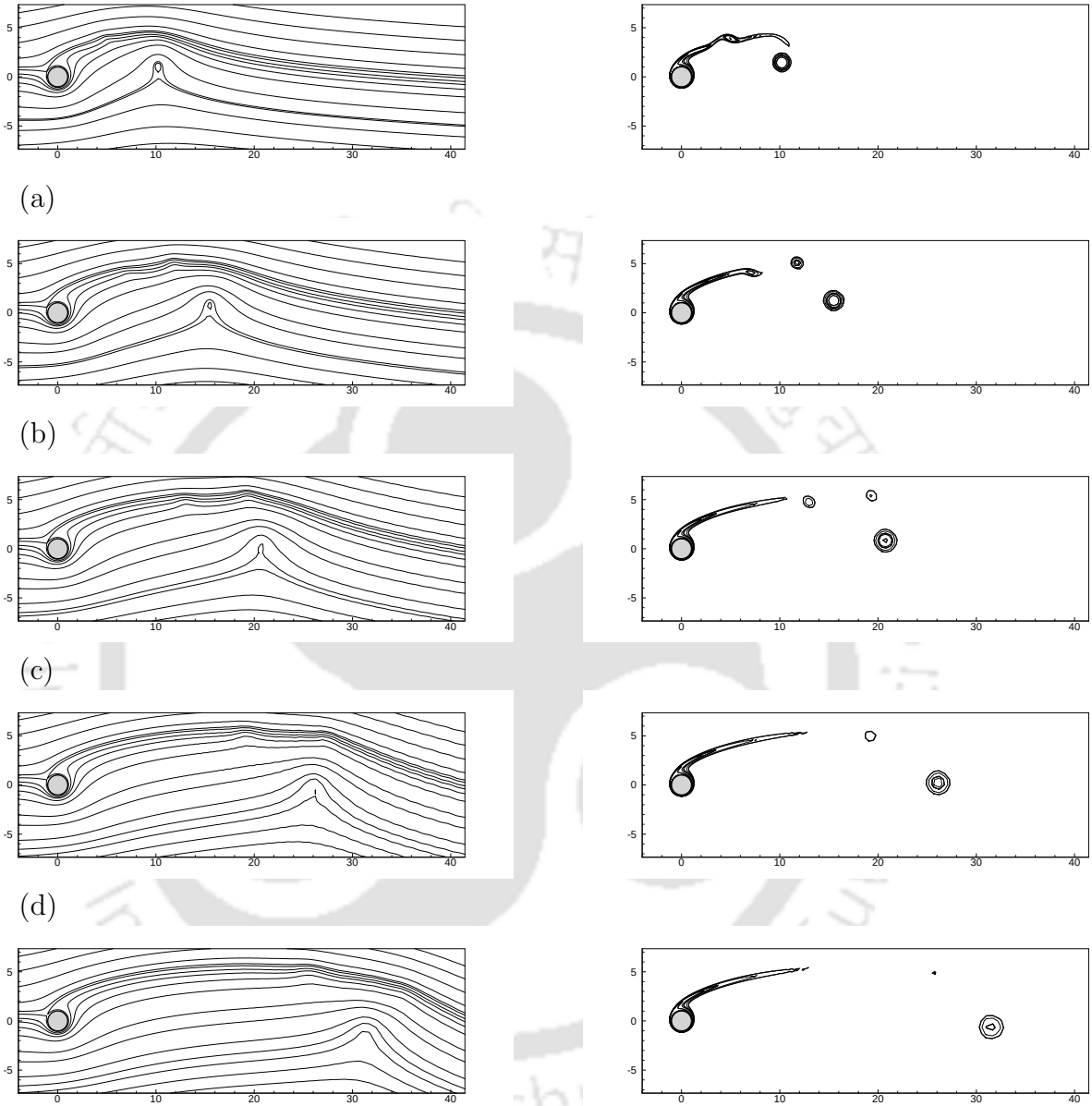

Figure 6.9: *Time evolution of stream lines (left) and vorticity contours (right) for* $Re = 1000$, $\alpha = 3.0$ *at time (a)* $t = 8.0$, *(b)* $t = 11.0$, *(c)* $t = 14.0$, *(d)* $t = 17.0$, *(e)* $t = 20.0$.

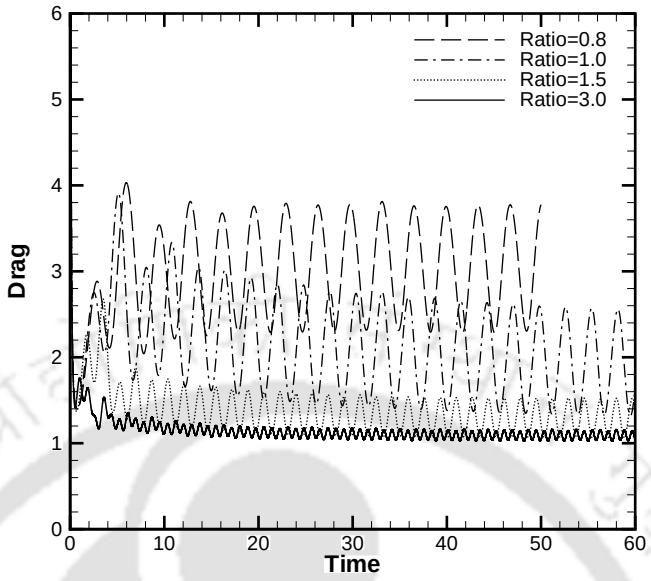

Figure 6.10: *Evolution of drag coefficients for* $Re = 150$, $A = 2$ *with different* f_f/f_0 *ratio.*

in table 6.1 with the experimental works of Thiria *et al.* [146] and numerical works of Sengupta and Bhumkar [127]. We have normalized the mean drag coefficient C_D of a particular rotary oscillation case by the mean drag coefficient C_{D_0} of a stationary cylinder at same Re. A strong agreement of the data can be seen here. Further, in figure 6.11, we present a qualitative comparison of computed vorticity contours for the case $Re = 150$, $A = 2$ and $f_f/f_0 = 1.0$ with the numerical works of Protas and Wesfreid [121] and experimental visualization of Thiria *et al.* [146]. A very close resemblance between the two numerical works can be seen. In the same vein another qualitative comparison in figure 6.12 of computed vorticity contours for the case $Re = 150$, $A = 2$ and $f_f/f_0 = 1.5$ with numerical results [127] and experimental results [146] clearly establishes the accuracy of the numerical results obtained by us. One can see that the second order accurate scheme developed by us is capable of capturing the details of the flow field and is comparable to the results obtained by the sixth order scheme of Sengupta and Bhumkar [127]. The computed streamlines and the post processed vorticity contours at time $t = 40.0$ for all the four cases are depicted in figure 6.13. Our computed (post processed) vorticity contours are in line with the detailed analysis carried out by Protas and Wesfreid [121].

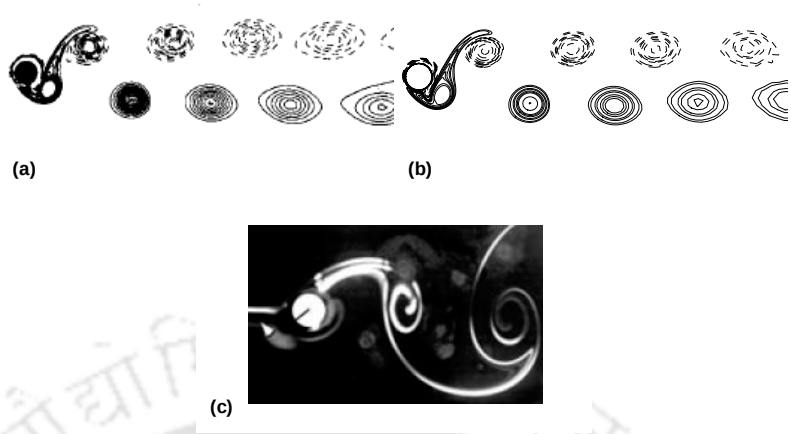

Figure 6.11: *Numerical vorticity contours obtain by (a) Protas and Wesfreid [121] is compared with numerical result obtained by (b) the present scheme and (c) the experimental results [146] for* $Re = 150$, $A = 2$, $f_f/f_0 = 1.0$.

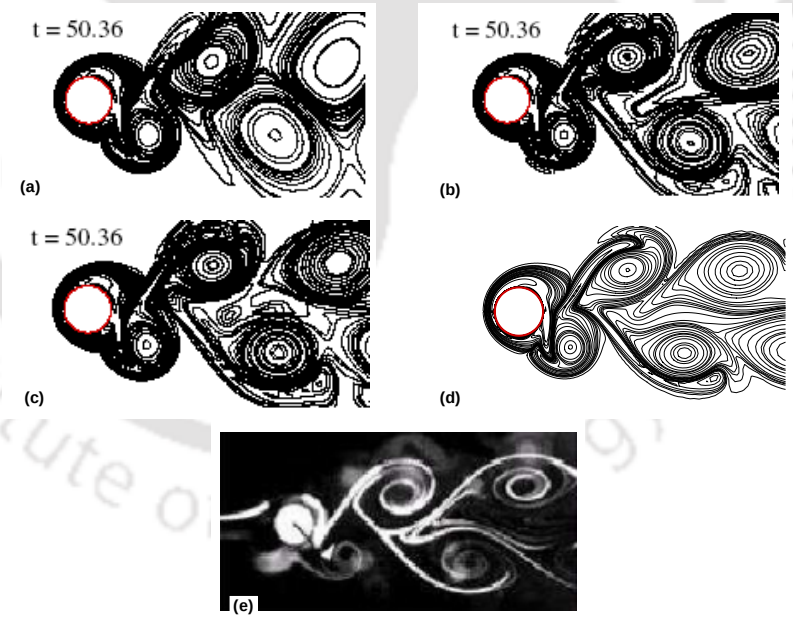

Figure 6.12: *Numerical vorticity contours obtain by Sengupta and Bhumkar [127] with different numerical schemes (a) 2nd order, (b) 4th order, (c) 6th order are compared with numerical results obtain by (d) the present scheme and (e) the experimental results [146] for* $Re = 150$, $A = 2$, $f_f/f_0 = 1.5$.

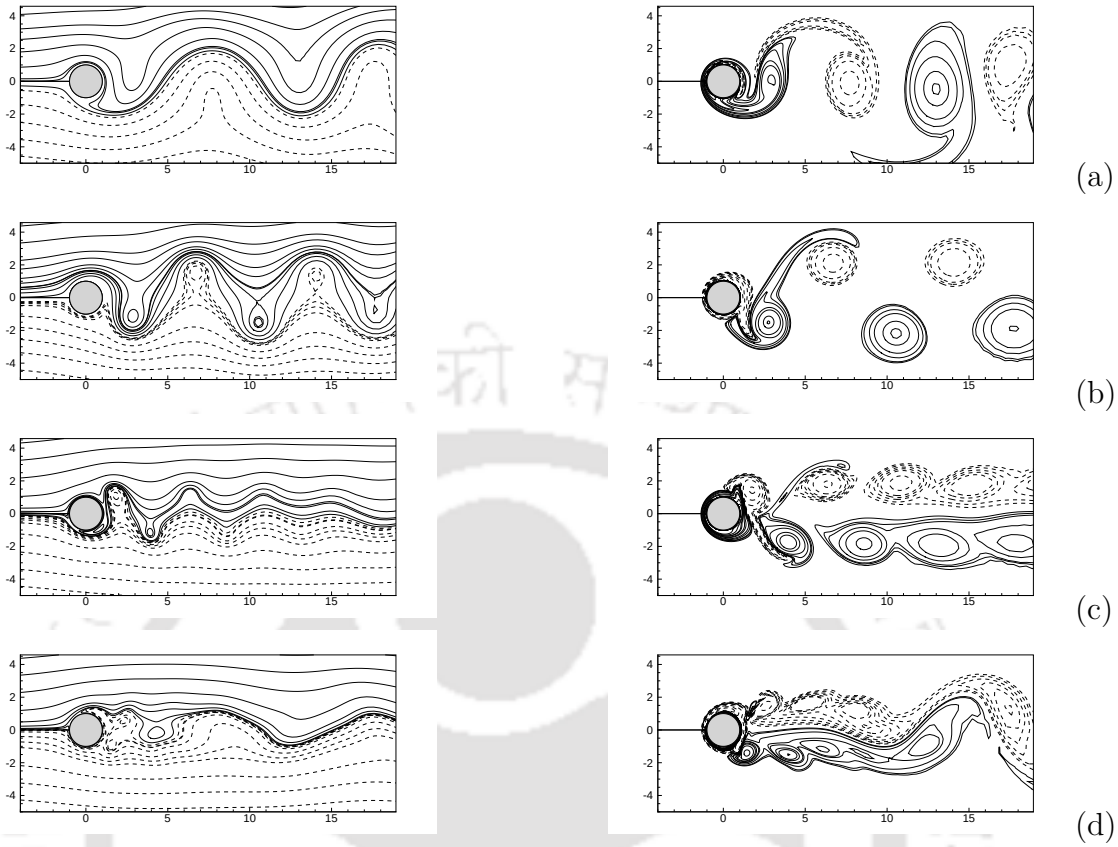

Figure 6.13: *Stream lines (left) and vorticity contours (right) (the dotted lines representing negative values of the contours) at* $Re = 150$, $A = 2$ *with (a)* $f_f/f_0 = 0.75$, *(b)* $f_f/f_0 = 1.0$, *(c)* $f_f/f_0 = 1.5$, *(d)* $f_f/f_0 = 3.0$.

6.3 In-line oscillating cylinder in a fluid at rest

6.3.1 Mathematical formulation and boundary conditions

The N-S equations in 2D for non-inertial or body fitted coordinate system that moves with a non-dimensional translational velocity $\widetilde{\boldsymbol{V}}(t) = (\widetilde{u}(t), \widetilde{v}(t))$ is given by

$$\frac{\partial}{\partial t}\bar{\boldsymbol{V}} + (\bar{\boldsymbol{V}}.\boldsymbol{\nabla})\bar{\boldsymbol{V}} = -\boldsymbol{\nabla}p + \frac{1}{Re}\nabla^2\bar{\boldsymbol{V}} - \dot{\widetilde{\boldsymbol{V}}}(t) \tag{6.1}$$

$$\boldsymbol{\nabla}.\bar{\boldsymbol{V}} = 0 \tag{6.2}$$

where otherwise the symbols $\widetilde{\boldsymbol{V}}$ have the same meaning as that given in Appendix A for $\boldsymbol{V}$. The bar over the flow variables signify their correspondence to the non-inertial frame. The corresponding stream function-vorticity formulation obtained

from equations (6.1) and (6.2) is

$$\bar{\psi}_{\bar{x}\bar{x}} + \bar{\psi}_{\bar{y}\bar{y}} = -\bar{\omega} \tag{6.3}$$

$$\frac{\partial}{\partial t}\bar{\omega} = \frac{1}{Re}\left(\bar{\omega}_{\bar{x}\bar{x}} + \bar{\omega}_{\bar{y}\bar{y}}\right) - \left(\bar{u}\bar{\omega}_{\bar{x}} + \bar{v}\bar{\omega}_{\bar{y}}\right) \tag{6.4}$$

Here stream function $\bar{\psi}$ and vorticity $\bar{\omega}$ are related to the velocities through $\bar{u} = \bar{\psi}_{\bar{y}}$, $\bar{v} = -\bar{\psi}_{\bar{x}}$, $\bar{\omega} = \bar{v}_{\bar{x}} - \bar{u}_{\bar{y}}$. The equations (6.3) and (6.4) being identical to equations (A.6) and (A.7) of Appendix A, the resulting biharmonic equation is also identical. Writing ψ for $\bar{\psi}$ to designate stream function in non-inertial frame we arrive at the biharmonic form (A.17) obtained in Appendix A.

In the present study the translational motion of the cylinder is prescribed by a simple harmonic oscillation

$$x(t) = -A_0\cos(2\pi ft) \Rightarrow \widetilde{u}(t) = 2\pi A_0 f\sin(2\pi ft), \quad y(t) = \text{constant} \Rightarrow \widetilde{v}(t) = 0,$$

where A_0 is the amplitude of the cylinder motion and f is the characteristic frequency of the oscillation. For the problem considered here, distances and velocities have been non-dimensionalized with respect to the diameter D and U_{max} respectively, where U_{max} is the maximum velocity of the cylinder motion. The two controlling parameters for this flow are the Reynolds number $Re = \dfrac{U_{max}D}{\nu}$ and the Keulegan-Carpenter number $KC = \dfrac{U_{max}}{fD}$, ν being the kinematic viscosity. For this problem we consider a cylinder with diameter $D = 1$.

We simulate the flow in a non-inertial frame attached to the cylinder without changing the position of the artificial far-stream boundaries [27, 8]. The relevant boundary conditions in non-inertial frame are as given below:

1. At the free-stream the time dependent velocity and stream function conditions are $(u(t), v(t)) = (-U_{max}\sin(2\pi ft), 0)$ and $\psi = u(t)y$ respectively.

2. On the surface of the cylinder $(u(t), v(t)) = (0, 0)$ and also $\psi = 0$.

The initial value of ψ has been set as zero. In the present work we have considered two different combination of Re and KC, they are $Re = 100$, $KC = 5$ and $Re = 210$, $KC = 6$. We compute using $\delta t = 0.002$ and grid 145×241.

6.3.2 Numerical results

Figure 6.14 shows the computed velocity profiles (using lines) in the oscillation direction and transverse direction at four different x locations *viz.* $x = -0.6D$,

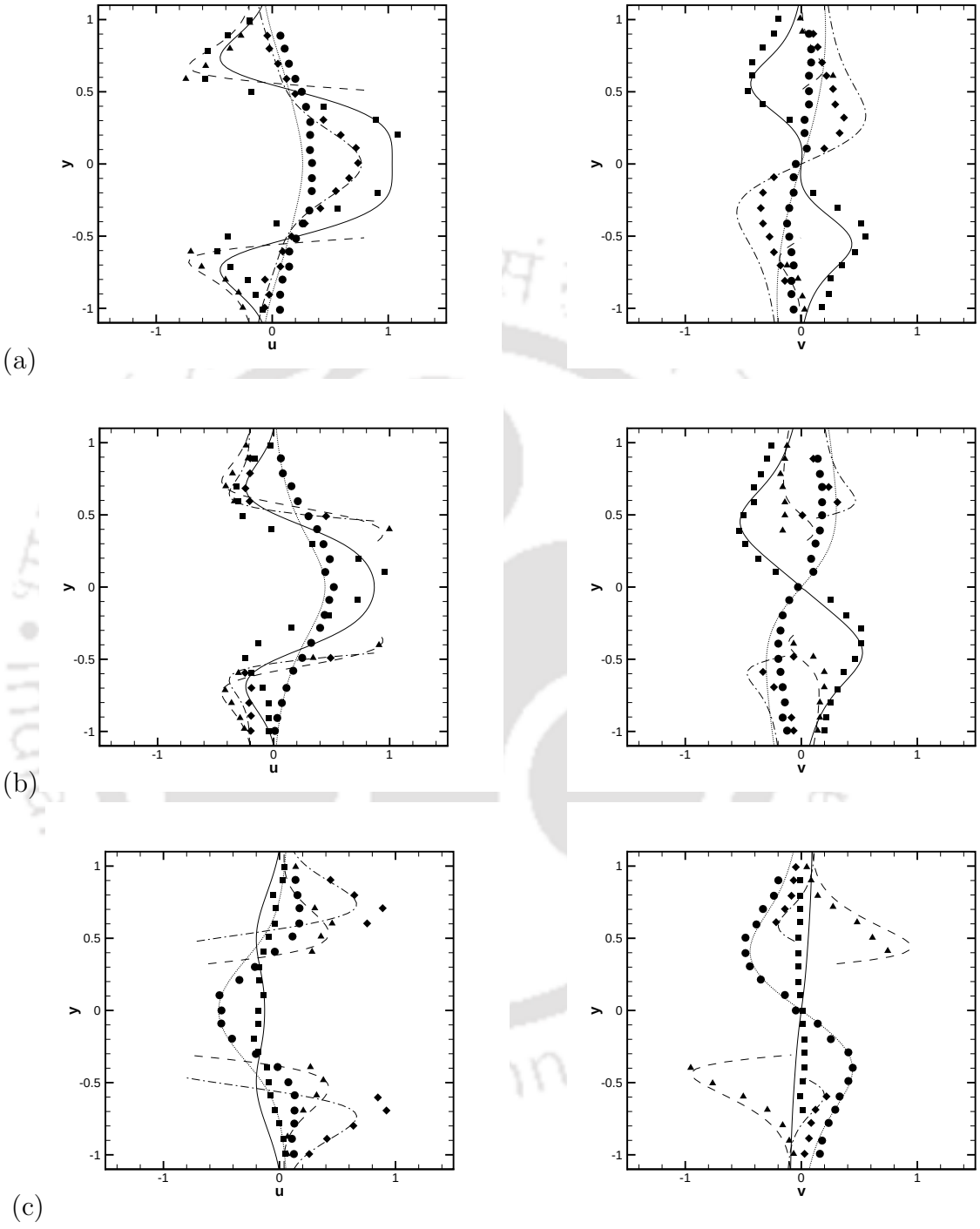

Figure 6.14: *Comparison of the velocity components with experimental results [45] at four cross-sections with* $x = -0.6D(-,\blacksquare)$, $0D(--,\blacktriangle)$, $0.6D(-\cdot-,\blacklozenge)$, $1.2D(\ldots,\bullet)$ *for phase angle (a)* 90^0, *(b)* 120^0, *(c)* 240^0.

Figure 6.15: *Stream lines (left) and vorticity contours (right) (the dotted lines representing negative values of the contours) at* $Re = 100$, $KC = 5$ *for phase angle (a)* 6^0, *(b)* 102^0, *(c)* 198^0, *(d)* 270^0.

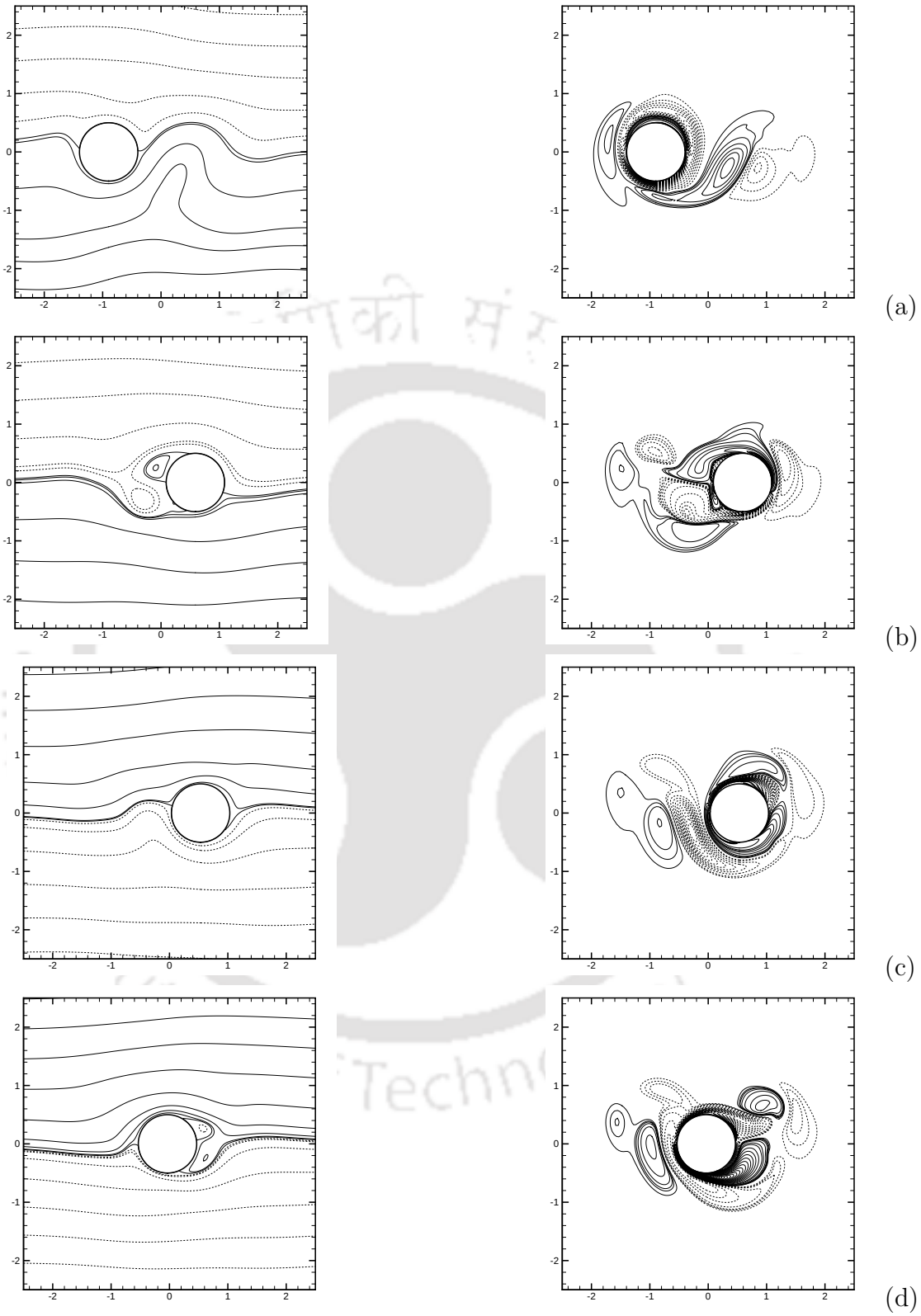

Figure 6.16: *Stream lines (left) and vorticity contours (right) (the dotted lines representing negative values of the contours) at* $Re = 210$, $KC = 6$ *for phase angle (a)* 20^0, *(b)* 128^0, *(c)* 236^0, *(d)* 272^0.

$0D$, $0.6D$ and $1.2D$ each computed at three different phase angles $2\pi ft = 90^0$, 120^0 and 240^0. This is compared with the experimental results of Dütsch et al. [45]. Note that there is a phase difference of 90^0 between our phase angle and that of [45] because of the different expressions of $x(t)$ considered. A good match with the experimental work can be seen.

In figure 6.15 we present computed stream function and vorticity contours for the phase angles 6^0, 102^0, 198^0 and 270^0 for $Re = 100$, $KC = 5$, and phase angles 20^0, 128^0, 236^0 and 272^0 for $Re = 210$, $KC = 6$ in figure 6.16. In all these figures, one can clearly see the formation of vortices in alternate directions as the cylinder oscillates from left to right and vice versa. The parameters chosen corresponds to the work of Dütsch et al. [45] and our results match very well with theirs. Note that the two combinations of parameters considered here represent fundamentally different flow structures. Corresponding to parameter combination $Re = 100$, $KC = 5$ the flow is characterized by stable, symmetric and periodic vortex shedding and we capture it quite effectively in figure 6.15. For $Re = 210$, $KC = 6$ vortices generated in each half of the cylinder period are known to convect to the same side of the plane of oscillation resulting in a V-type vortex street and this has been effectively captured in figure 6.16.

6.4 Conclusion

In this chapter we expand the scope of the fourth order biharmonic pure stream function formulation to problems with moving boundaries. In the process we also extend it to the problems requiring the use of non-inertial frame besides the traditional inertial frame. Three different flow configurations have been tested. Simulated results have been compared both qualitatively and quantitatively with the available benchmark numerical and experimental results and were found to be quite satisfactory. This provides a strong evidence of the capability and reliability of this newly proposed method.

Chapter 7

Flow Past Bluff Bodies with Varying Curvatures

7.1 Introduction

One of the most important topics in CFD is the simulation of unsteady incompressible flow in complex geometric settings using curvilinear coordinate system. Many studies have accomplished this for the flow past circular cylinder mainly because of its geometric simplicity. It would be worth studying other bluff bodies such as elliptic cylinders and aerofoils since engineering applications often involve flows over complex objects such as wings, blades, missiles *etc.* For such flows, thickness and angle of attack greatly influence the nature of separation and structure of wake. Moreover elliptic cylinders can be considered as a limiting case of a circular cylinder and flat plate. The purpose of this chapter is to investigate the performance of the scheme developed in Chapter 3 for simulating flows around bluff bodies with very high curvatures[1]. We are mainly interested in studying the unsteady flow past an elliptic cylinder and symmetric aerofoils. As identified by Nair and Sengupta [105], at high angles of attack the flow around elliptic and other aerofoils corresponding to moderately high Reynolds number is characterized by four main flow phenomena. These are (a) the instability of unsteady flow, (b) formation of bubble over the aerofoils, (c) interaction of vortices in the wake and (d) formation of alleyway because of which flow accelerates over the lower surface of the aerofoil and wraps around the vortices over the top surface of the aerofoil. Besides demonstrating these physically interesting phenomena, flows around aerofoils act as suitable test cases for establishing the robustness of numerical schemes.

[1]Part of this work is under review in *Comp. Fluids*

7.2 Flow past an elliptic cylinder with angle of attack

In this section, we are interested in conducting a series of simulations for the unsteady viscous flow over an inclined elliptic cylinder placed in a uniform stream. The last century has seen some outstanding experimental and numerical works [37, 64, 95, 105, 112, 118, 144] on this problem which continues to excite researchers in this century as well [16, 43, 119]. Early experimental studies on the uniform flow over inclined elliptic cylinders were carried out by Honji [64] and Taneda [144]. While Honji [64] observed the starting flow around an elliptic cylinder at 45^0 and 54^0 angles of incidence; Taneda [144] made a comprehensive visualization study of the same. The unsteady motions investigated by Taneda [144] include the impulsive start from rest, change of velocity, translatory oscillation, change of the angle of incidence, uniform rotation, rotatory oscillation and swimming motion. Among the pioneering numerical works on flow past elliptic cylinder the work of Lugt and Haussling [95] deserves special mention. In this work the authors have numerically time marched to steady state for $Re = 15$ and 30 at an angle of incidence 45^0 with aspect ratio 0.1. They have also captured the development of von Kármán vortex street for $Re = 200$ with different aspect ratios with angle of incidence fixed at 45^0. The numerical solutions to the uniform flow over an inclined elliptic cylinder were determined for moderate and large values of the time by Patel [118] and later by Nair and Sengupta [105]. Patel [118] considered the cases of $Re = 60$, 100, and 200 at various angles of incidence. Nair and Sengupta [105] in their work provided results for $Re = 3000$ and 10000 using a finite difference method with third and fifth order upwinding for the convection terms. Ohmi *et al.* [112] in 1990 investigated experimentally and numerically starting flows past an oscillating and translating elliptic aerofoil with aspect ratio 0.1 for Re ranging between 1500 and 10000 upto angle of incidence 45^0. Chou and Huang [37] used a semi-explicit finite difference scheme and reported α- and β- phenomena at an early stage of flow evolution for high Re flows. They also reported early and long time flow structures for $Re = 1000$ with aspect ratio 0.1 at different angles of incidence. In 2003 Dennis and Young [43] made a detailed and accurate study of steady 2D flow past an elliptic cylinder inclined to the oncoming stream at various angles for small to moderate values of Re. In recent works [16, 119] the authors have used the accurate solution of the problem of flow past elliptic cylinder to demonstrate the efficiency of their numerical procedures. In our work we consider

seven different combinations of Reynolds number, angle of attack and aspect ratio to simulate flows in various regimes. We also compare our results with the other results available in literature to demonstrate the versatility of our scheme.

7.2.1 Grid generation and numerical issues

Following Dennis and Young [43], we consider the elliptic transformation

$$x = \frac{\cosh\xi\cos(\eta+\Theta)}{2\cosh\xi_0}, \quad y = \frac{\sinh\xi\sin(\eta+\Theta)}{2\cosh\xi_0}$$

where Θ, called the angle of attack, is the angle made by the uniform free stream with the positive direction of x- axis and $\xi_0 = \tanh^{-1}(\Gamma)$, Γ being the ratio of minor and major axes of the cylinder, called the aspect ratio. Note that $\xi = \xi_0$ defines the surface of the cylinder with chord length (major axis) $c = 1$. The Reynolds number for the flow is defined as $Re = \frac{U_\infty c}{\nu}$, where U_∞ is the free stream velocity and ν is the kinematic viscosity. Apart from Re, the other parameters controlling the flow are Γ and Θ. For the flow past elliptic cylinder we consider free stream to be at a distance $R_\infty \approx 20c$ and $U_\infty = 1$ and compute using a grid of size 196×301. This typical grid of size 196×301 around an elliptic cylinder having aspect ratio $\Gamma = 0.2$ and angle of attack 45^0 is shown in figure 7.1. The boundary and initial conditions are derived from the philosophy discussed in section 4.3 for the flow past a stationary cylinder. The drag coefficient (C_D) and lift coefficient (C_L) are calculated by integration round the cylinder surface as given in [43]. For the sake of completeness we reproduce them here.

Considering C_{DP} and C_{DF} to be the pressure and friction components of drag respectively we have

$$C_D = C_{DP} + C_{DF}. \tag{7.1}$$

For the elliptic transformation considered above

$$C_{DP} = \frac{\cos\Theta\ \sinh\xi_0}{Re}\int_0^{2\pi}\left(\frac{\partial\omega}{\partial\xi}\right)_0\sin(\eta+\Theta)\mathrm{d}\eta - \frac{\sin\Theta\ \cosh\xi_0}{Re}\int_0^{2\pi}\left(\frac{\partial\omega}{\partial\xi}\right)_0\cos(\eta+\Theta)\mathrm{d}\eta,$$

$$C_{DF} = -\frac{\cos\Theta\ \cosh\xi_0}{Re}\int_0^{2\pi}\omega_0\sin(\eta+\Theta)\mathrm{d}\eta + \frac{\sin\Theta\ \sinh\xi_0}{Re}\int_0^{2\pi}\omega_0\cos(\eta+\Theta)\mathrm{d}\eta.$$

Similarly for the lift coefficient

$$C_L = C_{LP} + C_{LF} \tag{7.2}$$

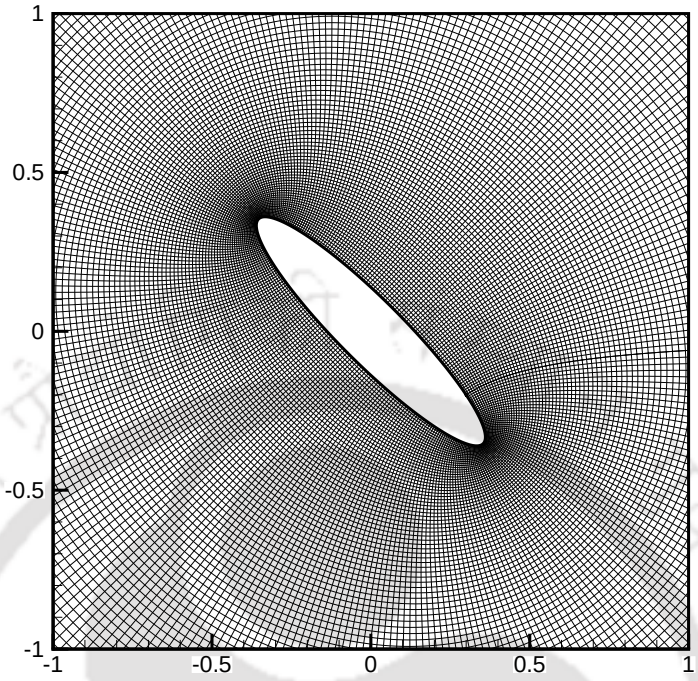

Figure 7.1: *Typical* 196×301 *grids around an elliptic cylinder having aspect ratio* 0.2 *and angle of attack* 45^0.

with

$$C_{LP} = -\frac{\cos\Theta\ \cosh\xi_0}{Re}\int_0^{2\pi}\left(\frac{\partial\omega}{\partial\xi}\right)_0\cos(\eta+\Theta)\mathrm{d}\eta - \frac{\sin\Theta\ \sinh\xi_0}{Re}\int_0^{2\pi}\left(\frac{\partial\omega}{\partial\xi}\right)_0\sin(\eta+\Theta)\mathrm{d}\eta,$$

$$C_{LF} = \frac{\cos\Theta\ \sinh\xi_0}{Re}\int_0^{2\pi}\omega_0\cos(\eta+\Theta)\mathrm{d}\eta + \frac{\sin\Theta\ \cosh\xi_0}{Re}\int_0^{2\pi}\omega_0\sin(\eta+\Theta)\mathrm{d}\eta.$$

7.2.2 Numerical results

We start our computation with $Re = 15$ and 30 at $\Theta = 45^0$, $\Gamma = 0.1$ and time march to steady state [43, 95] using $\delta t = 0.001$. We plot the evolution of drag and lift coefficients in figure 7.2(a) and compare C_D and C_L values obtained with the present scheme with those obtained by Lugt and Haussling [95] (by scaling the values using the present definitions), and Dennis and Young [43] in table 7.1. The streamlines at steady state corresponding to both the above flow configurations (figure 7.3 and figure 7.4) match extremely well with the published results.

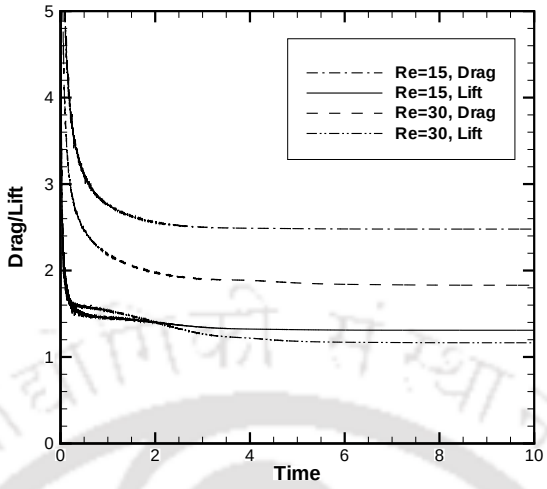

(a)

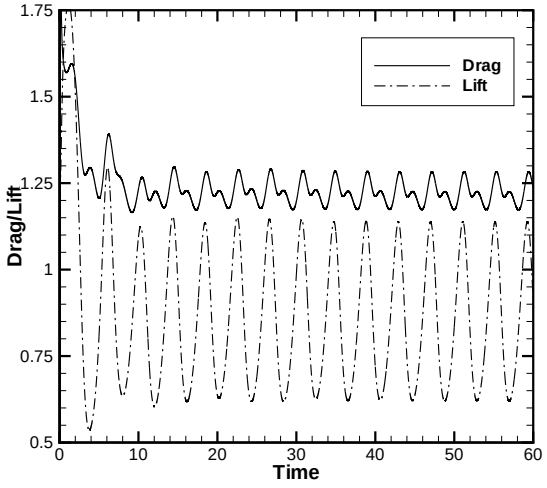

(b)

Figure 7.2: *Evolution of drag and lift coefficients for (a)* $Re = 15$ *and* $Re = 30$ *with* $\Gamma = 0.1$, $\Theta = 45^0$*; (b)* $Re = 163$ *with* $\Gamma = 0.2$, $\Theta = 45^0$.

Table 7.1: *Comparison of steady state drag and lift coefficients for* $Re = 15$ *and* $Re = 30$ *with* $\Theta = 45^0$, $\Gamma = 0.1$.

Re		Ref.[95]	Ref.[43]	Present
15	C_D	2.135	1.865	2.479
	C_L	1.310	1.050	1.309
30	C_D	1.430	1.402	1.829
	C_L	0.935	0.930	1.164

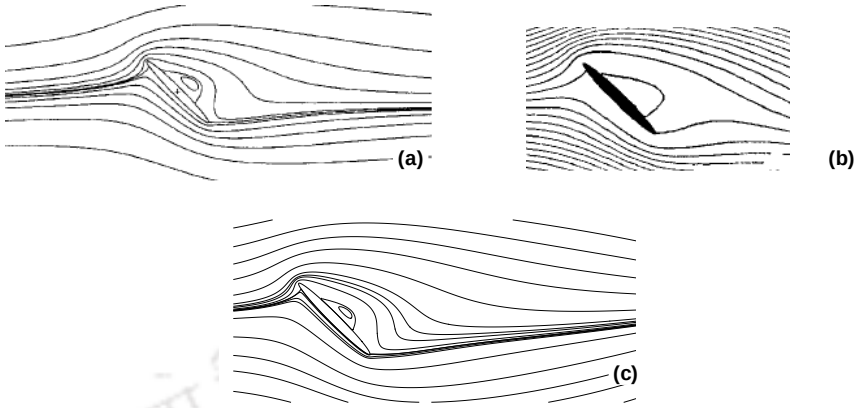

Figure 7.3: *Comparison of steady state stream lines for* $Re = 15$, $\Gamma = 0.1$, $\Theta = 45^0$, *(a) Dennis and Young [43], (b) Lugt and Haussling [95], (c) Present computation.*

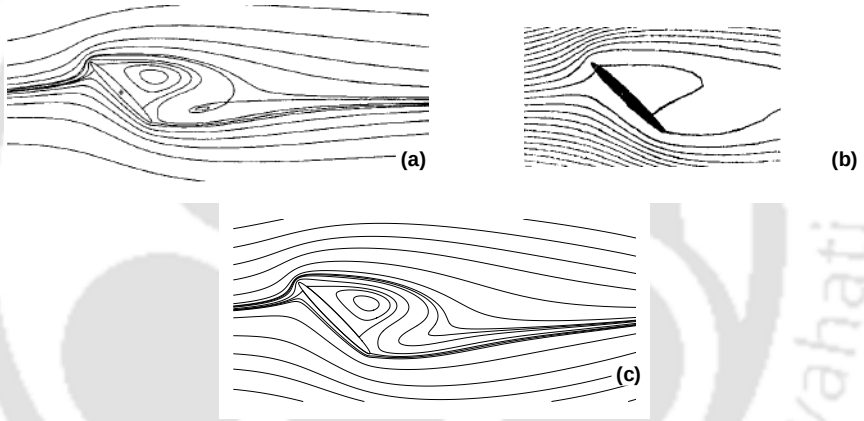

Figure 7.4: *Comparison of steady state stream lines for* $Re = 30$, $\Gamma = 0.1$, $\Theta = 45^0$, *(a) Dennis and Young [43], (b) Lugt and Haussling [95], (c) Present computation.*

We next consider the regime for which the flow field eventually becomes periodic. Here flow field ultimately leads to periodic vortex shedding. Specifically we consider three different combinations of flow parameters. In table 7.2 we compare our computed drag and lift for $Re = 200$, $\Theta = 45^0$ having $\Gamma = 0.2$ and $\Gamma = 0.1$ with those found in [95] for different times at its early stage of evolution and find a close match. The combination of parameters being considered next is $Re = 163$, $\Theta = 45^0$ and $\Gamma = 0.2$ which has been considered by Peng *et al.* [119] as well. The time evolution of drag and lift coefficients towards an asymptotic periodic state can be seen in figure 7.2(b). From the figure it is clear that within a very short time the flow assume periodic nature. Spectral analysis of a time sample of the

Table 7.2: *Time evolution of drag and lift coefficients for* $Re = 200$, $\Theta = 45^0$, $\Gamma = 0.2$ *and* $\Gamma = 0.1$ *(The values in parenthesis are from [95]).*

	$\Gamma = 0.2$				
t	0.84	1.585	2.395	3.205	4.42
C_D	1.552	1.605	1.471	1.271	1.298
	(1.565)	(1.735)	(1.508)	(1.350)	(1.340)
C_L	1.768	1.752	1.273	0.631	0.617
	(1.905)	(2.030)	(1.440)	(0.575)	(0.585)
	$\Gamma = 0.1$				
t	8.9	10.15	11.2	11.6	12.05
C_D	1.162	1.272	1.303	1.331	1.343
	(1.230)	(1.505)	(1.565)	(1.550)	(1.485)
C_L	0.854	1.327	0.945	0.867	0.829
	(0.810)	(1.545)	(1.280)	(1.060)	(0.910)

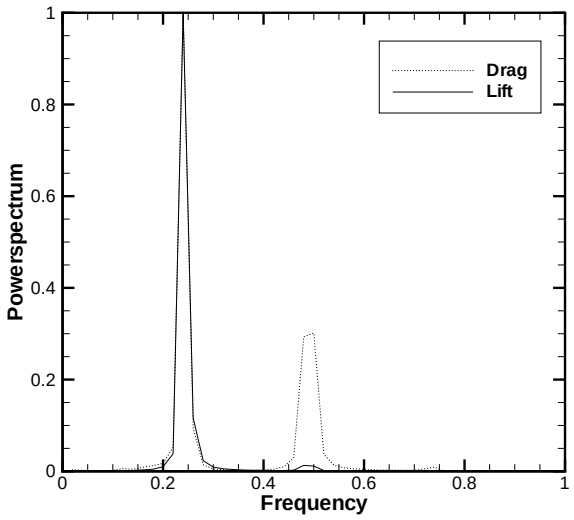

Figure 7.5: *Power spectrum of drag and lift coefficients for* $Re = 163$, $\Gamma = 0.2$, $\Theta = 45^0$.

drag and lift coefficients is carried out and the normalized power density spectra is shown in figure 7.5. We present the temporal evolution of streamlines and post processed vorticity contours over one complete vortex shedding cycle of duration T in figure 7.6. The evolution of von Kármán vortex street is clearly seen in these figures. Note that two eddies are shed just behind the cylinder within each period and are then convected away into the wake region. The staggered nature of the

Kármán shedding is clear from these plots. Figures 7.6(a) and 7.6(c) are half a vortex shedding cycle apart. The crests and troughs of the sinuous waves in the streamlines reflect the alternatively positive and negative vorticities of the eddies.

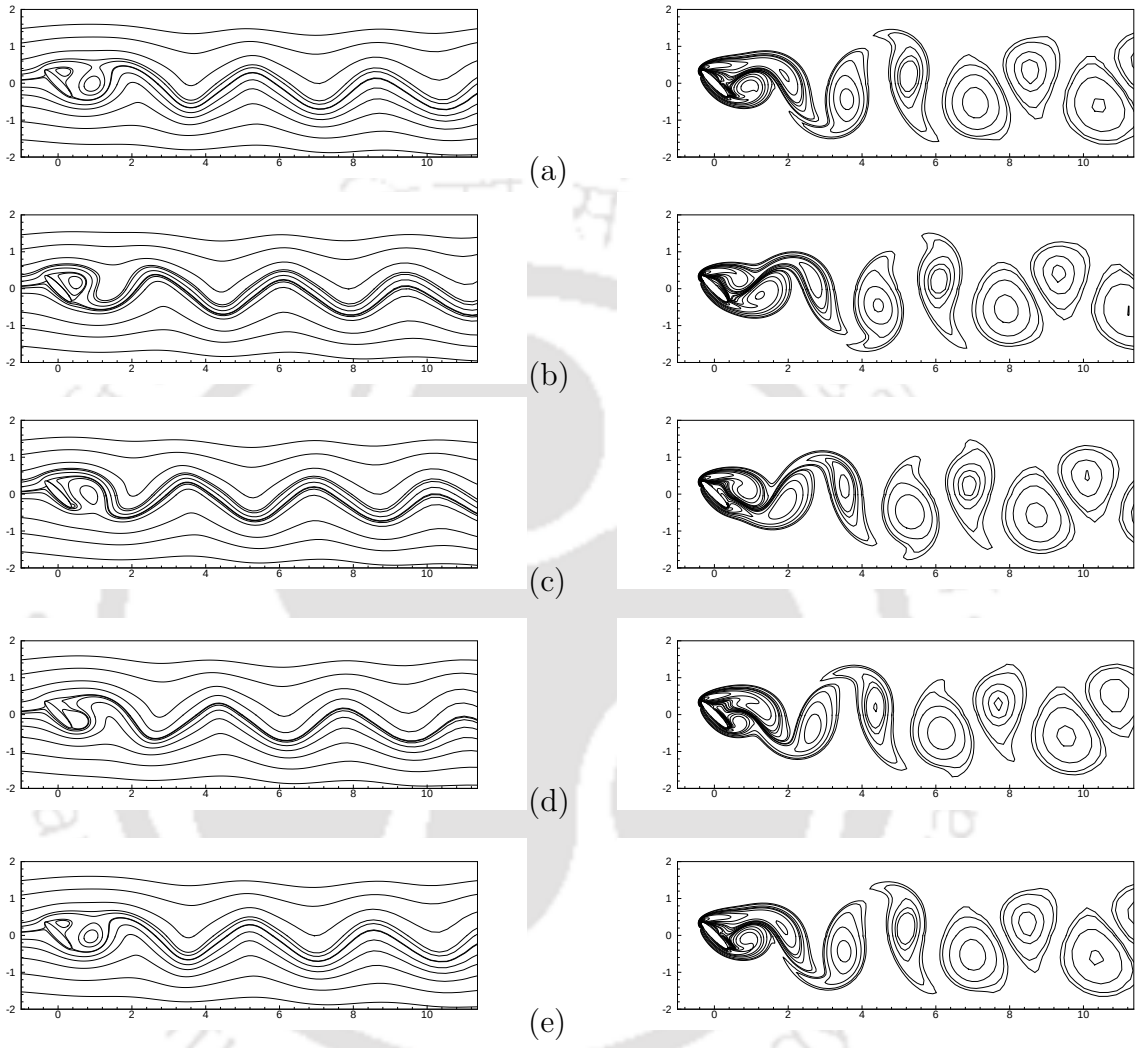

Figure 7.6: *Stream lines (left) and vorticity contours (right) depicting the flow past elliptic cylinder for* $Re = 163$, $\Gamma = 0.2$, $\Theta = 45^0$ *at (a)* $t = T$, *(b)* $t = T + \frac{T_0}{4}$, *(c)* $t = T + \frac{T_0}{2}$, *(d)* $t = T + \frac{3T_0}{4}$, *(e)* $t = T + T_0$.

Thereafter we consider the flow field with controlling parameters $Re = 1000$, $\Theta = 60^0$, $\Gamma = 0.1$. Here we take $\delta t = 0.0001$ in order to accurately resolve the α-phenomenon [37]. In figure 7.7(i) we present the early evolution of wake while the wake structure behind elliptic cylinder during shedding is shown in figure 7.7(ii). In figure 7.7(i) one can clearly see the formation of a main eddy along with a pair

of secondary vortices mimicking the α- phenomenon ($t = 1.0$ and $t = 1.5$) together with the first vortex shedding from the trailing edge ($t = 0.25$) which was reported in [37] as well. This α- phenomenon is also seen to appear alternately behind the tips of the elliptical cylinder ($t = 20.0$ and $t = 22.0$) for fully developed flow (figure 7.7(ii)).

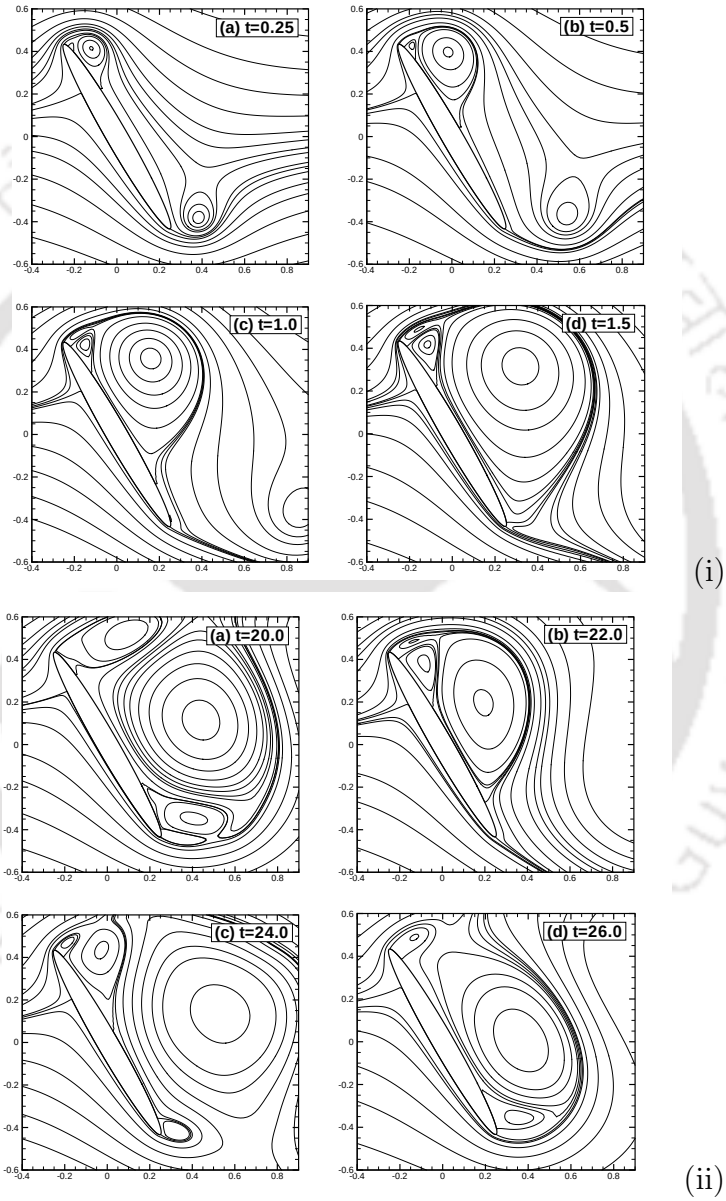

Figure 7.7: *(i) Early evolution of wake and (ii) Wake structure during shedding behind elliptic cylinder for* $Re = 1000$, $\Gamma = 0.1$, $\Theta = 60^0$.

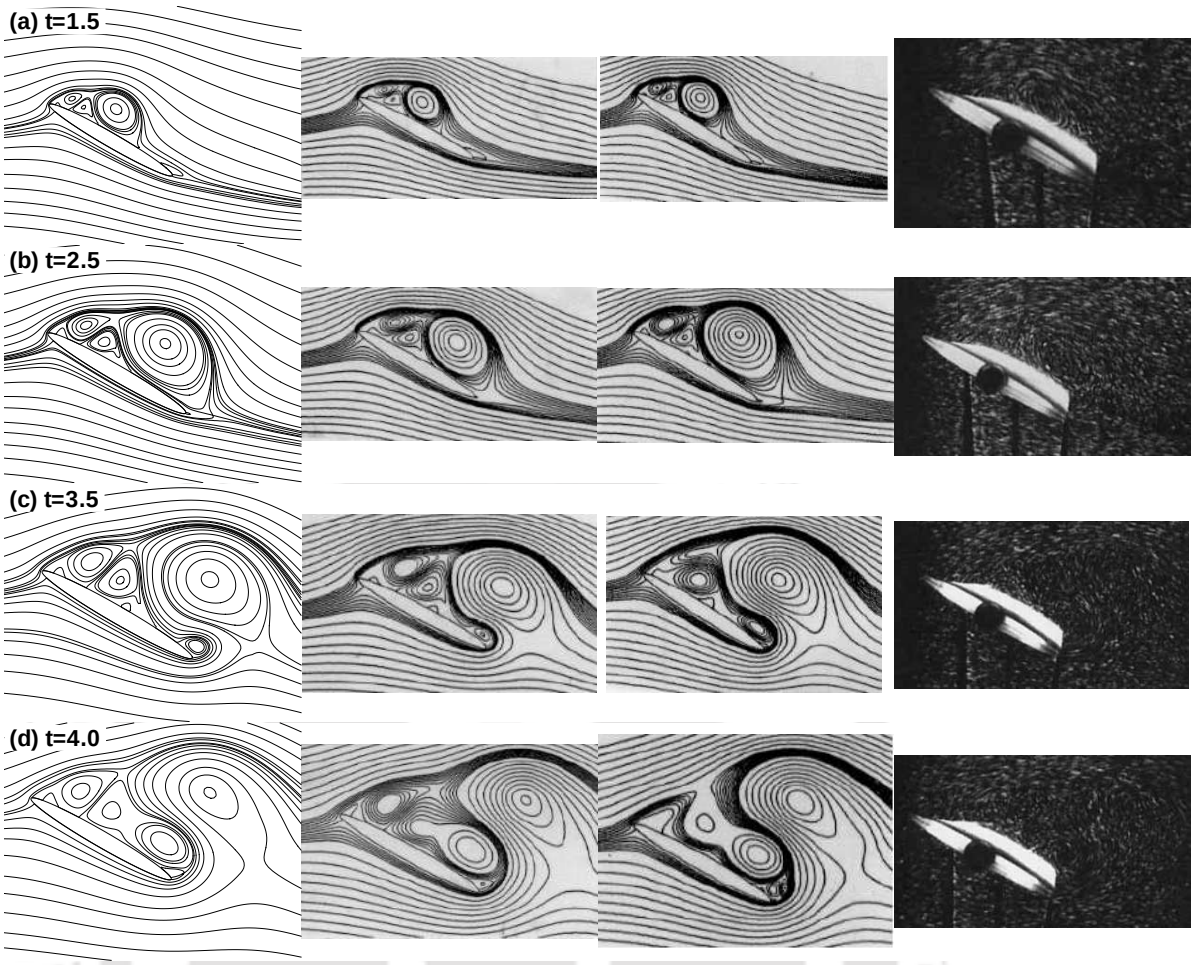

Figure 7.8: *Comparison of early evolution of stream lines between present computation (first column), numerical results by Nair and Sengupta [105] using 3rd order (second column) and 5th order (third column) upwinding and experiments by Ohmi* et al. *[112] for* $Re = 3000$, $\Gamma = 0.1$, $\Theta = 30^0$.

The last simulation in this section is for $Re = 3000$, $\Theta = 30^0$, $\Gamma = 0.1$. Motivation for this choice comes from the availability of some numerical [105] as well as experimental results [112]. As considered in [105] we take $\delta t = 0.0001$ for this case and accelerate the the free-stream velocity from a value of zero to unity in time 0.05. Thereafter $U_\infty = 1$ is maintained. In figure 7.8 we compare our numerical results for the early stages of evolution with the numerical results of [105] and the experimental results of [112]. At time $t = 1.5$ our second order accurate method reports exactly all the three leading edge vortices as well as a trailing edge bubble as reported by Nair and Sengupta [105] obtained through a fifth order upwinding scheme. At time $t = 2.5$ one can see the detachment and subsequent growth of the rearmost leading edge vortex in size. This is followed by the formation of alleyway

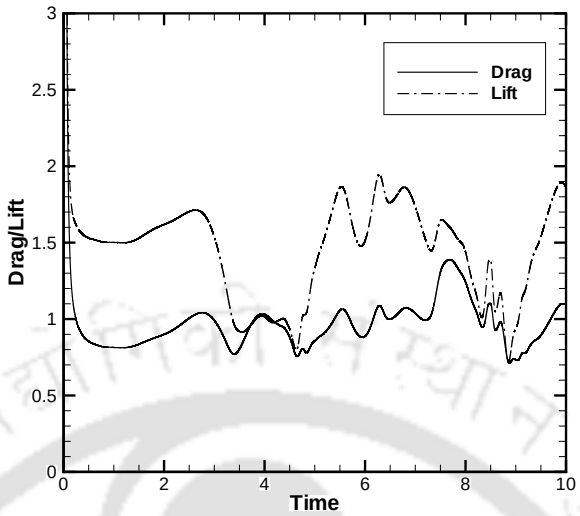

Figure 7.9: *Evolution of drag and lift coefficients for* $Re = 3000$, $\Gamma = 0.1$, $\Theta = 30^0$.

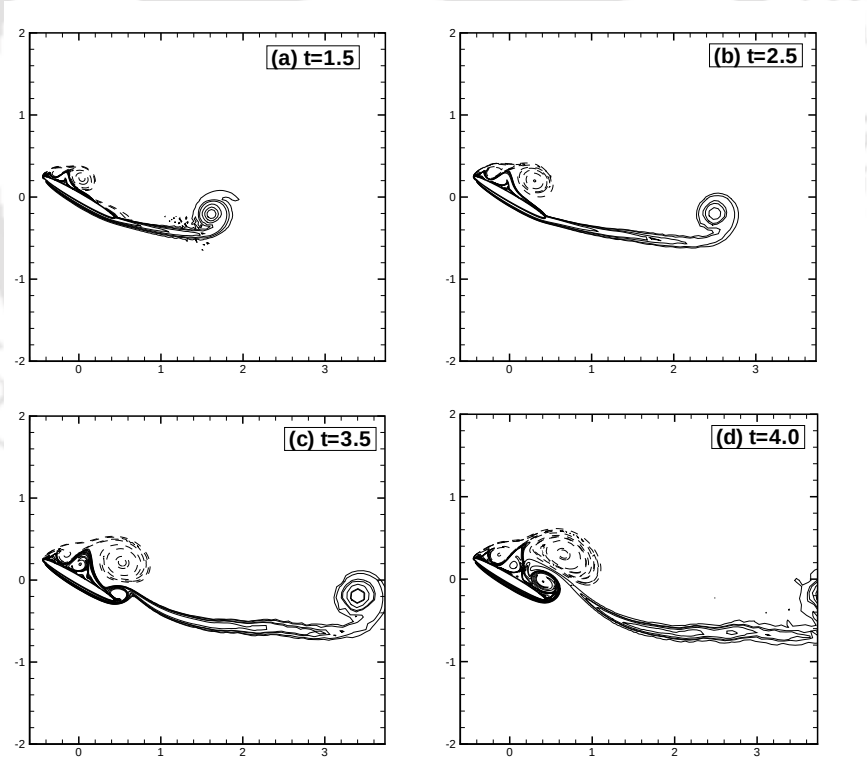

Figure 7.10: *Early evolution of vorticity contours for* $Re = 3000$, $\Gamma = 0.1$, $\Theta = 30^0$.

where the streamlines from the lower surface turn around the trailing edge bubble. As reported in [105], around this time due to the proximity of vortex, the drag

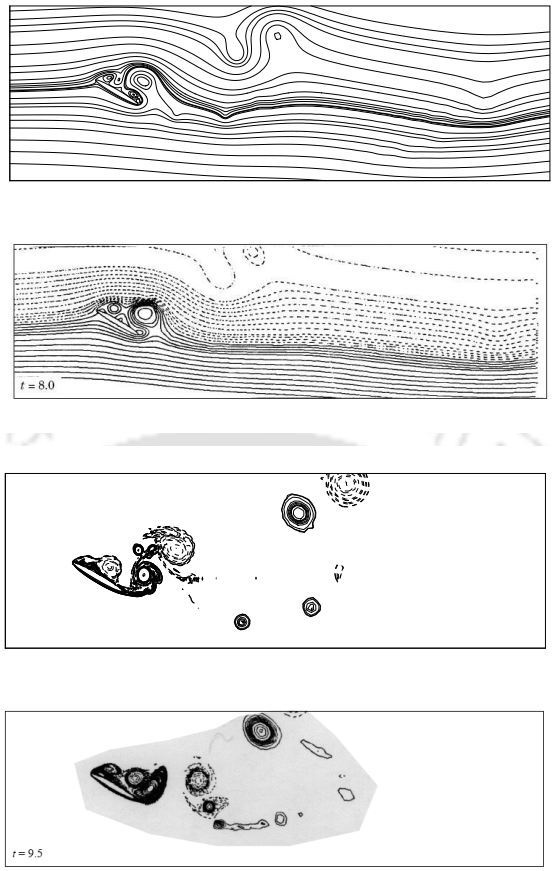

(i)

(ii)

Figure 7.11: *Comparison with the numerical results of Nair and Sengupta [105] (i) Stream lines at* $t = 8.0$ *and (ii) Vorticity contours at* $t = 9.5$ *for* $Re = 3000$, $\Gamma = 0.1$, $\Theta = 30^0$.

and lift attain local maxima and can be noted from figure 7.9. Note that in their work Nair and Sengupta [105] have obtained values of drag and lift coefficients only at some discrete times. But here we have shown a more detailed evolution. At $t = 3.5$ one can see the opening up of the large vortex and alleyway resulting in the rapid loss of drag and lift. At $t = 4.0$ a large recirculation region appear near the trailing edge increasing the drag. Note that at these different instances of times there are some differences between all three computational results although overall features are same. Moreover the quality of experimental visualization does not allow us to comment on supremacy of one numerical result over another. Vorticity contours corresponding to the above mentioned instances is shown in figure 7.10. Comparison of stream lines and vorticity at larger times have been made in figure 7.11. Again good comparison can be seen.

7.3 Flow past symmetric aerofoils with angle of attack

The last example in this thesis is the determination of unsteady flow past symmetric aerofoils NACA 0012 and NACA 0015. NACA here is the acronym of the National Advisory Committee for Aeronautics and is the predecessor of National Aeronautics and Space Administration (NASA). The literature contains some great classical [49, 113, 131] and modern [128, 136] experimental results as well as some supporting computational works on incompressible flow past these aerofoils. One of the earliest computational approach to flow past an aerofoil dates back to the work of Mehta and Lavan [100]. In 1975, they studied the problem of laminar flow past an impulsively started Joukowski aerofoil for $Re = 1000$. In 1985, Freymuth [49] in his experimental work, studied the effect of uniform acceleration on flow past a NACA 0015 aerofoil at different Reynolds numbers and angles of attack by flow visualization technique. He defined Reynolds number in terms of the uniform acceleration and the chord length of the aerofoil. Ohmi *et al.* [113] in 1991 gave experimental and computational results for a NACA 0012 aerofoil at 30^0 angle of attack for $Re = 3000$. In 1995, Shen and Loc [131] carried out numerical simulations for external flows around NACA 0012 for $Re = 1000$ and 10000 at angles of attack 20^0 and 34^0 by means of a domain decomposition method which combined a vortex method and a finite difference method. In the same year Morikawa and Grönig [103] investigated experimentally and numerically the leading edge vortex system around NACA 0015 due to both the unsteady motion and the aerofoil oscillation. Experimental investigation of flow field around an aerofoil continued with Soria *et al.* [136] in 2003 using multigrid cross-correlation digital particle image velocimetry (MCCDPIV) technique to measure the flow field around a NACA 0015 airfoil at 30^0 angle of attack where the flow is accelerated to a constant velocity from rest. In 2007 Sengupta *et al.* made a detailed experimental and numerical study of accelerated flow past NACA 0015 aerofoil for $Re = 5200$, 7968, and 35000 under different conditions for various angles of attack. They have also compared their results with earlier results available in literature.

Here we consider laminar flow past symmetric aerofoils NACA 0012 and NACA 0015. The main motivation here is to project the ability of the present method to reproduce the flow details in case of computationally and physically interesting symmetric aerofoils. For both the aerofoils we consider two different combinations of flow control parameters *viz.* Re and Θ. For NACA 0012 aerofoils, they are (a)

$Re = 1000$, $\Theta = 34^0$; (b) $Re = 3000$, $\Theta = 45^0$. In case of NACA 0015 aerofoils, we further consider two accelerated flow fields (c) $Re = 5200$, $\Theta = 90^0$ and (d) $Re = 8000$, $\Theta = 30^0$. These choices were inspired by the existence of numerous numerical results and experimental visualizations in the literature. The Re is based on the chord length c of the aerofoil and the free-stream speed U_∞. For cases (a) and (b) we consider the flow to start impulsively with $U_\infty = 1$, while for cases (c) and (d) we consider uniform acceleration where a unit non-dimensional velocity is attained, starting with zero velocity, in time 0.0521 and 2.5 respectively. As initial condition we take $\psi = 0 = \psi_\xi = \psi_\eta$. We also consider potential boundary condition at upstream and convective boundary condition for ψ at the downstream of the flow.

7.3.1 Grid generation

The first challenge for us in this problem is to model the NACA aerofoils and generate the surrounding grid using a conformal transformation. Here we use the conformal transformation

$$z = \lambda + c_1\frac{a}{\lambda} + c_2\frac{a^2}{\lambda^2}, \quad \lambda = ae^{I\zeta}, \quad \zeta = \xi + I\eta, \quad a = \frac{1}{2} - c_1.$$

For NACA 0012 we take $c_1 = 0.2238$ and $c_2 = 0.0165$; while for NACA 0015, $c_1 = 0.2165$ and $c_2 = 0.0180$. A comparison of the two aerofoils thus generated with the actual ones is presented in figure 7.12. We have found that the above transformation models the NACA aerofoils more closely then Joukowsky conformal transformation, which can also be used to generate the aerofoils. The computational grids for both these aerofoils at different angles of attack are shown in figure 7.13. We take the chord length $c = 1$ with its tip at the origin.

7.3.2 Flow past NACA 0012

Experiments on vortex formation for flows around NACA 0012 were carried out by Ohmi *et al.* [113]. These experiments were later supported by numerical works of Shen and Loc [131, 132]. Here we compute using 201×121 grid and taking $R_\infty \approx 12c$. For case (a) we consider $\delta t = 0.0005$ and for (b) $\delta t = 0.0001$. In figures 7.14 and 7.15 we present comparisons of the streamlines between the computed results and those reported in [132] for $Re = 1000$, $\Theta = 34^0$ showing excellent agreements. The time evolution of the flow structure is correctly reproduced and all the main and secondary vortices detected by the experimental visualizations are captured by our numerical simulation. To illustrate the vorticity field, the

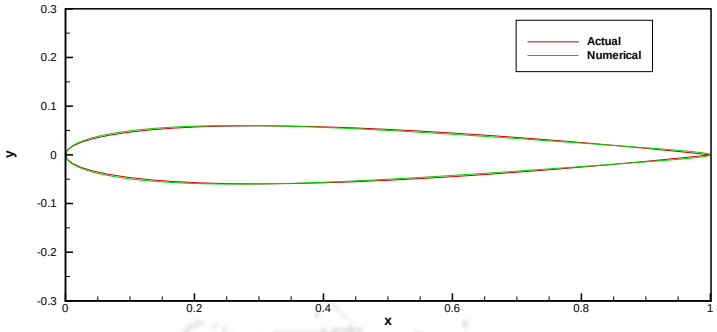

(a)

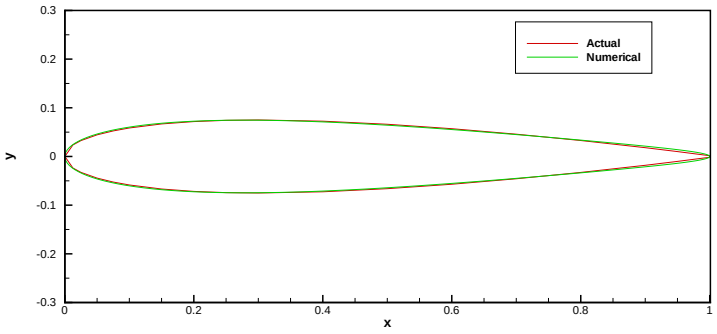

(b)

Figure 7.12: *Comparison with actual aerofoils (a) NACA 0012, (b) NACA 0015.*

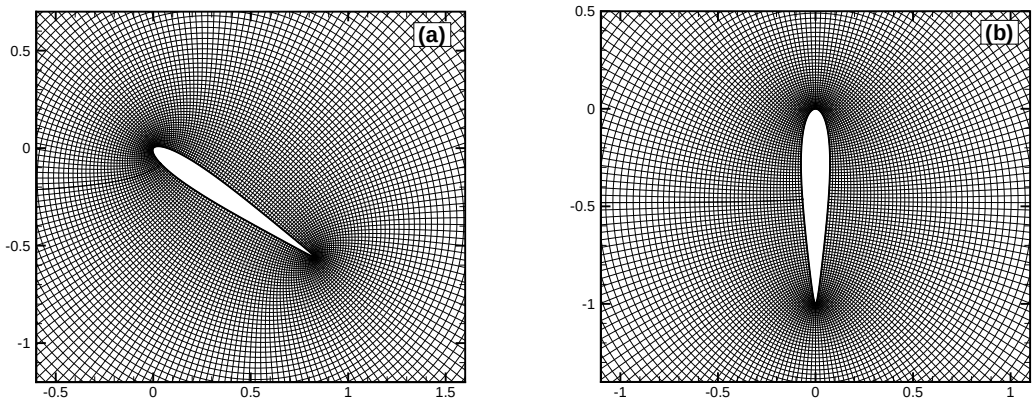

Figure 7.13: *Typical* 201×161 *grids around (a) NACA 0012 having angle of attack* 34^0*, (b) NACA 0015 having angle of attack* 90^0*.*

post processed vorticity contours corresponding to different times are presented in figure 7.16; similar comparison for $Re = 3000$, $\Theta = 45^0$ are carried out in figure

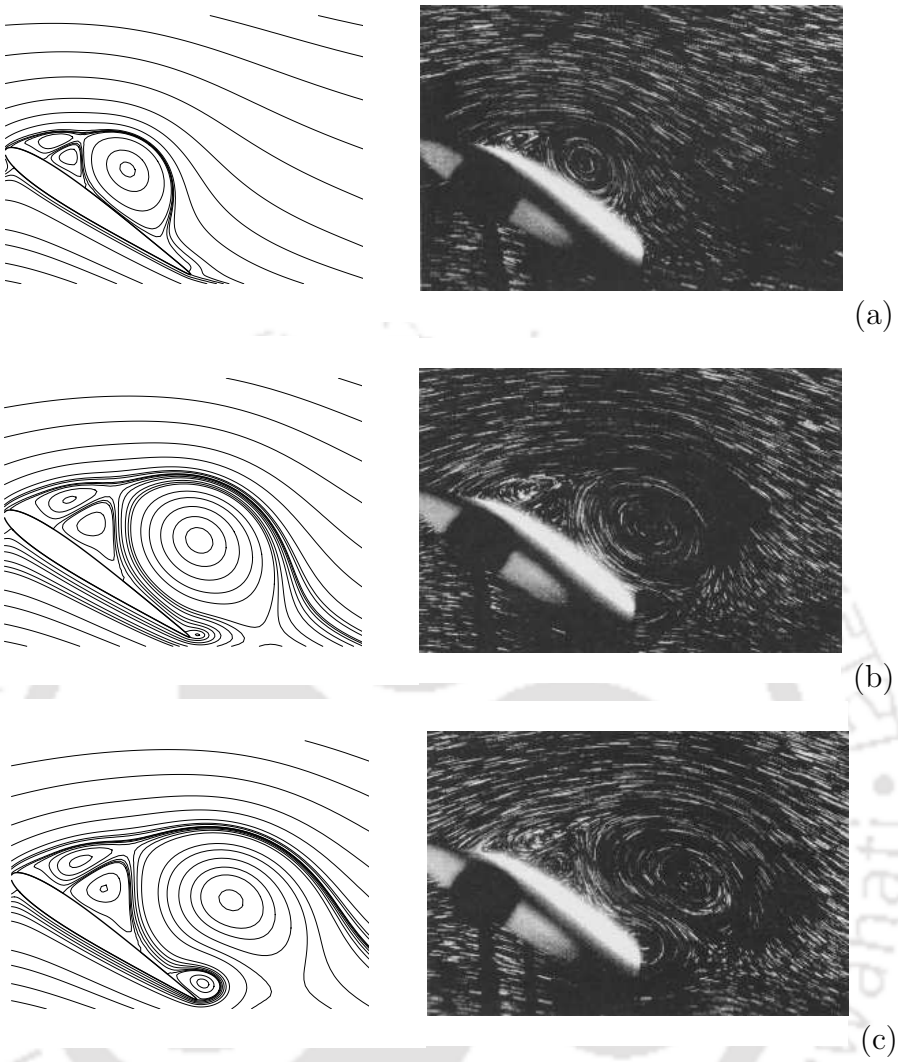

Figure 7.14: *Comparison of stream lines (left) with experimental visualizations [132] (right) for NACA 0012 with* $Re = 1000$, $\Theta = 34^0$ *at time (a)* $t = 1.6$, *(b)* $t = 2.8$, *(c)* $t = 3.2$.

7.17 and the associated vortex structures can be seen in figure 7.18. Though the experimental graphics are not very clear but as has been pointed out in [113], it is clear from the computed flow field that the initial wake follows an unsteady process consisting of the development of a large scale leading-edge vortex over the upper surface and subsequent detachment of that vortex, followed by the establishment of reverse streamlines on the upper surface and the subsequent development and shedding of the smaller trailing-edge vortex. The generation of leading- edge vortex with clockwise rotation and the trailing-edge vortex with counterclockwise rotation

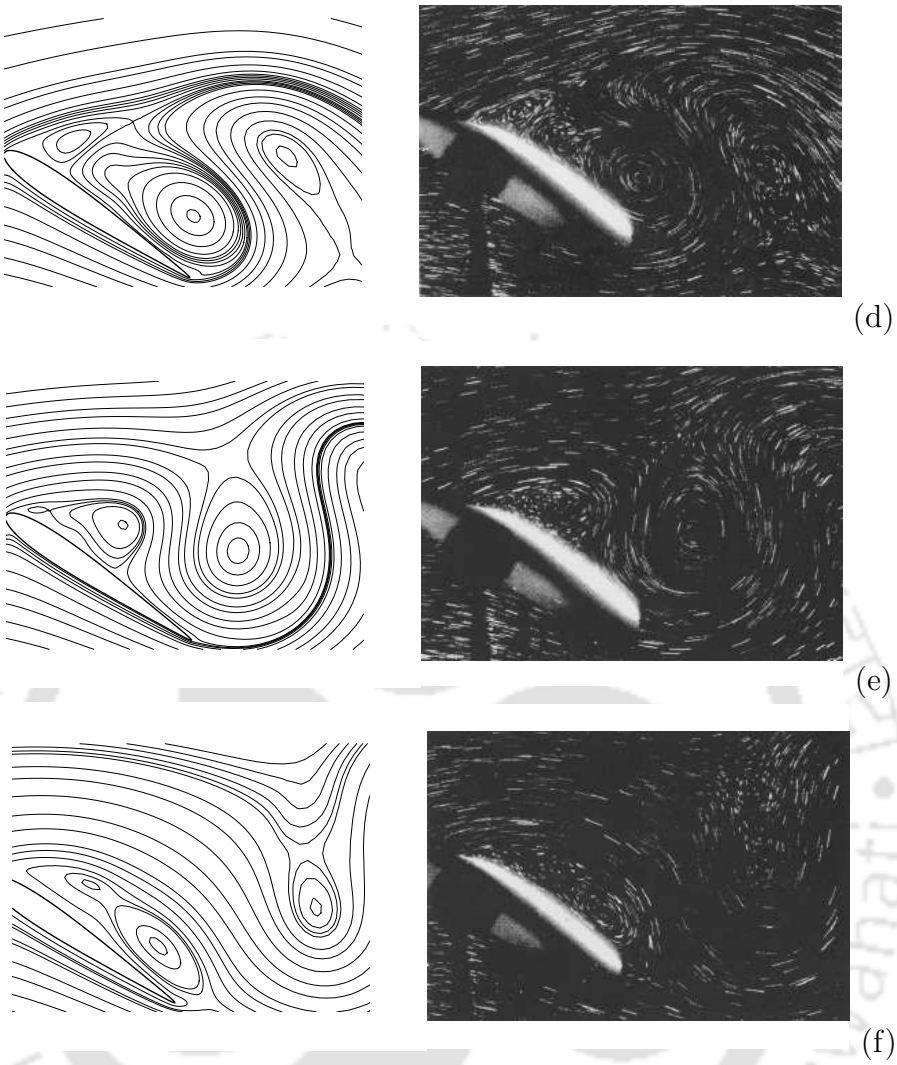

Figure 7.15: *Comparison of stream lines (left) with experimental visualizations [132] (right) for NACA 0012 with* $Re = 1000$, $\Theta = 34^0$ *at time (d)* $t = 4.0$, *(e)* $t = 4.8$, *(f)* $t = 5.6$.

can also be seen in figure 7.18.

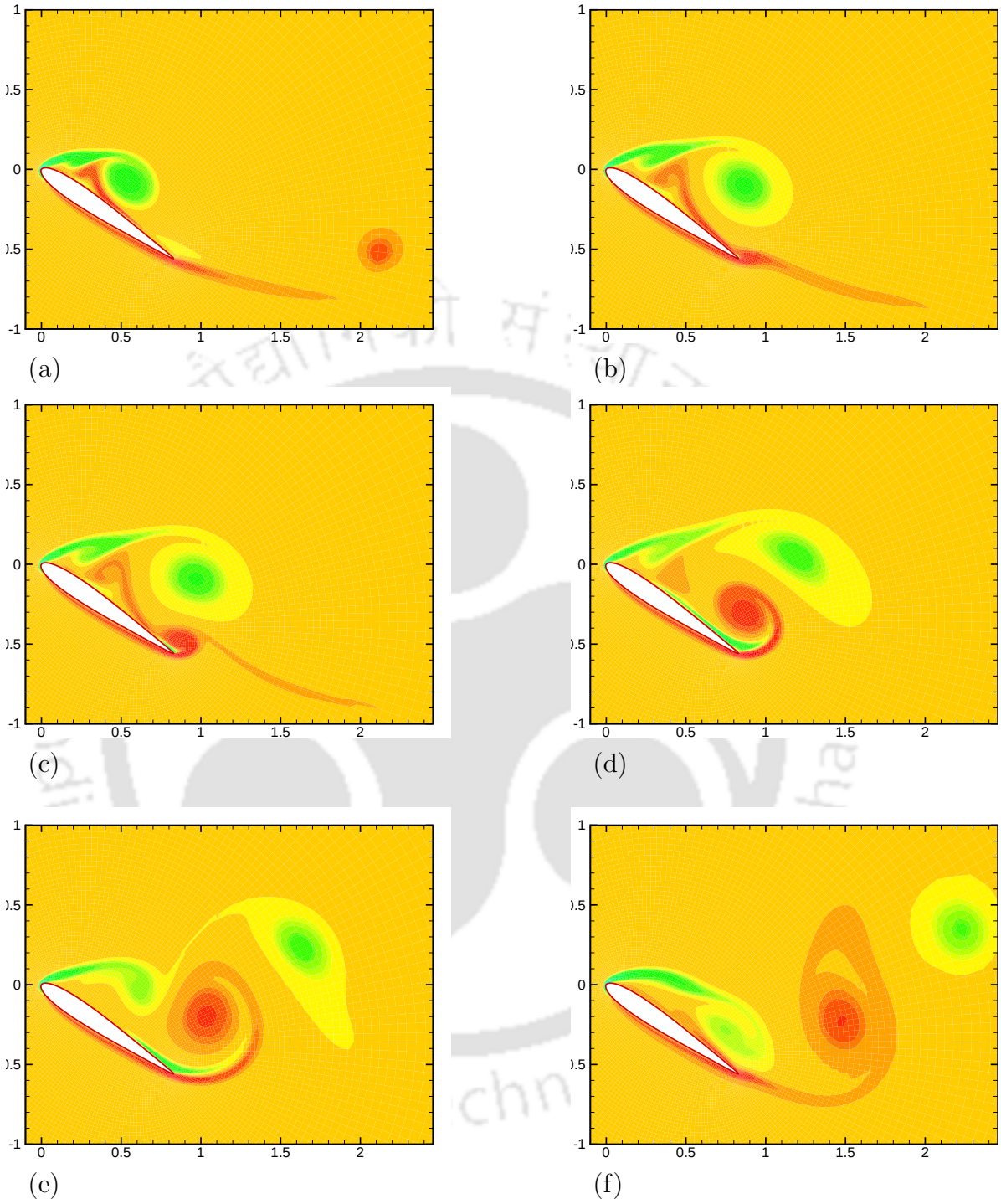

Figure 7.16: *Evolution of vorticity contours for NACA 0012 with* $Re = 1000$, $\Theta = 34^0$ *at time (a)* $t = 1.6$, *(b)* $t = 2.8$, *(c)* $t = 3.2$, *(d)* $t = 4.0$, *(e)* $t = 4.8$, *(f)* $t = 5.6$.

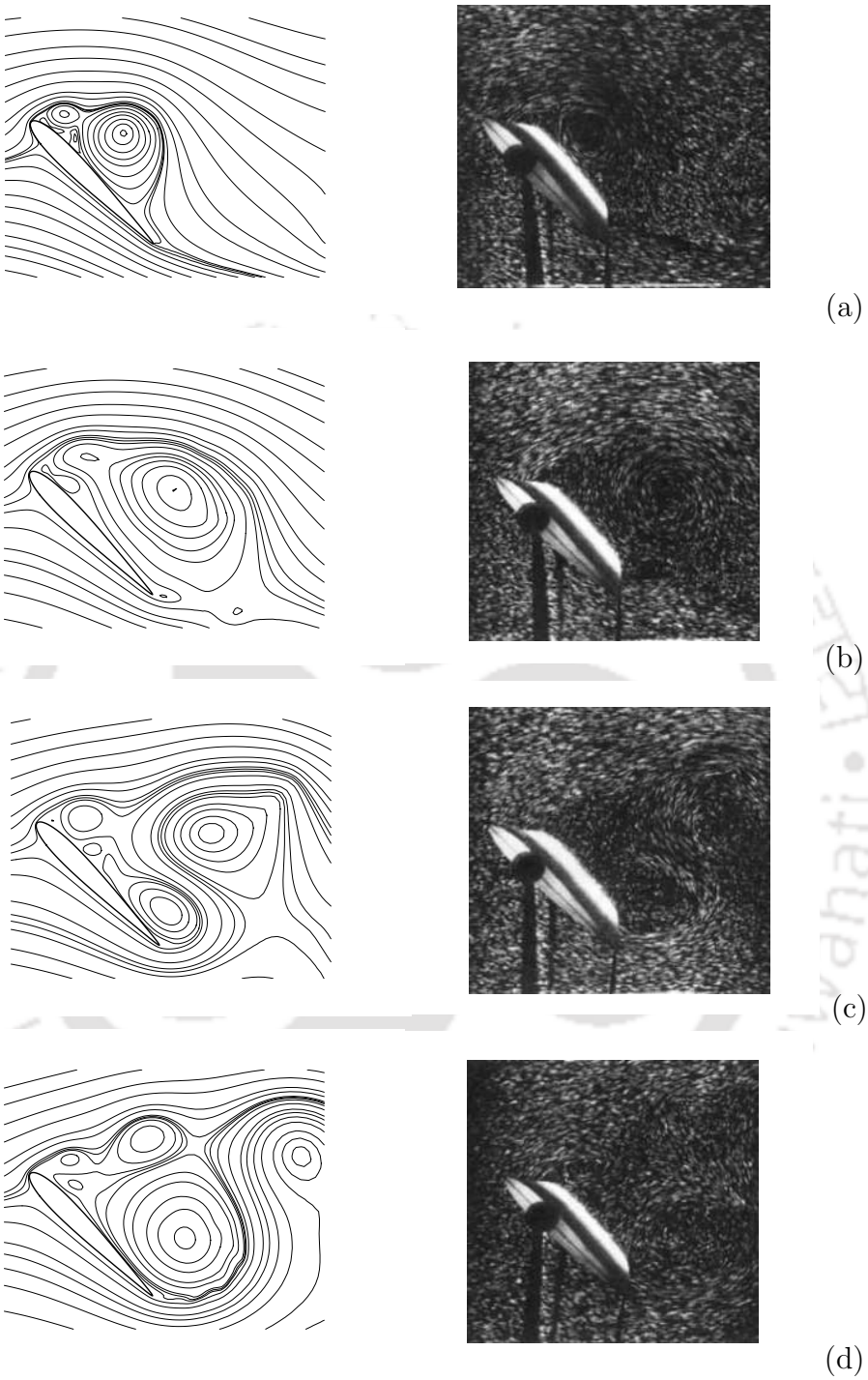

Figure 7.17: *Comparison of stream lines (left) with experimental visualizations [113] (right) for NACA 0012 with* $Re = 3000$, $\Theta = 45^0$ *at time (a)* $t = 1.5$, *(b)* $t = 2.5$, *(c)* $t = 3.5$, *(d)* $t = 4.5$.

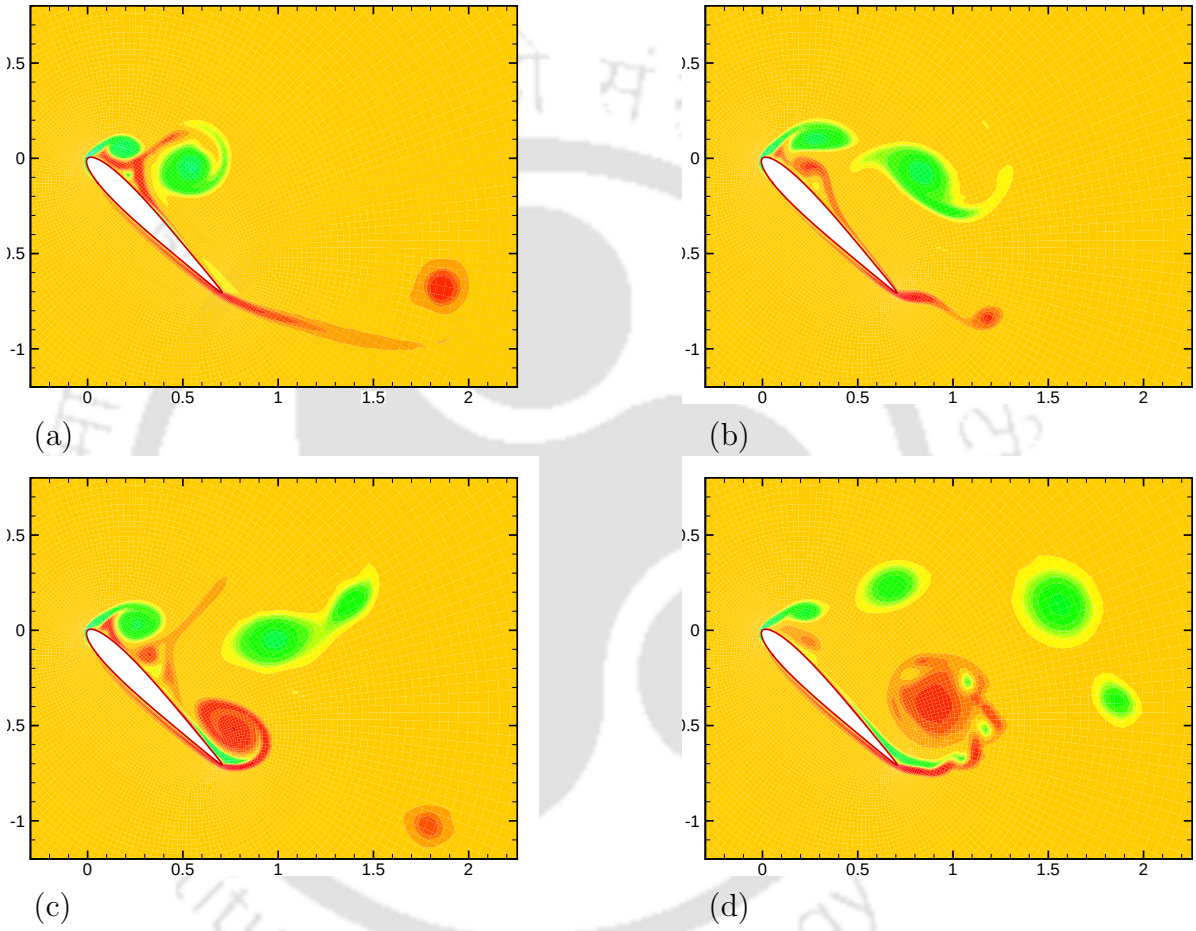

Figure 7.18: *Evolution of vorticity contours for NACA 0012 with* $Re = 3000$, $\Theta = 45^0$ *at time (a)* $t = 1.5$, *(b)* $t = 2.5$, *(c)* $t = 3.5$, *(d)* $t = 4.5$.

7.3.3 Flow past NACA 0015

Freymuth [49] experimentally studied the effect of uniform acceleration on flow past NACA 0015 aerofoil for different Re and angles of attack (Θ). It is well known that for a fixed Re, as Θ increases the shedding of vortices from the leading and trailing edges gets more pronounced. Note that in the above mentioned work, the Re has been defined in terms of the uniform acceleration and the chord length of the aerofoil. As pointed out by Sengupta *et al.* [128], the Re based on instantaneous speed, as defined here will vary linearly with time. We follow the convention adopted in [128] and firstly choose the combination $Re = 5200$ and $\Theta = 90^0$ to carry out computations in order to compare our results with the strong vortical structures that were seen in the experiments of Freymuth [49]. Since we are interested to accurately simulate flow near the aerofoil at an early stage so we consider $R_\infty \approx 4c$ and use a finer grid 301×121 with $\delta t = 0.0001$ for all our computations in this subsection. In figure 7.19 the vorticity contours are compared with the flow visualization experiment performed in [49]. The match between the computation and experiment is striking for the vortices that emanate from both leading and trailing edges. Our computation clearly captures the instability of the vortices shed from the top and bottom resulting in a train of smaller vortices. In figure 7.20 we present the evolution of streamlines, where as time progresses, the growth of two dissimilar bubbles, with the larger one on the trailing edge can be observed.

Another case is inspired by the works of Soria *et al.* [136] where the NACA 0015 aerofoil was held at 30^0 angle of attack. The flow here is accelerated uniformly from rest upto a desired free stream speed and once the free stream speed is attained it has been maintained thereafter. In figure 7.21, we compare our results with the first of the two experimental results reported in [136] for $Re = 8000$. It shows the temporal evolution of velocity and vorticity as the flow accelerates and shortly afterwards. From figure 7.21(a) it is clear that the leading edge separation starts after $t = 1.0$. This separation is captured by our numerical simulation in figure 7.21(b) at time $t = 2.0$ as reported in [136]. Figure 7.21(b) also confirms that the boundary layer remains attached to the downstream side of the aerofoil. As the acceleration phase gets over at time t=2.5, the velocity stays constant and flow becomes exceedingly complex; this can be seen in figure 7.21(c) which shows the development of strong shear layer at the leading edge at $t = 3.0$. Note that our computed figures on the left of figure 7.21 match well with the experimental visualization of [136] on the right. The evolution of streamlines for the NACA 0015

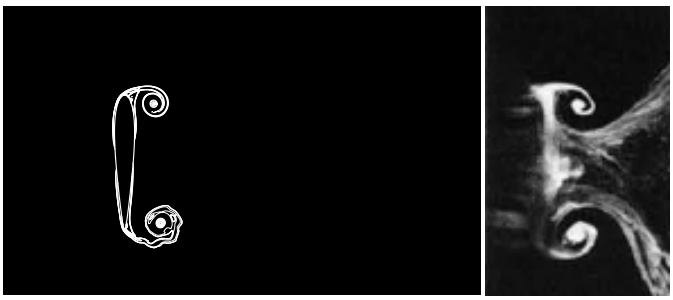

(a)

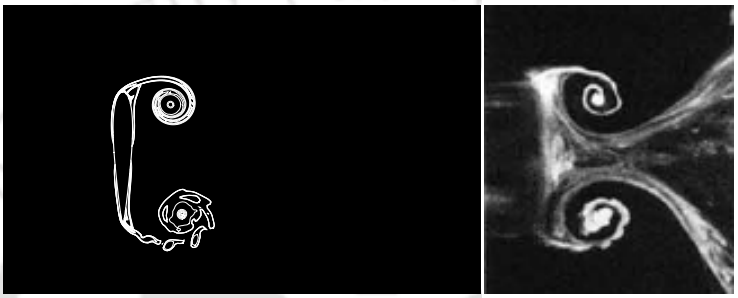

(b)

(c)

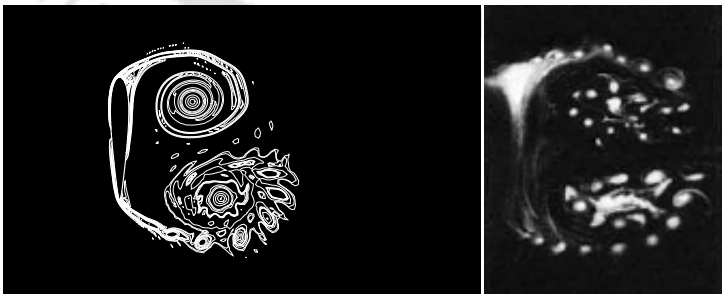

(d)

Figure 7.19: *Comparison of vorticity contours (left) with the visualization pictures (right) from Freymuth [49] for NACA 0015 with* $Re = 5200$, $\Theta = 90^0$ *at time* $t = 0.5, 0.9, 1.9$ *and* 2.2.

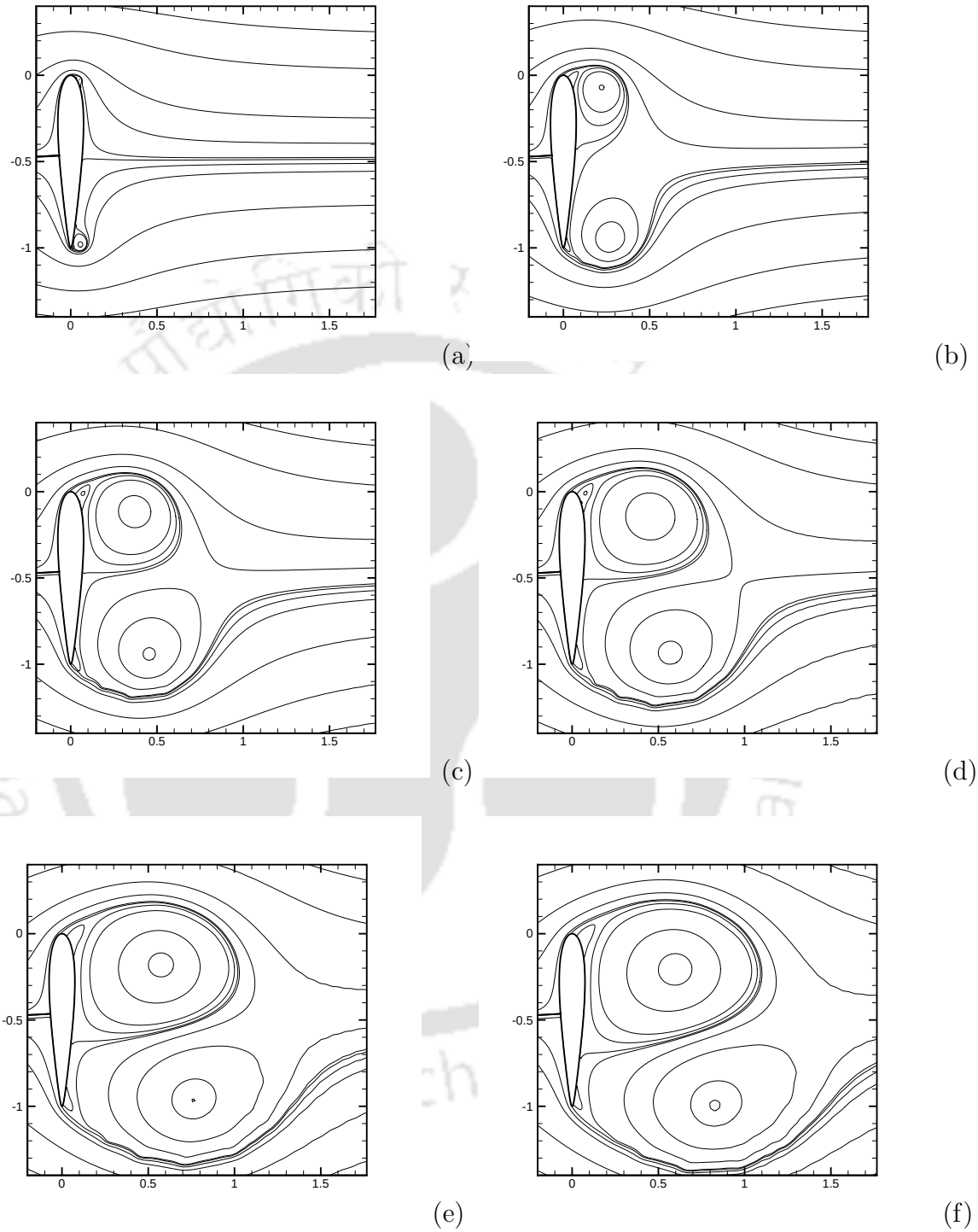

Figure 7.20: *Evolution of stream lines for NACA 0015 with* $Re = 5200$, $\Theta = 90^0$ *at time (a)* $t = 0.1$, *(b)* $t = 0.5$, *(c)* $t = 0.9$, *(d)* $t = 1.2$, *(e)* $t = 1.9$, *(f)* $t = 2.2$.

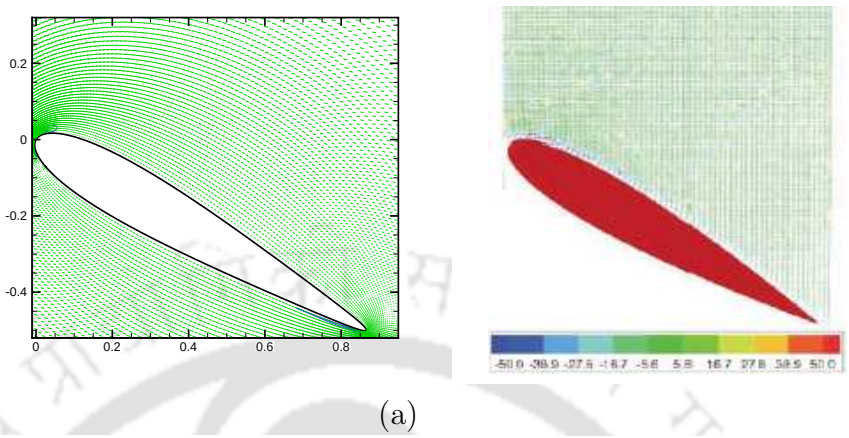

(a)

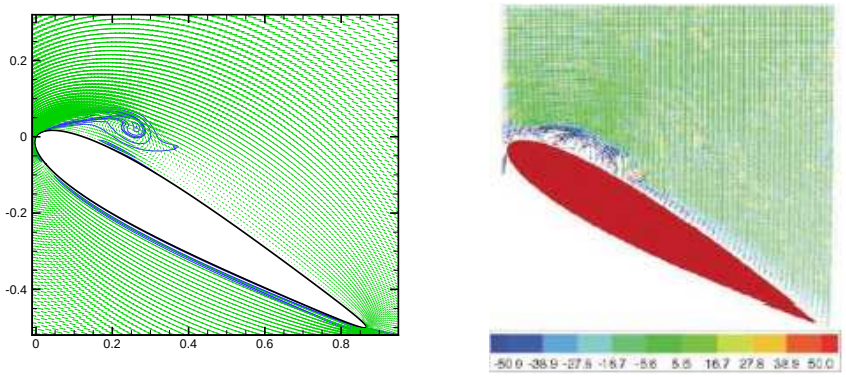

(b)

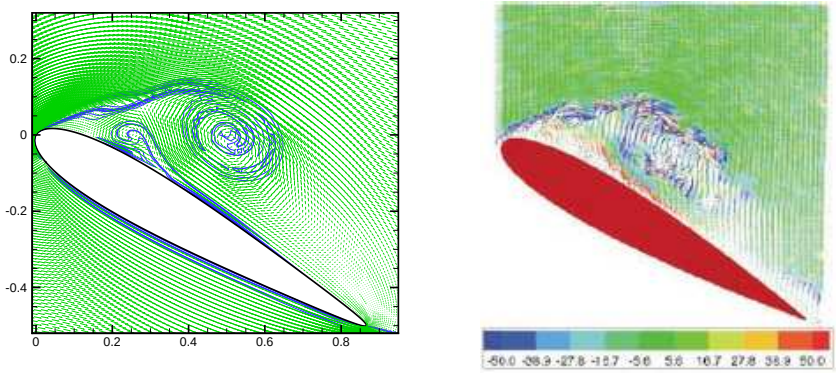

(c)

Figure 7.21: *Comparison of computed non-dimensional velocity and vorticity contours (left) with the experimental visualizations [136] for NACA 0015 with* $Re = 8000$, $\Theta = 30^0$ *at time (a)* $t = 1.0$, *(b)* $t = 2.0$, *(c)* $t = 3.0$.

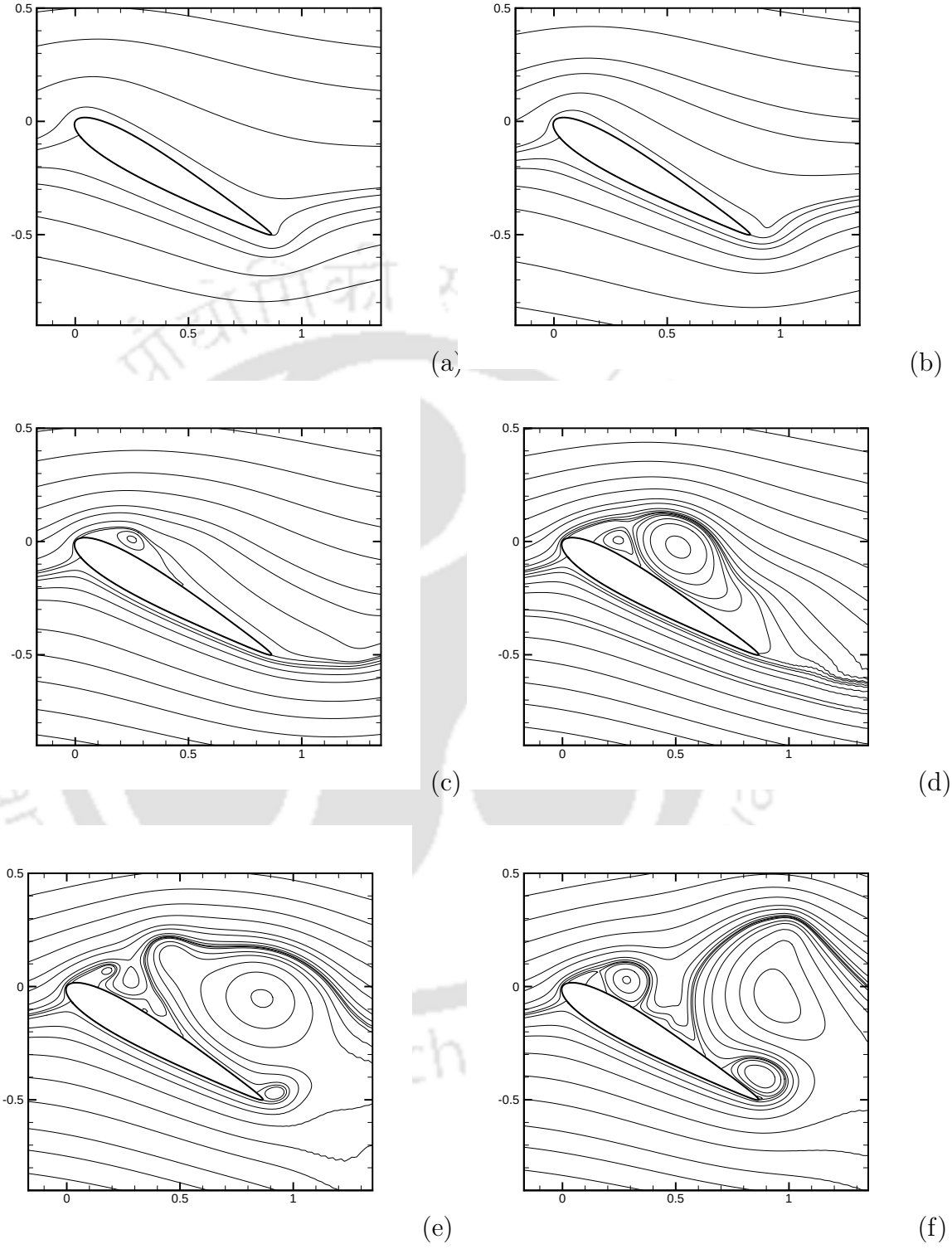

Figure 7.22: *Evolution of stream lines for NACA 0015 with* $Re = 8000$, $\Theta = 30^0$ *at time (a)* $t = 0.5$, *(b)* $t = 1.0$, *(c)* $t = 2.0$, *(d)* $t = 3.0$, *(e)* $t = 4.0$, *(f)* $t = 4.5$.

aerofoil at $\Theta = 30^0$ for $Re = 8000$ for different times can be seen in figure 7.22 and this shows that our pure stream function based formulation very accurately captures the physical phenomena.

7.4 Conclusion

In this chapter, we have demonstrated the robustness of our scheme by accurately simulating flows around elliptic and symmetric aerofoils. These cases represents flow around bluff bodies with varying curvatures with the NACA aerofoils representing the extreme case of having infinite curvature at the trailing edge. Having demonstrated the efficiency and robustness of our schemes for the most difficult cases, we can safely conclude that our scheme has the potential to resolve flow accurately in the most complicated geometric settings and most complex incompressible viscous flows.

Chapter 8

Conclusions and Future Works

8.1 Observations and remarks

The work is concerned with the development of compact schemes for fourth order biharmonic pure stream function formulation of Navier-Stokes equations. We have documented the versatility of the fourth order stream function formulation in simulating the dynamics of flow inside curved regions as well as fluid-embedded body interaction. We have also established the efficiency of the compact approach in general and the schemes developed here in particular. In contrast to the earlier works on compact discretization of biharmonic equation that are capable of handling problems in rectangular Cartesian coordinates the schemes developed here can accurately capture the fluid body interaction in some complicated domains that can be conformably mapped.

The highlights of the thesis include the following:

- We have developed a fourth order essentially compact scheme for steady N-S equations. The approach enables us to solve numerically the two dimensional steady state N-S equations on nonuniform grids in non-rectangular physical geometries that are expressible in terms of conformal mappings. To bring out different aspects of the scheme, we applied this new approach to four problems not only of varied physical complexities, but also on physical domains of different geometric settings: a problem with a known analytical solution, the flow past a constricted channel, the driven polar cavity and finally the motion past an impulsively started circular cylinder problem. The scheme has also been tested for its numerical convergence. The accuracy of the computed solutions can be judged by the results obtained in all the test cases on relatively coarser grids, which are in excellent agreement with analytical, experimental and established numerical results.

- We have developed an implicit, temporally and spatially second order accurate compact finite difference scheme for pure stream function formulation of the transient N-S equations. This formulation allowed us to effectively simulate unsteady viscous incompressible flows in irregular geometries that can be conformably mapped onto rectangular domains. We also carried out a stability analysis for the scheme and the numerical convergence is validated by capturing flow physics for constricted channel problem.

- We then proceeded to perform numerical experiments for flow past impulsively started circular cylinder and captured almost all of the interesting flow features associated with this flow for Re range of 5 to 9500. We extensively compared our results with the experimental and other numerical results available in literature both qualitatively and quantitatively. The robustness of the scheme and the effectiveness of the formulation can be gauged by the fact that it very accurately captures (i) the long time periodic nature of the flow for $50 \leq Re \leq 300$ characterized by von Kármán vortex street and (ii) the transient state phenomena *viz.* secondary phenomena for moderate Re ($300 \leq Re \leq 1000$) and α- and β- phenomena for higher ones ($3000 \leq Re \leq 9500$). We have also presented detailed analysis of the vortex shedding through streakline simulation.

- Next we used this newly developed finite difference scheme to discuss three different techniques, including an untested one in order to trigger asymmetry into the flow past circular cylinder around critical Reynolds number Re_c. Above this Re_c the flow is asymmetric and, as a consequence, vortex shedding occurs naturally in physical situations. But in numerical simulations, especially in finite difference set up, it is well known that the shedding process needs to be initiated artificially for flows in the threshold regime in the vicinity of Re_c. We started our computation by choosing $Re = 44$ and 50; in case of the former, the flow eventually retains its symmetry and for the latter, it settles into a periodic state. We further narrowed down the range of Re to establish that the critical Reynolds number resides in the regime $46.5 < Re_c \leq 47$ which is very close to the broadly agreed value of Re_c. We have also provided a brief comparison of the three perturbation techniques.

- We continue our numerical experiments and venture out to tackle problems with moving boundaries. In order to extensively investigate the efficiency of the scheme we apply it three problems *viz.* (a) circular cylinder rotating with

constant angular velocity, (b) circular cylinder spinning sinusoidally and (c) in-line oscillating circular cylinder.

- Finally we applied the scheme to the physically interesting problems of elliptic cylinders and symmetric aerofoils with various angles of attack. Again extensive comparison have been made with experimental and numerical results whenever available. Excellent match can be seen in all the cases.

The main focus in this thesis is the application of the technique which enables the use of the discretized version of a single semi linear biharmonic equation in order to efficiently simulate different fluid structures associated with flows around bluff bodies and enable us to obtain excellent comparison, both qualitatively and quantitatively, with established numerical and more so with experimental results. The algorithms developed here reproduces several published experimental and computational results corresponding to various Re for flow around a circular cylinder, rotating cylinder, oscillating cylinder, elliptic cylinder and aerofoils.

8.2 Scope for future works

We feel the work can lead to a host of different research possibilities. Some of these major possibilities are listed below:

- It will be interesting to generate numerical conformal grids inside as well as around some complex geometric domains and apply the schemes developed in this thesis to simulate flow around some less well studied problems.

- The compact schemes developed in this work have been applied only to incompressible viscous flow problems. We would be interested to extend these schemes to problems in multiphase flow and to model Raleigh-Benard convection in the presence of a melting or solidifying interface.

- We feel that it will be a worth while experience to develop compact schemes with transformation free non-uniform grids for the fourth order biharmonic pure stream function form of Navier-Stokes equation.

- We would also be interested in exploring biharmonic form of the Navier-Stokes equations in three dimensions and modify the compact schemes developed here to adopt to the same.

Appendix A

Derivation of Biharmonic Form of Navier-Stokes Equation in Conformably Transformed Plane

The N-S equations for incompressible viscous flows along with the equation of continuity in non-dimensional forms are

$$\frac{\partial}{\partial t}\boldsymbol{V} + (\boldsymbol{V}.\boldsymbol{\nabla})\boldsymbol{V} = -\boldsymbol{\nabla}p + \frac{1}{Re}\nabla^2\boldsymbol{V} \tag{A.1}$$

$$\boldsymbol{\nabla}.\boldsymbol{V} = 0, \tag{A.2}$$

where $\boldsymbol{V} = (u, v, w)$ is the velocity vector, p is the pressure, and $Re = \frac{UL}{\nu}$ is the Reynolds number based on characteristic length L and characteristic velocity U of the flow. For 2D flows considering $\boldsymbol{V} = (u, v, 0)$ to be the velocity field the above system of equations written along each component is

$$\frac{\partial}{\partial t}u + uu_x + vu_y = -p_x + \frac{1}{Re}\big(u_{xx} + u_{yy}\big) \tag{A.3}$$

$$\frac{\partial}{\partial t}v + uv_x + vv_y = -p_y + \frac{1}{Re}\big(v_{xx} + v_{yy}\big) \tag{A.4}$$

$$u_x + v_y = 0 \tag{A.5}$$

Introducing $\omega = \boldsymbol{\omega}.\widehat{k}$, the out-of-plane component of vorticity vector $\boldsymbol{\omega} = \boldsymbol{\nabla} \times \boldsymbol{V}$ and the stream function by $\boldsymbol{\psi} = (0, 0, \psi)$ the system of equations (A.3) - (A.5) reduces to

$$\psi_{xx} + \psi_{yy} = -\omega \tag{A.6}$$

$$\frac{\partial}{\partial t}\omega = \frac{1}{Re}\big(\omega_{xx} + \omega_{yy}\big) - \big(u\omega_x + v\omega_y\big). \tag{A.7}$$

Let the physical (x, y) plane be transformed into a computational (ξ, η) plane using the mapping

$$x = x(\xi, \eta), \quad y = y(\xi, \eta). \tag{A.8}$$

Under this transformation equations (A.6) and (A.7) in the computational plane becomes

$$a_1\psi_{\xi\xi} + e_1\psi_{\xi\eta} + b_1\psi_{\eta\eta} + c_1\psi_{\xi} + d_1\psi_{\eta} = f_1 \tag{A.9}$$

$$\frac{\partial}{\partial t}\omega = a_2\omega_{\xi\xi} + e_2\omega_{\xi\eta} + b_2\omega_{\eta\eta} + c_2\omega_{\xi} + d_2\omega_{\eta} \tag{A.10}$$

where

$$a_1 = \frac{1}{J^2}(x_\eta^2 + y_\eta^2), \quad b_1 = \frac{1}{J^2}(x_\xi^2 + y_\xi^2),$$

$$\begin{aligned} c_1 = \frac{1}{J^3}[&-y_\eta((x_\eta^2 + y_\eta^2)x_{\xi\xi} - 2(y_\eta y_\xi + x_\eta x_\xi)x_{\xi\eta} + (x_\xi^2 + y_\xi^2)x_{\eta\eta}) \\ &+x_\eta((x_\eta^2 + y_\eta^2)y_{\xi\xi} - 2(y_\eta y_\xi + x_\eta x_\xi)y_{\xi\eta} + (x_\xi^2 + y_\xi^2)y_{\eta\eta})], \end{aligned}$$

$$\begin{aligned} d_1 = \frac{1}{J^3}[&y_\xi((x_\eta^2 + y_\eta^2)x_{\xi\xi} - 2(y_\eta y_\xi + x_\eta x_\xi)x_{\xi\eta} + (x_\xi^2 + y_\xi^2)x_{\eta\eta}) \\ &-x_\xi((x_\eta^2 + y_\eta^2)y_{\xi\xi} - 2(y_\eta y_\xi + x_\eta x_\xi)y_{\xi\eta} + (x_\xi^2 + y_\xi^2)y_{\eta\eta})], \end{aligned}$$

$$e_1 = -\frac{2}{J^2}(y_\eta y_\xi + x_\eta x_\xi), \quad f_1 = -\omega,$$

$$a_2 = \frac{1}{ReJ^2}(x_\eta^2 + y_\eta^2), \quad b_2 = \frac{1}{ReJ^2}(x_\xi^2 + y_\xi^2),$$

$$\begin{aligned} c_2 = \frac{1}{J}(uy_\eta - vx_\eta) + \frac{1}{ReJ^3}[&-y_\eta((x_\eta^2 + y_\eta^2)x_{\xi\xi} - 2(y_\eta y_\xi + x_\eta x_\xi)x_{\xi\eta} + (x_\xi^2 + y_\xi^2)x_{\eta\eta}) \\ &+x_\eta((x_\eta^2 + y_\eta^2)y_{\xi\xi} - 2(y_\eta y_\xi + x_\eta x_\xi)y_{\xi\eta} + (x_\xi^2 + y_\xi^2)y_{\eta\eta})], \end{aligned}$$

$$\begin{aligned} d_2 = \frac{1}{J}(-uy_\xi + vx_\xi) + \frac{1}{ReJ^3}[&y_\xi((x_\eta^2 + y_\eta^2)x_{\xi\xi} - 2(y_\eta y_\xi + x_\eta x_\xi)x_{\xi\eta} + (x_\xi^2 + y_\xi^2)x_{\eta\eta}) \\ &-x_\xi((x_\eta^2 + y_\eta^2)y_{\xi\xi} - 2(y_\eta y_\xi + x_\eta x_\xi)y_{\xi\eta} + (x_\xi^2 + y_\xi^2)y_{\eta\eta})], \end{aligned}$$

$$e_2 = -\frac{2}{ReJ^2}(y_\eta y_\xi + x_\eta x_\xi),$$

where $J = x_\xi y_\eta - y_\xi x_\eta$ is the jacobian of the transformation. The velocity components u and v are

$$u = \frac{1}{J}\big(\psi_\eta x_\xi - \psi_\xi x_\eta\big), \tag{A.11}$$

$$v = \frac{1}{J}\big(-\psi_\xi y_\eta + \psi_\eta y_\xi\big). \tag{A.12}$$

If the transformation (A.8) is a conformal one *i.e.* of the form

$$z = z(\zeta), \tag{A.13}$$

$z = x + Iy$ and $\zeta = \xi + I\eta$; then the equations (A.9) and (A.10) with the help of expressions (A.11) and (A.12) simplify to

$$\psi_{\xi\xi} + \psi_{\eta\eta} = -J\omega, \tag{A.14}$$

$$\frac{\partial}{\partial t}\omega = \frac{1}{ReJ}\big(\omega_{\xi\xi} + \omega_{\eta\eta}\big) - \frac{1}{J}\big(\omega_\xi\psi_\eta - \omega_\eta\psi_\xi\big). \tag{A.15}$$

Note that in this case the jacobian of the transformation is, $J = x_\xi y_\eta - y_\xi x_\eta = x_\xi^2 + y_\xi^2 = x_\eta^2 + y_\eta^2$. Comparing equations (A.14) and (A.15) with the equations (A.6) and (A.7) we see that the ψ-ω formulation is invariant upto a scaling factor with respect to conformal transformation (A.13).

Eliminating ω from equations (A.14) and (A.15), we obtain the following form of the N-S equations

$$\begin{aligned} ReJ\frac{\partial}{\partial t}\big(\psi_{\xi\xi} + \psi_{\eta\eta}\big) &= \big(\psi_{\xi\xi\xi\xi} + 2\psi_{\xi\xi\eta\eta} + \psi_{\eta\eta\eta\eta}\big) \\ &\quad -\big(2C + Re\psi_\eta\big)\big(\psi_{\xi\xi\xi} + \psi_{\xi\eta\eta}\big) \\ &\quad -\big(2D - Re\psi_\xi\big)\big(\psi_{\xi\xi\eta} + \psi_{\eta\eta\eta}\big) \\ &\quad +\big(E + CRe\psi_\eta - DRe\psi_\xi\big)\big(\psi_{\xi\xi} + \psi_{\eta\eta}\big) \end{aligned} \tag{A.16}$$

where

$$C = \frac{J_\xi}{J}, \quad D = \frac{J_\eta}{J}, \text{ and } E = 2C^2 + 2D^2 - \frac{J_{\eta\eta}}{J} - \frac{J_{\xi\xi}}{J}.$$

Equation (A.16) can be written in the form

$$\begin{aligned} \frac{\partial}{\partial t}\nabla^2\psi &= a(\xi,\eta)\nabla^4\psi + b(\xi,\eta,\psi_\xi,\psi_\eta)\nabla^2\psi_\xi + c(\xi,\eta,\psi_\xi,\psi_\eta)\nabla^2\psi_\eta \\ &\quad + d(\xi,\eta,\psi_\xi,\psi_\eta)\nabla^2\psi \end{aligned} \tag{A.17}$$

with

$$a(\xi,\eta) = \frac{1}{ReJ}, \quad b(\xi,\eta,\psi_\xi,\psi_\eta) = \frac{1}{J}\left(-\frac{2C}{Re} - \psi_\eta\right),$$

$$c(\xi,\eta,\psi_\xi,\psi_\eta) = \frac{1}{J}\left(-\frac{2D}{Re} + \psi_\xi\right), \quad d(\xi,\eta,\psi_\xi,\psi_\eta) = \frac{1}{J}\left(\frac{E}{Re} + C\psi_\eta - D\psi_\xi\right).$$

The equation (A.17) is the transient biharmonic pure stream function form of the N-S equations in conformably transformed computational plane.

For steady flows considering $\frac{\partial}{\partial t} \equiv 0$ we obtain from equation (A.16)

$$\begin{aligned} \nabla^4\psi &= \big(2C + Re\psi_\eta\big)\nabla^2\psi_\xi + \big(2D - Re\psi_\xi\big)\nabla^2\psi_\eta \\ &\quad -\big(E + CRe\psi_\eta - DRe\psi_\xi\big)\nabla^2\psi, \end{aligned} \tag{A.18}$$

which is the steady biharmonic pure stream function form of the N-S equations in conformably transformed computational plane.

Bibliography

[1] Anderson Jr. JD, *Computational Fluid dynamics*, McGraw-Hill, New York, 1995.

[2] Batchelor GK, *An Introduction to Fluid Dynamics*, Cambridge University Press, Cambridge, 1993.

[3] Chung TJ, *Computational Fluid Dynamics*, Cambridge University Press, Cambridge, 2002.

[4] Kelly CT, *Iterative Methods for Linear and Nonlinear Equations*, SIAM Publications, Philadelphia, 1995.

[5] Landau LD and Lifshitz EM, *Fluid Mechanics*, Second Edition, Buterworth, Oxford, 1995.

[6] Panton RL, *Incompressible Flow*, Third Edition, Wiley India, New Delhi, 2006.

[7] Papamichael N and Stylianopoulos N, *Numerical Conformal Mapping Domain Decomposition and the Mapping of Quadrilaterals*, World Scientific Publishing Company, 2010.

[8] Pope SB, *Turbulent Flows*, Cambridge University Press, Cambridge, 2000.

[9] Roache P, *Verification and Validation in Computational Science and Egineering*, Hermosa Publishers, Albuquerque, 1998.

[10] Schinzinger R and Laura PAA, *Conformal Mapping Methods and Applications*, Dover Publication, New York, 2003.

[11] Schlichting H and Gersten K, *Boundary Layer Theory*, Eighth Edition, Springer-Verlag, New Delhi, 2001.

[12] Smith GD, *Numerical Solution of Partial Differential Equations: Finite Difference Methods*, Third Edition, Oxford University Press, New York, 1986.

[13] Tennhil JC, Anderson DA and Pletcher RH, *Computational Fluid Mechanics and Heat Transfer*, Second Edition, Taylor & Francis, Washington, 1997.

[14] Van Dyke M, *An Album of Fluid Motion*, The Parabolic Press, California, 1988.

[15] Zdravkovich MM, *Flow Around Circular Cylinders; vol 1: Fundamentals*, Oxford University Press, New York, 1997.

[16] Alben S. An implicit method for coupled flow-body dynamics, *J. Comput. Phys.* **227**:4912–4933, 2008.

[17] Altas I, Dym J, Gupta MM and Manohar RP. Multigrid solution of automatically generated high-order discretizations for the biharmonic equation, *SIAM J. Sci. Comput.* **19**:1575–1585, 1998.

[18] Badr HM, Coutanceau M, Dennis SCR and Menard C. Unsteady flow past a rotating circular cylinder at Reynolds numbers 10^3 and 10^4, *J. Fluid Mech.* **220**:459–484, 1990.

[19] Badr HM and Dennis SCR. Time-dependent viscous flow past an impulsively started rotating and translating circular cylinder, *J. Fluid Mech.* **158**:447–488, 1985.

[20] Badr HM, Dennis SCR and Young PJS. Steady and unsteady flow past a rotating circular cylinder at low Reynolds numbers, *Comp. Fluids* **17**:579–609, 1989.

[21] Bearman PW, Downie MJ, Graham MR and Obasaju ED. Forces on cylinders in viscous oscillatory flow at low Keulegan-Carpenter numbers, *J. Fluid Mech.* **154**:337-356, 1985.

[22] Ben-Artzi M, Chorev I, Croisille JP and Fishelov D. A compact difference scheme for the biharmonic equation in planar irregular domains, *SIAM J. Numer. Anal.* **47**:3087–3108, 2009.

[23] Ben-Artzi M, Croisille JP and Fishelov D. Convergence of a compact scheme for the pure streamfunction formulation of the unsteady Navier-Stokes system, *SIAM J. Numer. Anal.* **44**:1997–2024, 2006.

[24] Ben-Artzi M, Croisille JP and Fishelov D. A high order compact scheme for the pure-streamfunction formulation of the Navier-Stokes equations, *J. Sci. Comput.* **42**:216–250, 2010.

[25] Ben-Artzi M, Croisille JP, Fishelov D and Trachtenberg S. A pure-compact scheme for the streamfunction formulation of Navier-Stokes equations, *J. Comput. Phys.* **205**:640–664, 2005.

[26] Berthelsen PA and Faltinsen OM. A local directional ghost cell approach for incompressible viscous flow problems with irregular boundaries, *J. Comput. Phys.* **227**:4354–4397, 2008.

[27] Blackburn HM and Henderson RD. A study of two-dimensional flow past an oscillating cylinder, *J. Fluid Mech.* **385**:255–285, 1999.

[28] Blasius H. Grenzschichten in Flussigkeiten mit kleiner Reibung, *Z. Angew. Math. Phys.* **56**:1–37, 1908.

[29] Bouard R and Coutanceau M. The early stage of development of the wake behind an impulsively started cylinder for $40 < Re < 10^4$, *J. Fluid Mech.* **101**:583–607, 1980.

[30] Brezillon A, Girault G and Cadou JM. A numerical algorithm coupling a bifurcating indicator and a direct method for the computation of Hopf bifurcation points in fluid mechanics, *Comp. Fluids* **39**:1226–1240, 2010.

[31] Brüger A, Gustafsson B, Lötstedt P and Nilsson J. High order accurate solution of the incompressible Navier-Stokes equations, *J. Comput. Phys.* **203**:49–71, 2005.

[32] Chakravarthy S and Anderson D. Numerical Conformal Mapping, *Math. Comput.* **33**:953–969, 1979.

[33] Chen G, Li Z and Lin L-P. A Fast finite difference method for the biharmonic equations on irregular domains and its application to an incompressible Stokes flow, *Adv. Comput. Math.* **29**:113–133, 2007.

[34] Chew YT, Cheng M and Luo SC. A numerical study of flow past a rotating circular cylinder using a hybrid vortex scheme, *J. Fluid Mech.* **299**:35–71, 1995.

[35] Choi JI, Oberoi RC, Edwards JR and Rosati JA. An immersed boundary method for complex incompressible flows, *J. Comput. Phys.* **224**:757–784, 2007.

[36] Chou MH. Numerical study of vortex shedding from a rotating cylinder immersed in a uniform flow field, *Int. J. Numer. Meth. Fluids* **32**:545–567, 2000.

[37] Chou MH and Huang W. Numerical study of high-reynolds-number flow past a bluff object, *Int. J. Numer. Meth. Fluids* **23**:711–732, 1996.

[38] Christov CI, Marinova RS and Marinov TT. Does the stationary viscous flow around a circular cylinder exist for large Reynolds numbers? A numerical solution via variational imbedding, *J. Comput. Appl. Math.* **226**:205–207, 2009.

[39] Collins WM and Dennis SCR. Flow past an impulsively started circular cylinder, *J. Fluid Mech.* **60**:105–127, 1973.

[40] Coutanceau M and Bouard R. Experimental determination of the main features of the viscous flow in the wake of a circular cylinder in uniform translation. Part 2. Unsteady flow, *J. Fluid Mech.* **79**:257–272, 1977.

[41] Coutanceau M and Menard C. Influence of rotation on the near-wake development behind an impulsively started circular cylinder, *J. Fluid Mech.* **158**:399–446, 1985.

[42] Dennis SCR and Chang GZ. Numerical solution for study flow past a circular cylinder at Reynolds numbers up to 100, *J. Fluid Mech.* **42**:471–489, 1970.

[43] Dennis SCR and Young PJS. Steady flow past an elliptic cylinder inclined to the stream, *J. Engrg. Math.* **47**:101–120, 2003.

[44] Ding Y and Kawahara M. Three dimensional linear stability analysis of incompressible viscous flows using the finite element method, *Int. J. Numer Meth. Fluids* **31**:451–479, 1999.

[45] Dütsch H, Durst F, Becker S and Lienhart H. Low-Reynolds-number flow around an oscillating circular cylinder at low Keulegan-Carpenter numbers, *J. Fluid Mech.* **360**:249–271, 1998.

[46] Erturk E. Numerical performance of compact fourth order formulation of the navier-stokes equations, *Commun. Numer. Meth. Engrg.* **24**:2003–2019, 2008.

[47] Fornberg B. A numerical study of steady viscous flow past a circular cylinder, *J. Fluid Mech.* **98**:819–855, 1980.

[48] Franke R, Rodi W and Schonung B. Numerical calculation of laminar vortex-shedding flow past cylinders, *J. Wind Engrg. Ind. Aerodynamics* **35**:237–257, 1990.

[49] Freymuth P. The vortex patterns of dynamic separation: a parametric and comparative study, *Prog. Aerospace Sci.* **22**:161–208, 1985.

[50] Fuchs L and Tillmark N. Numerical and experimental study of driven flow in a polar cavity, *Int. J. Numer. Meth. Fluids* **5**:311–329, 1985.

[51] Giannetti F and Luchini P. Structural sensitivity of the first instability of the cylinder wake, *J. Fluid Mech.* **581**:167–197, 2007.

[52] Goldstein S and Rosenhead L. Boundary layer growth, *Proc. Cad. Phil. Soc.* **32**:392–401, 1936.

[53] Goodrich JW and Sox WY. Time-dependent viscous incompressible Navier-Stokes equations: The finite difference Galerkin formulation and streamfunction algorithms, *J. Comput. Phys.* **84**:207–241, 1989.

[54] Gresho PM. Incompressible fluid dynamics: some fundamental formulation issues, *Annu. Rev. Fluid Mech.* **23**:413–453, 1991.

[55] Gupta MM. High accuracy solutions of incompressible Navier-Stokes equations, *J. Comput. Phys.* **93**:343–359, 1991.

[56] Gupta MM and Kalita JC. A new paradigm for solving Navier-Stokes equations: streamfunction-velocity formulation, *J. Comput. Phys.* **207**:52–68, 2005.

[57] Gupta MM and Kalita JC. New paradigm continued: further computations with streamfunction-velocity formulation for solving Navier-Stokes equations, *Commun. Appl. Analysis* **10**:461–490, 2006.

[58] Gupta MM and Manohar RP. Direct solution of the biharmonic equation using noncoupled approach, *J. Comput. Phys.* **33**:236–248, 1979.

[59] Gupta MM, Manohar RP and Stephenson JW. Single cell high order scheme for the convectiondiffusion equation with variable coefficients, *Int. J. Numer. Meth. Fluids* **4**:641–651, 1984.

[60] He X and Doolen G. Lattice Boltzmann method on curvilinear coordinates system: flow around a circular cylinder *J. Comput. Phys.* **134**:306–315, 1997.

[61] Henshaw WD. A fourth-order accurate method for the incompressible Navier-Stokes equations on overlapping grids, *J. Comput. Phys.* **113**:13–25, 1994.

[62] Henshaw WD, Kreiss H-O and Reyna LGM. A fourth-order accurate difference approximation for the incompressible Navier-Stokes equations, *Comp. Fluids* **23**:575–593, 1994.

[63] Homann F. Einfluss grosser zähigkeit bei strömung um zylinder, *Forsch. auf dem Gebiete des Ingenieurwesens* **7**:1-10, 1936.

[64] Honji H. Starting flows past spheres and elliptic cylinders, *Rep. Res. Inst. Appl. Mech. Kyushu Univ.* **19**:271-281, 1972.

[65] Hu HH, Patankar NA and Zhu N. Direct numerical simulation of fluid-solid systems using the arbitrary Lagrangian Eulerian technique, *J. Comput. Phys.* **169**:427–462, 2001.

[66] Iliadis G and Anagnostopoulos P. Viscous oscillatory flow around a circular cylinder at low Keulegan-Carpenter numbers and frequency parameters, *Int. J. Numer. Meth. Fluids* **26**:403–442, 1998.

[67] Ingham DB. Note on the numerical solution for unsteady viscous flow past a circular cylinder, *J. Fluid Mech.* **31**:815–818, 1968.

[68] Ingham DB. Steady flow past a rotating cylinder, *Comp. Fluids* **11**:351–366, 1983.

[69] Ingham DB and Tang T. A numerical investigation into the steady flow past a rotating circular cylinder at low and intermediate Reynolds numbers, *J. Comput. Phys.* **87**:91–107, 1990.

[70] Ito K and Qiao Z. High order compact MAC finite difference scheme for the Stokes equations: augmented variable approach, *J. Comput. Phys.* **227**:8177–8190, 2008.

[71] Jackson CP. A finite-element study of the onset of vortex shedding in flow past variously shaped bodies, *J. Fluid Mech.* **182**:23-45, 1987.

[72] Jain PC and Rao KS. Numerical solution of unsteady viscous incompressible fluid flow past a circular cylinder, *Phys. Fluids Suppl.* **11**:57-64, 1969.

[73] Kalita JC, Dalal DC and Dass AK. A class of higher order compact schemes for the unsteady two-dimensional convection-diffusion equations with variable convection coefficients, *Int. J. Numer. Meth. Fluids* **38**:1111–1131, 2002.

[74] Kalita JC, Dass AK and Dalal DC. A transformation-free HOC scheme for steady convection-dffusion on non-uniform grids, *Int. J. Numer. Meth. Fluids* **44**:33–53, 2004.

[75] Kalita JC and Gupta MM. A streamfunction-velocity approach for the 2D transient incompressible viscous flows, *Int. J. Numer. Meth. Fluids* **62**:237-266, 2010.

[76] Kalita JC and Ray RK. A transformation-free HOC scheme for incompressible viscous flows past an impulsively started circular cylinder, *J. Comput. Phys.* **228**:5207–5236, 2009.

[77] Kalita JC and Sen S. The (9,5) HOC formulation for the transient Navier-Stokes equations in primitive variable, *Int. J. Numer. Meth. Fluids* **55**:387-406, 2007.

[78] Kang S, Choi H and Lee S. Laminar flow past a rotating circular cylinder, *Phys. Fluids* **11**:3312-3321, 1999.

[79] Karaa S. A high-order compact ADI method for solving three-dimensional unsteady convection-diffusion problems *Numer. Meth. PDE* **22**:983–993, 2006.

[80] Karaa S. High-order difference schemes for 2D elliptic and parabolic problems with mixed derivatives, *Numer. Meth. PDE* **23**:366–378, 2007.

[81] Karaa S and Zhang J. High order ADI method for solving unsteady convection-diffusion problems, *J. Comput. Phys.* **198**:1–9, 2004.

[82] Keulegan GH and Carpenter LH. Forces on cylinders and plates in an oscillating fluid, *J. Res. Natl. Bur. Stand.* **60**:423-440, 1958.

[83] Kiya M, Suzuki Y, Mikio A, and Hagino M. A contribution to the free stream turbulence effect on the flow past a circular cylinder, *J. Fluid Mech.* **115**:151-164, 1982.

[84] Koumoutsakos PK and Leonard A. High-resolution simulations of the flow around an impulsively started cylinder using vortex methods, *J. Fluid Mech.* **296**:1–38, 1995.

[85] Kovasznay LSG. Hot-wire investigation of the wake behind cylinders at low Reynolds numbers, *Proc. R. Soc. Lond. A* **198**:174-190, 1949.

[86] Kumar B and Mittal S. Prediction of the critical Reynolds number for flow past a circular cylinder, *Comput. Meth. Appl. Mech. Engrg.* **195**:6046-6058, 2006.

[87] Kupferman R. A central difference scheme for a pure streamfunction formulation of incompressible viscous flow, *SIAM J. Sci. Comput.* **23**:1–18, 2001.

[88] Lai M-C and Liu H-C. Fast direct solver for biharmonic equation on a disk and its application to incompressible flows, *Appl. Math. Comput.* **164**:679–695, 2005.

[89] Le DV, Khoo BC and Peraire J. An immersed interface method for viscous incompressible flows involving rigid and flexible boundaries, *J. Comput. Phys.* **220**:109-138, 2006.

[90] Lee D and Tsuei YM. A Hybrid adaptive gridding procedure for recirculating fluid flow problems, *J. Comput. Phys.* **108**:122–141, 1993.

[91] Li M, Tang T and Fornberg B. A compact fourth order finite difference scheme for the steady incompressible Navier-Stokes equations, *Int. J. Numer. Meth. Fluids* **20**:1137–1151, 1995.

[92] Lin B and Chandler-Wilde SN. Numerical conformal mapping and mesh generation for polygonal and multiply-connected regions, *J. Hydroinformatics* **02.4**:255–267, 2000.

[93] Loc TP. Numerical analysis of unsteady secondary vortices generated by an impulsively started circular cylinder, *J. Fluid Mech.* **100**:111–128, 1980.

[94] Loc TP and Bouard R. Numerical solution of the early stage of the unsteady viscous flow arround a circular cylinder: a comparison with experimental visualization and measurements, *J. Fluid Mech.* **160**:93-117, 1985.

[95] Lugt HJ and Haussling HJ. Laminar flow past an abruptly accelerated elliptic cylinder at 45° incidence, *J. Fluid Meeh.* **65**:711-734, 1974.

[96] Mai-Duy N, Howard S and Thanh T-C. A spectral collocation technique based on integrated Chebyshev polynomials for biharmonic problems in irregular domains, *Appl. Math. Modelling* **33**:284–299, 2009.

[97] Mancera PFA. A study of numerical solution of the steady two dimensional Navier-Stokes equations in a constricted channel problem by a compact fourth order method, *Appl. Math. Comput.* **146**:771–790, 2003.

[98] Mancera PFA and Hunt R. Fourth-order method for solving the Navier-Stokes equations in a constricting channel, *Int. J. Numer. Meth. Fluids* **25**:1119–1135, 1997.

[99] Marquet O, Sipp D and Jacquin L. Sensitivity analysis and passive control of cylinder flow, *J. Fluid Mech.* **615**:221–252, 2008.

[100] Mehta, UB and Lavan Z. Starting vortex, separation bubbles and stall: a numerical study of laminar unsteady flow around an airfoil, *J. Fluid Mech.* **67**:227–256, 1975.

[101] Mittal R, Iaccarino G. Immersed boundary methods, *Annu. Rev. Fluid Mech.* **37**:239–261, 2005.

[102] Mittal S and Kumar B. Flow past a rotating cylinder, *J. Fluid Mech.* **476**:303–334, 2003.

[103] Morikawa K and Grönig H. Formation and structure of vortex systems around a translating and oscillating airfoil, *Z. Flugwiss. Weltraumforsch* **19**:391–396, 1995.

[104] Morzynski M, Afanasiev K and Thiele F. Solution of the eigenvalue problems resulting from global non-parallel flow stability analysis, *Comput. Meth. Appl. Mech. Engrg.* **169**:161–176, 1999.

[105] Nair MT and Sengupta TK. Unsteady flow past elliptic cylinders, *J. Fluid Struct.* **11**:555–595, 1997.

[106] Nisi H and Porter AW. On eddies in air, *Phil. Mag. Ser. 6* **46**:754–768, 1923.

[107] Niu XD, Chew YT and Shu C. Simulation of flows around an impulsively started circular cylinder by Taylor series expansion and least squares-based lattice Boltzmann method, *J. Comput. Phys.* **188**:176–193, 2003.

[108] Nobari MRH and Naderan H. A numerical study of flow past a cylinder with cross flow and inline oscillation, *Comp. Fluids* **35**:393–415, 2006.

[109] Nobari MRH and Ghazanfarian J. A numerical investigation of fluid flow over a rotating cylinder with cross flow oscillation, *Comp. Fluids*, 2009; **38**:2026–2036.

[110] Norberg C. An experimental investigation of the flow around circular cylinder: influence of aspect ratio, *J. Fluid Mech.* **258**:287–316, 1994.

[111] Norberg C. Flow around a circular cylinder: aspects of fluctuating lift, *J. Fluid Struct.* **15**:459–469, 2001.

[112] Ohmi K, Coutanceau M, Loc TP and Dulieu A. Vortex formation around an oscillating and translating airfoil at large incidences, *J. Fluid Mech.* **211**:37–60, 1990.

[113] Ohmi K, Coutanceau M, Daube O and Loc TP. Further experiments on vortex formation around an oscillating and translating airfoil at large incidences, *J. Fluid Mech.* **225**:607–630, 1991.

[114] Padrino JC and Joseph DD. Numerical study of the steady-state uniform flow past a rotating cylinder, *J. Fluid Mech.* **557**:191–223, 2006.

[115] Pandit SK, Kalita JC and Dalal DC. A transient higher order compact scheme for incompressible viscous flows on geometries beyond rectangular, *J. Comput. Phys.* **225**:1100–1124, 2007.

[116] Pandit SK, Kalita JC and Dalal DC. A fourth-order accurate compact scheme for the solution of steady Navier-Stokes equation on non-uniform grids, *Comp. Fluids* **37**:121–134, 2008.

[117] Patel VA, Time dependent solutions of the viscous incompressible flow past a circular cylinder, *Comp. Fluids* **4**:13–27, 1976.

[118] Patel VA. Flow around the impulsively started elliptic cylinder at various angles of attack, *Comp. Fluids* **9**:435–462, 1981.

[119] Peng YF, Mittal R, Sau A and Hwang RR. Nested Cartesian grid method in incompressible viscous fluid flow, *J. Comput. Phys.* **229**: 7072–7101, 2010.

[120] Perry AE, Chong MS and Lim TT. The vortex-shedding process behind two-dimensional bluff bodies, *J. Fluid Mech.* **116**:77–90, 1982.

[121] Protas B and Wesfreid JE. Drag force in the open-loop control of the cylinder wake in the laminar regime, *Phys. Fluids* **14**:810–826, 2002.

[122] Roshko A. On the wake and drag of bluff bodies, *J. Aeronaut. Sci.* **22**:124–132, 1955.

[123] Sanyasiraju YVSS and Manjula V. Flow past an impulsively started circular cylinder using a higher-order semi compact scheme, *Phys. Rev. E* **72**:1–10, 2005.

[124] Sanyasiraju YVSS and Manjula V. Fourth-order semi-compact scheme for flow past a rotating and translating cylinder, *J. Sci. Comput.* **30**:389–407, 2007.

[125] Schreiber R and Keller HB. Driven cavity flows by efficient numerical techniques, *J. Comput. Phys.* **49**:310–333, 1983.

[126] Schuh H. Calculation of unsteady boundary layers in two dimensional laminar flow, *Z. Fluqwiss* **1**:122–133, 1953.

[127] Sengupta TK and Bhumkar YG. New explicit two-dimensional higher order filters, *Comp. Fluids* **39**:1848–1863, 2010.

[128] Sengupta TK, Lim TT, Sajjan SV, Ganesh S and Soria J. Accelerated flow past a symmetric aerofoil: experiments and computations, *J. Fluid Mech.* **591**:255–288, 2007.

[129] Sengupta TK, Singh N and Suman VK. Dynamical system approach to instability of flow past a circular cylinder, *J. Fluid Mech.* **656**:82–115, 2010.

[130] Sengupta TK, Suman VK and Singh N. Solving Navier-Stokes equation for flow past cylinders using single-block structured and overset grids, *J. Comput. Phys.* **229**:178-199, 2010.

[131] Shen WZ and Loc TP. Simulation of 2D external viscous flows by means of a domain decomposition method using an influence matrix technique, *Int. J. Numer. Meth. Fluids* **20**:1111–1136, 1995.

[132] Shen WZ and Loc TP. A coupling finite difference/particle method for the resolution of 2D Navier-Stokes equations in velocity-vorticity form, *Aerospace Science and Technology* **2**:97–109, 1997.

[133] Shiels D and Leonard A. Investigation of a drag reduction on a circular cylinder in rotary oscillation, *J. Fluid Mech.* **431**:297-322, 2001.

[134] Silva ALFLE, Silveira-Neto A and Damasceno JJR. Numerical simulation of two-dimensional flows over a circular cylinder using the immersed boundary method, *J. Comput. Phys.* **189**:351–370, 2003.

[135] Sleijpen GLG and van der Vorst HA. Hybrid bi-conjugate gradient methods for CFD problems, *Comput. Fluid Dyn. Rev.*, 1995.

[136] Soria J, New TH, Lim TT and Parker K. Multigrid CCDPIV measurements of accelerated fow past an airfoil at an angle of attack of 30^0, *Expe. Ther. Fluid Sci.* **27**:667–676, 2003.

[137] Spotz WF and Carey GF. High-order compact scheme for the steady stream-function vorticity equations, *Int. J. Numer. Meth. in Engrg.* **38**:3497–3512, 1995.

[138] Spotz WF and Carey GF. Formulation and experiments with high-order compact schemes for nonuniform grids, *Int. J. Numer. Meth. Heat and Fluid Flow* **8**:288–303, 1998.

[139] Spotz WF and Carey GF. Extension of high-order compact schemes to time dependent problems, *Numer. Meth. PDE* **17**:657–672, 2001.

[140] Stephenson JW. Single cell discretization of order two and four for biharmonic problems, *J. Comput. Phys.* **55**:65–80, 1984.

[141] Strikwerda JC. High-order accurate schemes for incompressible viscous flow, *Int. J. Numer. Meth. Fluids* **24**:715–734, 1997.

[142] Takami H and Keller HB. Steady two-dimensional viscous flow of an incompressible fluid past a circular cylinder, *Phys. Fluids* **12**(Suppl. II):11–51, 1969.

[143] Taneda S. Downstream development of wakes behind cylinders, *J. Phys. Soc. Jpn.* **14**:843–848, 1959.

[144] Taneda S. Visual study of unsteady separated flows around bodies, *Prog. Aerospace Sci.* **17**:287-348, 1977.

[145] Tatsuno M and Bearman PW. A visual study of the flow around an oscillating circular cylinder at low Keulegan-Carpenter numbers and low Stokes numbers, *J. Fluid Mech.* **211**:157–182, 1990.

[146] Thiria B, Durand SG and Wesfreid JE. The wake of a cylinder performing rotary oscillations, *J. Fluid Mech.* **560**:123–147, 2006.

[147] Thompson JF, Warsi ZUA and Mastin CW. Boundary-fitted coordinate systems for numerical solution of partial differential equations-a review, *J. Comput. Phys.* **47**:1–108, 1982.

[148] Tokumaru PT and Dimotakis PE. Rotary oscillation control of a cylinder wake, *J. Fluid Mech.* **224**:77-90, 1991.

[149] Tritton DJ. Experiments on the flow past a circular cylinder at low Reynolds numbers, *J. Fluid Mech.* **6**:547–567, 1959.

[150] Tryggvason G, Bunner B, Esmaeeli A, Juric D, Al-Rawahi N, Tauber W, Han J, Nas S and Jan Y-J. A front-tracking method for the computations of multiphase flow, *J. Comput. Phys.* **169**:708–759, 2001.

[151] Uzunoğlu B, Tan M, and Price WG. Low-Reynolds-number flow around an oscillating circular cylinder using a cell viscous boundary element method, *Int. J. Numer. Meth. Fluids* **50**:2317–2338, 2001.

[152] Wang S and Zhang X. An immersed boundary method based on discrete stream function formulation for two- and three-dimensional incompressible flows, *J. Comput. Phys.* **230**:3479–3499, 2011.

[153] Wang Z, Fan J and Cen K. Immersed boundary method for the simulation of 2D viscous flow based on vorticity-velocity formulations, *J. Comput. Phys.* **228**:1504–1520, 2009.

[154] Watson EJ. Boundary layer growth, *Proc. R. Soc. Lond. (A)* **231**:104–116, 1955.

[155] Weinan E and Liu J-G. Essentially compact schemes for unsteady viscous incompressible flows, *J. Comput. Phys.* **126**:122–138, 1996.

[156] Williamson CHK. Sinusoidal flow relative to circular cylinders, *J. Fluid Mech.* **155**:141–174, 1985.

[157] Williamson CHK. Oblique and parallel modes of vortex shedding in the wake of a circular cylinder at low Reynolds numbers, *J. Fluid Mech.* **206**:579–627, 1989.

[158] Williamson CHK. Vortex dynamics in the cylinder wake, *Ann. Rev. Fluid Mech.* **28**:477–539, 1996.

[159] Zdravkovich MM. Smoke observation of the observation of a Karman vortex street, *J. Fluid Mech.* **37**:491–496, 1969.